

# Solid Freeform Fabrication of Porous Calcium Polyphosphate Structures for Use in Orthopaedics

by

Yaser Shanjani

A thesis  
presented to the University of Waterloo  
in fulfillment of the  
thesis requirement for the degree of  
Doctor of Philosophy  
in  
Mechanical Engineering

Waterloo, Ontario, Canada, 2011

©Yaser Shanjani 2011

## **Author Declaration**

I hereby declare that I am the sole author of this thesis. This is a true copy of the thesis, including any required final revisions, as accepted by my examiners.

I understand that my thesis may be made electronically available to the public.

## Abstract

The focus of this dissertation is on the development of a solid freeform fabrication (SFF) process for the design and manufacture of porous biodegradable orthopaedic implants from calcium polyphosphate (CPP). Porous CPP structures are used as bone substitutes for regenerating bone defects and/or as substrates in formation of so-called “biphasic” implants for repair of damaged osteochondral tissues. The CPP implants can be utilized in the treatment of many musculoskeletal diseases, osteochondral defects, and bone tumours while replacement of the defect site is required.

In this study, the fabrication of CPP structures was developed through a powder-based SFF technique known as adhesive bonding 3D-printing. SFF is an advanced alternative to the “conventional” fabrication method consisting of gravity sintering of CPP pre-forms followed by machining to final form, as SFF enables rapid manufacturing of complex-shaped bio-structures with controlled internal architecture. To address the physical and structural properties of the porous SFF-made components, they were characterized using scanning electron microscopy, micro-CT scanning and mercury intrusion porosimetry. Specific surface area and permeability of the porous structures were also determined. Additionally, the chemical properties (crystallinity) of the specimens were identified by X-ray diffraction. The mechanical properties of the crystalline CPP material were also measured by micro- and nano-indentation. Moreover, the porous structures were tested by uniaxial and diametral mechanical compression to determine the compressive and tensile strengths, respectively. Furthermore, the effect of the stacked-layer orientation on the mechanical properties of the SFF-made constructs was investigated through the production of samples with horizontal or vertical stacked-layers. The properties of the SFF-made samples were compared with those of the conventionally-made CPP constructs. The SFF-made implants showed drastically higher compressive mechanical strength compared to the conventionally-formed samples with identical porosity. It was also shown that the orientation of the stacked-layer has substantial influence on the mechanical strengths.

Moreover, this thesis examined the ability of *in vitro* forming of cartilaginous tissue on the SFF-made substrates where the chondrocytes cellular response to the CPP implants was evaluated histologically and biochemically. In addition, an initial *in vivo* assessment of the CPP structures as bone substitutes was conducted using a rabbit medial femoral site model. Significant amount of new-bone was formed within the CPP porous constructs during the 6-week implantation period demonstrating appropriate biological response of SFF-made CPP structures for bone substitute applications.

Another accomplishment of this thesis was the development of a mathematical model which predicts the compact density of powder layers spread by a counter-rotating roller in the SFF technique. The results may be used in the control of the apparent density of the final implant.

The potential of the developed SFF method as an efficient and reproducible technique for the production of porous CPP structures for use in orthopaedics and musculoskeletal tissue regenerative applications was concluded.

## Acknowledgments

I would like to use this opportunity to thank the many people who helped me during the course of my Ph.D. research and study.

I would like to express my sincere gratitude to my supervisor, Dr. Ehsan Toyserkani, for his constant support, advice, and encouragement throughout the duration of this study. More than a supervisor, he has been a friend for me and encouraged me to achieve higher level of successes in my current and future career.

I'm deeply grateful to my supervisor, Prof. Robert M. Pilliar, for his supervision, guidance, encouragement, patience and support from the time that he generously accepted me as his student to the concluding stage of my thesis. Dr. Pilliar, I benefited from your very wise suggestions and kind mentorship, and it has truly been an honour for me working with a thoughtful scientist and genuine person like you.

I hereby acknowledge my thesis examining committee members Dr. Scott Hollister from the University of Michigan, Dr. John B. Medley, Dr. Maud Gorbet, Dr. William Melek, and Dr. Kaan Erkorkmaz from the University of Waterloo, for reviewing my thesis and providing useful comments. I would also like to thank professors, Dr. Naveen Chandrashekar, Dr. Sanjeev Bedi, Dr. Maud Gorbet, Dr. Steve F. Corbin, Dr. N. Venkata Reddy and Dr. Ajay Batish, whose classes I have attended during my Ph.D. at the University of Waterloo. They taught me the valuable knowledge I needed for my research. I would like to thank Dr. Mirahmadi and Dr. Sadodin, my B.Sc. and M.Sc. supervisors, who introduced the field of additive manufacturing to me and provided the opportunity for me to start my research in that area.

It is a pleasure to thank all the researchers in our wonderful collaborative group working on CPP project: Dr. Rita Kandel, Dr. Mark Gryn timer and Dr. N.J. Amritha De Croos from Mount Sinai Hospital, Dr. Mark Hurtig from Guelph University, Dr. Paul Zalzal from McMaster University, and Dr. Marcello Papini from Ryerson University for their supportive collaboration and guidance. It was fortunate for me that I had the opportunity to work with such a prestigious research group. This thesis would not have been possible without the collaboration of Eugene Hu and Svitlana Prada in the Institute of Biomaterial and Biomedical Engineering at the University of Toronto for CPP sintering. Many thanks for their patience and help. I would also like to thank the technical assistance and suggestions from Dr. Rizhy Wang from the University of British Columbia for nano-indentation, Ms. Nancy Valiquet from the University of Toronto for the *in vivo* test, Dr. N.J. Amritha De Croos from Mount Sinai Hospital for the *in vitro* cell culturing, Dr. Michel Furtado Araujo from the University of Toronto for micro-CT

scanning, Dr. Xiaogang Li, Yuquan Ding from the University of Waterloo for SEM imaging, Mehrdad Jabbarzadeh Gangeh from the University of Waterloo for image processing, Dr. Abolfazl Maneshi from the University of Waterloo for powder processing.

I would like to show my gratefulness to my friends and colleagues in the Multi-Scale Additive Manufacturing Laboratory at the University of Waterloo, Dr. Hamidreza Alemohammad, Mihaela Vlasea, Dr. Ehsan Forouzmeh, Ahmad Basalah, Negar Rasti, Dr. Masoud Alimardani, Christina Wei, Hanieh Aghighi, Hajar Sharif, and Ash Charls. For their assistance with some of my experimental tests and analysis, I wish to express my appreciation to undergraduate and co-op students, Dorothy Lui, Derek Yan, Jean Nassar, Sarah Mayer, and Ahmed Salam.

I would also like to acknowledge the Government of Ontario for Ontario Graduate Scholarship (OGS), University of Waterloo for President's Graduate Scholarship, International Doctoral Student Award, Doctoral Thesis Completion Award, and UW Graduate Scholarships, and Mr. Robbert Hartog for Robbert Hartog Graduate Scholarship, and the financial support from the Canadian Institutes of Health Research (CIHR), and the Natural Resources and Engineering Research Council (NSERC) of Canada.

It is a pleasure to thank my friends who were supportive since my arrival to Canada for studying and during the last five years, Mojtaba Haghghi, Arash Tajik, Hamidreza Alemohammad, Mihaela Vlasea, Mohammad Fakharzadeh, and Farjad Shadmehri, as well as my wonderful officemates, Jaho Seo and Morvarid Karimi. I had wonderful time with you and I would never forget your kindness towards me.

I owe my deepest gratitude to my beloved parents, Fariba and Yaghoub, who scarified themselves to raise me with faith, and were always supportive of anything I pursued in life. They have inspired me towards engineering and research. Thanks to my brother, Younes, for always being there for me. I would also like to thank my family in law for their kindness and support. Special thanks to my lovely wife, Salma, for her understanding and patiently supporting, which made this dissertation possible.

Lastly, I offer my regards to all of those who supported me in any respect during my education since primary school. It would have been next to impossible to do this thesis without what you taught me.

*To those who restlessly try to improve people's quality of life*

# Contents

Author’s Declaration .....	ii
Abstract.....	iii
Acknowledgments.....	v
Dedication.....	vii
Table of Contents.....	viii
List of Figures.....	xi
List of Tables.....	xvii
<b>Chapter 1 – Introduction and Literature Review.....</b>	<b>1</b>
1.1    Current Treatments for Bone and Cartilage Repair .....	2
1.1.1    Bone Defect Repair .....	2
1.1.2    Osteochondral Defects Repair .....	5
1.2    Calcium Polyphosphate.....	8
1.2.1    Calcium Polyphosphate for Bone and Osteochondral Regeneration.....	11
1.3    Fabrication of Bone Substitute and Osteochondral Implants.....	13
1.3.1    Conventional Fabrication Methods .....	13
1.3.2    Solid Freeform Fabrication.....	14
1.4    Motivations.....	23
1.5    Thesis Objectives .....	25
1.6    Thesis Outline.....	25
<b>Chapter 2 - Solid Freeform Fabrication of Calcium Polyphosphate Structures.....</b>	<b>26</b>
2.1    SFF Process: Materials and Methods .....	26
2.1.1    Materials.....	26
2.1.2    SFF of Porous CPP Structures .....	31
2.1.3    Conventional Fabrication of CPP .....	37
2.2    Characterization of the SFF process.....	39
2.2.1    SFF Dimensional Deviation Measurement.....	39
2.2.2    Sintering Shrinkage Measurement .....	40
2.3    SFF of CPP Structures with Geometrical Complexity .....	41
2.3.1    Anatomically-Shaped Structures .....	42
2.3.2    CPP implants with Channels .....	43
2.3.3    Dual-Structural Porous CPP constructs.....	47



2.3.4	CPP Structures with Macro-pores.....	50
2.4	Summary.....	52
<b>Chapter 3</b>	<b>– Characterization of SFF-made CPP Structures .....</b>	<b>53</b>
3.1	Structural Characteristics .....	53
3.1.1	Scanning Electron Microscopy (SEM) .....	53
3.1.2	Micro-CT Scanning.....	55
3.2	Physical Characteristics .....	58
3.2.1	Porosimetry Analysis .....	58
3.2.2	Specific Surface Area.....	64
3.2.3	Permeability.....	64
3.3	Chemical Characteristics.....	64
3.3.1	X-Ray Diffraction (XRD) Analysis .....	64
3.4	Mechanical Characteristics.....	65
3.4.1	Mechanical Properties of CPP Materials.....	65
3.4.2	Structural Mechanical Properties .....	71
3.5	Discussion .....	77
3.5.1	Discussion of the Anisotropic Properties of SFF-made CPP Structures.....	80
3.5.2	Prediction of Fracture Strength of Porous CPP Structures in Complex Loading Conditions.....	86
3.6	Summary.....	88
<b>Chapter 4</b>	<b>– Biological Response of CPP Constructs.....</b>	<b>90</b>
4.1	<i>In vivo</i> Performance of Porous CPP Bone Substitutes .....	90
4.1.1	CPP Plug Implantation Process.....	90
4.1.2	Qualitative Evaluation of Bone Ingrowth.....	92
4.1.3	Quantitative Analysis of Bone Ingrowth .....	97
4.1.4	Histology Analysis.....	104
4.2	<i>In vitro</i> Performance of CPP Substrates for Biphasic Osteochondral Implants .....	107
4.2.1	<i>In vitro</i> Articular Cartilage Formation on CPP Substrate .....	107
4.2.2	Assessment of Cultured Cartilage .....	108
4.3	Summary.....	112
<b>Chapter 5</b>	<b>– Effects of SFF Process Parameters on the Relative Density of SFF-made Structures: Mathematical Modeling .....</b>	<b>113</b>
5.1	Introduction .....	113
5.2	Mathematical Modeling.....	115

5.2.1	Model Description.....	115
5.2.2	Force Equilibrium and Constructive Model.....	118
5.3	Results and Discussion.....	122
5.4	Summary.....	129
<b>Chapter 6</b>	<b>– Conclusion and Future Work.....</b>	<b>130</b>
6.1	Conclusive Summary.....	130
6.2	Recommendations and Future Work.....	132
<b>Appendices</b>		
	Appendix A.....	139
	Material Properties of Polyvinyl Alcohol and Zb <sup>TM</sup> 58 Solvent.....	139
	Appendix B.....	140
	B-1. Permeability Calculation Procedure.....	140
	B-2. Fracture Criteria for SFF-H and CS CPP Discs.....	143
	Appendix C.....	144
	In Vivo Analysis Data.....	144
	C-1. Implantation Planning.....	144
	C-2. In Vivo Samples Image Processing Data.....	145
	C-3. MATLAB Code for Processing of BSE Images.....	148
	Appendix D.....	150
	Mathematical Modeling of Powder Compaction.....	150
	D-1. MATLAB Code.....	150
	D-2. Proposed Experimental Setup.....	152
	<b>References.....</b>	<b>155</b>

# List of Figures

Figure 1-1: Schematic of a biphasic osteochondral implant composed of scaffold for a porous bone substitute component and a scaffold-free *in vitro*-cultured cartilage component as shown in (a). The cartilage component will merge with the native cartilage while bone grows into the porous substitute after implantation as shown in (b). .....7

Figure 1-2: Schematic of adhesive bonding 3D-printer adapted from. The single steps of 3DP are symbolically depicted..... 16

Figure 1-3: Schematic of SFF process for production of anatomically-shaped implants..... 17

Figure 1-4: Schematic of the staircase effect. The boundary of layer-by-layer made structure does not match with the boundary of CAD model based on the curvature of the surface. The staircase effect influences the exterior surface of parts and causes high surface roughness. .... 22

Figure 2-1: SEM of PVA-CPP blend powder. PVA (smaller) and CPP (larger) particles are depicted. .... 28

Figure 2-2: SEM image of the as-received CPP powder; arrows depicted some of the dimensions greater than 150  $\mu\text{m}$ . .... 29

Figure 2-3: Distribution of CPP powder particles size: (a) Diagram showing the volume percent of particle diameters measured by modular particle size analyzer. The dashed lines signify the sieve range used to prepare the CPP powder (i.e. 75-150  $\mu\text{m}$ ), (b) 3D histogram of length and width of particles. .... 30

Figure 2-4: Retrofitted ZPrinter for prototyping of complex parts from biomaterials ..... 32

Figure 2-5: PVA connections between CPP particles in the green part before sintering (SEM image): PVA bonds connect the adjacent CPP particles together..... 33

Figure 2-6: Heat treatment protocol used for sintering of SFF-made CPP green parts..... 35

Figure 2-7: SEM images of final sintered SFF-made CPP structure showing all the PVA has been removed during the high temperature post-SFF process. .... 35

Figure 2-8: SFF-made cylindrical sample after post-sintering. The diameter and the height of the sample are 4 and 6 mm, respectively. .... 36

Figure 2-9: Schematic of: (a) SFF process showing the orientation of layers in xyz coordination, (b) SFF-V and (c) SFF-H cylinders; cylinders axes are perpendicular and parallel to the layers, respectively. .... 37

Figure 2-10: Detailed drawing of the platinum sintering crucible including Pt tube and base-mount: (a) dimensions of tube, (b) sectioned assembly view (adapted from [52]).. 38

Figure 2-11: Femoral condyle CPP implant: (a) CAD 3D model, (b) SFF-made part. ....	42
Figure 2-12: Fabricated medial portion of tibial plateau-shaped CPP structure; the top surface is intended for in vitro cartilage formation while bone ingrowth into the other surfaces allowing implant fixation to subchondral bone. ....	43
Figure 2-13: Detailed drawing of cylinders with 3 longitudinal channels.....	44
Figure 2-14: A randomly selected SFF-made CPP cylinder with 3 longitudinal channels. ....	44
Figure 2-15: SEM images of CPP cylinder with 3 channels: (a) radial cross section, (b) longitudinal cross section. ....	45
Figure 2-16: A lattice-shaped CPP sample fabricated using 45-75 $\mu\text{m}$ powder.....	46
Figure 2-17: A micro-channel in CPP lattice-shaped structure. Channels of 300 $\mu\text{m}$ were formed in the structure.....	46
Figure 2-18: A SFF-made proximal tibial-shaped CPP structure with straight micro-channels of $\sim 600 \mu\text{m}$ .....	47
Figure 2-19: Dual-porous structure CPP sample before sintering.....	48
Figure 2-20: SEM of the sintered dual-porous CPP sample: (a) 100X and (b) 50X. A transition region is depicted between fine and coarse regions. ....	49
Figure 2-21: Macro-pores generated through porogen leaching: (a) visual distribution and relative size of macro-pores, (b) a macro-pore of about 500 $\mu\text{m}$ . ....	51
Figure 3-1: SEM images (with different magnification levels) of final sintered SFF-made (SFF-V) CPP cylinder showing the three-dimensional interconnected porosity of the samples. ....	54
Figure 3-2: Micro-tomography of (a) CS, (b) SFF-V, and (c) SFF-H samples, top: radial cross sections, bottom: longitudinal cross section. The relatively-uniform distribution and interconnectivity of the pores are observed in the cross sections of all samples. ....	56
Figure 3-3: 3D models of (a) CS, (b) SFF-V, and (c) SFF-H samples generated using the micro-CT scans.....	57
Figure 3-4: Mercury intrusion porosimetry data of the sintered CPP cylinders. SFF-made (SFF-V) and CS structures have 5–258 and 5–225 $\mu\text{m}$ pore size range as well as 50 and 33 $\mu\text{m}$ mean pore sizes, respectively. ....	60
Figure 3-5: Micro-structure data of the SFF-V, SFF-H and CS CPP samples obtained by micro-CT scanning: (a) pore size distribution in the range of 5-140 $\mu\text{m}$ for SFF-made and 5-80 $\mu\text{m}$ for CS samples, (b) trabecular thickness distribution in the range of 20-160 $\mu\text{m}$ for SFF-made and 10-120 $\mu\text{m}$ for CS samples.....	62

Figure 3-6: Micro-structural properties of the (a) CS and (b) SFF-V samples obtained by micro-CT scanning: (left) pore size distribution color-map, (right) trabecular thickness distribution color-map. ....	63
Figure 3-7: XRD patterns of SFF-made and CS. The patterns are identical but there are small discrepancies in the peak intensities of the XRD patterns of SFF-made and CS samples. ....	65
Figure 3-8: Schematic of the nano-indentation process: SFF-V and SFF-H samples were tested in both parallel and perpendicular directions to the stacked-layers. ....	67
Figure 3-9: Typical load-displacement curves of nano-indentation on SFF-V, SFF-H and CS CPP samples. SFF-made parts are examined in two directions: parallel and perpendicular to layers. ....	67
Figure 3-10: Typical curves of (a) elastic modulus-displacement and (b) hardness-displacement obtained via nano-indentation on SFF-V, SFF-H and CS CPP samples. SFF-made parts are examined in two directions: parallel and perpendicular to layers. ....	68
Figure 3-11: Optical microscopic images of Vickers micro-indentation finger prints on CPP: (a) CS and (b) SFF-made samples. Sinter neck areas were targeted for indentation to measure the hardness on the formed neck. ....	70
Figure 3-12: Typical load-displacement curves of the sintered 6mm long SFF-V, SFF-H, and CS cylinders. The uniaxial compressive load was applied along the height of the cylinders with the crosshead rate of 0.2 mm/min. ....	72
Figure 3-13: Failure probability of sintered SFF-V, SFF-H, and CS samples under uniaxial compression. The quite similar slopes of the regression lines indicate that the Weibull moduli of all the samples are the same. ....	73
Figure 3-14: SEM images of fracture cleavage surface of (a) CS, (b) SFF-V and (c) SFF-H samples under the compressive load. The images indicate that the fractures occur in the CPP sinter neck regions. Bottom: Bitmap picture of the fracture cleavage areas. The fractures areas are shown in black. The portion of the black regions was calculated as shown. ....	74
Figure 3-15: Diametral compression test of a CPP cylindrical discs with 4 mm diameter and 2 mm height loaded along its diameter. A crack was occurred by the tensile stress appeared in the transverse direction of loading. ....	76
Figure 3-16: Failure probability of sintered SFF-V, SFF-H and CS samples under diametral compression. ....	77
Figure 3-17: Micro-pores located on the surface and within a sinter neck act as a source for crack initiation. ....	80
Figure 3-18: Schematic of spreading and compaction of CPP powder in the SFF process: CPP particles with the length larger than 150 $\mu\text{m}$ rotate and obtain a preferred orientation to fit best within the 150 $\mu\text{m}$ stacked-layers. ....	81

Figure 3-19: SEM images of fabricated CPP green part (SFF-V sample): (a) side view and (b) top view of stacked layers. The CPP particles have achieved a preferred orientation with their larger and flatter sides parallel to the stacked layers (top view) with inter-particle connections at their smaller facets and sharper edges in the orthogonal direction (pinpointed by arrows). ..... 82

Figure 3-20: SEM images showing contacts between CPP particles within the SFF-made green parts: (a) large facet contacts parallel to the layers with low driving force for sinter neck initiation and growth versus (b) sharp corners contacts across the layers that cause sinter neck initiation and growth with high rate during the viscous sintering process of CPP. .... 83

Figure 3-21: Schematic of CPP particles orientation and particle-particle contacts in the powder layer spread by counter rotating roller in SFF process: small facet-to-small facet contacts (A) i.e., small radii of curvature contacts occur in the direction parallel to stacked-layers while large facet-to-large facet contacts (B) i.e., large radii of curvature contacts occur in the direction normal to stacked-layers. .... 84

Figure 3-22: Failure elliptical iso-surfaces of SFF-V, SFF-H and CS CPP discs based on the Hoffman’s orthogonal brittle fracture criteria. SFF-V discs show higher strength (larger volume) with a symmetry in x and y directions (symmetry plane of 45°). SFF-H is stronger in x direction rather than y direction (symmetry plane smaller than 45°). CS discs are comparably weaker than SFF-made ones. .... 88

Figure 4-1: Implantation of CPP plugs in the defect site: (a) prepared defect site, (b) inserted CPP plug in the defect site. .... 91

Figure 4-2: Schematic of CPP implant inserted in the drilled defect site in the medial distal femur. Femur bone is shown from the distal view. .... 91

Figure 4-3: BSE images of radial cross sections: (a) SFF-V, (b) SFF-H and (c) CS samples. ... 93

Figure 4-4: BSE images of longitudinal cross sections(a) SFF-V, (b) SFF-H and (c) CS samples. .... 94

Figure 4-5: BSE images showing the integration of CPP constructs and host bone in the interface of (a) SFF-V, (b) SFF-H, and (c) CS implants and surrounding bone. .... 96

Figure 4-6: BSE images showing new bone formed in the core region of CPP implants in (a) SFF-V, (b) SFF-H, and (c) CS samples. .... 96

Figure 4-7: Schematic of sectioning of inserted CPP implants. Each implant was sectioned longitudinally and cross-sectionally related to femur and trough the center of the implant, generating four implant surfaces (anterior, posterior, distal and proximal) for quantitative analysis of bone ingrowth ..... 97

Figure 4-8: (a) BSE image of CPP implant containing new bone, (b) the segmented image of the BSE image representing three distinct regions: CPP (white), bone (grey) and void (black). .... 98

Figure 4-9: Percentage of voids that is filled with new bone in SFF-V, SFF-H, and CS CPP implants in the anterior (ANT), posterior (POST), distal (DIST), and proximal (PROX) aspects. No significant difference was observed between the CPP implant types and the different aspect in terms of the amount of bone ingrowth.....	99
Figure 4-10: Percentage of absolute amount of bone growth within the implants in SFF-V, SFF-H, and CS CPP implants in the anterior (ANT), posterior (POST), distal (DIST), and proximal (PROX) aspects. No significant difference was observed between the CPP implant types in terms of the amount of bone ingrowth.....	101
Figure 4-11: Percentage of degradation of SFF-V, SFF-H, and CS CPP implants in the anterior (ANT), posterior (POST), distal (DIST), and proximal (PROX) aspects.....	102
Figure 4-12 Histology image of a SFF-H implant (as a representative of SFF-made samples): green color represents for the mineralized bone tissue. Significant bone ingrowth is observed filling the pores of implant.....	105
Figure 4-13: Histology image (SFF-H): mineralized bone (green), osteoid (blue), and connective tissue (purple). Osteoids are actively forming new bone.....	106
Figure 4-14: Cartilage tissue cultured on top of CPP substrate.....	108
Figure 4-15: Biochemical comparison of SFF-made to CS. Cartilage cells were seeded as described in the Methods section on to the top surfaces of SFF-made and CS and cultured for 3 weeks. SFF-made was suitable as a substrate for cartilage tissue formation as there was no significant difference in DNA, proteoglycan (GAG), or collagen (OH-proline) content in SFF-made compared to CS. Results are pooled and expressed as mean $\pm$ standard error of the mean ( $n = 16$ ).....	109
Figure 4-16: Histological appearance of tissues after 3 weeks of culture. Substrates were seeded with cartilage cells as described in the methods section, grown for 3 weeks and removed from the top surface of SFF-made and CS substrates, fixed in formalin, and stained with (a) hematoxylin and Eosin or (b) toluidine blue. Left side of figure: SFF-made, Right side of figure: CS. * indicates where substrate was located.....	111
Figure 5-1: Schematic of powder spreading and compacting process via counter-rotating roller in the build chamber.....	114
Figure 5-2: Schematic diagram of forces and stresses acting on the powder densification zone. The loose powder is gradually compacted (as shown by darker gray-scale) by the roller pressure. A slab of powder with an infinitely small thickness is depicted on which the applied stresses are determined.....	117
Figure 5-3: Variation of normal contact pressure distribution along the densification zone (calculated for $\mu_p=0.5$ , $h_s=130 \mu\text{m}$ (0.005 in), $R=10 \text{ mm}$ , $\rho_{\text{initial}}=30\%$ , and $\alpha_{\text{in}}=0.2 \text{ Rad}$ ). The effect of the roller-powder coefficient of friction on the normal contact pressure is also shown.....	123
Figure 5-4: Variation of the longitudinal stress distribution along the densification zone (calculated for $\mu_p=0.5$ , $h_s=130 \mu\text{m}$ (0.005 in), $R=10 \text{ mm}$ , $\rho_{\text{initial}}=30\%$ , and $\alpha_{\text{in}}=0.2$	

Rad). The effect of the roller-powder coefficient of friction on the longitudinal stress is also shown. ....	123
Figure 5-5: Variation of relative density distribution along the densification zone for some possible coefficient of friction between the roller and powder (calculated for $\mu_p=0.5$ , $h_s=130 \mu\text{m}$ (0.005 in), $R=10 \text{ mm}$ , $\rho_{\text{initial}}=30\%$ , and $\alpha_{\text{in}}=0.2 \text{ Rad}$ ).....	124
Figure 5-6: Effect of the coefficient of friction between the loose and compacted powder on the relative density distribution along the densification zone (calculated for $\mu_r=0.3$ , $h_s=130 \mu\text{m}$ (0.005 in), $R=10 \text{ mm}$ , $\rho_{\text{initial}}=30\%$ , and $\alpha_{\text{in}}=0.2 \text{ Rad}$ ).....	125
Figure 5-7: Effect of the powder layer thickness on the relative density distribution along the densification zone (calculated for $\mu_p=0.5$ , $\mu_r=0.3$ , $R=10 \text{ mm}$ , $\rho_{\text{initial}}=30\%$ , and $\alpha_{\text{in}}=0.2 \text{ Rad}$ ). ....	126
Figure 5-8: Relative density of compacted powder layer vs. the adjusted layer thickness (calculated for $\mu_p=0.5$ , $\mu_r=0.3$ , $R=10 \text{ mm}$ , $\rho_{\text{initial}}=30\%$ , and $\alpha_{\text{in}}=0.2 \text{ Rad}$ ).....	126
Figure 5-9: Effect of the initial apparent density of powder on the relative density along the densification zone (calculated for $\mu_p=0.5$ , $\mu_r=0.3$ , $h_s=130 \mu\text{m}$ (0.005 in), $R=10 \text{ mm}$ , and $\alpha_{\text{in}}=0.2 \text{ Rad}$ ). ....	127
Figure 5-10: Relative density variation vs. initial apparent density of powder (calculated for $\mu_p=0.5$ , $\mu_r=0.3$ , $h_s=130 \mu\text{m}$ (0.005 in), $R=10 \text{ mm}$ , and $\alpha_{\text{in}}=0.2 \text{ Rad}$ ). ....	128
Figure B-1: The process of determining $l_{\text{max}}^e$ for SFF-made porous CPP structures.....	141
Figure B-2: The process of determining $l_{\text{max}}^e$ for CS CPP structures.....	142
Figure D-1: Schematic of experimental setup for powder compaction analysis.....	154



# List of Tables

Table 1-1: Calcium phosphate ceramics family .....	9
Table 2-1: Material systems utilized in the SFF of CPP. ....	27
Table 2-2: Dimensional variation of SFF-made (only SFF-V) CPP cylinders (n=10).....	39
Table 2-3: Sintering shrinkage in SFF-V and SFF-H samples in x, y and z directions (n=10). The x, y, and z directions are illustrated in Figure 2-9.....	41
Table 3-1: Average volume percent porosity of CPP structures using the Archimedes method, mercury porosimetry, and micro-CT scan analysis. ....	59
Table 3-2: Micro-structural characteristics of the SFF-V, SFF-H and CS porous CPP structures measured by micro-CT scanning and mercury intrusion.....	61
Table 3-3: Mechanical properties (Young’s modulus, nano- and micro-hardness) of SFF-V, SFF- H and CS CPP samples in two directions: parallel and perpendicular to layers. ....	71
Table 3-4: Uniaxial compressive strengths and Weibull moduli of the CS, SFF-V and SFF-H CPP cylinders (n=10).....	72
Table 3-5: Diametral tensile strengths and Weibull moduli of the CS, SFF-V, SFF-H CPP samples (n=10). ....	76
Table 5-1: Nomenclature representing the parameters utilized for mathematical modeling of counter-rotating roller powder compaction.....	118
Table A-1: Material properties of PVA .....	139
Table A-2: Constituent materials of Zb <sup>TM</sup> 58 solvent .....	139
Table C-1: Insertion table of CPP implants .....	144
Table C-2: Results of processing of BSE images of implanted CPP plugs .....	145
Table D-1: Components of powder compression experimental test .....	153

# Chapter 1

## Introduction and Literature Review

Orthopaedic problems, including bone and joint pathogenesis that lead to tissue degeneration, represent a major cause of pain and physical disability. Bone loss due to trauma and disease such as osteoporosis, osteogenesis imperfecta, and osteonecrosis is a serious health problem requiring skeletal reconstruction. According to National Osteoporosis Foundation (NOF), over 10 million Americans suffer from osteoporosis and this figure will rise to approximately 14 million by 2020 [1]. Also, osteogenesis imperfecta affects up to 50,000 Americans [2]. Annually, about 4,000,000 operations involving bone repair are performed around the world [3].

In addition, most of the oral, maxillofacial and craniofacial defects need bone reconstruction [4]. For instance, partial and complete bone defect in edentulous patients resulting from a variety of causes such as infection, trauma, and tooth loss need alveolar bone augmentation before prosthetic-driven dental implant therapy [5].

In addition, studies have revealed that amongst all musculoskeletal problems, arthritis and joint disease have the highest occurrence [6]. Osteoarthritis, by far the most common type of arthritis seen especially among older people, has been estimated to affect 27 million Americans over age 25 [7]. In osteoarthritis, articular cartilage degenerates and damage to the articular cartilage may influence joint functionality since this tissue has a poor intrinsic capacity for self-regeneration [8, 9]. Such conditions result in inflammation and lack of mobility as well as extreme pain and discomfort. Moreover, full-thickness defects of cartilage surface usually lead to degeneration of the subchondral and chondroid bone (the interface between bone and cartilage) [10].

Due to an ageing world population and the large increase of active elderly individuals, development of techniques to replace, restore, or regenerate bone and joint tissue has become a major clinical trust in orthopaedic, spinal, dental, and maxillo- and cranio-facial surgery.

## 1.1 Current Treatments for Bone and Cartilage Repair

### 1.1.1 Bone Defect Repair

#### 1.1.1.1 Bone Grafts

The current method for treating bone defects is to fully or partially replace the damaged bone using bone grafts. For that purpose, autografts (transplants of tissue from one site to another within the same individual [11-13]) is the gold standard available option clinically utilized. In grafting, surgeons transplant small fragments of bone to a recipient site. Upon transplantation, the fragment acts as a framework for the regeneration of lost bone. This technique can also be used for reconstruction following resection of tumorous bone segments [14]. Despite the encouraging results reported for autografts, this approach suffers from several limitations including pain associated with graft harvesting [15], availability of sufficient transplantable bone [16], and possibility of infection, fracture, paresthesia, nerve injury, as well as donor-site morbidity [2, 15, 17]. Furthermore, autografts may resorb prior to complete healing and may not provide sufficient bone for repair of large defects [2].

Allografts (transplants of tissue from genetically non-identical members from the same species collected from cadavers or living donors [13]), and xenografts (transplants of tissue from another species [13, 18]) are also currently used as clinical treatments for bone repair [11, 19]. However, they are considered as poor alternatives due to the possibility of disease transmission and immunologic rejection [20]. Allografting also suffers from the lack of donor availability [21]. In grafting, proper geometry matching of the grafts to the defect site is usually not possible [22].

#### 1.1.1.2 Bone Graft Substitutes

Concerns over the use of autogenous or allogeneic bone grafts have been an incentive to use synthetic materials as bone graft substitutes [23, 24]. There is a limited range of synthetic materials including polymers, metals, ceramics and composites proposed for bone repair, substitution, or augmentation as osteoconductive fillers or space-makers to achieve bone coalescence.

Traditionally, orthopaedic and dental implants have been composed of metals such as cobalt-chromium-molybdenum (Co-Cr-Mo) alloy [25], stainless steel [26], titanium (or titanium alloy)

[27] and tantalum [28]. Fatigue, corrosion and wear of the implant, tissue infection, and poor implant-tissue interface are limitations (short-term and long-term) that have been associated with the use of Co-Cr-Mo alloy and stainless steel implants [2, 26, 29, 30]. Moreover, stress-shielding due to the significantly greater elastic modulus of Co-Cr-Mo alloy and stainless steel metals and the resulting greater stiffness of the implants compared to natural bone can cause bone loss around the implant and eventually lead to implant loosening and failure [2, 31]. Despite all the advantages of titanium foams and tantalum scaffolds as orthopaedic components such as high corrosion resistant [32], low modulus of elasticity avoiding stress-shielding [33-35], excellent *in vivo* biocompatibility [36] and desired bone healing performance as well as mechanical integration [28, 37], there is an area of concern regarding the use of these materials in bone repair which is their poor resorption properties in biological environment (i.e., they are non-biodegradable). In addition, a negative aspect of titanium alloys is their relative poor wear and frictional properties [38]. The wear debris present an enormous surface area for electrochemical dissolution and release of ions [38], which is a major factor contributing to possible clinically-relevant hypersensitivity [39, 40]. Moreover, manufacturing of titanium products is complex and challenging, and the cost associated with titanium machining is high [41].

Polymers including natural polymers (such as collagen) and synthetic polymers (such as poly(lactic acid) (PLA) [42], poly(lactic-co-glycolic acid) (PLGA) [43], poly(methyl methacrylate) (PMMA) [44], polysulfone (PS) [45], polycarbonate (PC) [46], polycaprolactone (PCL) [47], polydioxanone (PDS) [48], and poly(ether ether ketone) (PEEK) [49]) available in the form of injectable resin-based products or solid products have been extensively used for bone repair [50]. In particular, synthetic biodegradable/bioresorbable polymers are controllable in terms of physico-chemical properties and have been successfully used in clinical applications [34]. PMMA provides an excellent primary bonding with bone, but it does not promote a biological secondary fixation [34]. Biodegradable implants reduce the stress shielding effect and enable post-operative diagnostic imaging, the drawback associated with most metals [50]. Also, others have stated that polymers exhibit desired strength and resistance to mechanical restraints and fatigue, good integration with bones and muscles [50, 51]. However, major limitation of these porous polymeric materials is their relatively low modulus and strength properties making them unsuitable for load-bearing bone substitute applications [52]. In addition, the degradation rate of some biopolymers is too high which may influence the mechanical strength of the bone substitute during the bone repair period [53].

Ceramics are used in the bone defect treatment since they are mainly durable if loaded in compression and do not breakdown by corrosion [54]. Calcium phosphates (such as

hydroxyapatite (HA) [55-60], tri-calcium phosphate (TCP) [20, 55, 61], mixed-calcium phosphate consisting of mixtures of HA and TCP [62] as well as other type of ceramics (such as calcium carbonate [63], calcium sulfate [64]) and glasses (silicate- and phosphate-based [65-68]) have been studied for bone graft substitute applications [24, 69, 70]. Amongst all of ceramic bone graft substitutes, calcium phosphates have a particular position due to their excellent biocompatibility stemming from similar composition to natural bone. For instance, hydroxyapatite (which mainly composes the mineral component of natural bone [71]) binds to bone [33]. Calcium orthophosphates have been studied as bone repair materials for more than 80 years [72].

Ceramics are utilized as granules (particulates) or porous blocks. The bulk forms have been investigated as porous structures designed to allow bone ingrowth [59, 73]. Particulates can be used to fill irregular-shaped defects [74] or in sites requiring bone augmentation in pre-implantation processes [75]. Porous bulk of synthetic ceramics formed in appropriate geometry have a wide use in replacement of diseased or severely traumatized bone. However, ceramics are too brittle to provide enough structural support in load-bearing regions and with very low strength in tension [76], fracture toughness and fatigue resistance [77]. The mechanical properties of calcium phosphates greatly depend on their porosity and structure. A trade-off between mechanical and structural parameters is inevitable [78]. A comprehensive review of the mechanical behaviour of calcium phosphates for application in bone replacement and repair is available in [79].

The incorporation of an inorganic phase (ceramics such as calcium phosphates) into a bioabsorbable polymer matrix [80, 81] enhances the mechanical properties of porous structure [82], the degradation rate of the polymer and the bioactivity of bone substitute [83]. However, the adhesion between the organic and inorganic components of the composite material is one of the main concerns that need to be solved [34].

Ideally, a desired bone substitute should be replaced in time by mature bone with a transient of mechanical support [84]. Thus, recently, interests have been shifted from non-bioresorbable materials towards more reactive and bioresorbable materials. The degradation rate of some biomaterials are not suitable for bone regeneration (i.e., they absorb either too quickly or too slowly) and the degradation needs to be moderated, for instance, by mixing with other biomaterial components [34].

### 1.1.1.3 Market Demand for Bone Substitute

Annually, more than 500,000 bone grafting procedures are performed in the United States and 2.2 million worldwide in order to repair bone defects in orthopaedics and dentistry [85]. Although autografts, if available, are still used in bone repair procedures, the market for the use of allografts and bone graft substitutes is growing.

The annual revenue of bone graft substitutes is about 1.3 billion US dollars (in 2006), with a yearly market growth of about 10% [84]. The market for bone grafts in the United States is estimated to reach \$3.3 billion by 2013, according to a report by Frost [86].

Synthetic materials for bone graft substitutes comprise only about 15% of the market, but the growth rate is close to 15% per year, driven by multiple factors such as, cost-effectiveness, and improved physician understanding of clinical indications and experience and confidence in their use, as well as outcomes of synthetics [84, 87]. However, despite 15 to 20 years of clinical experience with various synthetic substitutes, there have been few well-designed, controlled clinical trials of these implants [87].

## 1.1.2 Osteochondral Defects Repair

Since adult articular cartilaginous tissue has a limited capacity for self-repair, diseased or traumatic damages to articular cartilage can affect joint function [8, 88]. However, chondrocytes (cells which produce and maintain the cartilaginous matrix [89]) are able to reconstruct at least part of their extracellular matrix *in vitro* [90] and *in vivo* if appropriately treated [91].

Currently, replacement of damaged skeletal joints with synthetic prostheses represents the common treatment for end-stage disease [92]. Total joint replacement is a final suggestion of physicians reserved for the most severe and recalcitrant forms of osteoarthritis primarily in elderly individuals. Patients must suffer and manage joint pain by taking medicine and physical therapies during the time between the appearance of the first symptoms of the joint defect/disease and joint replacement surgery. With current joint replacement treatments, younger patients commonly have to undergo multiple revision surgical procedures to replace the implant [93-95]. Furthermore, this treatment is not appropriate for focal defects [96]. According to statistics associated with knee and hip joint replacements and revision surgeries in the United States and Canada over almost a decade, a significant increasing number of patient hospitalization was related to joint replacement (about 500,000 total knee replacements and

250,000 total hip replacements); on average about 35,000 patients needed revision of hip/knee replacement in the United States annually [6].

A best possible solution for osteochondral defects would be to repair focal cartilage and subchondral defects in their early stages and prevent further progressive tissue damage. A few clinically-used techniques are available for biological repair of focal cartilage defects, such as mosaicplasty [97, 98], autologous chondrocyte implantation [99] and allografting using donor joint segments [100]. These techniques provide pain relief while at the same time slowing the progression of joint deterioration thereby delaying partial or total joint replacement surgery. The mosaicplasty technique (i.e., harvesting grafts consisting of a superficial cartilaginous layer and an underlying subchondral bone from non-weight bearing regions of the donor sites within the same joint [101]) suffers from several limitations including amount of available material, donor site morbidity, formation of fibrocartilage in interstices between transplanted osteochondral plugs, difficulty in placing the plugs congruent with the joint surface [101-103], and difficulty in matching the geometry of the grafts with the injured site [22]. Allografts are limited in supply and can be associated with disease transmission [104].

The recent efforts have focused on the development of tissue engineering methods to produce “biphasic constructs” consisting of a superficial cartilaginous component (corresponding to articular cartilage) and an underlying mineralized bone substitute component (corresponding to subchondral bone) as a promising approach to restore the biological and mechanical functionality of the defect site [22, 98, 98]. Biphasic constructs are designed to facilitate the growth of two different tissues (i.e., cartilage and bone) and satisfy different bio-mechanical requirements. This technique enables the repair of bone and cartilage tissues simultaneously. The bone substitute part of the biphasic construct is intended to allow secure fixation of the implant in bone [105]. Cells obtained from the patient’s soft or hard tissues can be seeded onto or into a 3D porous structure which provides the support for cells to proliferate, differentiate and form tissue. The 3D porous structure also defines the ultimate shape of new tissue [105]. Upon implantation, the porous structure degrades in time while the tissue grows *in vivo* [106].

Some bioresorbable materials, particularly calcium polyphosphate (CPP), have shown a remarkable potential for such applications. Osteochondral biphasic CPP constructs have been developed *in vitro* to repair focal cartilage defects [107, 108]. In a novel technique proposed by Waldman et al. [107], biphasic constructs are produced through seeding of chondrogenic cells directly on top of a porous substrate made from an osteoconductive biomaterial (calcium polyphosphate - CPP) to culture a cartilage tissue. Hyaline cartilage forms on the surface and within the near-surface pores thereby resulting in mechanical anchorage of the *in vitro*-formed

cartilage to the CPP substrate. After implant insertion into an articular joint defect site, it was observed that the *in vitro*-grown cartilage merges with the native surrounding cartilaginous tissue while new bone grows into the remaining unfilled pores of the porous CPP substrate (Figure 1-1). The bioresorbable bone substitute component will gradually be replaced by new bone after implantation assuming its appropriate rate of degradation. Promising results were obtained by Kandell et al. [109] in an *in vivo* sheep model.

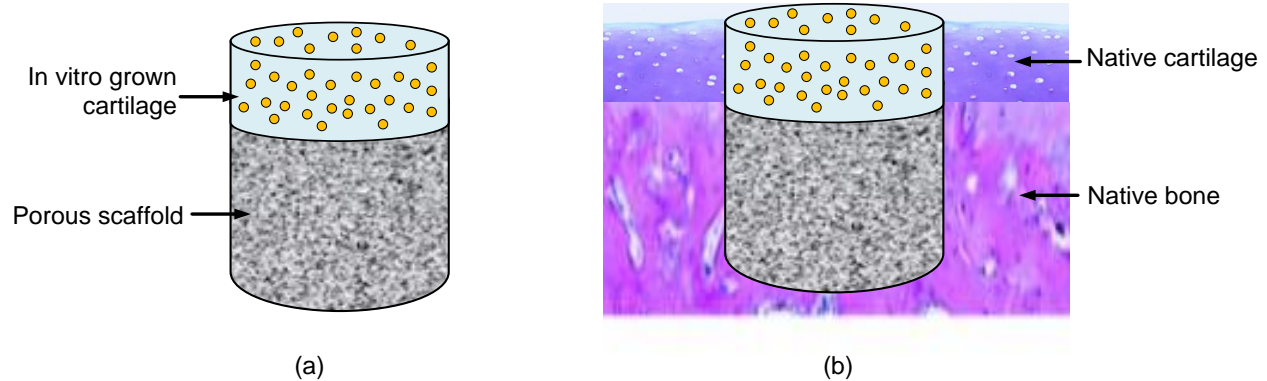


Figure 1-1: Schematic of a biphasic osteochondral implant composed of scaffold for a porous bone substitute component and a scaffold-free *in vitro*-cultured cartilage component as shown in (a). The cartilage component will merge with the native cartilage while bone grows into the porous substitute after implantation as shown in (b).

Wang et al. [110] formed biphasic structures with an extracellular matrix (ECM) containing a large proportion of collagen type II and glycosaminoglycans onto substrates from PLLA, poly(D,L-lactide) (PDLLA), and collagen-hydroxyapatite. The *in vitro*-formed cartilage was integrated with the subchondral base in 7 weeks.

Other approaches used different structures for the cartilage and bone components [111-113]. The different tissues (bone and cartilage) have formed *in vitro* within the respective porous structures and combined into a single composite osteochondral graft by suturing or adhering together the two layers. Chondrocytes and periosteal-derived cells were cultured *in vitro* on poly(glycolic acid) (PGA) mesh and PLGA/poly(ethylene glycol) foam, respectively, to independently generate the cartilage and bone layers [111]. The generated cartilaginous and bone-like tissues were then sutured together followed by culturing in osteogenic medium for an additional period.

Heterogeneous (i.e., multi-layered) structures composed of two distinct components have been utilized for osteochondral tissue engineering [22]. Sherwood et al. [114] developed a construct consisting of a 90% porous D,L-PLGA/L-PLA cartilage section and a 55% porous



L-PLGA/TCP bone substitute component. Integrated layers of PLLA and HA as cartilage and bone substitute constituents seeded with chondrocytes and human gingival fibroblasts, respectively, were used in another investigation [115].

Using a single homogeneous scaffold and two different cell types having chondrogenic and osteogenic capacity represents another approach to engineer osteochondral composites [22]. PCL honeycomb-like structures were fabricated through fused deposition modeling technique [116]. Human bone marrow derived mesenchymal precursor cells (MPC) and human rib chondrocytes were cultured sequentially and the composite constructs were co-cultured *in vitro* in medium containing osteogenic supplements.

In addition to biocompatibility, materials used as bone and/or subchondral substitutes should possess certain essential characteristics. The ideal bone substitution component should be osteoconductive to provide cell adhesion through a suitable surface chemistry and/or topography to allow possible integration with host bone [117]. Also, the ability to degrade in biological environment at a preferred rate is desired in order to allow timely replacement by new bone.

The abovementioned tissue engineering methods are still in the research stage and have not been clinically utilized. Vascularization of the subchondral region, integration of implants with the host tissue, and the formation of hyaline-like cartilage without reversal to a fibrous-cartilage tissue compose the areas for future studies and research in this field [10].

## 1.2 Calcium Polyphosphate

Recently, calcium polyphosphate (CPP) ceramic, an inorganic linear chain polymeric biomaterial, has been studied as a possible bone substitute material due to (1) its composition (calcium and phosphate forming the mineral phase of bone), (2) its mechanical properties approximating cancellous bone, and (3) its degradability in biological environments [52, 96]. CPP, with a chemical composition of  $[\text{Ca}(\text{PO}_3)_2]_n$  and with the calcium to phosphate ratio of 0.5, is formed by the repeated condensation of the oxygen-bridged phosphate tetrahedral groups  $(\text{PO}_4)^{3-}$  into a linear chain network structure. Depending on the starting components and the process parameters, CPP can be produced as an amorphous phosphate glass or a crystalline structure [52]. The sintering characteristics of CPP (to form crystalline structures) were investigated by Filiaggi et al. [118].

CPP differs from other calcium phosphates in terms of chemical composition and specifically Ca/P molar ratio [119, 120]. This difference leads to a distinction in basicity resulting in

different solubility and degradation rates *in vivo* [72]. Some of the synthetic calcium phosphate ceramics and their chemical compositions are listed in Table 1-1.

Table 1-1: Calcium phosphate ceramics family [52, 119, 120]

Ca:P	Chemical Formula	Chemical Name	Mineral Name
0.5	$[\text{Ca}(\text{PO}_3)_2]_n$	Calcium polyphosphate (CPP)	---
1.0	$\text{CaHPO}_4$	Dicalcium phosphate (DCP)	Monetite
1.0	$\text{CaHPO}_4 \cdot 2\text{H}_2\text{O}$	Dicalcium phosphate dehydrate (DCPD)	Brushite
1.33	$\text{Ca}_8(\text{HPO}_4)_2(\text{PO}_4)_4 \cdot 5 \text{H}_2\text{O}$	Octocalcium phosphate (OCP)	---
1.43	$\text{Ca}_{10}(\text{HPO}_4)(\text{PO}_4)_6$	---	Whitlockite
1.5	$\text{Ca}_3(\text{PO}_4)_2$	Tricalcium phosphate (TCP)	---
1.67	$\text{Ca}_{10}(\text{PO}_4)_6(\text{OH})_2$	---	Hydroxyapatite (HA)
2.0	$\text{Ca}_4\text{P}_2\text{O}_9$	Tetracalcium phosphate (TTCP)	---

CPP is biodegradable and the degradation products (calcium and phosphate) do not provoke an inflammatory reaction if the degradation rate is slow [52, 109, 121]. The degradation of CPP, like all calcium phosphate ceramics in a biological environment, occurs through a physicochemical process (dissolution and precipitation via hydrolysis mechanism [52]). The investigations suggest that the hydrolysis of crystalline CPP in an aqueous-based solution is slow [122]. The overall rate of physicochemical dissolution depends on several factors, including surface area per unit weight of the material, crystallinity of the material, degree of polymerization, solubility, and the extent of changes in both the pH and chemical composition of the incubating fluid. The reaction results in the elevation of calcium and phosphate ions in the medium and changes in pH level. CPP degrades faster in lower pH level solutions [123].

As an inorganic polymer, the degree of polymerization of CPP has a great effect on its properties. The higher the degree of polymerization, the slower is the rate of degradation. Also, for a given degree of polymerization, the degradation rates decrease in the order of amorphous CPP >  $\alpha$ -CPP >  $\beta$ -CPP >  $\gamma$ -CPP. Complete degradation of CPP as reported by others occurs between 17 days (for amorphous CPP) and one year (for  $\gamma$ -CPP), tested *in vitro* [124]. *In vivo*, in addition to physicochemical processes, cell-mediated degradation may also occur after implantation [121].

The degradation products of CPP, similar to the other bioresorbable calcium phosphate materials, may promote new bone formation. Calcium and phosphate ions regulate bone metabolism [125, 126]. Calcium ions have a profound influence on osteoblast proliferation and osteoclast regulation [84, 125, 126]. The mineralization rate is regulated and enhanced by phosphate ions [84]. Considering its effect on cell activity, bioresorbable calcium phosphate can be considered as drug [84]. Moreover, osteoclasts enhance the resorption of calcium phosphate materials and provoke the release of calcium and phosphate ions which in turn decreases the activity of osteoclasts [84]. Consequently, the bioresorption process is self-mediated. The biological properties of CPP bone graft substitutes, in comparison with non-resorbable implants such as hydroxyapatite, are preferred/better for promoting or inducing bone formation. CPP gradually degrades and facilitates bone repair *in situ*. The effect on bone regeneration of CPP bone substitutes may be considered as a tissue engineering approach since the formation of new tissue is influenced by constructs that guide and enhance tissue regeneration, and temporarily support mechanical loads.

CPP exhibits superior biological properties compared to bioglass. Bioglass reacts with body fluids (dissolution of the surface of the glass and release of mineral ions) that result in precipitation of hydroxycarbonate apatite nanocrystals on the bioglass surface. The apatite layer enhances the protein absorption and generation of bone matrix and bone growth as well as allowing micromechanical interlocks of osteoid and new bone at the interface [127, 128]. The  $\text{Ca}^{2+}$  and  $(\text{PO}_4)^{3-}$  ions result in a  $\text{SiO}_2$ -enriched surface region that stabilizes the modified bioglass surface and prevents its continuing of dissolution [129].

### 1.2.1 Calcium Polyphosphate for Bone and Osteochondral Regeneration

The porous nature of the CPP structures provides (1) a construct to allow bone ingrowth resulting in secure anchorage of the CPP into the host bone after a period following implantation and (2) a substrate to anchor cartilage formed on its surface and within the subsurface zone [107].

The potential of CPP, as a material for biodegradable synthetic bone substitute applications, is demonstrated through some investigations [52, 109, 121, 124, 130]. Studies have demonstrated the biocompatibility of porous CPP and indicated its rate of degradation *in vitro* [52] as well as bone ingrowth *in vivo* [121]. The investigations were conducted using porous CPP substrates with a porosity of approximately 35–40 volume% formed by a conventional sintering method. The sintering of the amorphous particles involved a two-step process [131] with conditions selected appropriately for different powder compacts and different particle sizes. In brief, to form cylindrical rods, amorphous CPP powder was poured into cylindrical Pt tubes and subjected to a two-step annealing/sintering procedure in air [52, 131]. In an early study (prior to use of the 2-step sinter/anneal process) [52], CPP powder with a finer particle size (106-150  $\mu\text{m}$ ) displayed higher apparent density (~67% vs. 55%) but wider pore size distribution (10-180  $\mu\text{m}$  vs. 10-150  $\mu\text{m}$ ) compared with coarser powder (150-250  $\mu\text{m}$ ). Overall, a significant percentage (~50%) of the interconnecting pores was of the desired size (~100  $\mu\text{m}$ ). The diametral compression testing revealed about 4 times higher strength for the higher density finer powder samples (i.e. ~24 MPa vs. 6 MPa). A rapid initial fall-off of strength due to aging in an tris-buffered solution within the first day or so followed by a more gradual continuing strength loss was observed [52]. Overall, porous CPP structures can be formed with micro-structural features suitable for bone ingrowth and with strengths required for load-bearing bone substitute applications using the conventional sintering procedure. It was also demonstrated that the sintered CPP rods promote rapid bone ingrowth and can be tailored in terms of *in vivo* degradation rate through the appropriate selection of the starting particle size and heat-treatment conditions [121]. In 12 weeks to 1 year, the amount of new bones formed was comparable to the natural bone volume found at similar sites in a rabbits. It was demonstrated that the degradation of the CPP construct is inversely proportional to the original particle size.

The use of a CPP substrate with appropriate interconnected porosity (pore size and volume percent), allows for the seeding of chondrocyte cells on the top surface and the formation of a continuous layer of tissue anchored to the substrate surface yielding a biphasic construct for osteochondral tissue engineering purposes [96, 107-109]. Mechanical stimulation during the *in*

*in vitro* processing has been shown to enhance cartilage formation [132-135]. The cultured cartilage tissue resembled hyaline cartilage with type II collagen and large proteoglycans similar to native cartilage [107]. The mechanical properties of the *in vitro*-formed tissue can be improved by multi-axial mechanical stimulation (cyclic shear and compression loading) [134-136]. The interface shear strength of cartilage-CPP can be further increased by forming a calcified region adjacent to the CPP substrate [137].

The potential of CPP-cartilage biphasic constructs for repairing focal cartilage defects has been investigated by implanting them into prepared sites in sheep knee femoral condyle sites [96, 109]. Evaluation at 9 months suggested that these could be used successfully for osteochondral defect repair. Importantly, the implanted tissue showed maturation and there was bone ingrowth into the bone interfacing region of the porous CPP structure resulting in secure implant fixation. Also, the mechanical properties of the cartilaginous tissue improved after implantation of the *in vitro*-cultured biphasic CPP constructs. Lateral integration to the adjacent native cartilage occurs after a period following implant insertion [109].

In another study, Lien et al. [138] developed a novel osteochondral scaffold of a CPP-gelatin assembly for articular joint repair. Their scaffold consisted of four layers: (1) a porous CPP layer as the osseous component, (2) a dense TCP layer to prevent blood vessel penetration and also to withstand shear, (3) a porous CPP layer for fixation of bone to cartilage, and (4) a porous gelatin layer imitating the cartilage zone. Cartilaginous tissue (Wistar rat model) was successfully developed *in vitro* on the formed structures in four weeks.

The investigation of CPP bone substitutes has been extended from simple regular or tapered cylindrical forms to more complex geometry. To form complex-shaped CPP bone substitutes, the machining characteristics of crystalline porous CPP were investigated in a study by Rouzrokh et al. [139]. Cutting speeds and conditions to produce suitable porous surfaces were determined through milling studies. The results were utilized in operating a 5-axis computer numerical controlled (CNC) machine to form a medial tibial plateau implant for sheep studies (no reference at this time).

Porter et al. [140, 141] undertook a feasibility study to show that stereolithography apparatus (SLA) as a liquid-based solid freeform fabrication method could be used for forming parts made from CPP powders. The study used very fine CPP powders (<25  $\mu\text{m}$  particle size) with a photosensitive liquid monomer as a binder and a He-Cd laser to achieve initial polymerization of the monomer resulting in CPP particle-to-particle bonding. It was shown that after final polymerization of the samples containing 25 volume % CPP, polymer burn-off could be achieved and CPP particle consolidation resulted using a 585°C or 600°C sintering treatment. The

resulting sintered parts suggested that solid freeform fabrication (SFF) of CPP parts was feasible and led to the present study for fabricating porous CPP constructs using a powder-based SFF technique.

Aside from bone substitute and joint reconstruction applications, porous CPP constructs may be utilized for bone augmentation. For dental implants to be successful, the quality and quantity of bony tissue in jawbone must be sufficient to support the implants. If this is not the case, a bone augmentation procedure is necessary before implant can be placed (preprosthetic reconstructive surgery) [5]. In addition, acetabular augmentation during hip joint replacement [142] can be conducted using porous CPP structures in lieu of other currently available bone substitutes. The biocompatibility, bioresorption, osteoconductive properties and bone substitution capacity of CPP combine to produce a suitable porous structure for bone substitutes/augments. Moreover, CPP may also be a candidate for use in spinal fusion procedures. These proposed applications need further research and investigations.

### **1.3 Fabrication of Bone Substitute and Osteochondral Implants**

Fabrication of the porous structures with suitable characteristics represents a major challenge in the engineering of bone substitutes and osteochondral biphasic implants.

#### **1.3.1 Conventional Fabrication Methods**

Conventional methods for manufacturing porous structures, including solvent casting plus particulate leaching [143], gas foaming [144], fibre bonding [145], phase separation [146], melt molding [43], and emulsion freeze drying [147] have some inherent limitations with limited capability to precisely control the matrix architecture in terms of size, shape, interconnection, orientation, distribution of pores, and construction of internal channels within the implant/scaffold structure [148] and can only partially fulfill the requirements for bone substitutes and osteochondral implants. The control of the scaffold architecture with these conventional techniques is process dependent, rather than design dependent which is a major drawback. The production of patient-customized scaffolds by such techniques is expensive and time consuming.

In addition, it is generally not feasible to produce complex porous 3D structures by conventional material removal manufacturing techniques (such as CNC machining) since they

work in a top-down approach, starting from a large solid block of material and machining it into a smaller complex-shaped product [78]. Another major drawback is the fact that removing material from highly porous block of material is a challenging issue as it may cause undesired micro- and macro-fractures, material smearing and pores clogging that affect the surface porosity. Moreover, complex anatomically-shaped porous 3D structures are particularly demanding and infeasible to produce by conventional approaches [78].

### **1.3.2 Solid Freeform Fabrication**

Solid Freeform Fabrication (SFF), also known as Additive Manufacturing (AM), as a computer-aided manufacturing technique, is a unique approach for achieving extensive and detailed control over an implant's internal and external architecture [149]. In SFF, parts with external geometrical complexity can be built through adding and stacking materials, layer upon layer [150]. Since SFF utilizes a layered manufacturing concept, it may be possible to determine the internal micro-architecture of 3D objects by controlling process parameters [151]. Utilizing SFF enhances the control over mechanical properties of a structure, biological effects and degradation kinetics, and allows tissue-engineered grafts to be tailored for specific applications [149]. In addition, SFF can be coordinated with computerized image-based methods for designing hierarchical-featured bone substitute/scaffolds [152]. Such a method may be a reliable approach to fulfill the conflicting requirements of bone substitute structures such as porosity and mechanical strength. The following section describes the state-of-the-art SFF technique for the fabrication of bone substitutes and osteochondral implants.

#### **1.3.2.1 Principles of SFF**

SFF enables structures to be built by selectively adding materials, layer by layer, as specified by a computer program [153, 154]. Each layer represents the shape of the cross section of a computer-aided-design (CAD) model at a certain level [150]. In the 1990s, SFF was applied in the fabrication of complex-shaped scaffolds [149-151].

SFF systems can be categorized, based on the initial form of the chosen materials as (1) liquid-based, (2) solid-based, and (3) powder-based. In most liquid-based SFF methods, a photo-curable liquid resin solidifies, when it is irradiated by a UV beam. Stereolithography (SLA) and solid ground curing (SGC) are two methods of this type. Solid-based systems require solid materials in different forms such as paper sheets in laminated object manufacturing (LOM),

polymer filament in fused deposition modeling (FDM), and thermoplastics in multi-jet modelling (MJM). The starting material can be a wide range of thermoplastic, composite, metal and ceramic particulates in powder-based methods [153].

In powder-based SFF techniques such as three-dimensional printing (3DP), selective laser sintering (SLS), direct metal laser sintering (DMLS) and electron beam melting (EBM), metal, ceramic, polymer, and composite in powder form are used to form either final parts or pre-form structures [153]. The following methodology describes the steps for fabrication of parts using a powder-based SFF technique:

(a) 3D modeling:

- 1) A 3D component is modeled by a CAD system.
- 2) The solid/surface model is then converted into an STL format, which tessellates the surfaces of the model with polygons.

(b) Data conversion and transmission:

- 3) A computer program slices the 3D model into 2D cross sections.
- 4) On the sliced sections, the XY trajectories for the binding mechanism are generated.

(c) Building:

- 5) A thin layer of powder is prepared with a certain thickness (in most of the powder-based SFF methods). The powder bed acts also as a physical support for the printed parts, simultaneously [78].
- 6) Raw powder particles are bound and solidified to create the entire component according to the cross sections and XY trajectories. The component is called a “green part”, since it is in a loosely-bonded state.
- 7) Post-processing, including the binder removal, furnace sintering, and infiltration of the green part is conducted (in case it is necessary) [153].

SLS, DMLS, and EBM techniques have been used for fabrication of porous structures for use in orthopaedic and dental application using titanium alloy, stainless steel, HA, TCP, and biopolymers [47, 155-165].

Since CPP, the bio-ceramic used in this study, is available in powder form, a powder-based SFF-technique should be suitable for producing CPP bone substitutes and osteochondral



implants. The powder-based SFF technique which is utilized in this study to form CPP porous structures was an adhesive bonding three-dimensional printing (3DP) method. A general description of 3DP method is presented in the following section.

### 1.3.2.2 Powder-based Three Dimensional Printing by Adhesive Bonding

In this method, the 3D parts are created by the adhesive bonding of powder particles as the base material, according to the sliced cross-section data of a CAD model. Each layer of powder is selectively joined by the ink-jet printing of a binder material on the areas where the part is to be formed [166]. The process is repeated layer by layer until the entire part is completed. This technique was invented and developed by Michal J. Cima and co-workers (US Patent 5340656A) in 1993 at the Massachusetts Institute of Technology (MIT) [167]. Figure 1-2 is a schematic diagram of the 3DP process in more detail.

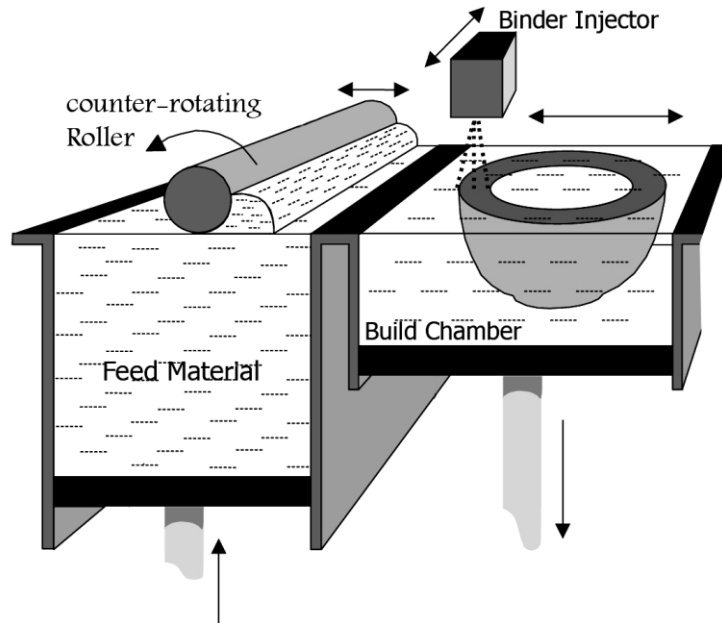


Figure 1-2: Schematic of adhesive bonding 3D-printer adapted from [168]. The single steps of 3DP are symbolically depicted

From a material aspect, a crucial advantage of 3DP is that almost any powder (from synthetic and natural polymers to ceramics, metals, as well as composites of the aforementioned material, [148]) can be used in the 3DP method; most of them should be combined with an

adequate binder. This method can be adapted for the building of ceramic-based constructs for tissue engineering applications [169].

The geometrical freedom inherent in the SFF techniques (such as 3DP) facilitates the production of sophisticated implant designs to fit complex tissue defects using CT scanning that is described in detail in [60, 170-173]. In summary, the first step consists of CT scanning or MRI followed by the differentiation of different tissues through contrast segmentation. Then, the segmented regions are reconstructed and converted into an accurate 3D voxel-based [171] or a CAD model. Using the CAD model, an implant is designed to fill the defect region and exported in a special STL data format which is commonly used in SFF techniques. The process chain is depicted in Figure 1-3.

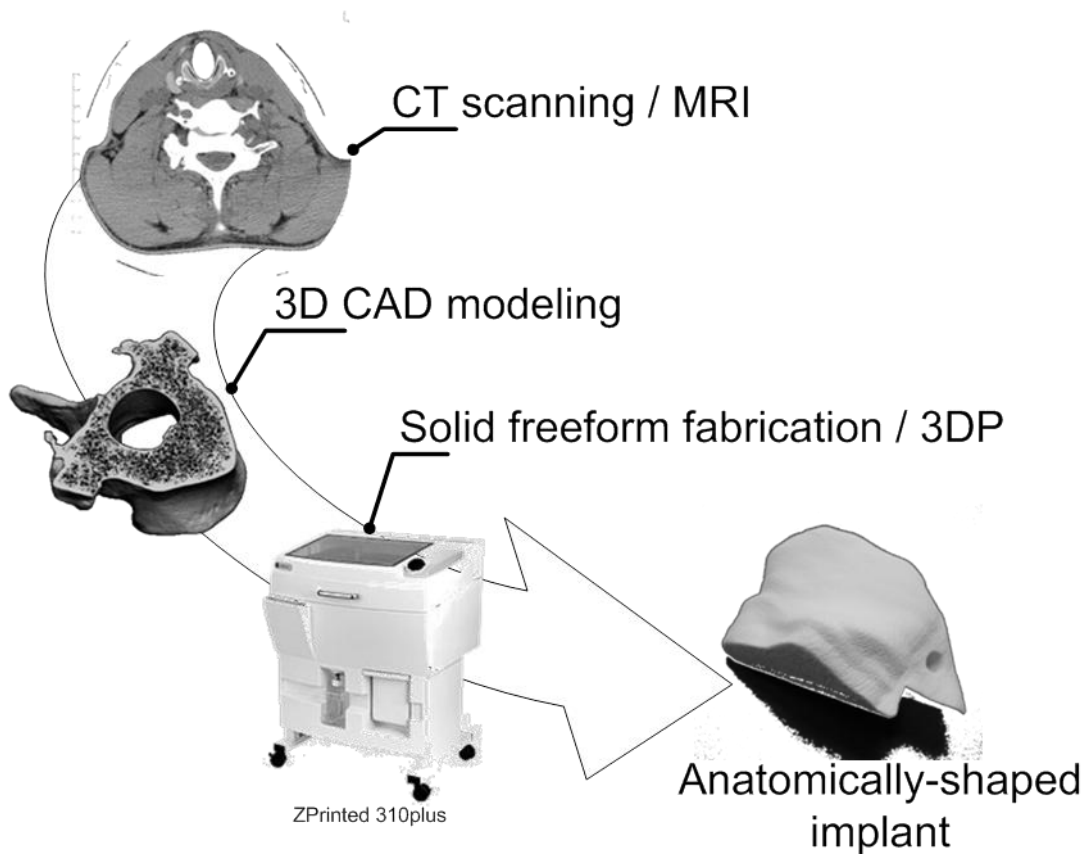


Figure 1-3: Schematic of SFF process for production of anatomically-shaped implants.

In the following, most of the studies conducted on using the 3DP technique for production of bone substitutes and osteochondral implants are reviewed and the corresponding challenges and restrictions are discussed.

### 1.3.2.3 SFF of Bone and Osteochondral Implants

Different SFF techniques such as SLS, SLA, and FDM have been widely utilized in the field of bone tissue engineering [148]. Well-developed reviews of the application of various SFF techniques for bone and osteochondral tissue engineering are available [78]. In the following, some of the pioneer studies conducted on the use of the 3DP method of SFF for forming bone scaffolds and osteochondral implants are noted including a focus on the direct 3DP of calcium phosphate materials.

The pioneering work of the researchers at MIT resulted in the tissue engineering scaffolds, manufactured from PLLA and PLGA by printing chloroform onto a bed of these powders [174-176]. The chloroform swells, partially dissolves the polymer, and eventually binds the adjacent particles [150]. The scaffolds' surfaces were also modified by printing lines of 0.2% poly(ethylene-oxide)/poly(propylene-oxide) (PEO-PPO-PEO) copolymers in chloroform by Park et al. [175]. Also, a non-automated 3D-printer was used to study the scaffold fabrication with poly PCL and PEO prepared in a powder size of 45-75 and 75-150  $\mu\text{m}$ . The binder was a chloroform-PCL solution. It was indicated that SFF offers several building strategies for drug delivery devices [149]. Moreover, one of the earlier investigations on fabricating scaffolds by SFF, which utilized PLGA (85:15) powder mixed with salt sodium chloride (NaCl), was conducted by Kim et al [177]. Each scaffold was  $8\times 7\text{ mm}^2$  with designed channels of 800  $\mu\text{m}$  and pores of 45-150  $\mu\text{m}$  resulting from the salt leaching with distilled water. The overall porosity was reported as 60%. The scaffolds of PLGA were used for liver tissue engineering.

Cima et al. [178] also developed TheriForm<sup>TM</sup> [179], one of six licenses of 3DP, for medical products, including tissue engineering and drug delivery. In 2001, Zeltinger et al. [180] employed TheriForm<sup>TM</sup> to construct PLLA scaffolds with highly accurate and reproducible morphologies. Cells of different types were cultured on the scaffolds and their suitability to support tissue formation was successfully demonstrated. Sherwood et al. [114] developed an osteochondral scaffold using the TheriForm<sup>TM</sup> process. The upper cartilage portion was 90% porous and composed of PLGA and PLA. The lower, cloverleaf-shaped bone portion was 55% porous and consisted of a PLGA/TCP composite. A gradient of materials and porosity was used for the transition region between these two sections to prevent delamination. They concluded that the fabricated scaffolds had desirable mechanical properties for *in vivo* applications such as full joint replacement.

Lam et al. [181] used the 3D-printer Z402 from Zcorporation, and commercially available natural biomaterial powders (i.e., cornstarch (50%), dextran (30%) and gelatine (20%)) and a

water-based binder to fabricate scaffolds with various designed pore sizes and interconnectivities. They infiltrated the porous scaffolds with a solution of PLLA (75%) and PCL (25%) in methylene chloride to increase mechanical strength. Using natural biomaterials with water (as the binder) eliminated the problem of having toxic residuals. However, a lengthy post-processing route was required to waterproof the product because the prototyped scaffold was water-soluble.

Researchers have expanded the application of SFF to fabrication of calcium phosphate implants. For instance, the SFF method has received interest in fabrication of scaffolds with HA. Roy et al. [182] produced HA scaffolds using TheriForm™ technology, where 25 volume % poly(acrylic acid)(PAA), 0.5 volume % glycerine, and 74.5 volume % water were used to bind HA particles. They showed that the porous HA scaffolds with engineered macroscopic channels have a significantly higher percentage of new bone area in comparison with porous HA scaffolds without channels. In addition, Seitz et al. [183] 3D-printed HA parts followed by sintering at 1250°C in a high temperature air furnace. Samples with inner channels with a dimension down to 450 µm and wall thickness down to 330 µm were produced with strength equal to 22 MPa. They also utilized a fluidized bed granulator to modify particle size and morphology of the powder used [184]. Will et al. [185] also formed HA scaffolds by SFF for use in tissue engineering of bone graft substitutes. They fabricated scaffolds with apparent porosity varying from 30 to 64% using different very fine and coarse powder combinations and sintering temperatures. They performed *in vivo* testing using male Lewis rats where successful vascularization was observed within 4 weeks. Also, SFF and characterization of HA/apatite-wollastonite glass ceramic composite was performed by Suwanprateeb et al. [186]. Samples sintered at 1300°C for 3 hours exhibited the flexural modulus and strength of approximately 35 GPa and 77 MPa, respectively. *In vitro* studies showed non-toxicity of the samples. A new calcium phosphate layer formed on the surface of samples after 1 day soaking in simulated body fluid (SBF). Osteoblast cells with normal morphology attached on the surface of composites.

Leuker et al. [187] used spray-dried HA-granulates containing polymeric additives to improve bonding and flowability in SFF processing. A water soluble polymer blend (Schelofix) was utilized as the binder to fabricate cylindrical specimens with 500 µm channels. By histological evaluations, they demonstrated that their samples were suitable for bone replacement. The effect of binder concentration in adhesive pre-coated particles on part strength in SFF method was investigated by Chumnanklanga et al. [188]. Maltodextrin, as a binder/adhesive, was coated onto HA particulates. They determined that the strength of the sintered HA increased with increasing green strength which, in turn, rose with increasing the binder concentration and pre-

coated particle size. Also, it was observed that increasing the amount of binder resulted in higher porosity, which decreased strength.

Gbureck et al. [189] developed a novel SFF process to manufacture bone substitutes with programmed architecture. They basically combined SFF technique with calcium phosphate cement chemistry in which biphasic  $\alpha/\beta$ -TCP powder (30  $\mu\text{m}$ ) reacted with an injected phosphoric acid solution to form a matrix of DCPD and unreacted TCP. The compressive strengths of the fabricated samples were 0.9–8.7 MPa (after printing depending on the acid concentration) and 22 MPa (by additional hardening of the samples by washing in phosphoric acid). In another study, custom-made TCP/calcium pyrophosphate bone substitutes were fabricated by Gbureck et al. [190] using SFF. TCP powder and a liquid phase of phosphoric acid were used for that purpose. After a heat treatment, the primary formed matrix of brushite was converted to calcium pyrophosphate. Heat treatment to 1200°C resulted in considerable weakening of the formed structures. However, further heating to 1300°C gave a compressive strength of 40 MPa due to densification of the ceramic.

Recently, Bergmann et al. [191] produced SFF-made custom implants from a composite of  $\beta$ -TCP and a bioactive glass (similar to the 45S5 Henchglass®). The composite benefited from the bioresorption properties of the  $\beta$ -TCP and the adjustability of the bioactive glass from inert to bioresorbable. The four point bending strength of their samples was equal to 15 MPa after sintering. SFF of TCP also has been successfully tested using arabic gum as a binder and cellulose as a porogen [192]. The pre-formed structures were treated to remove the binder and then sintered. Compression and 3-point bend testing of 60 to 70% porous samples showed bending strengths of 0.08 to 2.6 MPa, compressive strengths of 0.1 to 3 MPa and Young's modulus values of 0.06 to 0.3 GPa.

A mixture of TTCP as a reactive component and  $\beta$ -TCP as a biodegradable filler was used in Khalyfa et al.'s [193] SFF study. An aqueous citric acid solution was also used as a binder. The samples were underwent a post-processing procedure including sintering and polymer infiltration to improve the mechanical properties. *In vitro* biocompatibility testing indicated the capability of the new powder-binder system as efficient bone substitutes and scaffolds for bone tissue engineering.

Moreover, SFF of calcium aluminate cement was investigated by Maier et al. [194] through water injection into a biphasic mixture of tricalcium aluminate and dodecacalcium hepta-aluminate. The porosity was reduced from 50% after printing to 20% after post-treatment and resulted in an increase of compressive strength from 5 to 20 MPa.

A recent study by Detsch et al. [195] analyzed the resorption of SFF-made structures from pure HA and  $\beta$ -TCP as well as a biphasic mixture of HA and TCP by osteoclast-like cells. Measured cell proliferation and cell viability indicated good *in vitro* biocompatibility whereby osteoclast-like cells resorbed calcium phosphate surfaces. HA-TCP scaffolds showed the most capable surface to serve as SFF-made bone substitutes.

In a promising study, Gbureck et al. [196] reported a new direct process for SFF of calcium phosphate structures at room temperature (low-temperature). They fabricated model bioceramic implants from brushite and HA and deposited organic and inorganic angiogenic factors at the end of closed pores of the implants. After 15-day implantation period, blood vessels grew into the entire length of the pore (7 mm) with angiogenic factors whereas they had only extended 2 mm into the factor-free open pores of the implants.

In a promising study conducted by Igawa et al. [170], a mixture of 5% sodium chondroitin sulfate, 12% disodium and 83% distilled water was injected onto  $\alpha$ -TCP powders with mean particle diameter of 10  $\mu\text{m}$  in the SFF process to make a 60% porous structure. Tailored bone implants were designed to fit defects and were 3D-printed with horizontal cylindrical holes for possible facilitation of vascular invasion and bone regeneration. After 24 weeks *in vivo* testing in animal skull defects, histological analysis revealed substantial new bone formation inside the cylindrical holes of the samples as well as existence of bone marrow. Also, osteoclasts were observed resorbing regenerated bone throughout the cylindrical holes. In another study, Saijo et al. [197] used the same technique to reconstruct maxillofacial defects through implanting their 3D-printed artificial anatomically-shaped constructs in ten patients (human) with maxillofacial deformities. Using custom implants reduced the operation time due to the minimal need for size adjustment and fixing manipulation. Partial union between the implant and host bone tissue was detected by the CT images and no serious adverse reactions were observed.

The reviewed studies showed the notable capability of adhesive bonding SFF/3DP technique for production of porous bone and osteochondral scaffolds/implants. In summary, porous ceramic structures with ~5% to 70% porosity have been created by SFF and mechanical strengths as high as 70 MPa have been obtained. In addition, *in vitro* and *in vivo* animal studies (rats, rabbits, mice and goats) have shown desired biocompatibility and osteoconductivity of various 3D-printed ceramic scaffolds [185, 198-200]. Comparisons with xenografts and autografts suggested promising results for those structures. The reported results on the fabrication of porous scaffolds by the 3D-printing method indicate some positive as well as some negative characteristics (see below) in tissue engineering applications.

### 1.3.2.4 Advantages and Shortcomings of SFF

In the SFF (3DP) of porous implants/scaffolds, the micro-structure and geometry of the part can be tailored by varying the printer scan speed and the flow rate of the liquid binder. The simplicity and versatility of this method enable the processing of a wide range of biomaterials, including polymers, ceramics, and metals. Also, since 3D-printers operate at room temperature, processing of temperature sensitive materials may be possible [151]. In addition, because each layer is spread over the support of preceding layers, overhanging features (e.g., T-shaped parts) can be fabricated without any extra support material.

However, one drawback of the powder-supported and powder-filled structures is that the internal unbound powders must be removed from the complex channels deep within the structures, if the part is designed to be highly porous or channelled. The surface roughness and the aggregation of the powdered materials may also cause material trapping within the pores and channels [149]. Moreover, the exterior geometry and the accuracy of the SFF-made implants is an important concern. The exterior surface is affected (1) by the layer thickness determining the SFF resolution in the vertical direction and the amount of staircase effect [201] and (2) by the powder particle size which determines the surface roughness of the final part. Powder particle size also limits the resolution and the smallest feasible features [78].

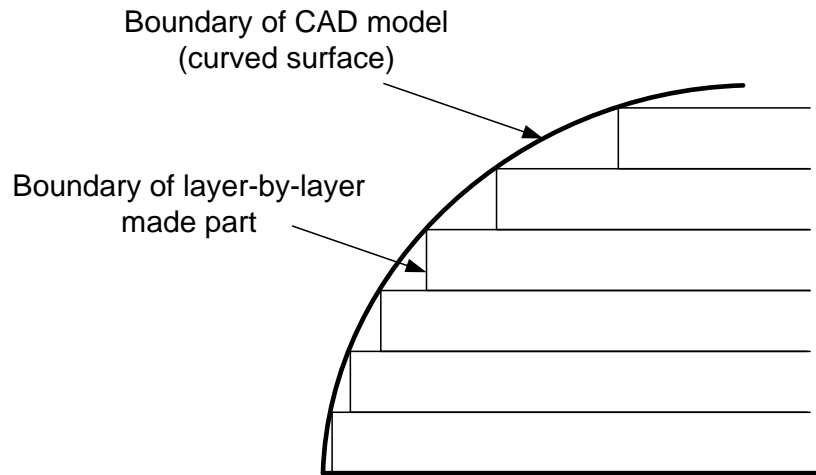


Figure 1-4: Schematic of the staircase effect. The boundary of layer-by-layer made structure does not match with the boundary of CAD model based on the curvature of the surface. The staircase effect influences the exterior surface of parts and causes high surface roughness.

Moreover, the mechanical properties of the SFF-made constructs are other considerations that need to be addressed [151]. During de-powdering (i.e., removing of loose particles from the

green parts), weak bonds within the filigree/lattice structure (mostly thin features) might break and result in damage. However, the mechanical strength of the SFF-made structures can be improved 3 to 4-fold by a post-print hardening/sintering or aqueous conversion post-processing. The compressive strength of post-processed constructs has been reported higher than the values reported for commercial bone graft substitutes [196]. The compressive strength of the SFF-made calcium phosphate structures have been measured in the range of 1-77 MPa [78]. There is always a trade-off between mechanical strength and micro-structure of the constructs made by this method.

In addition, for processing polymers as well as metal or ceramic/polymer composites, some SFF techniques may rely heavily on the use of organic solvents as binders to dissolve the polymer powders in the printed regions. These materials can act as cytotoxic contaminants if not fully removed during processing. For example, even after one week drying, 0.5 weight % of chloroform remains on samples composed of PLA as reported by Giordano et al. [174] for bone reconstruction.

## 1.4 Motivations

As the literature suggests, the field of regenerating musculoskeletal systems is growing rapidly, where biodegradable calcium phosphates have shown successful applications in this area. Particularly, recent studies have illuminated the potential of CPP in the repair of bone and osteochondral damaged regions. In addition, it was demonstrated that the application of the SFF technique in formation of implants/bone substitutes from different calcium phosphates is expanding. The up-to-date findings provide support for further clinical studies of the SFF-made artificial bone substitutes.

Despite studies on the formation of porous structures by conventional sintering of prepared CPP powders, no study on the use of powder-based SFF for production of CPP porous structures with controlled micro-structure have been reported prior to the present research. Also, according to literature, there is no record of SFF of calcium phosphates for biphasic osteochondral (bone and cartilage) tissue engineering.

Anatomically-shaped CPP structures are conventionally produced through the formation of large sintered blocks followed by CNC machining to the final shape. The machining of CPP blocks is a time consuming process which must be conducted with specific operating conditions including certain feed rate and spindle speed. In addition, the machining process results in a considerable waste of CPP material which, in turn, increases the fabrication cost. Formation of



undesired micro-cracks and surface geometry of CPP constructs due to cutting forces may also reduce the mechanical strength, durability, and osseointegration of implants. In addition, internal architecture with feature sizes in the range of less than 500  $\mu\text{m}$  and curved channels cannot be produced in CPP constructs by machining. SFF technique has potential for producing anatomically-shaped bone substitutes and osteochondral biphasic implants from CPP powder that may eliminate the above-mentioned concerns.

Powder-based SFF methods, also offer the potential of tailoring the micro-structural properties (e.g. porosity and pore morphology) of the final part by modifying parameters of the powder layer spreading/deposition process (e.g. layer thickness). These modifications, in turn, may alter component mechanical properties. To the best knowledge of the author, only a few studies have been conducted on the influence of the powder-based SFF process parameters on the biomechanical properties of porous implants. A few studies are devoted to the analysis of anisotropic properties of parts built by the powder-based SFF methods. SFF-made structures may possess anisotropic physical properties in directions parallel or perpendicular to the stacked layers due to the additive layer manufacturing process. Orientation of stacked-layers might also have an influence on the *in vivo* performance of the implants and bone ingrowth within the porous structure. No literature has been identified on the effects of the powder deposition process and layer stacking layout on the micro-structural or mechanical properties of the constructs. No mathematical modeling has been proposed to predict the physical properties of SFF-made structures such as their apparent density for given process parameters such as powder layer thickness.

In addition, although there are many well-developed investigations in the SFF of porous constructs, few studies exist for the fabrication of bone substitutes with controlled internal structure. Particularly, SFF of structures with designed heterogeneous micro-structure has not been reported. Controlled internal architectures and heterogeneous micro-structures provide the opportunity for tailoring the biomechanical properties of implants and controlling the biological response after implantation.

Furthermore, in addition to the reproducibility of SFF-made constructs, production of patient-specific porous implants is also important. This represents an area requiring further studies. Also, there is an increasing need in joint reconstruction, spinal arthrodesis, and maxillofacial surgery for which large and complicated substitutes are required. Thus, the scaling up of tissue engineered products to the dimensions of a patient is also of interest, where it calls for an efficient low-cost automated manufacturing process.

## 1.5 Thesis Objectives

The main objective of the thesis is to develop information for, “*solid freeform fabrication of porous calcium polyphosphate structures with suitable characteristics for bone substitute and osteochondral tissue engineering applications.*”

To meet this goal, the following tasks are conducted:

**Fabrication:** producing porous CPP constructs by SFF technique,

**Characterization:** analyzing the engineering properties (i.e., physical, chemical, structural, and mechanical properties) of the SFF-formed CPP constructs,

**Biocompatibility Study:** analyzing biological response of SFF-formed CPP constructs through an *in vivo* model (for bone repair) and *in vitro* cell culturing (for forming biphasic osteochondral implants),

**Mathematical Modeling:** developing a mathematical model to estimate the porosity of the structures made by powder-based SFF technique.

## 1.6 Thesis Outline

The present thesis consists of six chapters. The problem definition, previous literature contributions as well as the scope of objectives are provided in Chapter 1. In Chapter 2, the SFF of porous CPP structures is described. The prototyping, post-processing, and characterization of CPP constructs (cylinders, complex-shaped, and dual-porous structure) are experimentally investigated. Chapter 3 covers the characterization of the SFF-made CPP structures in terms of chemical, structural and mechanical properties. In Chapter 4, *in vitro* and *in vivo* biological responses to the SFF-formed CPP constructs are described. In Chapter 5, the counter-rotating rolling compaction, which is used in the SFF process for spreading and compacting of the powder layers, is mathematically modeled. The thesis ends with Chapter 6 which addresses the conclusion and suggested future work.

## Chapter 2

# Solid Freeform Fabrication of Calcium Polyphosphate Structures

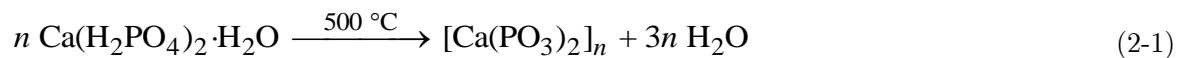
This chapter describes studies on the solid freeform fabrication (SFF) of calcium polyphosphate (CPP) porous structures by employing the adhesive bonding method. Detailed description of material system and a developed fabrication method is addressed. In addition, the geometrical accuracy of samples produced by this method is assessed. The potential of the developed technique for the fabrication of anatomically-accurate CPP implants with controlled and designed internal architecture is investigated.

### 2.1 SFF Process: Materials and Methods

#### 2.1.1 Materials

In this study, a mixture of amorphous CPP and polyvinyl alcohol (PVA) powder was used for the SFF of porous osteochondral implants. CPP was used as the main candidate biomaterial and its properties were described in detail in the previous chapter. PVA was utilized as a sacrificial polymeric binder agent in the SFF process.

In order to produce CPP powder using a method described previously [52], calcium phosphate monobasic monohydrate powder,  $(\text{Ca}(\text{H}_2\text{PO}_4)_2 \cdot \text{H}_2\text{O}, \text{CPMM})$  (J.T. Baker, Phillipsburg, NJ), was first dehydrated by heating at  $500^\circ\text{C}$  for 10 hour in air, resulting in a CPP formation through the following condensation reaction:



The resulting powder is melted at 1100°C followed by rapid quenching of the melt to form a glassy calcium polyphosphate frit. This was subsequently ground and the desired particle size fraction (75 to 150  $\mu\text{m}$  for this study), selected by screening<sup>1</sup>. This amorphous CPP powder was then used for preparing the SFF-formed samples as described below, and sintered using appropriate procedures to form porous samples of desired density with interconnected pores of appropriate pore size opening. A 75-150  $\mu\text{m}$  powder size was selected to be used in this study based on the outcomes of the previous CPP investigations [52, 109, 121].

The PVA powder (86-89% hydrolyzed, Low Molecular Weight – Alfa Aesar) was ground and sieved to <63  $\mu\text{m}$  using standard sieve No. 140 (Dual Manufacturing Co., Chicago, ILL, US). PVA is hydrophilic and can be used in combination with water-based solutions.

An aqueous solvent (Zb<sup>TM</sup>58) (Z Corporation, Burlington, MA, US) was used to be injected on the material mixture in the SFF process. The materials and their specification are listed in Table 2-1.

Table 2-1: Material systems utilized in the SFF of CPP.

	<b>Material</b>	<b>Specification</b>
<b>Bio-ceramic</b>	calcium polyphosphate (CPP)	75-150 $\mu\text{m}$
<b>Binder</b>	polyvinyl alcohol (PVA)	86-89% hydrolyzed Low molecular weight
<b>Aqueous Solvent</b>	Zb <sup>TM</sup> 58	Material properties is available in Appendix A

The CPP and 10 weight % PVA powders were mixed for 4 hours using a roll jar mill (US Stoneware, Ohio, US). It was observed that lower percentage of PVA did not provide sufficient green strength for the post-SFF treatment of samples made with 75-150  $\mu\text{m}$  powder size. A scanning electron micrograph of the PVA-CPP powder blend used in the SFF process is shown in Figure 2-1. The scanning electron microscopy (SEM) images (secondary electron emission) were obtained through (HITACHI S-2500, Hitachi, Japan). The CPP samples were first sputter-

---

<sup>1</sup> The preparation of CPP powder was conducted by Youxin Hu in the institute of Biomaterials and Biomedical Engineering at the University of Toronto.

coated with gold (10 nm) (SPI Sputter<sup>TM</sup>, SPI Supplier Division of Structure Prob Inc, West Chester, PA, USA) to make them electrically conductive. The electron accelerating voltage was set to 10 kV. The same setting applies for all SEM scans which are presented in this study unless noted.

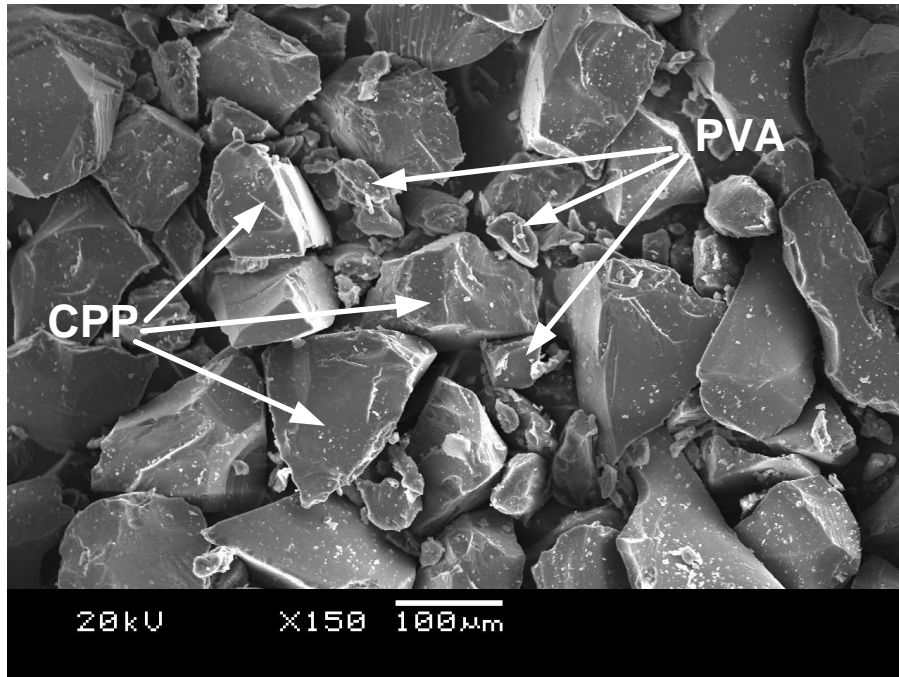


Figure 2-1: SEM of PVA-CPP blend powder. PVA (smaller) and CPP (larger) particles are depicted.

#### 2.1.1.1 Powder particle size

The particle size distribution of the starting amorphous CPP powder was analyzed through a modular particle size analyzer (Mastersizer S Version, Malvern Instruments Ltd., UK) using ethanol as the carrier medium. It should be noted that ethanol does not affect the CPP particles. In addition, CPP particle size was analyzed using 10 different SEM images which were randomly selected from CPP powders. The two apparent dimensions (length and width) of the particle facets captured by the SEM images (Figure 2-2) were measured using the MATLAB Image Processing Toolbox.

The distribution histograms of the starting CPP powder particle sizes used for forming the sintered structures are shown in Figure 2-3. The curve obtained by the modular particle size analyzer (Figure 2-3a) indicates a distribution with an average size of  $170 \pm 57 \mu\text{m}$ , median of 164

$\mu\text{m}$  and skewness value of 0.41 suggesting a non-uniform distribution skews towards the coarser particles. The dashed lines signify the sieve range used to separate the CPP powders (i.e., 75-150  $\mu\text{m}$ ). As seen, a large portion of the powder distribution was out of the sieve range.

Also, Figure 2-3b shows the 3D histogram of the CPP particle lengths and widths measured using SEM images (Figure 2-2). The average particle length and width were calculated as  $102\pm 32\ \mu\text{m}$  and  $172\pm 48\ \mu\text{m}$ , respectively. The size of the particles' third dimension, considering that the particles have a plate-like shape, should also be smaller than 150  $\mu\text{m}$  to be able to pass throughout the screening sieve. In Figure 2-2, the arrows depict some of the particle dimensions which are larger than 150  $\mu\text{m}$  (= layer thickness used in the SFF process that will be described later). It should be noted that this analysis was repeated for two other CPP powders which were produced separately. The results were in good agreement.

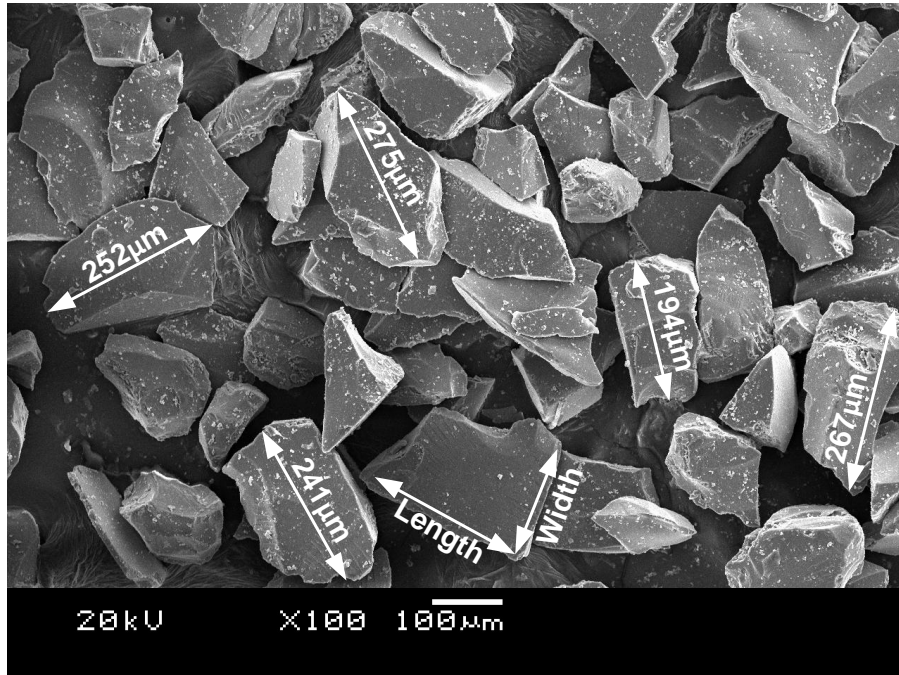
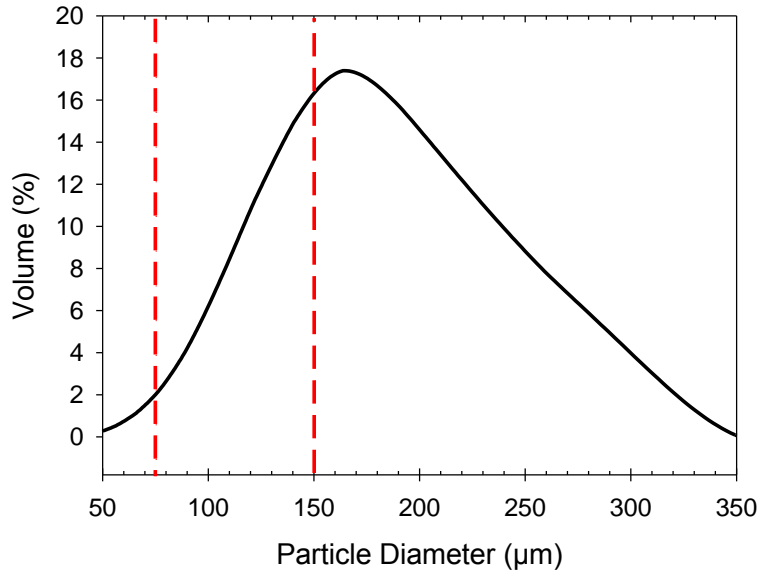
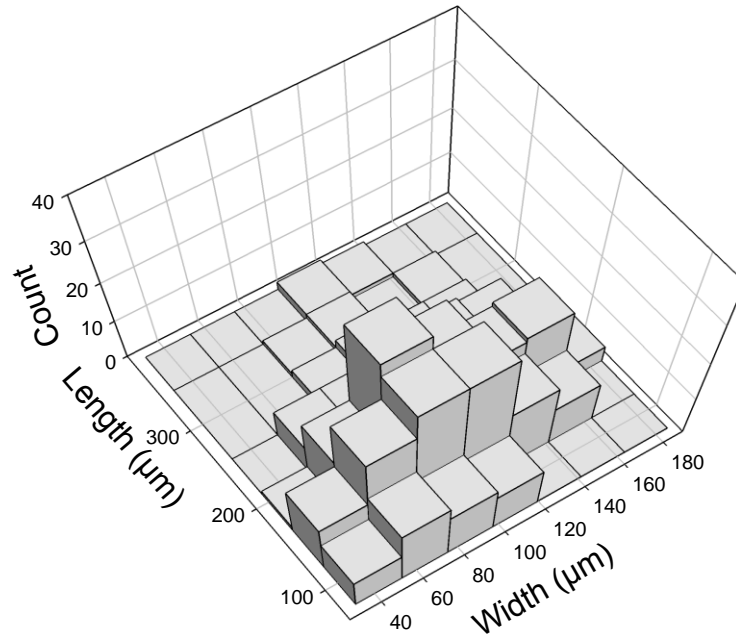


Figure 2-2: SEM image of the as-received CPP powder; arrows depicted some of the dimensions greater than 150  $\mu\text{m}$ .



(a)



(b)

Figure 2-3: Distribution of CPP powder particles size: (a) Diagram showing the volume percent of particle diameters measured by modular particle size analyzer. The dashed lines signify the sieve range used to prepare the CPP powder (i.e. 75-150  $\mu\text{m}$ ), (b) 3D histogram of length and width of particles.

CPP-PVA powder with particle size distribution as noted above showed an acceptable flowability which is an essential requirement for building up thin powder layers. It also made possible removal of loose powder from the printed part (de-powdering) [78]. Moreover, this powder size prevented agglomeration of particles which may occur when inter-particular forces dominate gravitational forces [78].

## **2.1.2 SFF of Porous CPP Structures**

### 2.1.2.1 Green Part Fabrication

The process starts with 3D modeling of the desired geometry in the CAD environment. A standard computer-aided design (CAD) package, SolidWorks Ver.2006 (SolidWorks Corp., Concord, MA, USA) was used to obtain the design of the CPP implants. The 3D models were exported in the STL (stereolithography) format for uploading into the 3D-printing software (ZPrint™), where the models were sliced into 2D layers.

A 3D-printing machine (Zprinter 310plus, Z Corporation, Burlington, MA, US) was retrofitted (Figure 2-4) for the layer-by-layer fabrication of CPP parts. In the SFF process, each layer of the CPP-PVA powder was collected from the feeding chamber and spread over the building chamber using a counter-rotating roller that traveled from the feeding side to the building side. In addition to the spreading, the roller evenly applied a compaction force on the powder layers. The layer thickness was adjusted through the machine software (ZPrint™) equal to 150  $\mu\text{m}$ . The working temperature was also adjusted to 38°C.



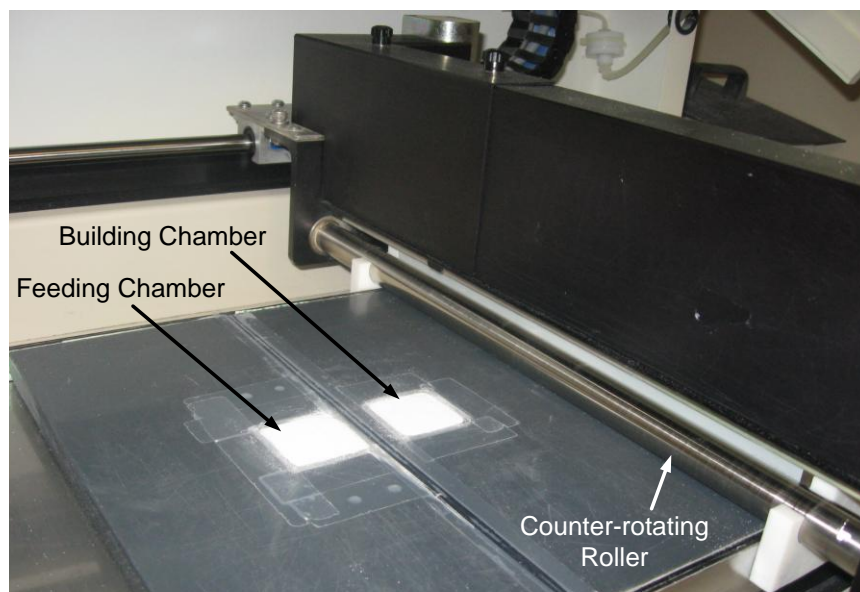


Figure 2-4: Retrofitted ZPrinter for prototyping of complex parts from biomaterials

CPP particles mixed with PVA were bonded to each other during the particle layering procedure by injection of Zb<sup>TM</sup>58 (aqueous solvent) onto the initial blend powder, which dissolves the PVA particles resulting in formation of adhesive bonds between the adjacent CPP particles (Figure 2-5). Hardening is caused by precipitation of the polymer during solvent drying. The resulting “green” pre-forms were strong enough to allow subsequent handling. The initial strength after printing and before post-processing steps (e.g. sintering) is referred as “green strength”. The green strength of the CPP green parts relies mainly on the strength of the PVA-bonds between adjacent CPP particles as well as the strength of the PVA-bonds between adjacent layers [78]. It was determined empirically that at least 10 weight percent PVA was required to achieve acceptable green strength with the CPP particles of the size used in this study. The subsequent sintering process results in the desired densification and strength development.

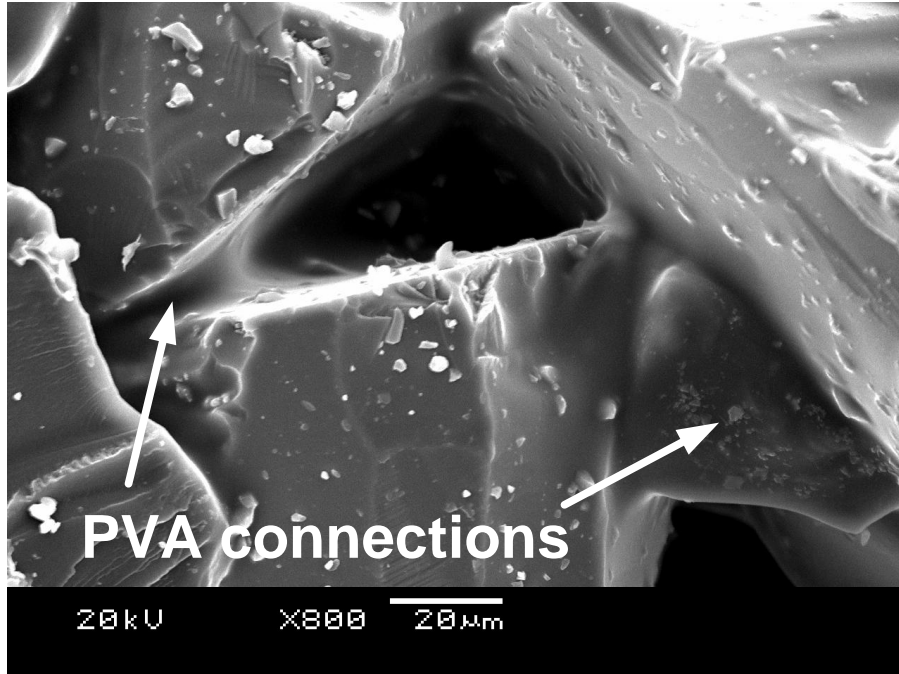


Figure 2-5: PVA connections between CPP particles in the green part before sintering (SEM image): PVA bonds connect the adjacent CPP particles together.

The wettability of PVA-aqueous solution, in contact with the CPP particles, is a critical factor influencing the printing accuracy and the green strength of the SFF-made object [202]. Powder wetting depends on a number of parameters such as the viscosity of PVA solution as well as the powder shape and size [78]. As Figure 2-5 displays, PVA dissolved in the solvent resulted in good wetting of the CPP particles which in turn caused strong inter-connecting bridges between the particles. The capillary pressure draws the binder into the interparticle connections. In addition, to minimize the total surface energy of the powder material system, the injected fluid pulls adjacent particles together to form spherical agglomerates of polymeric binder and ceramic particles [203]. Furthermore, mechanical interlocking of CPP particles has a noticeable influence on the mechanical integrity and green strength of the CPP parts [202]. Particle shape and packing density of powder bed govern the mechanical interlocking of CPP particles within the green parts.

### 2.1.2.2 Post-SFF Treatment

The SFF-made green parts then undergo a post-SFF treatment<sup>2</sup> to (1) burn-off the polymeric binder (400°C for 1 hour, a temperature below the glass transition temperature ( $T_g$ ) of the amorphous CPP), and (2) densify the CPP powder through a 2-step patented process [131]. During the 400°C, one hour anneal, the PVA-containing binder is burned off. However, the porous CPP structure retains sufficient strength, presumably as a result of some mechanical interlocking of the irregular CPP particles and possibly some initial particle-particle sinter neck formation. Following binder burn-off, samples retained sufficient strength for handling through the sintering treatment. The samples were treated using a 2-step annealing process with temperatures and times selected to yield the desired density. The 2-step annealing process allows rapid sinter neck formation between the amorphous powders primarily through a viscous flow sintering mechanism [118] while the second higher temperature anneal, 950°C in this study, results in the formation of the final crystalline CPP structure with only minimal further change in density from that formed through the step-1 sinter anneal. The heat treatment process is depicted in Figure 2-6.

During the post-SFF sintering, all binder and residual products (i.e. carbon following binder decomposition after the 400°C anneal) appeared to have been removed following the 950°C sinter anneal, (compare Figure 2-5 and Figure 2-7 which show SEM images of CPP structures before and after sintering, respectively).

---

<sup>2</sup> The post-SFF process was conducted by Youxin Hu and Dr. Svitlana Prada in the Institute of Biomaterials and Biomedical Engineering at the University of Toronto.

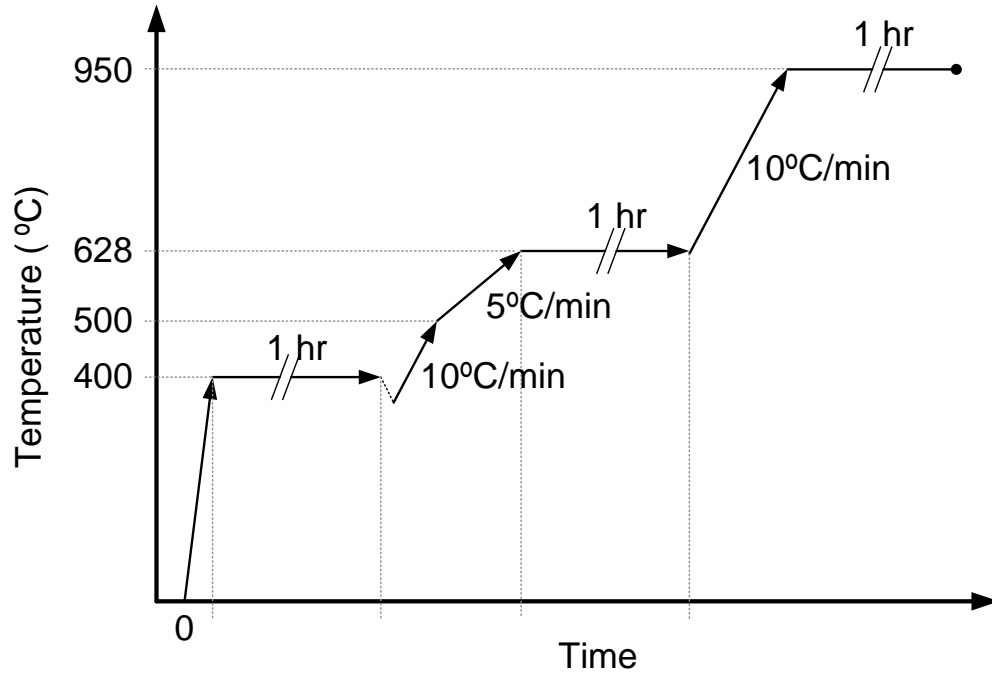


Figure 2-6: Heat treatment protocol used for sintering of SFF-made CPP green parts.

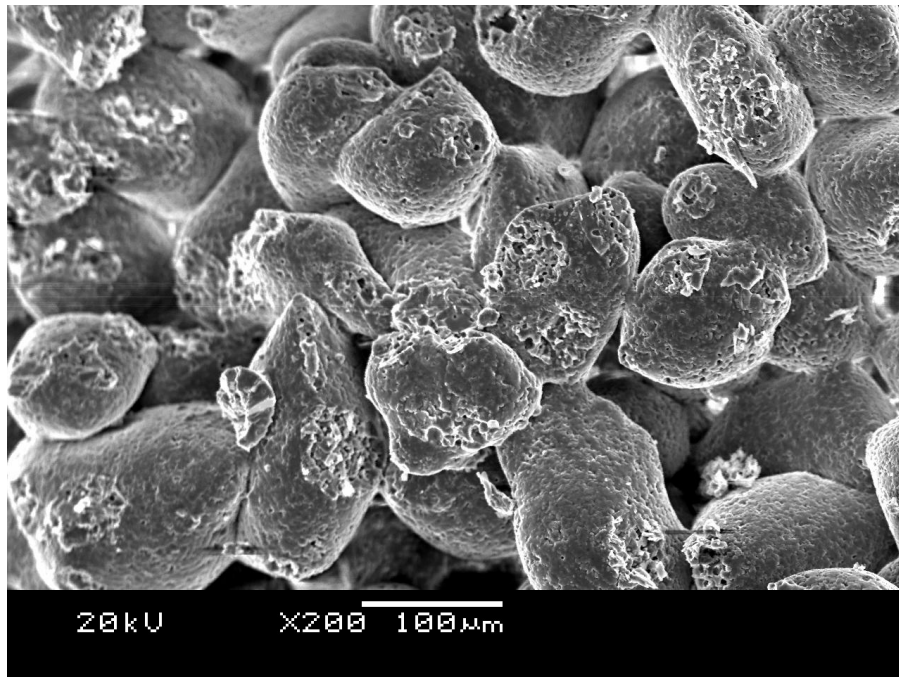


Figure 2-7: SEM images of final sintered SFF-made CPP structure showing all the PVA has been removed during the high temperature post-SFF process.

In this study, cylindrically-shaped samples with diameters of 4 mm and height of 6 mm (for characterization of physical, mechanical properties and in vivo animal test) or 2 mm (for mechanical characterization and cartilage tissue culture studies) were prepared by SFF followed by sintering. Figure 2-8 shows a typical 6 mm long SFF-made cylindrical sample after post-SFF sintering. As seen, the CPP structure has the required geometric appearance and mechanical integrity.

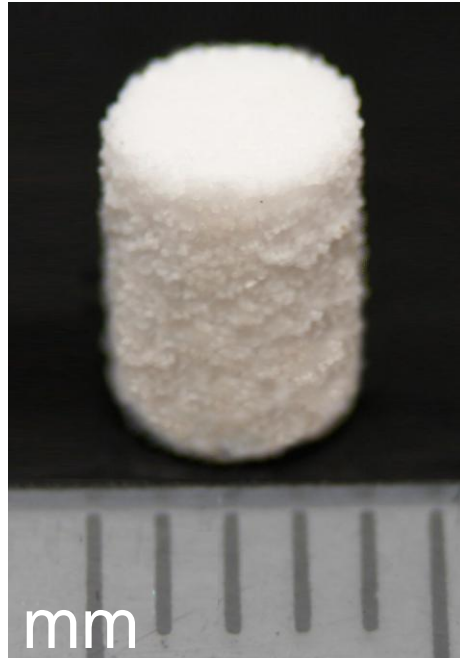


Figure 2-8: SFF-made cylindrical sample after post-sintering. The diameter and the height of the sample are 4 and 6 mm, respectively.

### 2.1.2.3 Samples' Stacking Orientation: Vertical vs. Horizontal

In order to study the influence of the orientation of the stacked-layers on the physical, mechanical and biological properties of the CPP structures, the cylindrical parts were fabricated in two ways:

- (a) The axis of cylinders was oriented perpendicular to the powder stacked-layers (z direction shown in Figure 2-9a). Hereafter, those vertically-made CPP samples are called SFF-V (Figure 2-9b).
- (b) The axis of cylinders was oriented parallel to the powder stacked-layers (x direction). The horizontally-made CPP samples are called SFF-H (Figure 2-9-c).

The orientation of parts in the building chamber is chosen by the operator as the pre-step of the SFF process. In this work, it was hypothesized that the “layered nature” of the SFF process plays an important role in the properties of the fabricated CPP structures. This effect is investigated through analysis and comparison of the micro-structural and mechanical properties of the vertically and horizontally-made porous CPP cylinders.

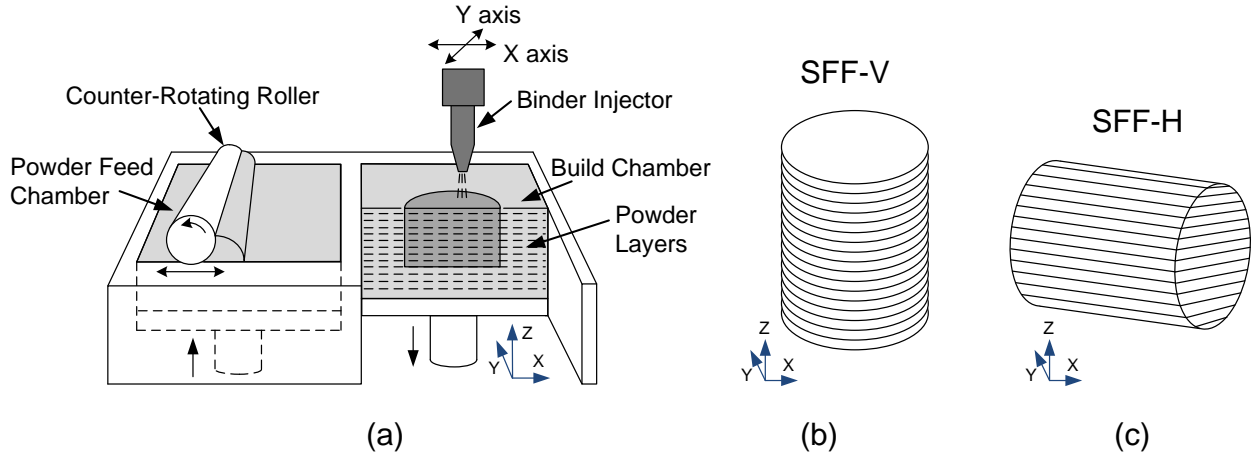


Figure 2-9: Schematic of: (a) SFF process showing the orientation of layers in xyz coordination, (b) SFF-V and (c) SFF-H cylinders; cylinders axes are perpendicular and parallel to the layers, respectively.

### 2.1.3 Conventional Fabrication of CPP

Conventionally-sintered (so-called CS) samples were prepared as “control samples” for comparison of physical and chemical characteristics, mechanical properties, suitability for use in forming cartilage-CPP biphasic implants, and in vivo bone ingrowth.

In the conventional fabrication process, porous CPP samples were prepared from the 75-150  $\mu\text{m}$  powder using a gravity sintering method. For this purpose, the CPP powder was poured into cylindrical Pt tubes (Figure 2-10). The tubes were then vibrated for approximately 5 seconds to assist in packing the powders and reaching the required compact density without any significant separation of different powder size fractions. Final porous structures were produced by sintering at 950°C for 1 hour in an air muffle furnace (heat-up rate 10°C/min) [131]. The sintering protocol was 10°C/min to 500°C, 5°C/min to 585°C holding for 1 hr, 10°C/min to

950°C holding for 1 hr. The sintered long samples were then cut into 4 mm diameter and 6 mm long cylinders using a diamond wafering blade.

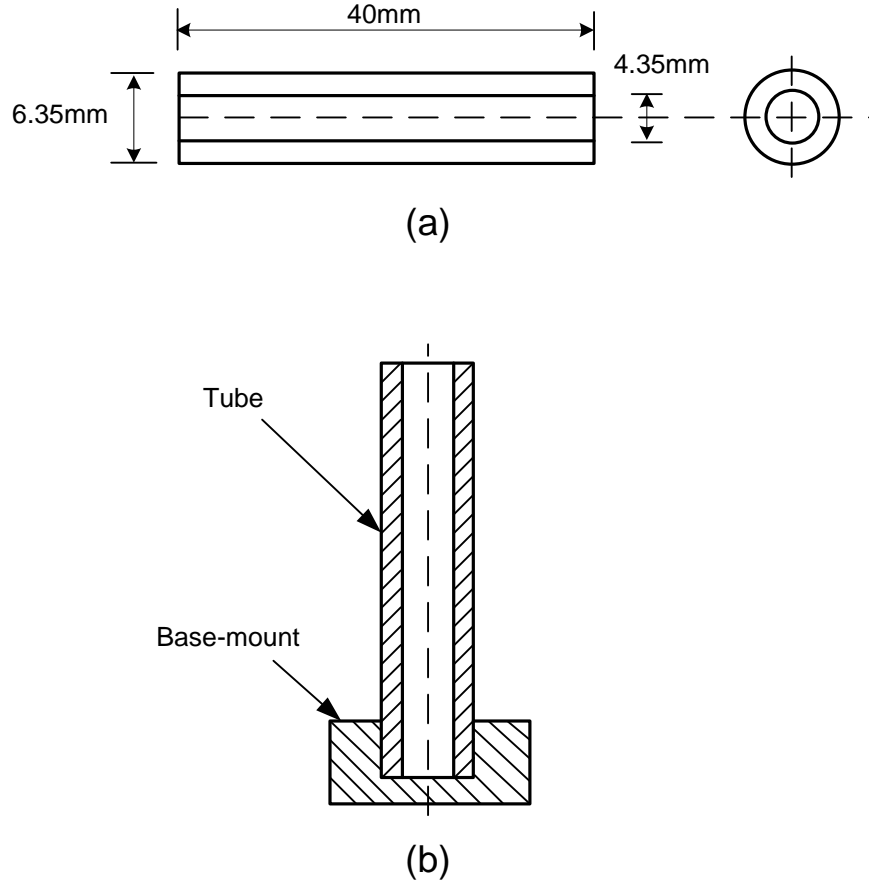


Figure 2-10: Detailed drawing of the platinum sintering crucible including Pt tube and base-mount: (a) dimensions of tube, (b) sectioned assembly view (adapted from [52]).

It should be noted that the sintering conditions were selected appropriately for the SFF and the conventionally-made powder compacts where different first step-sinter temperatures were used (higher for the SFF-made CPP) due to the dissimilar initial packing densities of the two compacts. Both sample types were given a final sinter anneal at 950°C to develop the desired crystalline structure.

## 2.2 Characterization of the SFF process

The developed SFF process was assessed by measuring the geometrical accuracy of the produced samples. The SFF-made samples are subject to dimensional deviations, which stem from two sources: (i) expansion during the SFF process and (ii) shrinkage during the post-SFF sintering process. In addition, the exterior of the CPP parts is limited by the layer thickness (150  $\mu\text{m}$ ) and the staircase effect [201] as well as the powder particle size determining the surface roughness of the final part. The dimensional deviation of the CPP green parts and the shrinkage of the sintered structures were determined and reported in this sub-section.

### 2.2.1 SFF Dimensional Deviation Measurement

In fabrication of CPP green parts, the dimensional deviations from the original CAD models of the cylindrical samples were determined from sample diameter and height measurements using the following equations:

$$\text{Green Part Dimensional Deviation}_{SFF} = \frac{d_{SFF} - d_{CAD}}{d_{CAD}} \quad (2-2)$$

where  $d$  is the dimensional feature (diameter or height) of the structure. The dimensions were measured by a digital calliper (ABSOLUTE-DIGIMATIC, Mitutoyo Corp., Japan). The mean values were averaged from three readings. The target dimension, CAD model dimension, absolute green part deviation, and the percent deviation for the vertically SFF-made cylindrical samples are listed in Table 2-2.

Table 2-2: Dimensional variation of SFF-made (only SFF-V) CPP cylinders (n=10)

Dimensional Feature	Target dimension (mm)	Target green part dimension (mm)	CAD model dimension (mm)	Absolute green part dimensional expansion ( $\mu\text{m}$ )	Green part dimensional deviation
Diameter	4.0 $\pm$ 0.1	4.8	4.2	~600	+14 $\pm$ 1%
Height	6.0 $\pm$ 0.1	6.9	6.3	~600	+9 $\pm$ 1%



In addition, samples with rectangular cross sections of 4 mm by 4 mm were formed to investigate the dimensional deviations in x versus y directions. The results suggested about 100  $\mu\text{m}$  more dimensional expansion in the x direction which is negligible considering the CPP particle size.

As listed in Table 2-2, the dimensions of the 3D-printed parts are larger than those of the CAD model. The absolute dimensional increase in the green parts was the same ( $\sim 600 \mu\text{m}$ ) for both diameter and height. This suggests that excessive infiltration of the injected solvent is identical in both directions.

The dimensional deviation may be attributed to excessive infiltration of the injected solvent within the powder bed as well as the printhead resolution and accuracy of the positioning devices. In addition, resolution and dimensional deviation of green part depends on binder and powder properties, powder packing density, and drying rate of the binder [78]. Experiments demonstrated that the higher the temperature of the powder bed, the higher the penetration of the aqueous solvent. A 2.5% increase in size was measured for an approximately 30°F (from 70 to 100°F) increase of temperature.

The resolution of the objects made by similar SFF techniques is generally at least twice the dimension of the powder particle size [204] and a high resolution can only be achieved by using a fine powder. However, there is a trade-off between flowability of powder and resolution since dry and fine particles tend to agglomerate resulting in poor flowability [78].

### 2.2.2 Sintering Shrinkage Measurement

Measuring the sintering dimensional deviation can be used to monitor the sintering process [205]. The shrinkage of CPP structures which took place in the sintering stage was determined in three orthogonal directions (i.e. x and y parallel to stacked-layers and z perpendicular to stacked-layers) using the following equations:

$$\textit{Shrinkage} = \frac{d_s - d_{SFF}}{d_{SFF}} \quad (2-3)$$

where  $d$  is the dimensional feature of the structure while  $SFF$  and  $S$  refer to the green and the sintered samples, respectively. The dimensional measurements were repeated three times using a digital calliper (ABSOLUTE-DIGIMATIC, Mitutoyo Corp., Japan) and the average measurements were reported.

The sintering shrinkages in three directions (x and y: parallel to the stacked-layers, z: perpendicular to the stacked-layers) for the SFF-V and SFF-H samples are listed in Table 2-3. The vertically and horizontally-made SFF samples showed dissimilar shrinkages in the directions parallel (~17%) and perpendicular (~12%) to the stacked-layers indicating greater shrinkage across the radial cross-sections of the SFF-V and along the height of the SFF-H cylinders. The reason for this phenomenon will be discussed in the next chapter. The CS samples showed  $8\pm 1\%$  sintering shrinkage.

Table 2-3: Sintering shrinkage in SFF-V and SFF-H samples in x, y and z directions (n=10). The x, y, and z directions are illustrated in Figure 2-9.

Shrinkage Direction		SFF-V	SFF-H
Parallel to the stacked-layers	x	$17\pm 1\%$	$17\pm 1\%$
	y	$17\pm 1\%$	$18\pm 1\%$
Perpendicular to the stacked-layers	z	$12\pm 1\%$	$12\pm 2\%$

This dimensional expansion is partially compensated by the shrinkage that occurs during the sintering process. Since the shrinkage is highly reproducible, it can be compensated for by scaling the initial CAD model prior to printing. Dimensional changes in the green and sintered stages are used to determine the correction factor (anisotropic) to be applied to the CAD models. A scale-up compensation factor of 5% was determined for this experiment using the data of Table 2-2 and Table 2-3. By applying the correction factor to the CAD models, dimensional accuracy of about  $\pm 100 \mu\text{m}$  is feasible, in spite of sintering shrinkage. Considering the size of CPP particles (nominal 75-150  $\mu\text{m}$ ), the dimensional accuracy falls in an acceptable range. It suggests that the developed process can be used for fabrication of osteochondral implants within desired dimensional tolerances.

### 2.3 SFF of CPP Structures with Geometrical Complexity

The potential of the proposed technique for fabrication of the CPP implants with complex geometry and controlled internal architecture was evaluated through producing some (1) anatomically-shaped, (2) channelled, and (3) dual-structural porous CPP constructs as described below.

### 2.3.1 Anatomically-Shaped Structures

A portion of a sheep femoral condyle of sheep was chosen to be fabricated (This represents a part of an ongoing study for partial joint regeneration [Kandel et al.]). For this purpose, first of all, CT scans of the femoral condyle were obtained. The 3D model of the region of interest (ROI) was obtained using Mimics software (Materialise NV, Leuven, Belgium) in which different tissues in the dataset were differentiated through contrast segmentation. Then, the segmented CT slices were reconstructed into a 3D model. A desired portion of 16 mm by 16 mm was selected to be built by the SFF method. The sample was fabricated through the regular process described previously. Figure 2-11 shows the CAD 3D model, SFF-made green part.

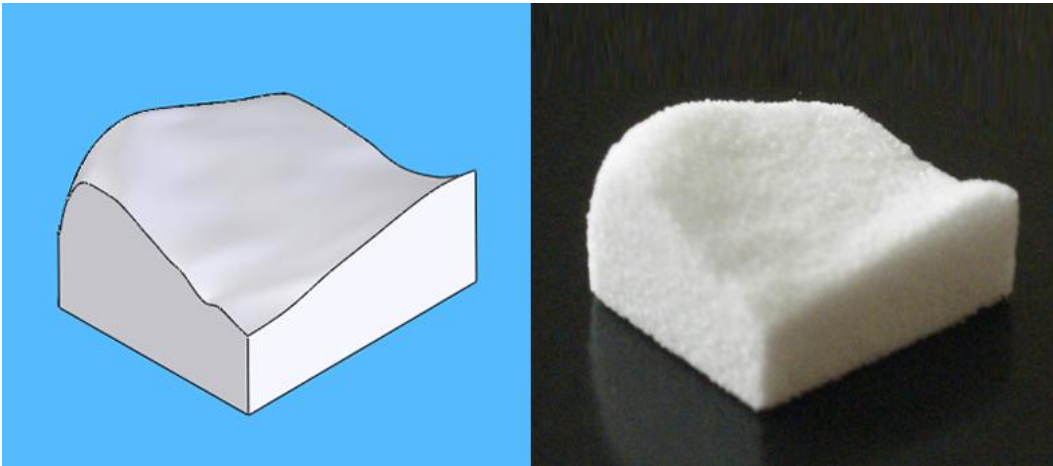


Figure 2-11: Femoral condyle CPP implant: (a) CAD 3D model, (b) SFF-made part.

As part of another ongoing study for forming tissue engineered joint resurfacing implants [Kandel et al.], SFF was utilized to produce anatomically-shaped structures. For that purpose, the 45-75  $\mu\text{m}$  CPP powder was used to form a component matching the medial half of tibial plateau of a sheep knee joint as shown in Figure 2-12. It was shown that the geometrical freedom of the SFF-based method allows sophisticated design of implants based on CT/MRI scans. However, further studies are required to obtain geometrical factors to compensate the effect of anisotropic shrinkage in large implants in order to completely fit complex bone defects.



Figure 2-12: Fabricated medial portion of tibial plateau-shaped CPP structure; the top surface is intended for in vitro cartilage formation while bone ingrowth into the other surfaces allowing implant fixation to subchondral bone.

It is important that the exterior geometry of the implant mimic the anatomic shape of the tissue to be replaced in order to guide the formation of new tissue in the intended space and provide a suitable fixation to host bone in the clinical situation. Direct contact between the defect site border (host bone) and the implant enhances the rate of integration with the host tissue. Thus, the shape and dimensions of the SFF-formed anatomically-shaped constructs should be compared with the original CAD model. 3D scanning could be used to this end.

### **2.3.2 CPP implants with Channels**

Transportation of cells, nutrients and cellular waste products in large implants can be facilitated through micro-channels which connect the core region of an implant to the surrounding media [206]. While these have been made using conventional sintering with channels formed by machining or introducing sacrificial elements [personal communication with Dr. R.M. Pilliar and Y. Hu], SFF offers an attractive alternative for forming these structures. In an attempt to study the feasibility of forming micro-channels within the CPP structures, cylinders of 6 mm diameter and 9 mm height were targeted with three channels of 500  $\mu\text{m}$  located on a 1 mm pitch diameter (Figure 2-13).

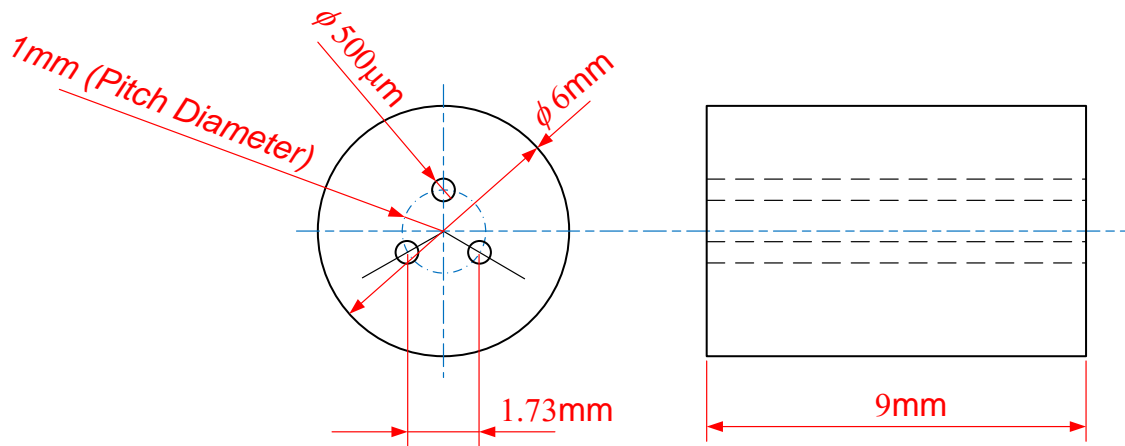
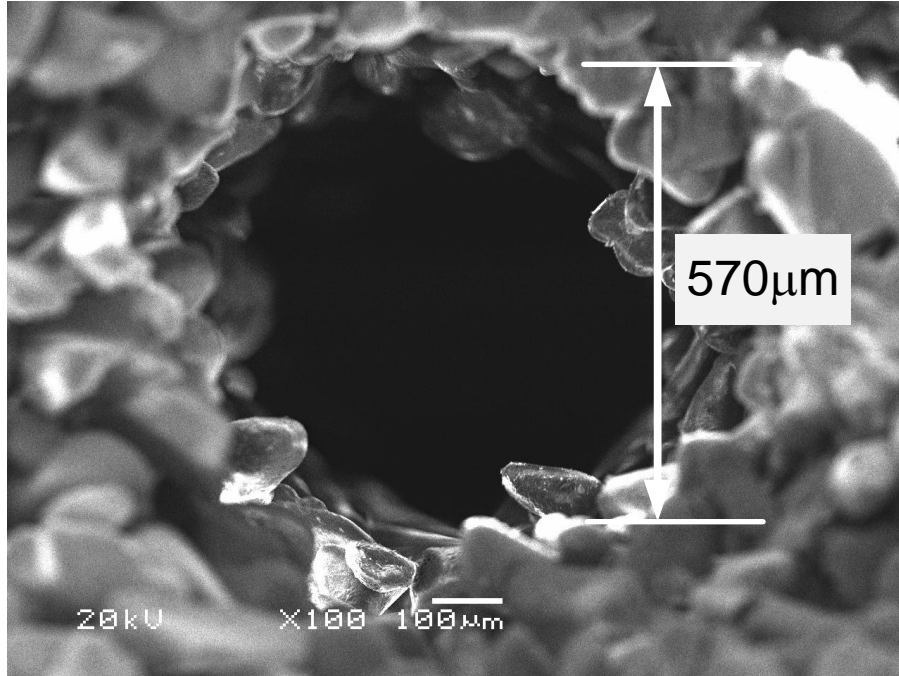


Figure 2-13: Detailed drawing of cylinders with 3 longitudinal channels.

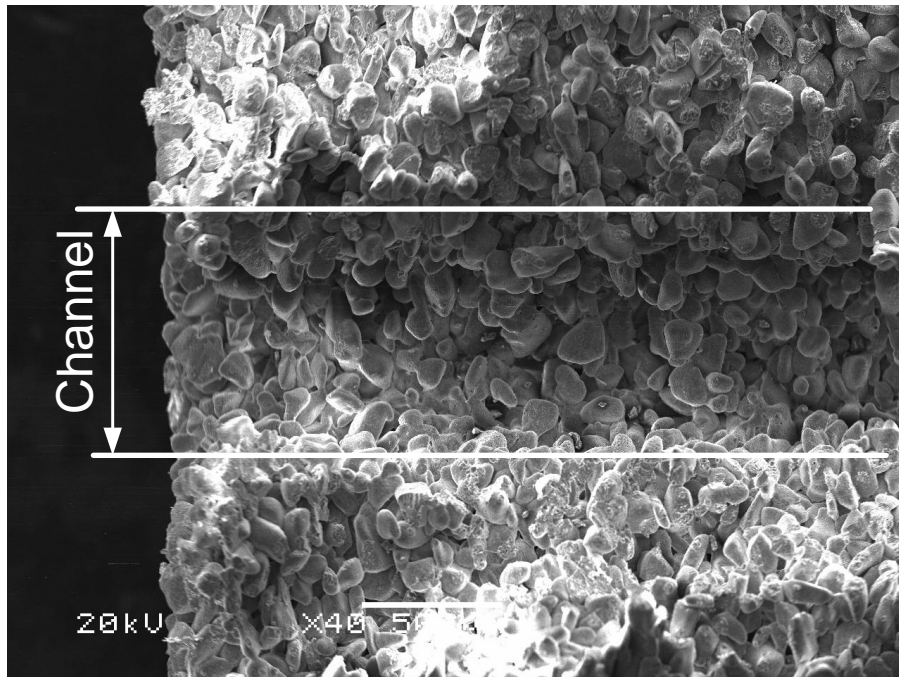
To obtain CPP structures with dimensions close to the targeted values, CAD models were prepared using the compensation factors found previously for 75-150  $\mu\text{m}$  powder. Air blowing through a 620  $\mu\text{m}$  syringe needle was applied to remove trapped loose powder within the channels. Finally, the samples were sintered with the regular protocol as described previously. A sintered CPP cylinder with three channels is shown in Figure 2-14. The channel size and pitch diameter were measured using SEM images of the samples (Figure 2-15) and were equal to 570  $\mu\text{m}$  and 1 mm, respectively. The measurement revealed that the final dimensions are in the range of the acceptable nominal tolerance of the SFF process which is  $\pm 100 \mu\text{m}$ .



Figure 2-14: A randomly selected SFF-made CPP cylinder with 3 longitudinal channels.



(a)



(b)

Figure 2-15: SEM images of CPP cylinder with 3 channels: (a) radial cross section, (b) longitudinal cross section.

To demonstrate the capability of the developed SFF technique to produce scaffolds with tiny inner channels, lattice-shaped cubes of  $5\text{ mm} \times 5\text{ mm} \times 5\text{ mm}$  with rectangular channels of  $300\text{ }\mu\text{m} \times 300\text{ }\mu\text{m}$  (Figure 2-16) were designed and built using  $45\text{-}75\text{ }\mu\text{m}$  CPP powder. An SEM image of a micro-channel produced within the lattice-shaped sample is shown in Figure 2-17.

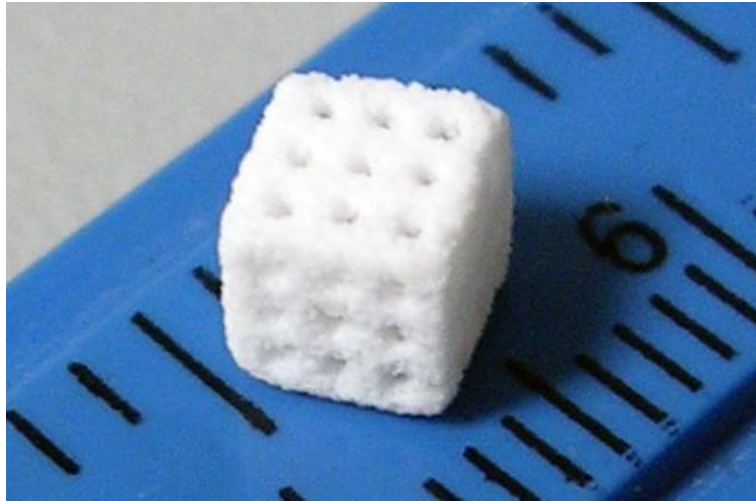


Figure 2-16: A lattice-shaped CPP sample fabricated using  $45\text{-}75\text{ }\mu\text{m}$  powder.

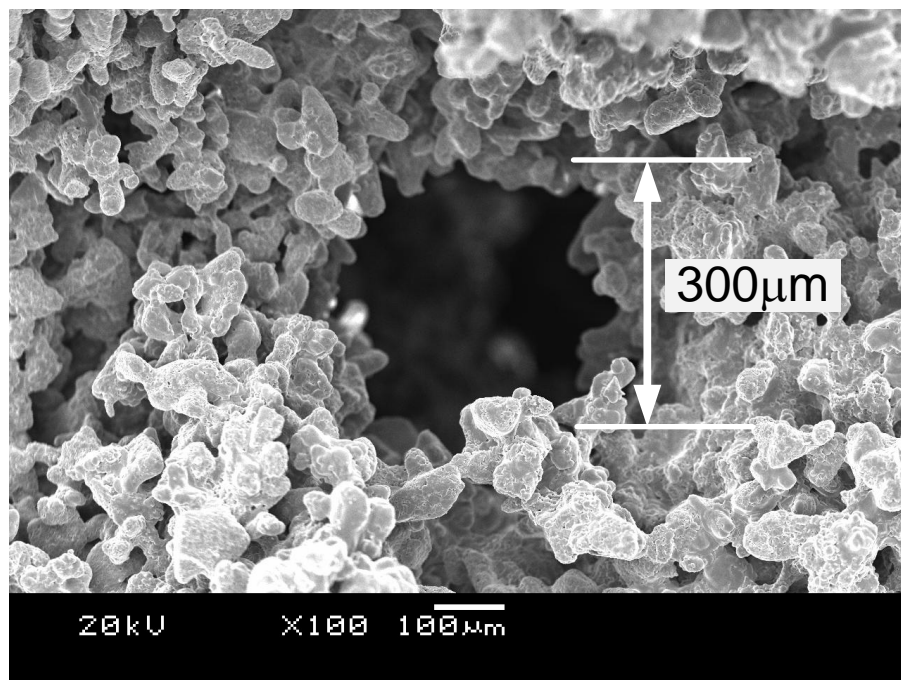


Figure 2-17: A micro-channel in CPP lattice-shaped structure. Channels of  $300\text{ }\mu\text{m}$  were formed in the structure.

In another study, rectangular micro-channels of  $\sim 600 \mu\text{m} \times 600 \mu\text{m}$  with 1.25 mm spacing distance were also incorporated in large anatomically-shaped (proximal tibial-shaped) implants formed using 45-75  $\mu\text{m}$  CPP powder as shown in Figure 2-18.

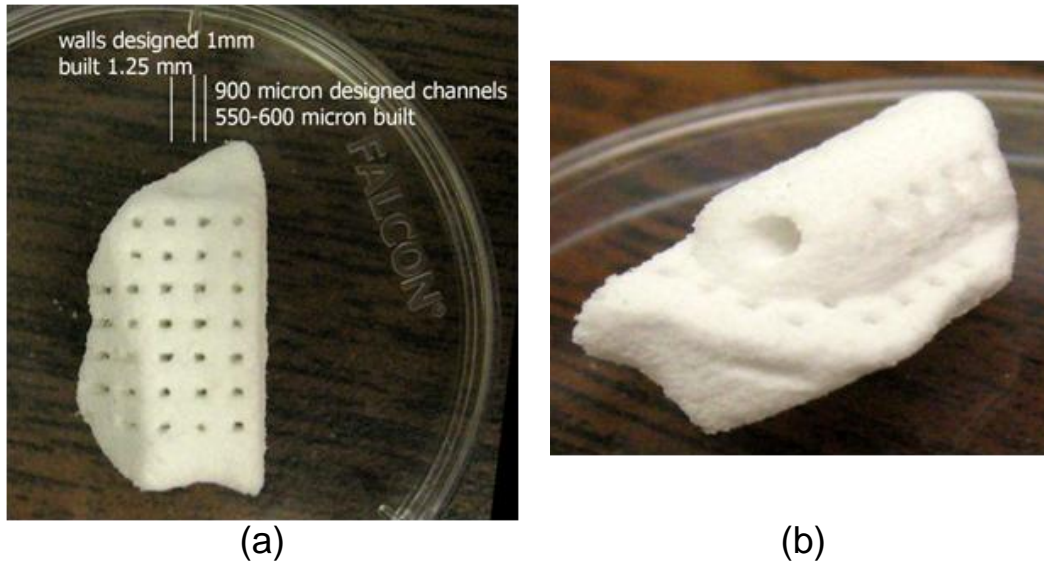


Figure 2-18: A SFF-made proximal tibial-shaped CPP structure with straight micro-channels of  $\sim 600 \mu\text{m}$ .

It was shown that the fabrication of CPP constructs with straight micro-channels is practical using the SFF process developed in this study. De-powdering of simple cavities and channels needs a minimum diameter of five times the average particle size [78]; however, in this study channels as large as approximately three times the average particle size were formed where CPP powder size of 45-75  $\mu\text{m}$  and 75-150  $\mu\text{m}$  was used.

### 2.3.3 Dual-Structural Porous CPP constructs

Implants with heterogeneous properties and with different micro-structure in an outer shell region (denser with smaller pores) and an inner core region (more porous with larger pores) may be preferred for biphasic osteochondral implants since such a structure mimics the micro-structure of natural subchondral bone [207]. Initial attempts to form dual-structural porous CPP constructs have been conducted previously using CS method [personal communication with Dr. R.M. Pilliar].



To fabricate CPP dual-structural porous constructs by SFF, the 45-75  $\mu\text{m}$  (fine) and 106-150  $\mu\text{m}$  (coarse) powders were utilized for the top thin substrate and bottom scaffold portion, respectively. The powder feeding chamber of the SFF machine was filled with fine powder followed by the coarse powder. Thus, the sample was built in sequential layers with the coarse lower density structure followed by a higher density region. Figure 2-19 illustrates a SFF-made dual-structural porous CPP sample. After sintering, the diameter of the sample is larger within the coarse region compared with the denser fine region. This might be due to the higher solvent penetration through the coarse PVA-CPP mixture. Different densification characteristics may also contribute.

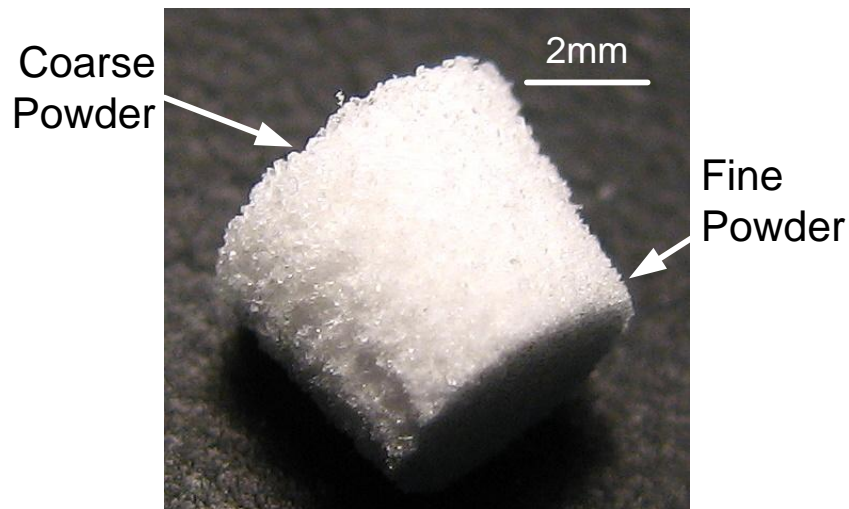
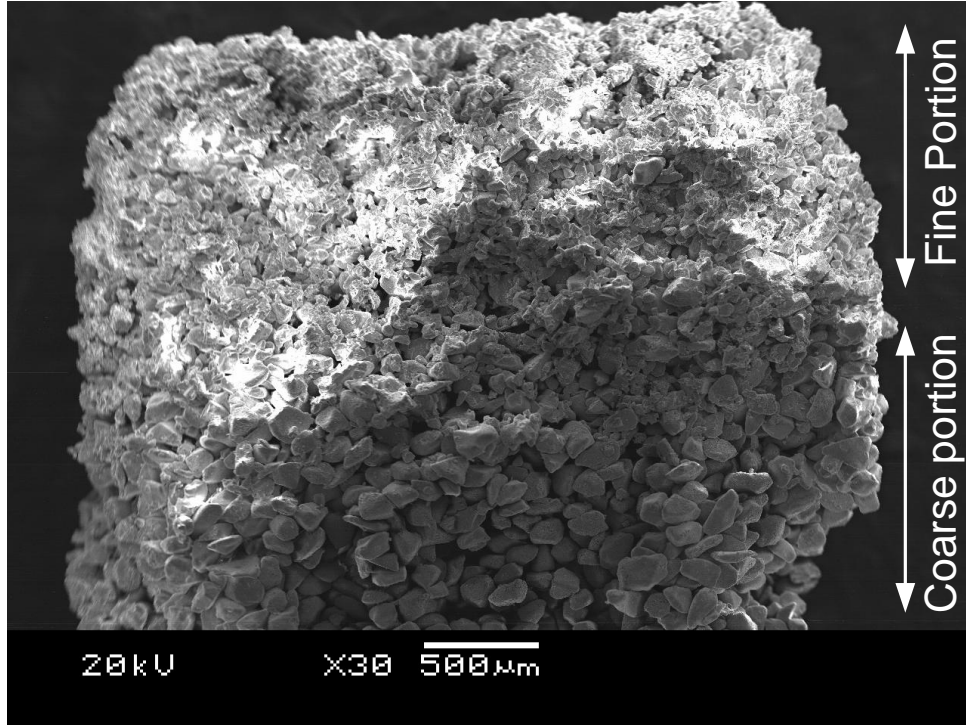
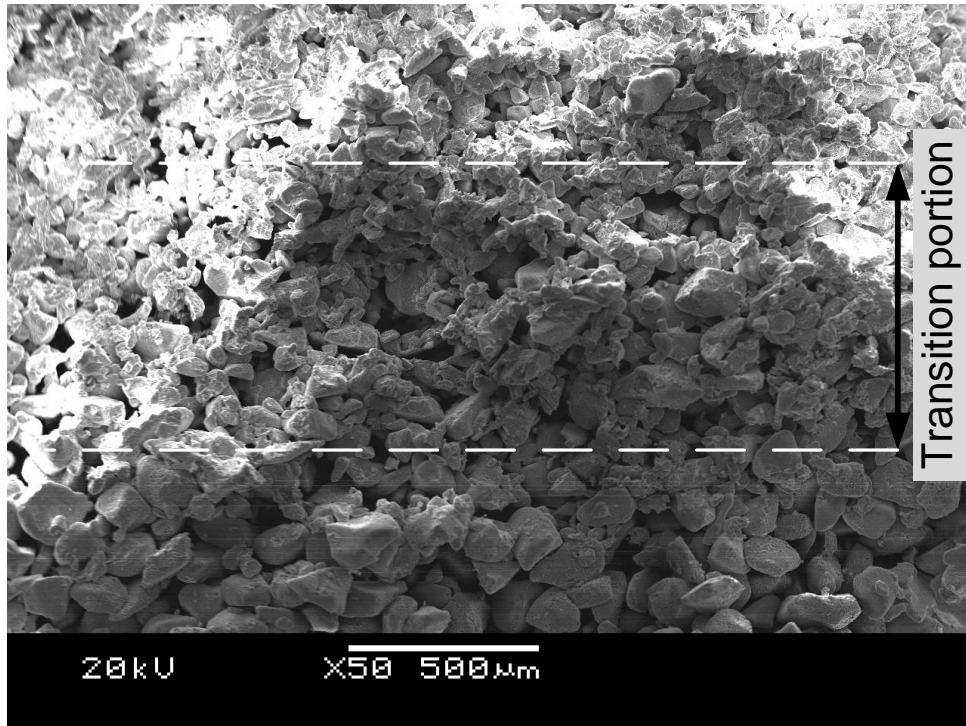


Figure 2-19: Dual-porous structure CPP sample before sintering.

In addition, the micro-structure of dual-structural porous CPP constructs is reflected in Figure 2-20. The  $\sim 1$  mm top portion with the fine particles is distinctive (finer structure). The thin transition region shown in Figure 2-20b is composed of both fine and coarse powders.



(a)



(b)

Figure 2-20: SEM of sintered dual-structural porous CPP sample: (a) 100X and (b) 50X. A functionally-graded micro-structure as well as a transition region is depicted between fine and coarse regions.

### 2.3.4 CPP Structures with Macro-pores

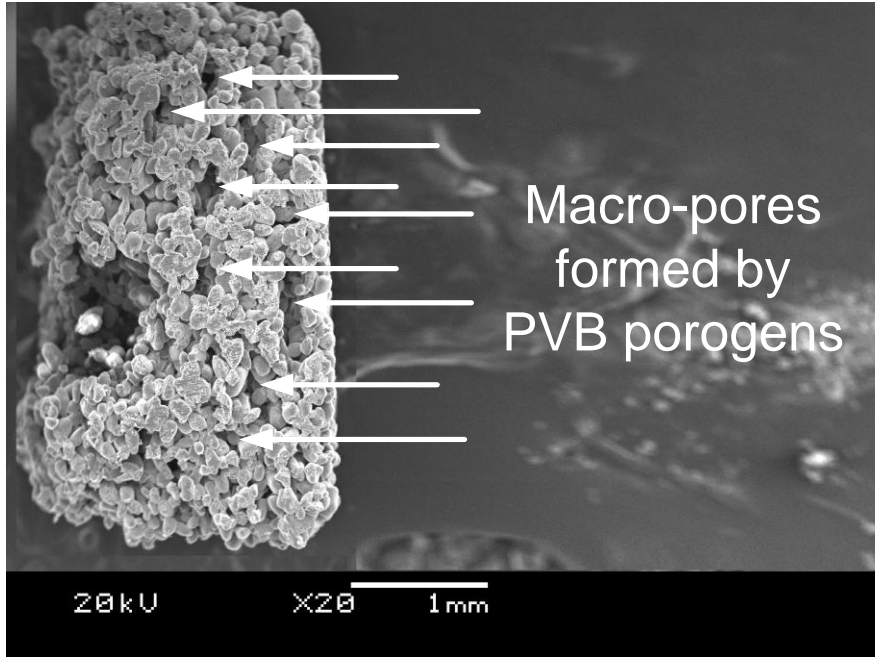
It has been shown that the regeneration of tissues by synthetic substitutes is dependent on the porosity and pore size of the supporting 3D structure. A high porosity is required for cells accommodation and blood vessels formation [208]. There is no consensus regarding the optimal pore size for bone regeneration in bone substitute constructs [209] although macro-porous structures with interconnecting pores with diameter of 100-800  $\mu\text{m}$  have been reported to be needed for bone ingrowth [61]. However, structures for bone regeneration are suggested to mimic the natural bone which is a hierarchical structure. Thus, macro-pores of about 100  $\mu\text{m}$  and larger are essential for sufficient density of invading cells and for governing the global level of mechanical properties. In addition, micro-pores in the range of 1-10  $\mu\text{m}$  have been suggested for the individual cell attachment and activity [152].

The fusion of particles during the sintering process does not eliminate all the gaps and micro-spaces between the particles, introducing randomly-distributed micro-pores to the structure. The SFF-made CPP constructs include micro-pores after sintering (which is characterized in detail in the next chapter). However, macro-porosity can be intentionally introduced into the material by adding volatile substances (porogens = pore generators) before sintering at high temperatures. Macro-pores are formed when the volatile materials are released. Porogen leaching is commonly used for the generation of macro-pores within structures [210].

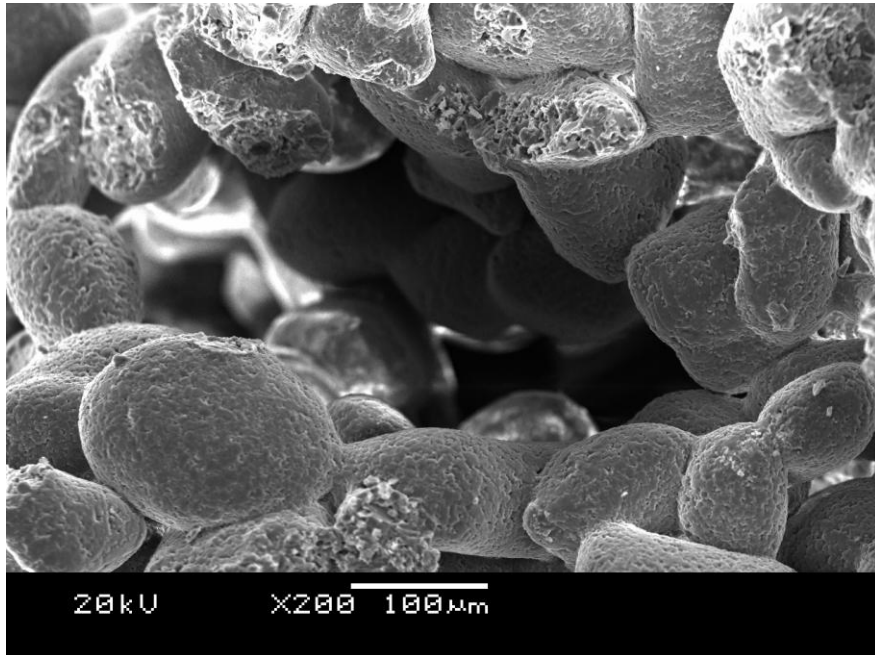
As explained in the previous chapter, one of the disadvantages of the powder-based SFF techniques is that loose powder traps in small features (such as holes) and cannot be readily removed from the part. As a result, selectively forming pores/voids in the range of hundreds of micrometers is not feasible. In this study, porogen leaching technique was used in combination with the SFF method in order to form macro-pores within SFF-made CPP structures. The term “macro-pores” is used to differentiate them from the micro-pores which are generated in the porous CPP structures after sintering.

As a preliminary investigation of combining the porogen leaching method with the SFF technique, 150-250  $\mu\text{m}$  particles of polyvinyl butyral (PVB), as the pore generators (porogens), were manually inserted within the CPP powder layers in sequential steps between the printings of each two layers during the SFF process (automation of the porogen insertion process is under development). For some samples, the porogens were leached out by soaking the green parts in ethanol, where the 65°C ethanol was kept circulated and refreshed for 4 hr. For the other samples, the PVB particles were burned-out during the first step of the post-processing in 400°C. A fabricated sample through the combination of SFF and porogen leaching methods

including macro-pores of about 200 to 500  $\mu\text{m}$  are shown in Figure 2-21. No significant difference was discerned between the pores produced by the two different mentioned leaching methods (alcohol leaching and burning-out).



(a)



(b)

Figure 2-21: Macro-pores generated through porogen leaching: (a) visual distribution and relative size of macro-pores, (b) a macro-pore of about 500  $\mu\text{m}$ .

## **2.4 Summary**

This chapter described the SFF process for fabrication of porous CPP structures using the adhesive bonding method. The preliminary attempts for fabrication of CPP cylinders with a desired geometrical accuracy were conveyed. To study the potential of the developed method to fabricate complex anatomically-shaped implants constructs, dual-porous structures, and channelled cylinders were formed using different CPP powder size. In addition, porogen leaching was combined with SFF to produce macro-pores in CPP samples. The developed SFF method demonstrates significant potential for formation of bone and osteochondral substitutes. It was observed that the SFF-prototyped parts have an adequate geometrical features and structural integrity to be used for tissue engineering applications.

## Chapter 3

# Characterization of SFF-made CPP Structures

In this chapter, the morphological analysis and physical characterization of SFF-made CPP structures are addressed. In addition, the chemical composition and mechanical properties (compressive and diametral tensile strengths) in orthogonal directions of the CPP samples are analyzed and the effect of layer stacking orientation on mechanical behaviour of such structures is studied. The characteristics of the SFF-made samples are compared with samples made through the conventional sintering technique.

### 3.1 Structural Characteristics

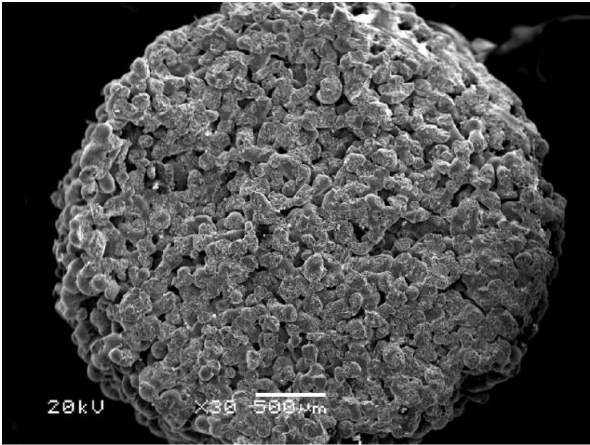
Scanning electron microscopy and micro-CT scanning were used to characterize the structure of the porous CPP samples.

#### 3.1.1 Scanning Electron Microscopy (SEM)

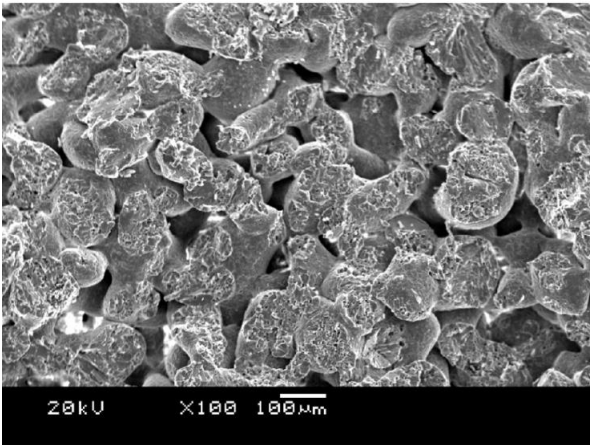
In this study, the post-SFF sintered samples were examined by secondary electron emission scanning electron microscopy (SEM, JSM-6460, Jeol Ltd. Akishima, Tokyo). The samples were first sputter-coated with gold (10 nm thick film) (SPI SputterTM, SPI Supplier Division of Structure Prob Inc, West Chester, PA, USA) to make them electrically conductive. A 20 kV accelerating voltage was used for the SEM assessments.

The SEM images of the sintered SFF-made (SFF-V) structure is shown in Figure 3-1, with virtually uniform distribution of porosity from the periphery to the center of the sample and a well-developed structural integrity. In the SEM micrographs of the sintered parts (Figure 3-1b and c), the three-dimensional interconnected nature of the porosity is evident. The well-

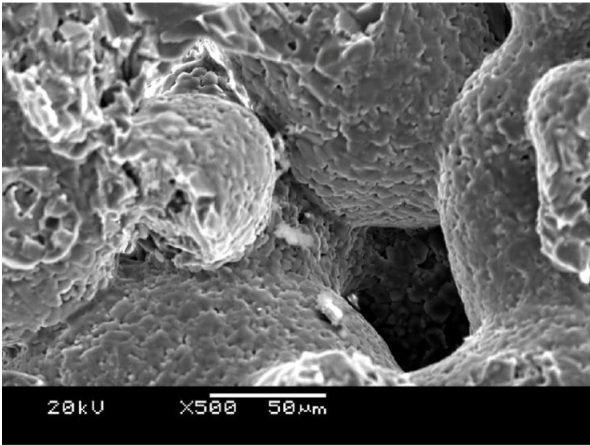
developed sinter necks with sinter neck dimensions approaching the adjoining particle dimensions are observed in many regions.



(a)



(b)



(c)

Figure 3-1: SEM images (with different magnification levels) of final sintered SFF-made (SFF-V) CPP cylinder showing the three-dimensional interconnected porosity of the samples.

### 3.1.2 Micro-CT Scanning

Micro-CT scanning was used to obtain sliced views as well as 3D models of the internal and external structure of the CPP samples.

Porous CPP samples were scanned by a high-resolution micro-computed tomography machine (MicroCT40, Scanco Medical, Basserdorf, Switzerland). The CT-scanner was set to operate at 70 kV, 114  $\mu$ A, and resolution of 6  $\mu$ m. The acquisition files were obtained at 1000 projections with 2,048 samples each (per 180° of rotation), 0° angle increments, 300 ms of integration time, and 1 frame averaging. Structure porosity, pore distribution, and pore wall thickness distribution were calculated by the Scanco software. The scan images were also used for visual analysis of the micro-structures. Micro-CT scans were also used to generate virtual 3D structures of the scanned objects.

The micro-CT scans of the radial and longitudinal cross sections of the CPP samples as well as the generated 3D models of the vertically SFF-made (SFF-V), horizontally SFF-made (SFF-H) and conventionally-sintered (CS) samples are shown in Figure 3-2 and Figure 3-3. Relatively uniform distributions of interconnected network of pores within the CPP structures are observed. However, the sintered particles and pores in the SFF-made samples appear coarser than in the CS samples.



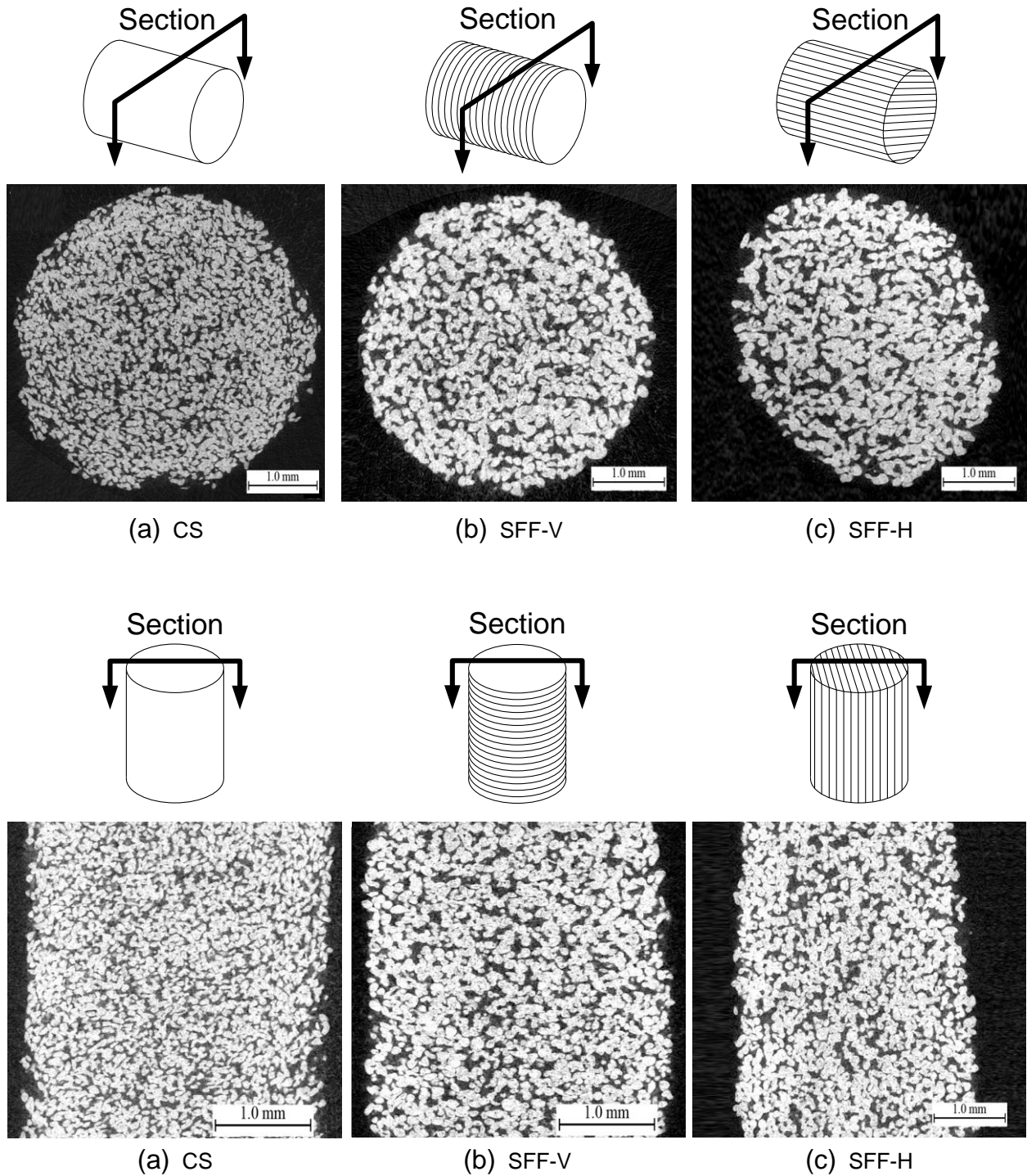
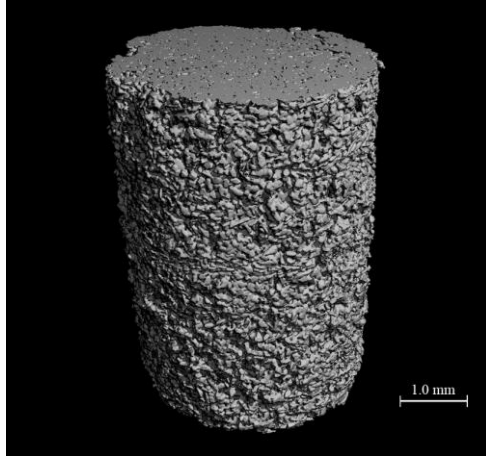
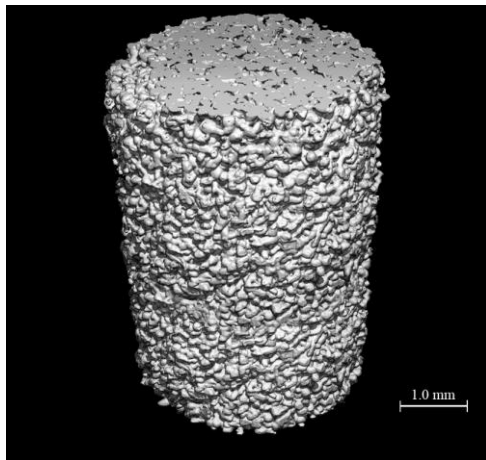


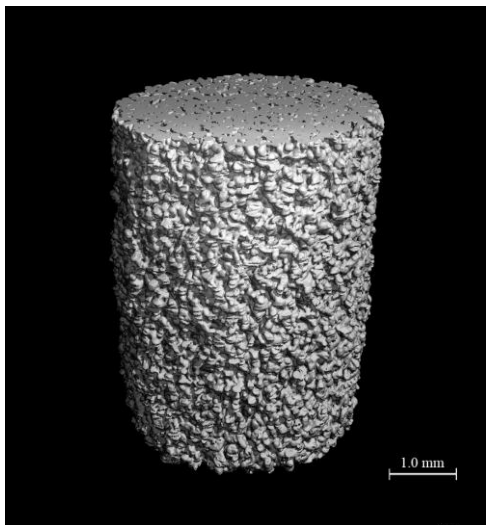
Figure 3-2: Micro-tomography of (a) CS, (b) SFF-V, and (c) SFF-H samples, top: radial cross sections, bottom: longitudinal cross section. The relatively-uniform distribution and interconnectivity of the pores are observed in the cross sections of all samples.



(a) CS



(b) SFF-V



(c) SFF-H

Figure 3-3: 3D models of (a) CS, (b) SFF-V, and (c) SFF-H samples generated using the micro-CT scans.

## 3.2 Physical Characteristics

### 3.2.1 Porosimetry Analysis

The porosity of each sintered sample was determined using three methods: (1) ethanol displacement (Archimedes method), (2) mercury intrusion porosimetry, and (3) micro-CT scanning.

For the Archimedes method, an ethanol bath attached to a microbalance (Sartorius YDK01 Density determination Kit, Sartorius AG, Goettingen, Germany) was used, according to ASTM C373. The percent porosity of the samples was determined using the bulk density of the sintered samples ( $n=10$ ) and the theoretical density of non-porous CPP, which is equal to  $2.85 \text{ g/cm}^3$  [52], through the following equation:

$$\text{Porosity} = \left(1 - \frac{\rho_{bulk}}{2.85}\right) \times 100 \quad (3-1)$$

In addition, the porosity and pore size distribution within the CPP samples were measured using mercury intrusion porosimetry (Poremaster, Quantachrome Instruments, Boynton Beach, FL, USA). The experiment was conducted in two steps: low pressure (0-55 psi) and high pressure (0-60 kpsi) to collect the micro- and nano-scale pore data.

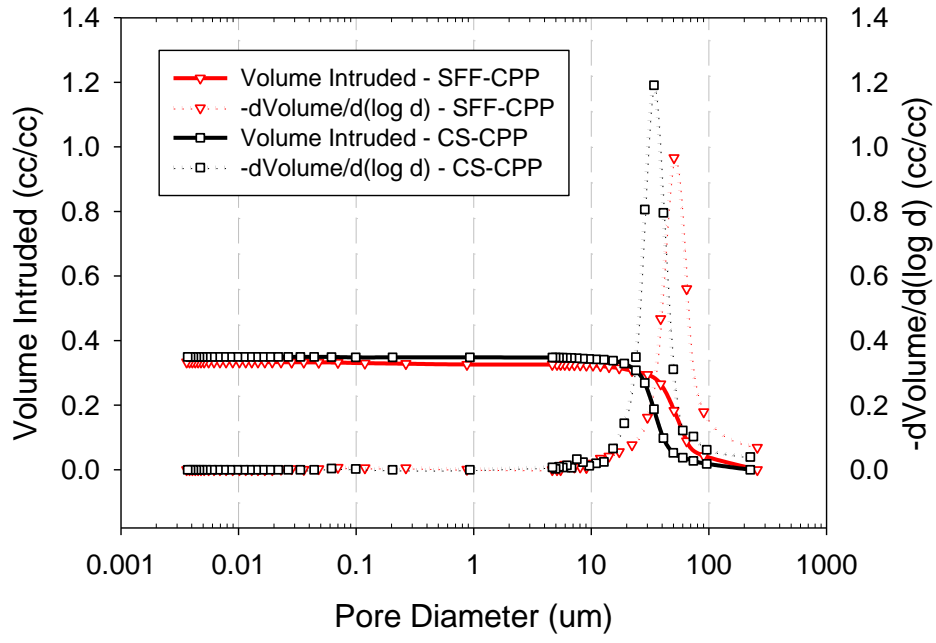
Furthermore, the porous CPP samples were scanned using high-resolution micro-computed tomography (MicroCT40, Scanco Medical, Basserdorf, Switzerland). The specifications of the experiment were described in the morphology analysis section. Structure porosity, pore size distribution and mean pore size, as well as mean size and distribution of trabecular thickness (inter-pore wall thickness) were calculated using the Scanco software.

The average volume percent porosity of the fabricated SFF-V, SFF-H and CS cylinders was determined through the Archimedes method, mercury porosimetry, and micro-CT scanning as listed in Table 3-1. The results of mercury porosimetry and micro-CT scan are considered more reliable [211].

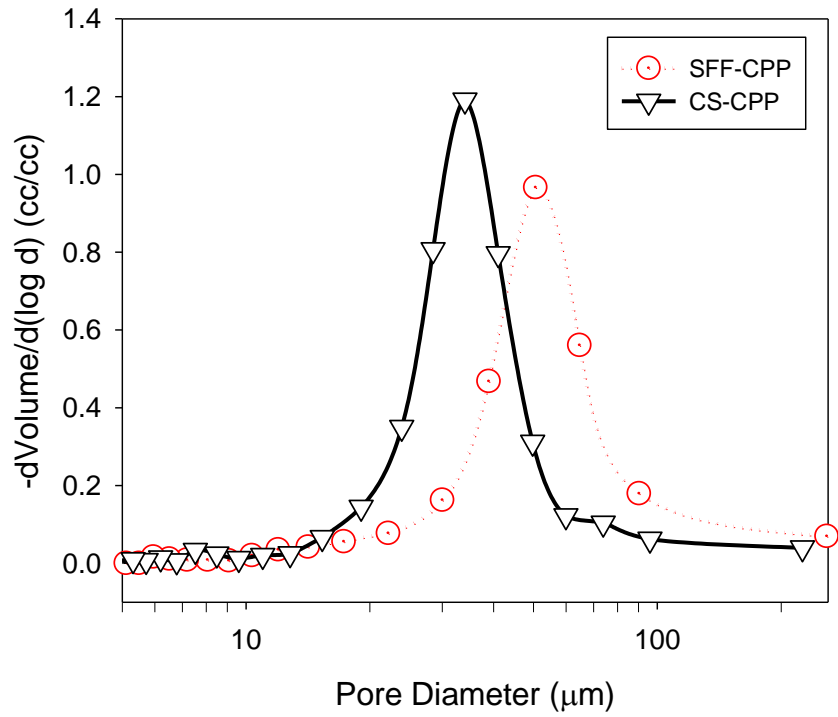
Table 3-1: Average volume percent porosity of CPP structures using the Archimedes method, mercury porosimetry, and micro-CT scan analysis.

Method	Ethanol Displacement (Archimedes) (n=10)	Mercury Intrusion (n=5)	Micro-CT Scanning (n=1)
Porosity	38±1%	35%	32-35%

Figure 3-4 shows the mercury porosimetry data of the SFF-made (SFF-V) and CS samples. The figure suggests that despite the same volume percent porosity of the SFF-made and CS samples (~35%), there is an apparent difference in pore size distribution where the SFF-formed samples have a wider pore size range (5-258 vs. 5-225  $\mu\text{m}$ ) and a larger mean pore size (~50 vs. 33  $\mu\text{m}$ ). In addition, pores of 50-500 nm (intra-particle as well as at some inter-particle junctions) were observed for both SFF and CS samples.



(a)



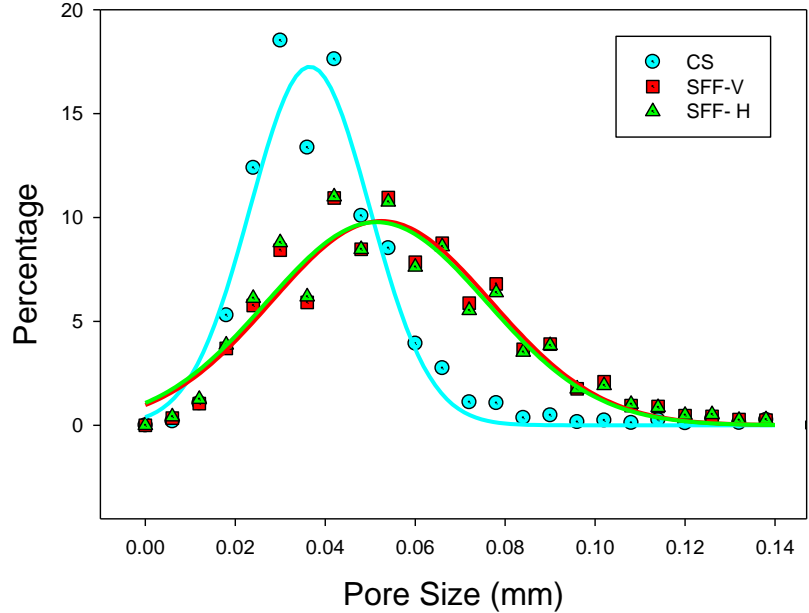
(b)

Figure 3-4: Mercury intrusion porosimetry data of the sintered CPP cylinders. SFF-made (SFF-V) and CS structures have 5–258 and 5–225 μm pore size range as well as 50 and 33 μm mean pore sizes, respectively.

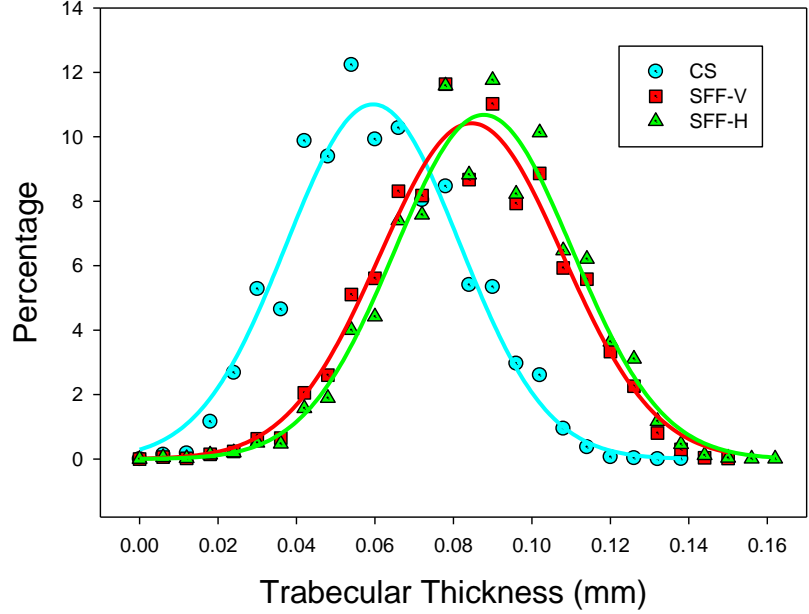
In addition, the distribution of the pore size and trabecular thickness of the SFF-V, SFF-H, and CS samples obtained by micro-CT scanning are plotted in Figure 3-5. The figure suggests that the vertically and horizontally SFF-made samples include porous structures with similar pore size (56  $\mu\text{m}$ ) and range (~5-140  $\mu\text{m}$ ) as well as similar trabecular thickness (84  $\mu\text{m}$ ) and range (~20-160  $\mu\text{m}$ ). Also, CS samples include smaller pores (~5-80  $\mu\text{m}$ , 38  $\mu\text{m}$  on average) and thinner trabecular structure (~10-120  $\mu\text{m}$ , 64  $\mu\text{m}$  on average) between pores/voids. The distribution color-map of the trabecular thicknesses and pore sizes are also shown in Figure 3-6. The micro-CT results are in agreement with the mercury porosimetry. The micro-structural characteristics of the porous CPP structures are presented in Table 3-2.

Table 3-2: Micro-structural characteristics of the SFF-V, SFF-H and CS porous CPP structures measured by micro-CT scanning and mercury intrusion.

Method	Feature		SFF-V	SFF-H	CS
Micro-CT	Pore Size ( $\mu\text{m}$ )	Mean	56	56	38
		Range	~5-140	~5-140	~5-80
	Trabecular Thickness ( $\mu\text{m}$ )	Mean	84	87	64
		Range	~20-160	~20-160	~10-120
Mercury Intrusion	Pore Size ( $\mu\text{m}$ )	Mean	50	-	33
		Range	~5-258	-	~5-225



(a)

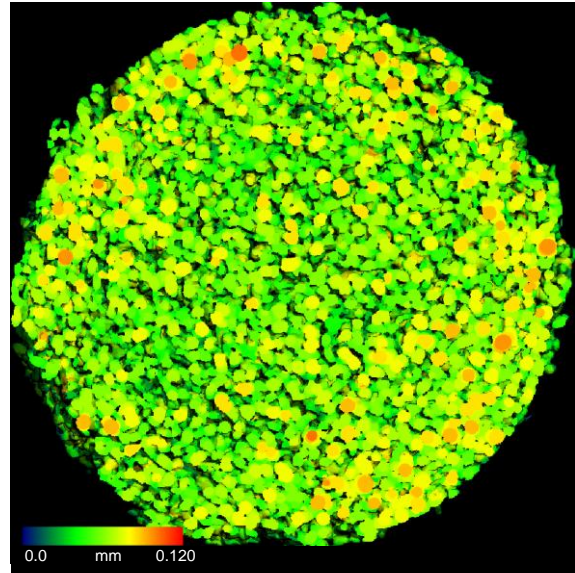
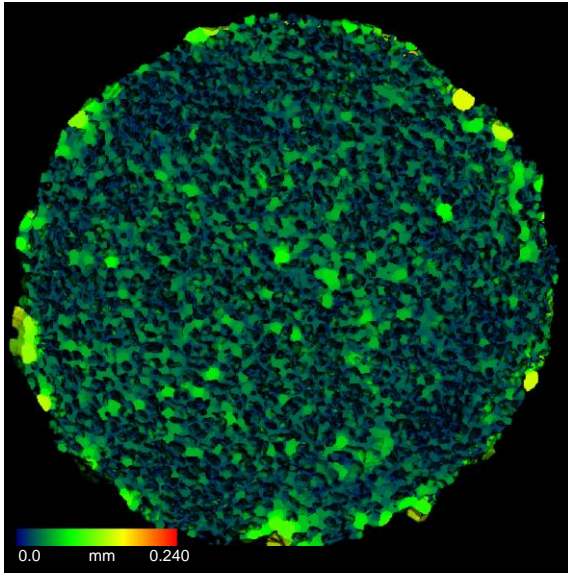


(b)

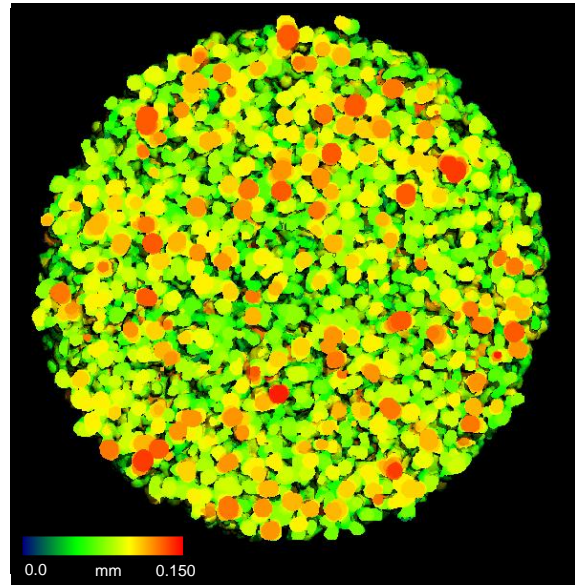
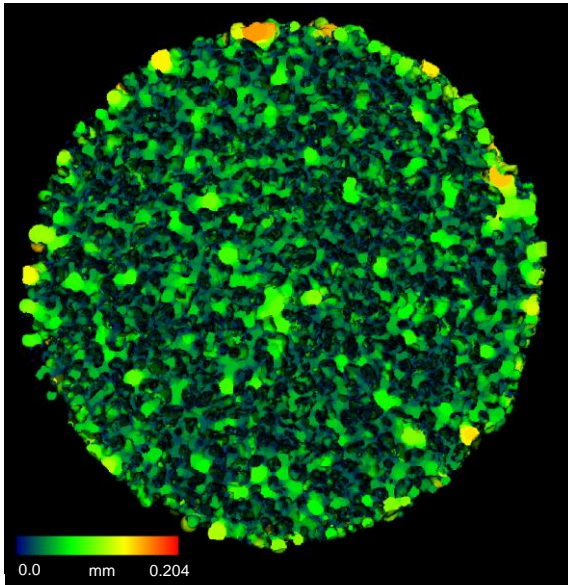
Figure 3-5: Micro-structure data of the SFF-V, SFF-H and CS CPP samples obtained by micro-CT scanning: (a) pore size distribution in the range of 5-140  $\mu\text{m}$  for SFF-made and 5-80  $\mu\text{m}$  for CS samples, (b) trabecular thickness distribution in the range of 20-160  $\mu\text{m}$  for SFF-made and 10-120  $\mu\text{m}$  for CS samples.

Pore size

Trabecular thickness



(a)



(b)

Figure 3-6: Micro-structural properties of the (a) CS and (b) SFF-V samples obtained by micro-CT scanning: (left) pore size distribution color-map, (right) trabecular thickness distribution color-map.



### 3.2.2 Specific Surface Area

Based on the micro-CT data, 3D CAD model of the CPP structures was generated using Mimics software (Materialise NV, Leuven, Belgium). Using the generated CAD model, the specific surface area of the samples was calculated and determined to be equal to 24 and 31  $\text{mm}^2/\text{mm}^3$  for the SFF-made and CS structures, respectively.

### 3.2.3 Permeability

Mercury intrusion can be used to characterize the portions of porous structures that dominate hydraulic permeability as proposed by Katz et al. [212, 213]. Permeability (hydraulic conductivity) of the SFF-made and CS CPP porous structures was calculated using the raw porosimetry data obtained by mercury intrusion method. The detailed procedure for calculating permeability is presented in Appendix B. Permeability of the SFF-made structures was determined to be  $2.2 \times 10^{-12} \text{ m}^2$ . Smaller pore size of the CS structures resulted in lower permeability ( $=1.0 \times 10^{-12} \text{ m}^2$ ).

## 3.3 Chemical Characteristics

### 3.3.1 X-Ray Diffraction (XRD) Analysis

X-ray diffraction (XRD) analysis was undertaken (SA-HF3, Rigaku, Japan) to characterize the crystallography of the CPP sintered parts (SFF-formed and sintered as well as conventionally-sintered). The XRD was conducted using a step scan size of  $2\theta = 0.02$  between 10 and 90 degrees. For the XRD assessment, the samples were crushed to a fine powder with a pestle and mortar.

The XRD patterns of the SFF-made and CS crystalline CPP samples sintered at 950 °C are shown in Figure 3-7. The similarity in the variation of the relative intensity on the XRD patterns for the sintered samples and samples shown in a previous study [214] indicates that the resulting sintered CPP is  $\beta$ -CPP. The patterns are consistent indicating that PVA and the aqueous solvent have not introduced any additional phases or residuals.

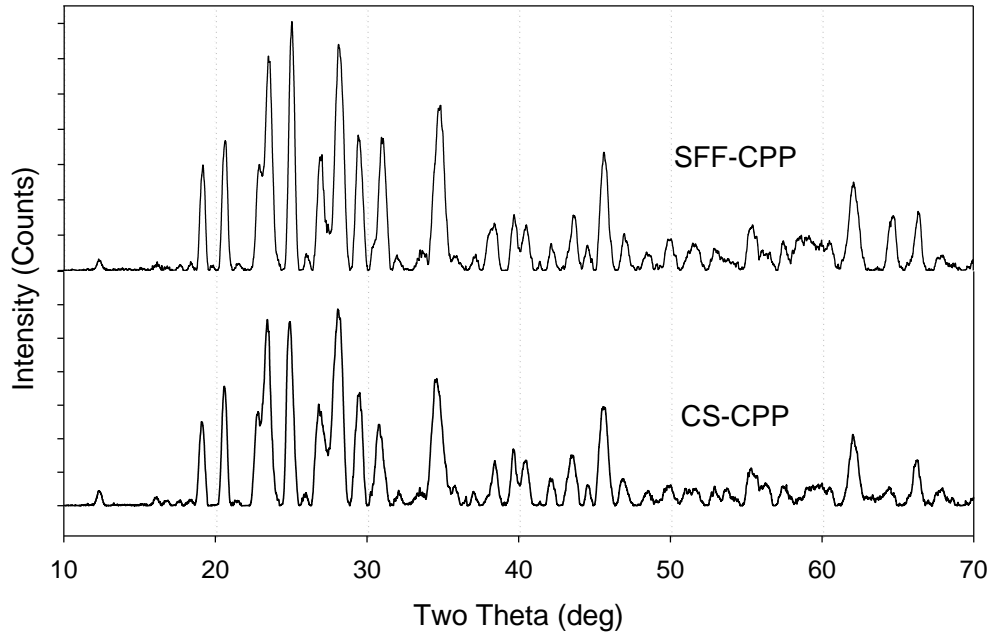


Figure 3-7: XRD patterns of SFF-made and CS. The patterns are identical but there are small discrepancies in the peak intensities of the XRD patterns of SFF-made and CS samples.

### 3.4 Mechanical Characteristics

Mechanical assessments of the formed CPP samples are described in two parts. The first part is devoted to the assessment of mechanical properties corresponding to the material of the CPP samples whereas the second part is on the characterization of structural mechanical properties of the porous CPP constructs.

#### 3.4.1 Mechanical Properties of CPP Materials

The intrinsic mechanical properties of the sintered (crystallized) CPP material (NOT the CPP structures), including modulus of elasticity and hardness, were measured through nano- and micro-indentation experiments.

### 3.4.1.1 Nano-indentation

For nano-indentation test, the CPP samples were embedded in EpoThin low viscosity epoxy resin (Buehler Ltd., Lake Bluff, IL) and polished with 1  $\mu\text{m}$  diamond suspension (Buehler Ltd., Lake Bluff, IL) followed by mechanical vibration polishing using 0.05  $\mu\text{m}$  colloidal silica suspension as polishing medium.

A commercial nano-indentation system (Nano Indenter XP System, MTS Nano Instruments, Oak Ridge, TN, USA) equipped with a Berkovich diamond tip (AccuTip) was used to evaluate the mechanical properties (including modulus of elasticity and nano-hardness) of the sintered CPP material in the three fabricated structures: SFF-V, SFF-H, and CS<sup>3</sup> using continuous stiffness measurement mode (CSM). The amplitude and frequency of the sinusoidal signal was 2 nm and 45 Hz, respectively. The measurements were displacement controlled with penetration depth of 2000 nm for dry conditions. The strain rate (loading rate/load) was set to 0.05 s<sup>-1</sup>, and the allowable drift rate was set to 0.1 nm/s for increased accuracy. The values for hardness and modulus of elasticity were calculated from the average of the 1000 nm depth from 500 nm to 1500 nm. 10 indentation points were targeted for the test on each sample. For the SFF samples, the nano-indentation test was done in two planes: (1) across the radial sections and (2) along the longitudinal sections of the cylinders (Figure 3-8). Typical load-displacement curves of nano-indentation testing are presented in Figure 3-9. Also, typical curves of material properties (modulus of elasticity and hardness) evaluation test are shown in Figure 3-10. As shown in the figure and listed in Table 3-3, Young's modulus and nano-hardness of all three CPP structures are reasonably identical. It was also concluded that the mechanical properties of the crystalline CPP was isotropic.

---

<sup>3</sup> The nano-indentation test was conducted by Dr. Rizhi Wang at the University of British Columbia.

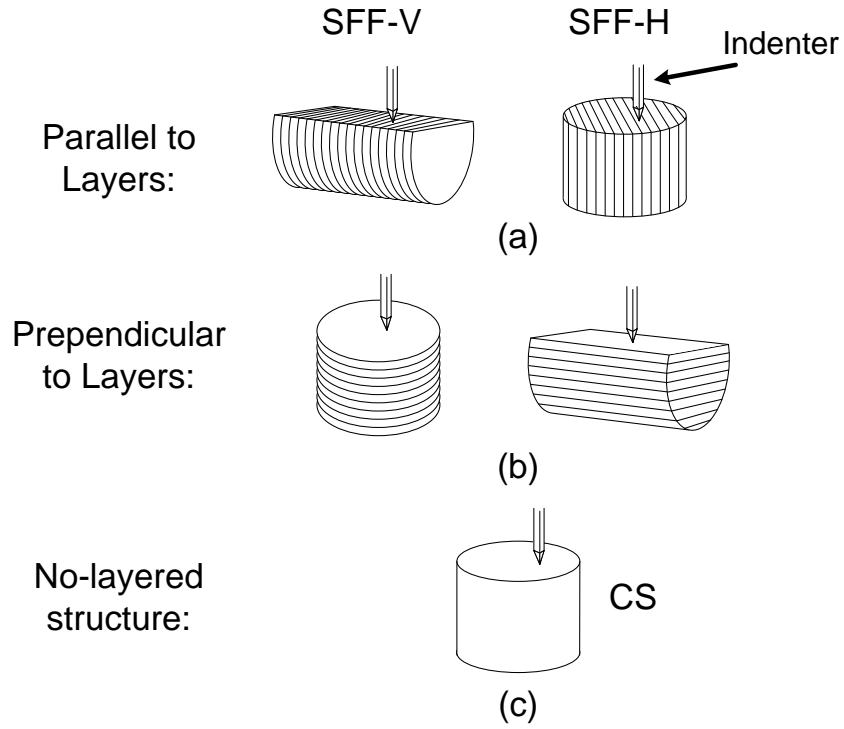


Figure 3-8: Schematic of the nano-indentation process: SFF-V and SFF-H samples were tested in both parallel and perpendicular directions to the stacked-layers.

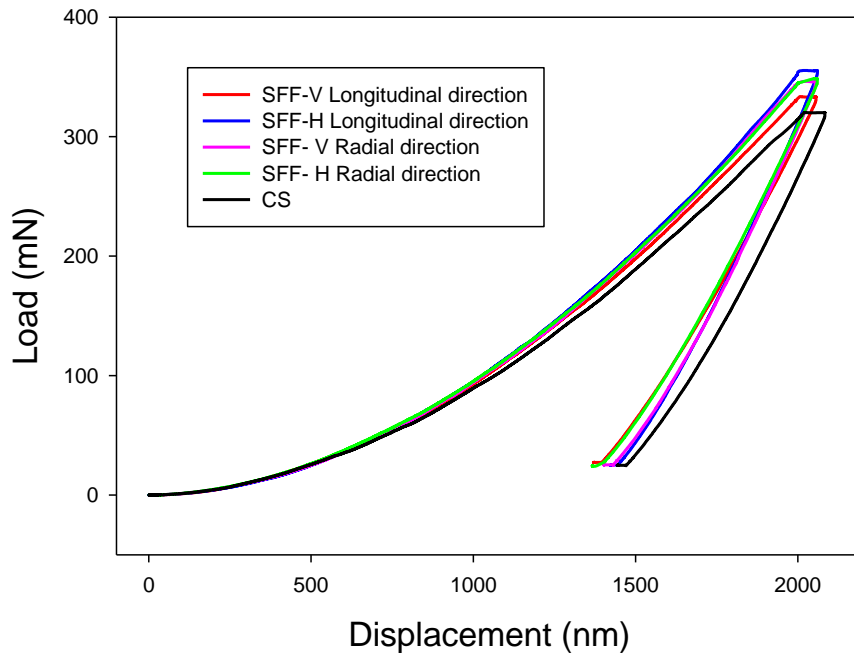


Figure 3-9: Typical load-displacement curves of nano-indentation on SFF-V, SFF-H and CS CPP samples. SFF-made parts are examined in two directions: parallel and perpendicular to layers.

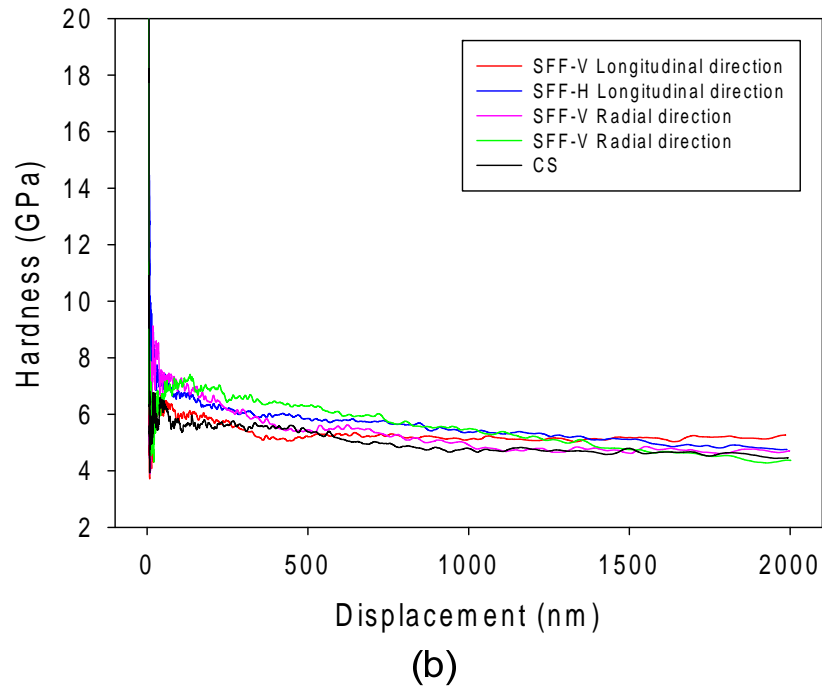
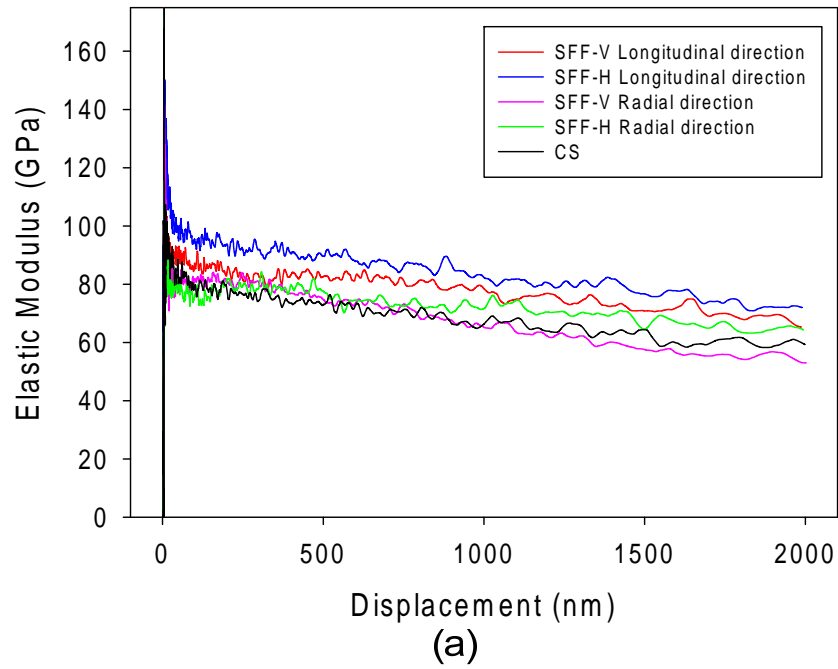


Figure 3-10: Randomly selected curves of (a) elastic modulus-displacement and (b) hardness-displacement obtained via nano-indentation on SFF-V, SFF-H and CS CPP samples. SFF-made parts are examined in two directions: parallel and perpendicular to layers.

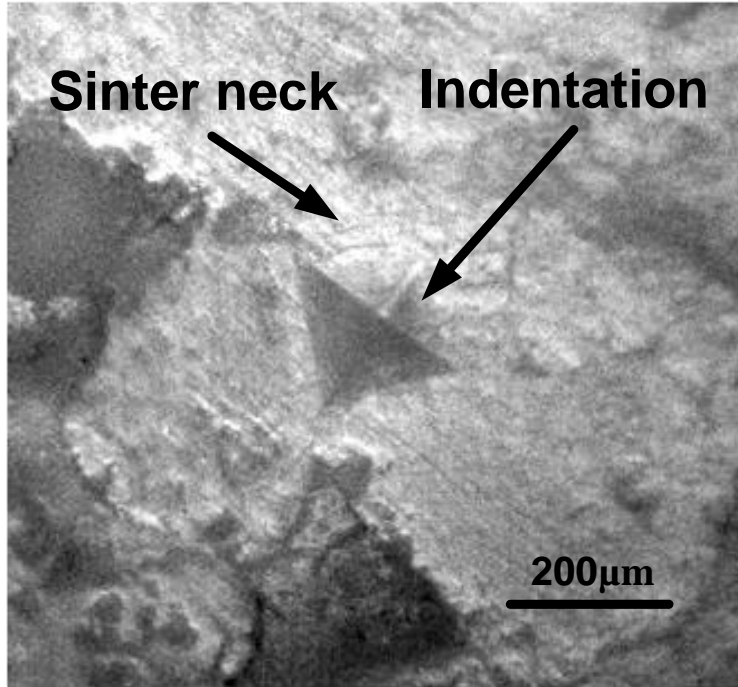
### 3.4.1.2 Micro-indentation

In order to evaluate the micro-hardness of the CPP material, the specimens were embedded in epoxy mounting medium and polished on various grades of silicon carbide paper down to 1200 grit. The hardness of the specimens was analyzed by a Leco micro-hardness tester (MHT series 200, Leco, Michigan, US). A 300 gr load was applied to the specimens for 10 sec using a pyramid-shaped diamond indenter. The diagonals of the formed indent were then measured at 10X magnification and the Vickers hardness number calculated using the following equation:

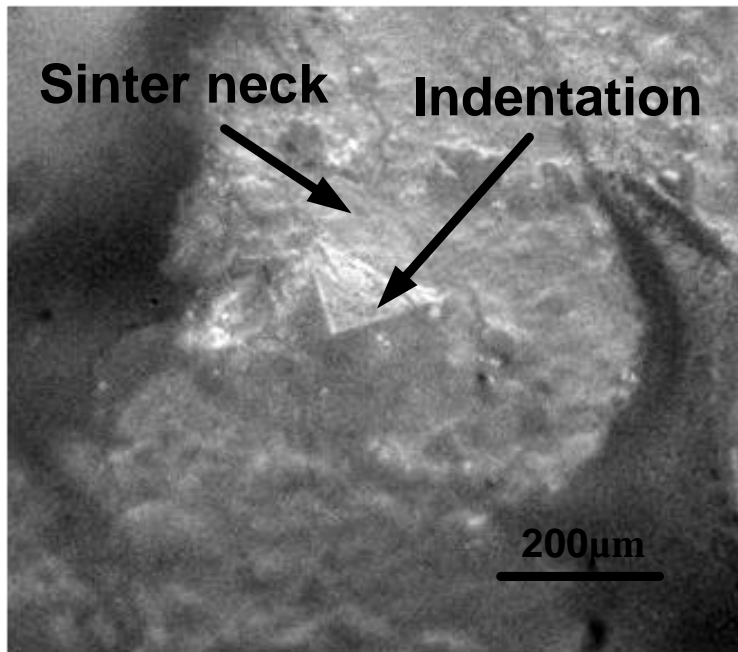
$$VHN = \frac{1854.4 \times P}{d^2} \quad (3-2)$$

where  $P$  is the applied load in grams and  $d$  the mean of the two measured diagonals in micrometers. Each specimen was indented 8 times on the sintering necks selected from different sides of the sample.

The optical microscopy images of the Vickers micro-indentation on the CPP structures are shown in Figure 3-11. As depicted in the figure, the indentation target point was selected to be on the sinter necks between CPP particles. The indenting load produced indentations that were placed as nearly as possible within a single sinter neck. The results are included in Table 3-3 and revealed that the hardness of the crystalline CPP material is similar for the SFF-made and CS structures. In addition, it was shown that, in SFF-made structures, although higher sinter shrinkage was observed in the direction parallel to the stacked-layers, the hardness in that direction did not differ from the direction normal to the stacked-layers.



(a)



(b)

Figure 3-11: Optical microscopic images of Vickers micro-indentation finger prints on CPP: (a) CS and (b) SFF-made samples. Sinter neck areas were targeted for indentation to measure the hardness on the formed neck.

Table 3-3: Mechanical properties (Young’s modulus, nano- and micro-hardness) of SFF-V, SFF-H and CS CPP samples in two directions: parallel and perpendicular to layers.

	SFF-V			SFF-H			CS		
	E (GPa)	n-H (GPa)	$\mu$ -H (HV)	E (GPa)	n-H (GPa)	$\mu$ -H (HV)	E (GPa)	n-H (GPa)	$\mu$ -H (HV)
<b>Parallel to layer</b>	62.16± 5.74	5.73± 0.59	30.83± 10.10	67.52± 5.29	5.79± 0.25	30.83± 10.10	61.42± 7.50	5.33± 0.75	30.41± 11.15
<b>Perpendicular to layer</b>	60.00± 7.32	5.73± 0.33		59.71± 9.25	5.61± 0.62		61.42± 7.50	5.33± 0.75	30.41± 11.15

### 3.4.2 Structural Mechanical Properties

The compressive and tensile mechanical strengths of the porous CPP structures were assessed through uniaxial and diametral compression tests.

#### 3.4.2.1 Uniaxial Compression

Uniaxial compression tests were conducted using a mechanical testing instrument with a 1 kN load-cell (Instron 5548 Micro-Testing, MA, USA) and a cross-head loading rate of 0.2 mm/min. A population of 10 samples (cylinders of 4 mm in diameter and 6 mm in height) of each type of CPP structure was employed for this investigation. The ultimate compressive strength was evaluated using the load–displacement curve with the peak load from the curve and the initial cross-sectional area of the sample. Randomly selected compression load-displacement curves of sintered samples are shown in Figure 3-12. The compressive strengths of the SFF-made and CS samples are listed in Table 3-4.



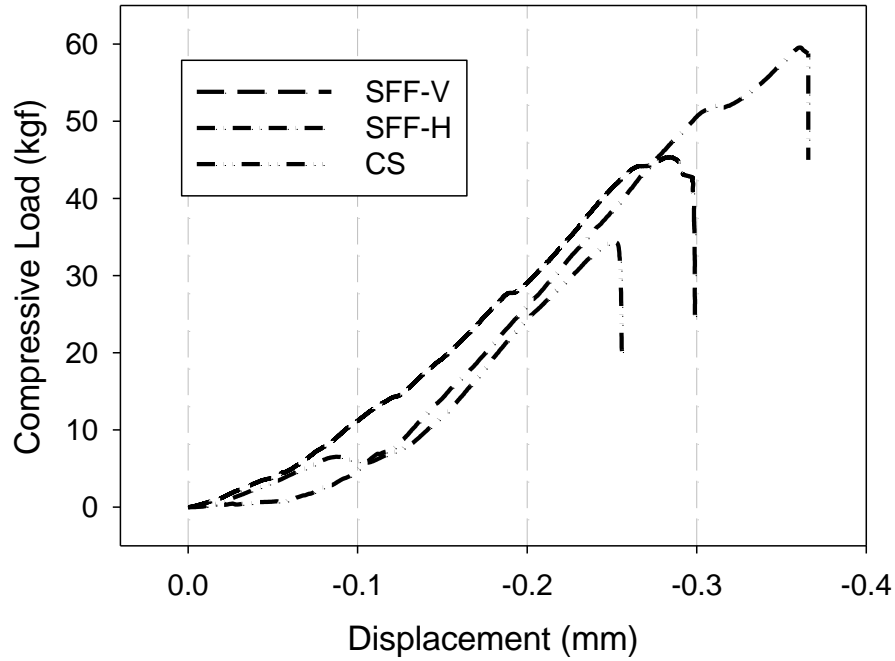
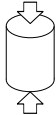

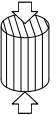


Figure 3-12: Typical load-displacement curves of the sintered 6mm long SFF-V, SFF-H, and CS cylinders. The uniaxial compressive load was applied along the height of the cylinders with the crosshead rate of 0.2 mm/min.

Table 3-4: Uniaxial compressive strengths and Weibull moduli of the CS, SFF-V and SFF-H CPP cylinders (n=10).

Mechanical Properties	CS 	SFF-V 	SFF-H 
Strength (MPa)	21.06±4.51	33.86±6.32	50.17±4.74
Weibull Modulus	4.45 (R <sup>2</sup> =0.96)	5.23 (R <sup>2</sup> =0.94)	9.93 (R <sup>2</sup> =0.88)

In addition, Figure 3-13 shows the failure probability for the applied stresses in the CPP structures as determined by the following equation [215]:

$$P = 1 - \exp[-(\sigma / \sigma_0)^m] \quad (3-3)$$

where  $P$  is the failure probability, and the Weibull modulus,  $m$ , and scale value,  $\sigma_0$ , are adjustable parameters. Weibull modulus, a dimensionless number, represents the reproducibility of the mechanical strength of the CPP structures. In Figure 3-13, the straight lines are the best fits using the linear regression function by which the Weibull modulus is calculated as listed in Table 3-4.

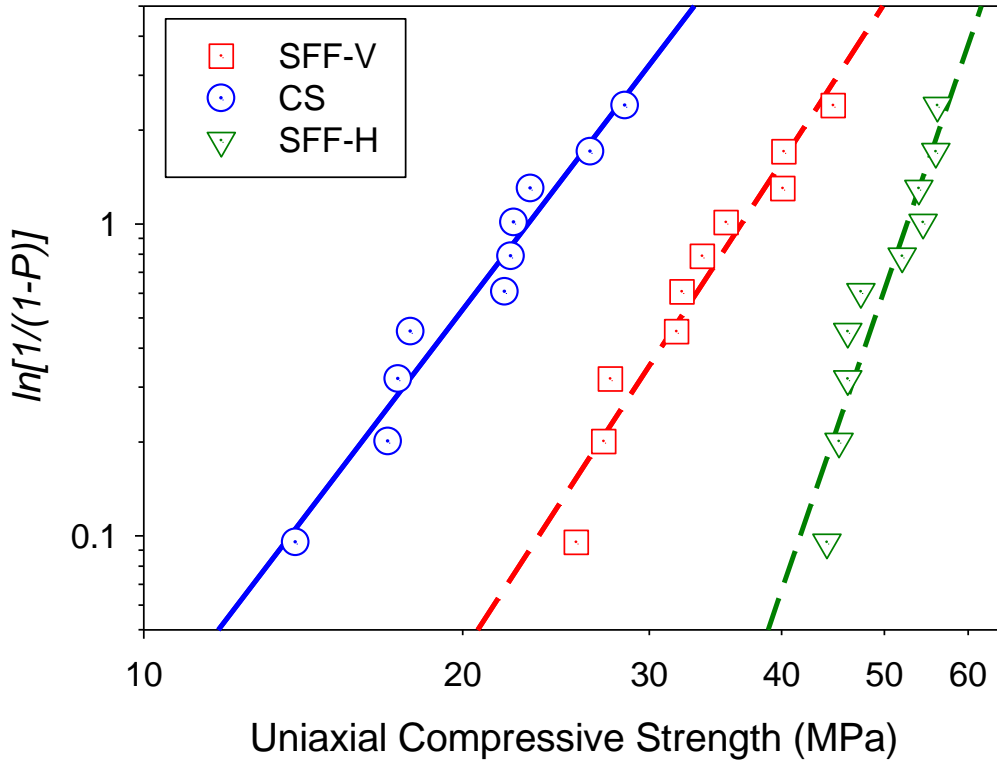


Figure 3-13: Failure probability of sintered SFF-V, SFF-H, and CS samples under uniaxial compression. The quite similar slopes of the regression lines indicate that the Weibull moduli of all the samples are the same.

#### 3.4.2.1.1 Fracture Surface Analysis

SEM images of the fracture surface resulting in the uniaxial compression tests are depicted in Figure 3-14. The SEM imaging was conducted as explained in Section 3.1.1. The figures suggest that fracture occurs primarily by crack propagation through the sinter necks. A comparison of the size of the fractured areas discloses that the horizontally made structure (SFF-H) comprises larger fracture areas than the vertically and CS samples. This can be considered a reason for the higher strength of the SFF-H samples. A quantitative analysis of the representative SEM images (only one image) revealed that the percent fracture cleavage area of the SFF-V, SFF-H and CS

CPP parts were about 35%, 46% and 20%, respectively. The ratio of the fracture cleavage area percentages are in agreement with the ratio of the compressive strengths of the CPP structures.

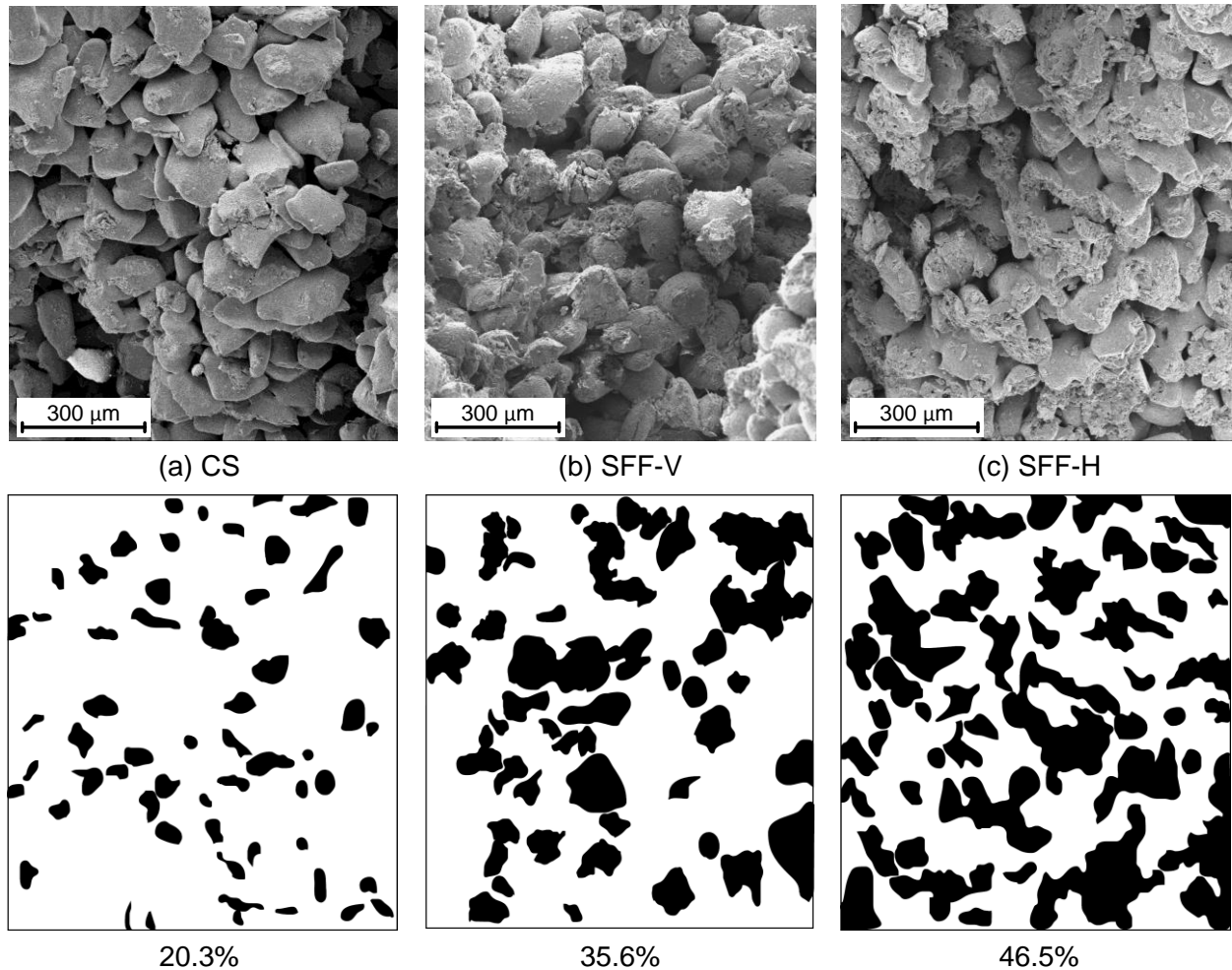


Figure 3-14: SEM images of fracture cleavage surface of (a) CS, (b) SFF-V and (c) SFF-H samples under the compressive load. The images indicate that the fractures occur in the CPP sinter neck regions. Bottom: Bitmap picture of the fracture cleavage areas. The fractures areas are shown in black. The portion of the black regions was calculated as shown.

### 3.4.2.2 Diametral Compression

Although bone substitutes are expected to be subjected to compressive loads in most of the implantation sites selected for their use (e.g., acetabular bone void fillers and proximal tibial resections), their tensile strength is of importance when they are exposed to bending loads. Diametral compression of cylindrical disc samples has been applied widely in order to estimate

the tensile strength of brittle materials [216-221]. The routine direct tensile test samples are more expensive to make, a consideration if a large number of specimens is to be tested [221].

To estimate the diametral tensile strength, 10 cylindrical disc samples of the proposed CPP structure with 4 mm diameter and 2 mm height were fabricated and loaded in compression radially (edgewise) along their diameter using the mechanical testing instrument (Instron 5548 Micro-Testing, MA, USA) with a 1 kN load-cell and crosshead loading rate of 0.2 mm/min. The experimental setup is shown in Figure 3-15. The compressive load generates a tensile stress in the transverse direction of loading, which is considered to be constant near the center of the disc. The fracture stress/tensile strength can be calculated using the relation equal to:

$$\sigma = \frac{2P}{\pi \cdot D \cdot t} \quad (3-4)$$

where  $P$  is the maximum compressive load (corresponding to fracture),  $D$  and  $t$  are the diameter and thickness (length) of the samples, respectively [221]. For the SFF-H samples, 10 samples were oriented under the crosshead with stacked-layers normal to the loading direction and another 10 samples were oriented at  $90^\circ$  to this direction (i.e., the compressive load was applied as nearly as possible either along or perpendicular to the stacked-layers, although some small alignment error might have occurred). Only those sample in which fracture path occurred more or less vertically (i.e., along the diameter) and insignificant crushing took place at the crosshead-sample contact region were recorded as acceptable test samples.

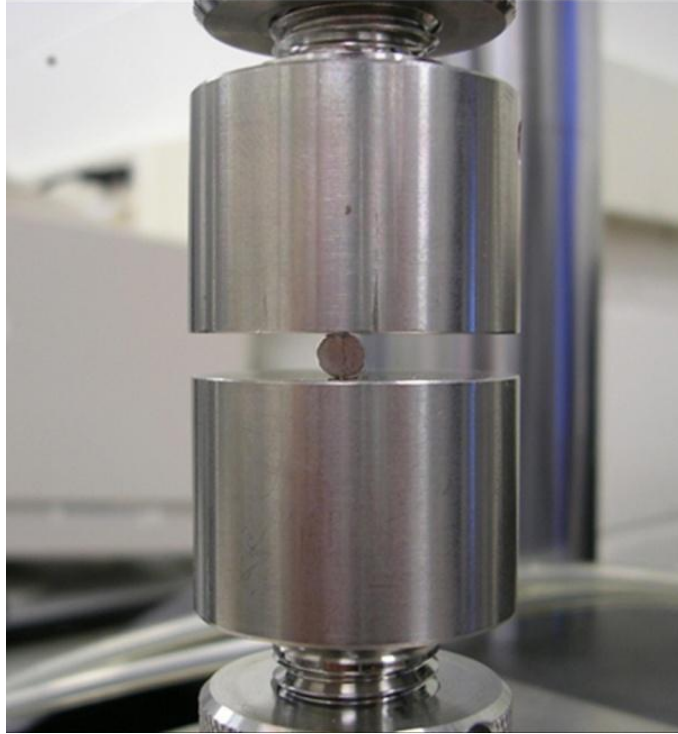
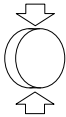





Figure 3-15: Diametral compression test of a CPP cylindrical discs with 4 mm diameter and 2 mm height loaded along its diameter. A crack was occurred by the tensile stress appeared in the transverse direction of loading.

The measured diametral tensile strengths of the SFF-made samples are listed in Table 3-5. In addition, Figure 3-16 shows the failure probability for the applied stresses in the CPP structures for diametral compression testing. In the figure, the straight lines are the best fits using the linear regression function by which the Weibull modulus is calculated as listed in Table 3-5.

Table 3-5: Diametral tensile strengths and Weibull moduli of the CS, SFF-V, SFF-H CPP samples (n=10).

Mechanical Properties	CS 	SFF-V 	SFF-H 	SFF-H 
Strength (MPa)	7.42±2.52	7.15±1.06	6.39±0.88	6.94±1.25
Weibull Modulus	2.60 (R <sup>2</sup> =0.98)	6.54 (R <sup>2</sup> =0.97)	6.88 (R <sup>2</sup> =0.90)	5.34 (R <sup>2</sup> =0.93)

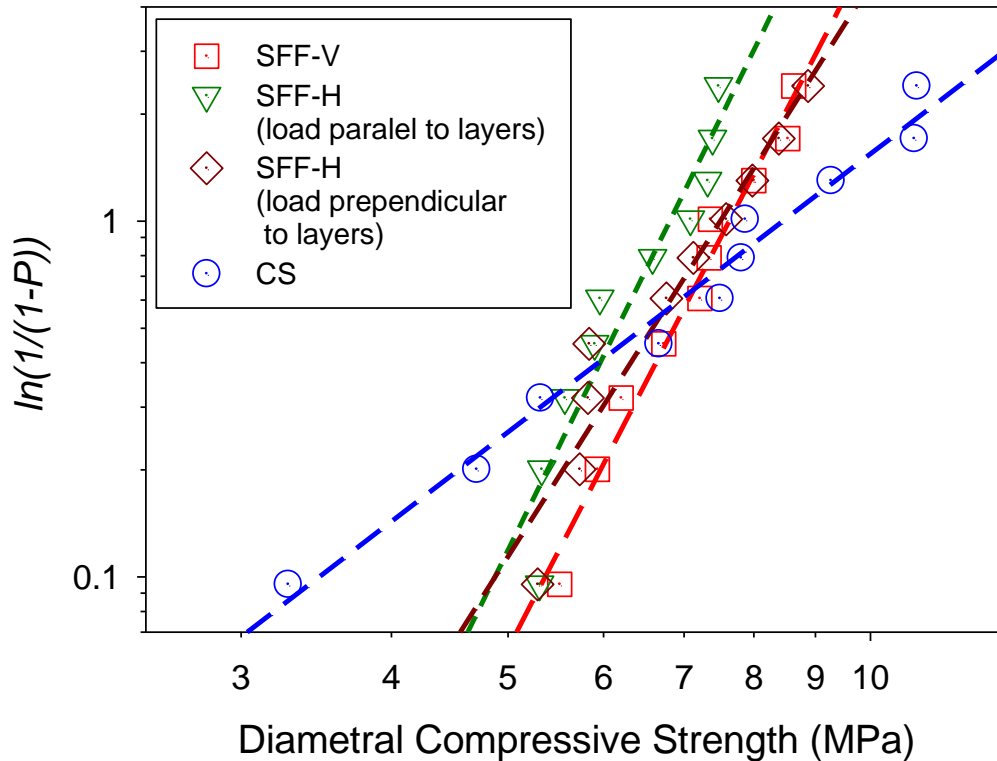


Figure 3-16: Failure probability of sintered SFF-V, SFF-H and CS samples under diametral compression.

### 3.5 Discussion

The physical, structural, chemical and mechanical properties of the SFF-made porous CPP structures were investigated and compared with those of the porous structures formed through the conventional sintering technique.

The XRD patterns related to SFF-made and CS crystalline CPP materials were consistent indicating that PVA and the aqueous solvent have not introduced any additional phases or residuals although there were small discrepancies in the peak intensities of the XRD patterns. The discrepancies may be related to the crystal size difference or a result of CPP fracture mode during milling and crushing of samples for XRD analysis or other unidentified factors.

The morphological characterization revealed a three-dimensional interconnected porosity within the sintered CPP structures (Figure 3-1 and Figure 3-2). The well-developed sinter necks with sinter neck dimensions approaching the adjoining particle dimensions in many regions may contribute to the compressive strength of the porous structure as described below. The quantitative evaluation of the internal structure showed a desired level of porosity (~35 volume

%) and pore size range (5-140  $\mu\text{m}$ ) for the bone substitution purposes. Despite the same volume percent porosity of the SFF and CS samples ( $\sim 35\%$ ), there is a significant difference in pore size distribution where the SFF-formed samples have a wider pore size range (5-140 vs. 5-80  $\mu\text{m}$ ) and a larger mean pore size ( $\sim 50$  vs.  $\sim 30$   $\mu\text{m}$ ). In addition, pores of 50-500 nm (intra-particle as well as at some inter-particle junctions) were observed for both SFF and CS samples. They are believed to represent fine pores and surface features related to the volume change resulting from the amorphous-to-crystalline CPP transformation that occurs during annealing to the final sinter temperature of 950°C. Pores larger than 50  $\mu\text{m}$  influence the osteogenic processes while micro-pores ( $<10$   $\mu\text{m}$ ) provide higher specific surface area resulting in higher bone-inducing protein adsorption, ion exchange, and bone-like apatite formation through dissolution and reprecipitation [78]. The measured pore size distribution within the porous CPP structures provided specific surface area and permeability determined equal to 24  $\text{mm}^2/\text{mm}^3$  and  $2.2 \times 10^{-12}$   $\text{m}^2$  for the SFF-made structures. Smaller pore size of the CS structures resulted in higher specific surface area (31  $\text{mm}^2/\text{mm}^3$ ) but lower permeability ( $1.0 \times 10^{-12}$   $\text{m}^2$ ). This suggests that the requirement for cell infiltration into and accommodation within the SFF-made CPP implants is provided. This supports the results presented through in vivo studies as reported in Chapter 4.

The apparent difference in the trabecular thickness (on average  $\sim 20$   $\mu\text{m}$  larger in the SFF-made structures), which was also reflected in the micro-CT images as larger sintered CPP particles (Figure 3-2), may be due to the different sinter annealing procedures (described in the previous chapter) used to achieve equivalent volume percent porosity in the two sample types. The layer-by-layer construction of the SFF-made samples results in a lower initial particle packing density ( $\sim 45\%$  for the SFF-made compared with 55% for the CS samples), presumably a result of the more gentle packing during layer-by-layer particle addition or the effect of the added PVA preventing as dense a packing. Thus, the SFF-formed samples required a higher first-step sinter temperature in order to approach the desired 65% theoretical full density during the viscous flow stage of sinter neck formation and densification of the amorphous particles as described by Filiaggi et al.[118]. The higher first-step sinter temperature required for the SFF-made samples presumably resulted in greater atom transport resulting in more substantial sinter neck formation and larger particles (i.e., an Ostwald ripening type of phenomenon [222]).

Primarily, the CPP structure which comprises stronger bonds and larger sinter necks between particles is able to bear higher mechanical loads. The remarkable difference between the compressive strength of the SFF-made and CS structures may be attributed to the larger trabecular thickness found in the SFF-made samples as described previously (Figure 3-4), considering that the mechanical properties (modulus of elasticity) of the crystalline CPP

material for the SFF-made and CS samples was identical as measured by nano-indentation. In addition, larger trabecular thickness means larger radii of curvature at the concavo-convex cusps at the sinter necks regions that, in turn, result in lower stress concentrations at those regions.

The compressive strengths of 6 mm long SFF-V (34 MPa) and SFF-H (50 MPa) structures are between those reported for human cortical bone (140–213 MPa) and cancellous bone (4–7 MPa) [223]. Thus, the compressive strength of the SFF-made CPP samples appears adequate for forming porous bone substitutes. In addition, it is comparable to other calcium phosphate structures (HA or TCP) with similar porosity fabricated by either additive manufacturing (e.g. 6 MPa [190], 21 MPa [200], 22 MPa [189], 30 MPa [57] and 45 MPa [224]) or other methods (e.g. 12 MPa [225] and 45 MPa [226]). In addition, the Weibull moduli (~5 and 10) are in an acceptable range for ceramics [227] and comparable with the reported Weibull modulus of structures made from different bioceramics (e.g. 3.2–9.3 for 39% porous HA [224], 1.8–2.7 for 50% porous HA/TCP [56]).

Under uniaxial and diametral compressive loads, after a certain elastic deformation, the CPP samples show a negligible inelastic deformation and sudden development of fracture cleavages and fracture surfaces that is typical fracture behaviour of brittle materials. In general, brittleness is characterized by notable differences in tensile and compressive strength and highly scattered strength data [228]. Numerous studies have been reported on the analysis of compression and tensile strength, stiffness, and fracture resistance of porous ceramic structures [229-236]. Fracture of brittle porous ceramic materials is determined primarily by the energy required to propagate a crack through the structure. In brittle crystalline materials like CPP, it is assumed that cracks are initiated in high stress regions (stress concentration sites) [237]. The presence of pores and the geometry of sinter neck regions within the CPP materials studied herein provide stress concentration sites where crack initiation will occur (Figure 3-17). Subsequently, the cracks will propagate in an overall direction more or less normal to the direction of tensile force application and along a path of least resistance to crack progress. It is also noteworthy that although in diametral compression test, theoretically, the condition of tensile failure occurs at the center of the cylinder according to the Griffith criterion for homogenous isotropic materials [221] in porous brittle materials, the existing micro-pores and flaws indicate the exact point of failure initiation since they form stress concentrators and cause the crack initiation and propagation [233, 237].



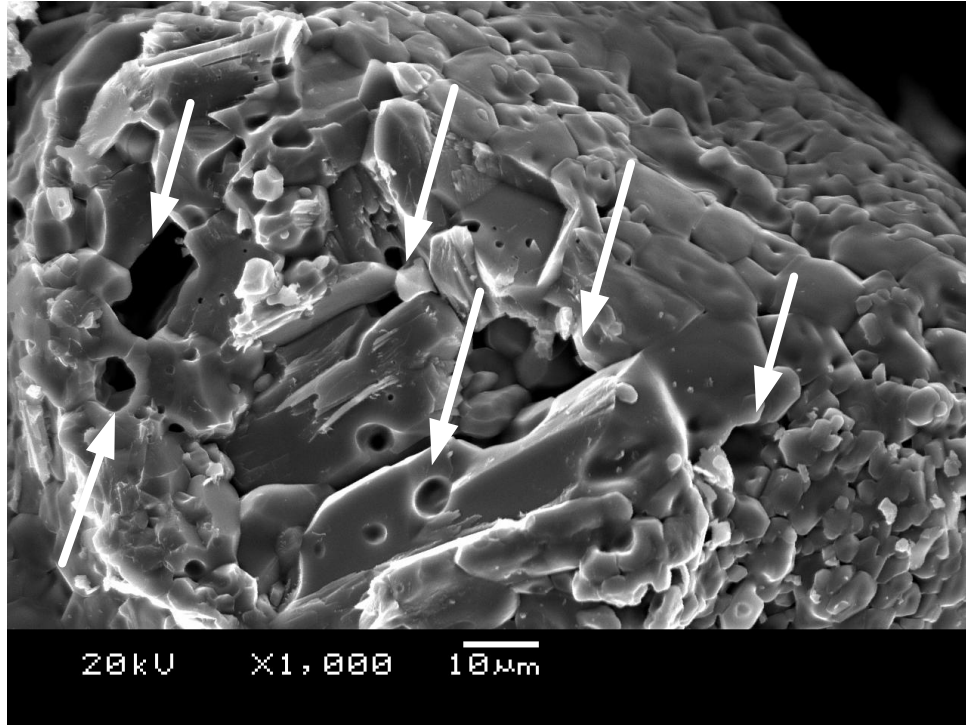


Figure 3-17: Micro-pores located on the surface and within a sinter neck act as a source for crack initiation

### 3.5.1 Discussion of the Anisotropic Properties of SFF-made CPP Structures

The similar pore size and trabecular thickness of the vertically and horizontally-made SFF structures suggested that their mechanical properties should be comparable. However, a notable distinction between their compressive strengths was detected although their moduli of elasticity were almost equal. The SFF-H cylinders with stacked-layers parallel to the compressive load were about 54% stronger (50 vs. 34 MPa) than the SFF-V samples in which the compressive load was applied normal to their constituent layers. The distinction between their mechanical compressive strength may be attributed to the difference of their internal micro-architecture as discussed below.

Since the only difference in the manufacturing of SFF-V and SFF-H was the part orientation in the SFF build chamber (i.e., the alignment of the fabricated part with respect to the powder layers), the analysis of powder layer preparation and spreading may help identify the source of such a difference in the mechanical behaviour under compressive load.

As explained previously, in the SFF process, the counter-rotating roller collects a certain amount of powder from the feeding chamber and spreads the collected powder with a thickness

of 150  $\mu\text{m}$  over the building chamber. In this process, the accumulated powder in front of the roller flows into and is trapped within the 150  $\mu\text{m}$  gap between the roller surface and the underlying layer. As noted previously, the majority of CPP particles included one dimensional feature greater than 150  $\mu\text{m}$  (average length equal to 172  $\mu\text{m}$ ). As a result, these particles are laid down in a manner to allow them to fit into the gap between the roller and the underlying layer of particles i.e., their longer dimension oriented as illustrated schematically in Figure 3-18. The largest sides ( $>150$   $\mu\text{m}$ ) of the particles display a preferred orientation being almost parallel to the layers (xy plane in Figure 2-9). This situation may result in the establishment of a specific particle architecture and orientation in the CPP green part.

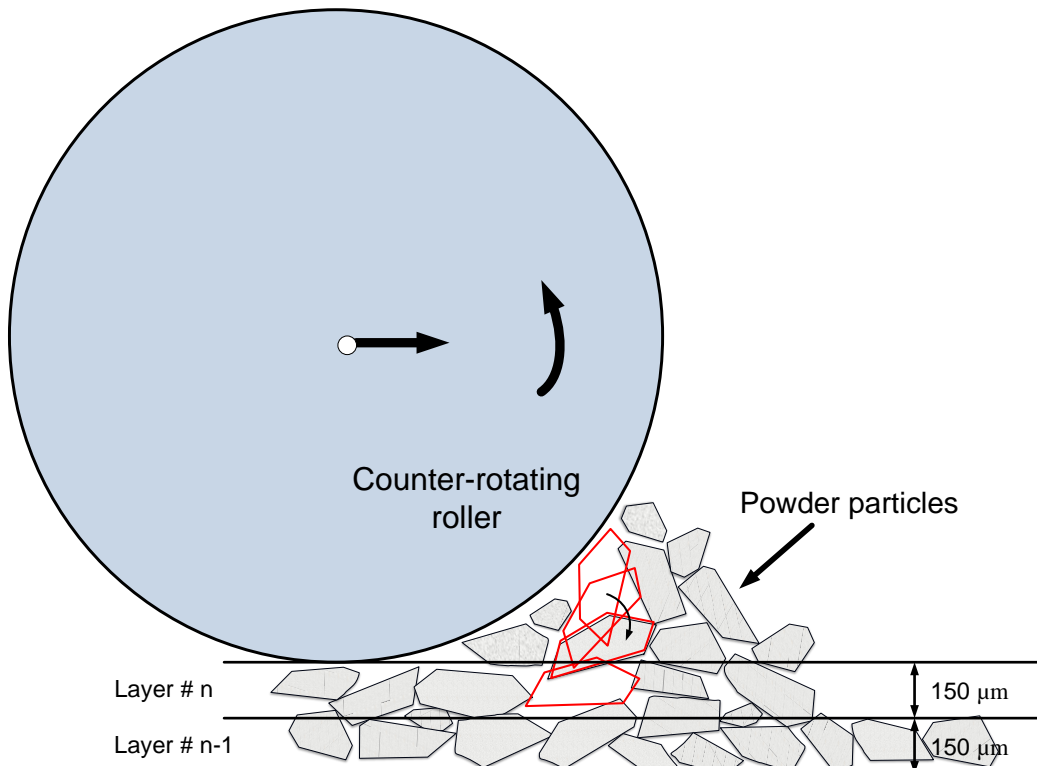


Figure 3-18: Schematic of spreading and compaction of CPP powder in the SFF process: CPP particles with the length larger than 150  $\mu\text{m}$  rotate and obtain a preferred orientation to fit best within the 150  $\mu\text{m}$  stacked-layers.

This effect can be observed in the SEM images of the prototyped CPP green parts (SFF-V sample - Figure 3-19) where the packed particles are shown from the side view/y direction (Figure 3-19a) and top view/z direction (Figure 3-19b). The side view depicts the particles positioned to form a brick-like pattern displaying the smaller-dimensioned surfaces (side surfaces) of the particles. In contrast, the larger facets of the primarily plate-like particles are

readily apparent in the top view. Consequently, Inter-particle connections occurred predominantly either via the larger facets oriented parallel to the build plane contacting each other (Figure 3-20a) or through contacts between the smaller “edge” facets in the transverse direction (Figure 3-20b). The preferred orientation and contacts between CPP particles are illustrated schematically in Figure 3-21.

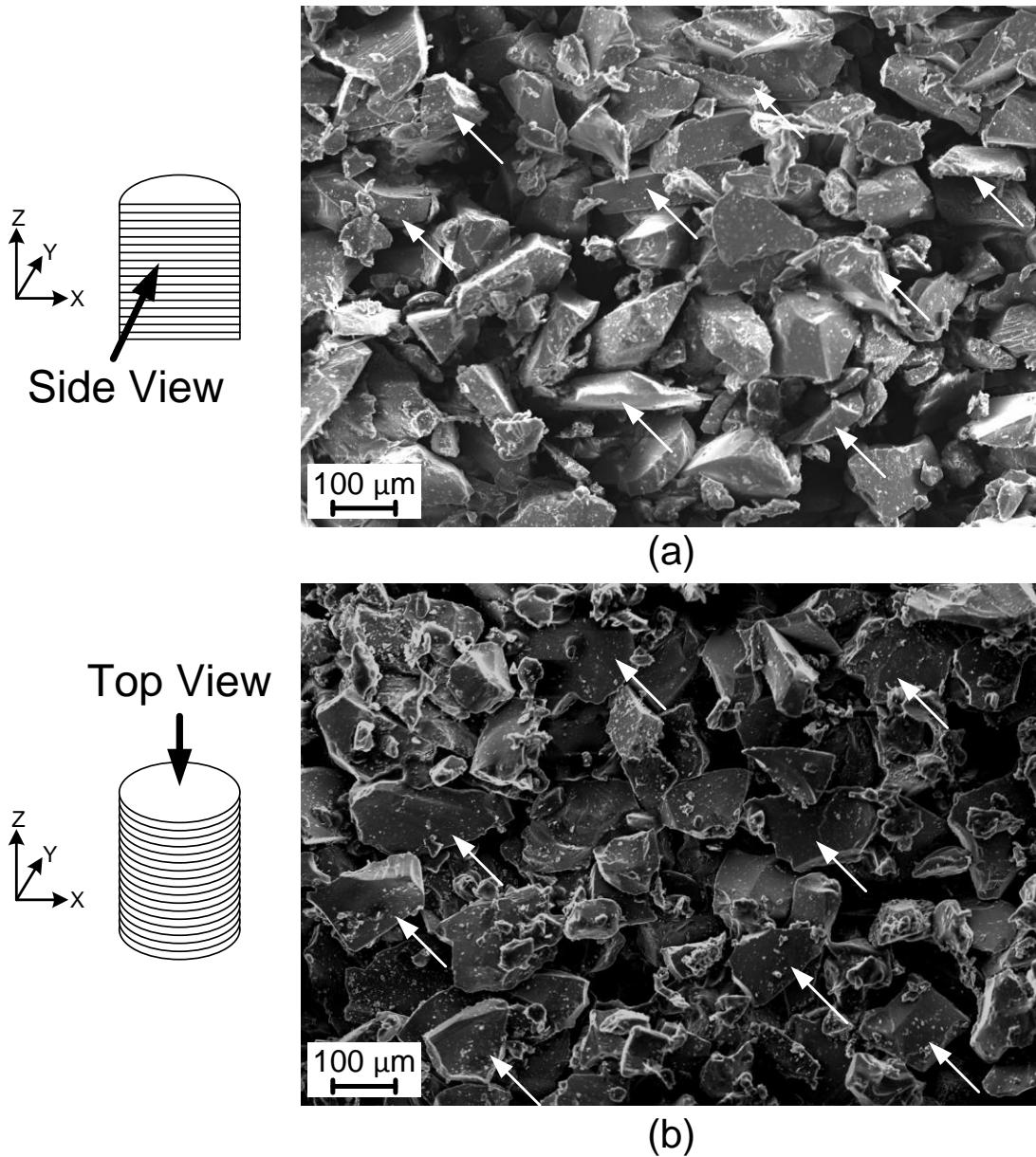
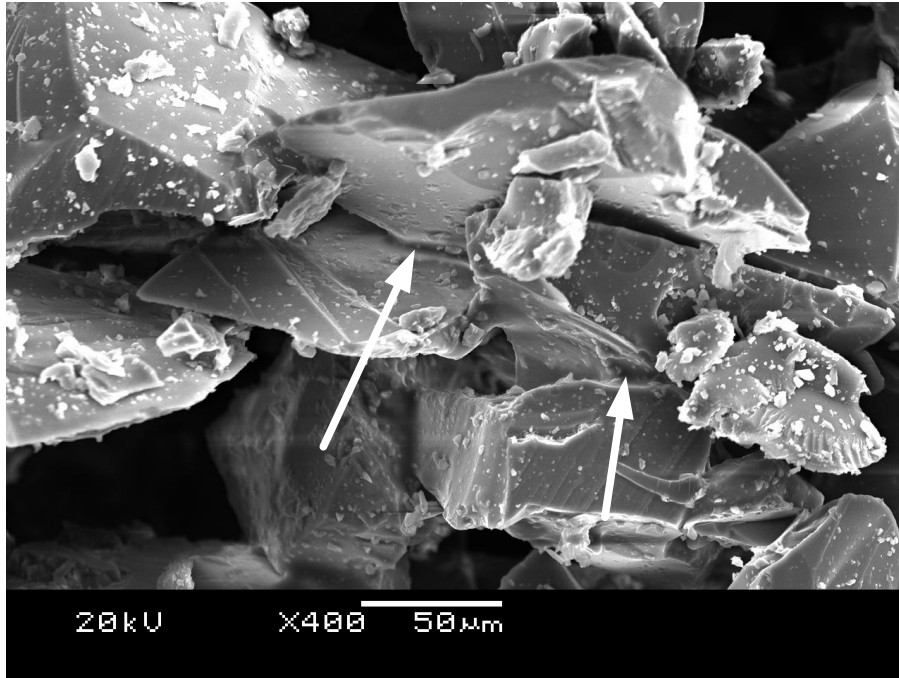
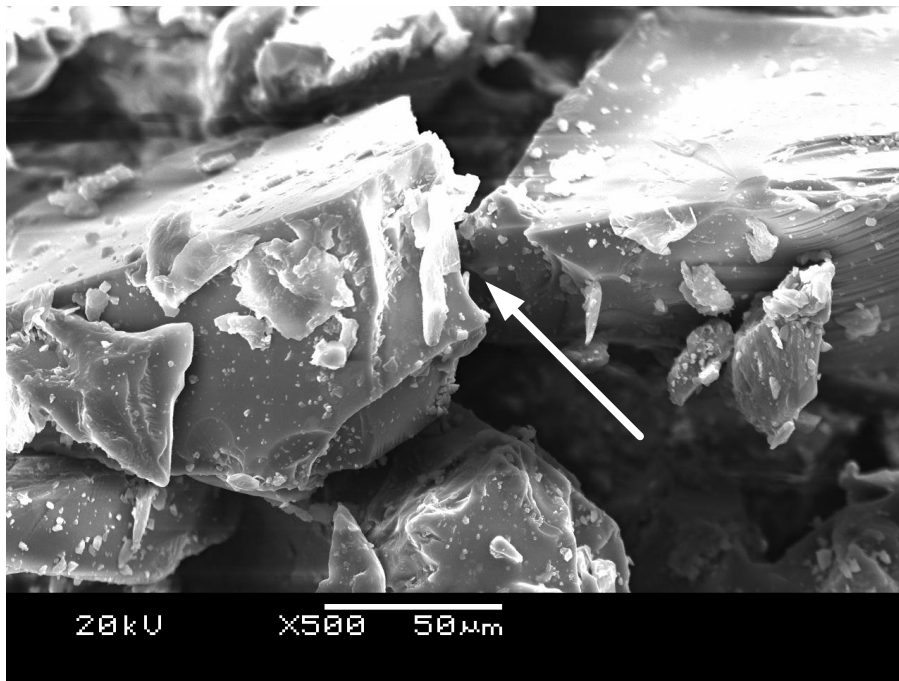


Figure 3-19: SEM images of fabricated CPP green part (SFF-V sample): (a) side view and (b) top view of stacked layers. The CPP particles have achieved a preferred orientation with their larger and flatter sides parallel to the stacked layers (top view) with inter-particle connections at their smaller facets and sharper edges in the orthogonal direction (pinpointed by arrows).



(a)



(b)

Figure 3-20: SEM images showing contacts between CPP particles within the SFF-made green parts: (a) large facet contacts parallel to the layers with low driving force for sinter neck initiation and growth versus (b) sharp corners contacts across the layers that cause sinter neck initiation and growth with high rate during the viscous sintering process of CPP.

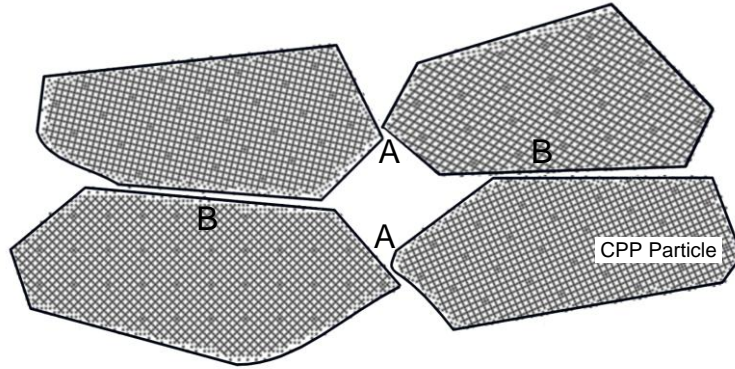


Figure 3-21: Schematic of CPP particles orientation and particle-particle contacts in the powder layer spread by counter rotating roller in SFF process: small facet-to-small facet contacts (A) i.e., small radii of curvature contacts occur in the direction parallel to stacked-layers while large facet-to-large facet contacts (B) i.e., large radii of curvature contacts occur in the direction normal to stacked-layers.

As noted in chapter 2, sintering shrinkage measurements revealed that samples shrank 5% more in the direction parallel to the stacked-layers compared to the perpendicular direction (17% vs. 12%). The observed difference may be attributed to the aforementioned preferred orientation effect and resulting arrangement of CPP particles in the green parts. At the initial stage of the sintering, the geometric arrangement of the particles and their specific shape as characterized by local radii of curvatures of contacting inter-particle surfaces determine the rate of sintering and sinter neck formation which in turn determine the characteristics of the sintered part [205, 238]. Basically, large radii of curvature contacts have lower driving force for sinter neck formation compared with smaller radii of curvature contacts. The densification rate (degree of sintering) resulting from atom transfer is higher for smaller radii of curvature contacts [205]. This is especially true in the viscous material transport regime which is considered to be the dominant sintering mechanism for the amorphous CPP particles [118] as well as surface diffusion. This may explain the higher densification and shrinkage observed in the direction parallel to the stacked-layers where inter-particle contact predominantly involves smaller radii of curvature and sharper contact zones. In addition, the small discrepancies in the peak intensities of the XRD patterns of the SFF-made and CS samples, may be attributed to the preferred orientation of CPP particles during layer-by-layer powder deposition in the SFF process.

Considering the above hypothesis, the SFF-made CPP constructs are structurally transversely isotropic being mainly symmetric about an axis normal to a plane of isotropy (build plane/xy plane in Figure 2-9) and with lower shrinkage in the z direction. This matter may explain the difference observed in compressive strength for the SFF-V and SFF-H samples.

For the samples used in this study, the cracks propagate in an overall direction more or less normal to the cylinder axis and along a path of least resistance to crack progress. For samples oriented with smaller diameter sinter necks (i.e., those formed by larger radii of curvature contacts) predominantly normal to the cylindrical sample axis (i.e. larger particle facets oriented normal to the axis), lower compressive strength is expected. In contrast, for the SFF-made CPP samples prepared with the build planes parallel to the applied force direction (i.e., SFF-H), more energy is required to propagate cracks through the more substantial sinter neck zones that are dominant in the transverse direction.

In contrast with the compressive strength data, the slopes of the load-displacement curve of the CPP specimens (SFF-V, SFF-H, and CS) are almost equal. The slope of load-displacement curves obtained from uniaxial compression of ceramic structures with such geometry (4 mm diameter and 6 mm height) does not identify the effective Young's modulus accurately. However, several theoretical and experimental studies have been dedicated to the discovering of the effect of porosity on the elastic constants of ceramic materials [239, 240]. The approach proposed by Boccaccini and Fan [241] incorporates the contiguity and topological parameters of pores into the determination of the mechanical properties of porous structures which is expressed as:

$$\frac{E^*}{E} = \frac{(1 - \varepsilon)^2 \cdot R}{\varepsilon + (1 - \varepsilon) \cdot R} \quad (3-5)$$

where  $\varepsilon$  is porosity and  $R$  is the mean size ratio of pores to the solid grains. This model has shown very good agreement with experimental data [242]. This model predicts an effective Young's modulus of about 20 GPa for SFF-made and 21 GPa for CS samples (considering  $R$  is about 0.6 for SFF-made and 0.66 for CS samples, respectively, according to the micro-CT scan data). Collapse of the porous structures in the initial stages of the compressive loading [243] might be one of the reasons behind the difference between the Young's moduli calculated using the theoretical model and the slope of the load-displacement curve.

As far as the tests ascertained, unlike the uniaxial compression strength, the diametral tensile strength of the SFF-V, SFF-H and CS samples were not significantly different despite the fact that for the SFF-H samples it was attempted to align them under the pressing crosshead in such a way that the compressive load was applied either parallel or perpendicular to the stacked-layers. Lower tensile strengths would be expected for the SFF-H samples in the diametral compression test and while a lower average strength was found (6.39 MPa for the samples with

stacked-layers parallel to the loading direction in which the particles oriented to form smaller sinter necks in the direction of crack propagation – Table 3-5), the differences were not significant. In general, for ceramics, the strength is significantly lower in tension compared to compression and ceramic structures are less sensitive to geometric features under tension. That might explain the quite similar strengths of SFF-made and CS samples in the diametral compression test. In addition, the SFF-made parts include slightly rough surface finish which is introduced by the formation of the staircase effect of the stacked-layers [201]. Consequently, the potential of stress concentrators being present on the surface resulting in early fracture is high.

### 3.5.2 Prediction of Fracture Strength of Porous CPP Structures in Complex Loading Conditions

Using the obtained values of compressive and tensile fracture strengths, the brittle yield/fracture strength of the CPP structures in a complex-loading condition (including compression, tension, and torsion in 3D space) can be characterized. Several failure criteria have been proposed for isotropic brittle materials [244] and some of them are specific to anisotropic structures [245]. In this study, the modified Hill's orthotropic yield criterion is utilized which in general form is:

$$C_1(\sigma_y - \sigma_z)^2 + C_2(\sigma_z - \sigma_x)^2 + C_3(\sigma_x - \sigma_y)^2 + C_4\sigma_x + C_5\sigma_y + C_6\sigma_z + C_7\tau_{yz}^2 + C_8\tau_{zx}^2 + C_9\tau_{xy}^2 = 1 \quad (3-6)$$

where  $C_1$  to  $C_9$  are nine material parameters which are determined from compressive, tensile and shear strengths in three orthogonal directions [228]. As noted previously, the SFF samples are transversely isotropic. Thus, the material properties reduce to 5 independent ones (two tensile, two compressive, and one shear strengths).

As an example, the failure criterion is simplified to the following equations for SFF-V structures with thickness comparatively smaller than other dimensional features such as discs. Disc shape was chosen in order to be able to visualize the failure criteria.

$$SFF - V : C_{1V}(\sigma_y)^2 + C_{2V}(\sigma_x)^2 + C_{3V}(\sigma_x - \sigma_y)^2 + C_{4V}\sigma_x + C_{5V}\sigma_y + C_{9V}\tau_{xy}^2 = 1 \quad (3-7)$$

where

$$\begin{aligned}
C_{1V} &= C_{2V} = \frac{1}{2}(F_{tz} \cdot F_{cz})^{-1} \\
C_{3V} &= \frac{1}{2}\left[2 \cdot (F_t \cdot F_c)^{-1} - (F_{tz} \cdot F_{cz})^{-1}\right] \\
C_{4V} &= C_{5V} = F_t^{-1} \cdot F_c^{-1} \\
C_{9V} &= F_{sxy}^{-1} \\
(F_{sxy} \text{ was estimated equal to } \frac{F_c}{2})
\end{aligned} \tag{3-8}$$

where  $F_c$  and  $F_t$  are compressive and tensile strengths in xy plane,  $F_c$  and  $F_t$  are compressive and tensile strengths in z direction, and  $F_{sxy}$  is shear strength. The failure relations for the SFF-H and CS discs can also be simply derived correspondingly (Appendix B).

Figure 3-22 graphically represents the failure condition in the  $\sigma_x, \sigma_y, \tau_{xy}$  stress space for the SFF-V, SFF-H, and CS discs. As seen, the volume and the angle of the major axis of the ellipsoidal fracture failure iso-surface are different for the SFF-V, SFF-H, and CS discs with identical porosity. It means, their mechanical behavior differ under a similar loading condition. The importance of this issue is raised when the CPP structures are used as bone substitutes in load bearing sites. Since the loading condition strongly depends on the implantation site in the patient's body, it may be reasonable to assume that depending on the implantation site, one CPP structure (SFF-V, SFF-H or CS) may bear loads better and provide better mechanical performance. It is noteworthy that the fracture ellipsoid corresponding to the CS samples is comparably smaller than that of the SFF-made samples and its symmetric shape is due to its more isotropic mechanical properties. In contrast, SFF-V has formed the largest fracture ellipsoid. Although the SFF-H cylinders showed higher compressive strength, SFF-V samples may be stronger in other geometries (such as discs) and other loading conditions.



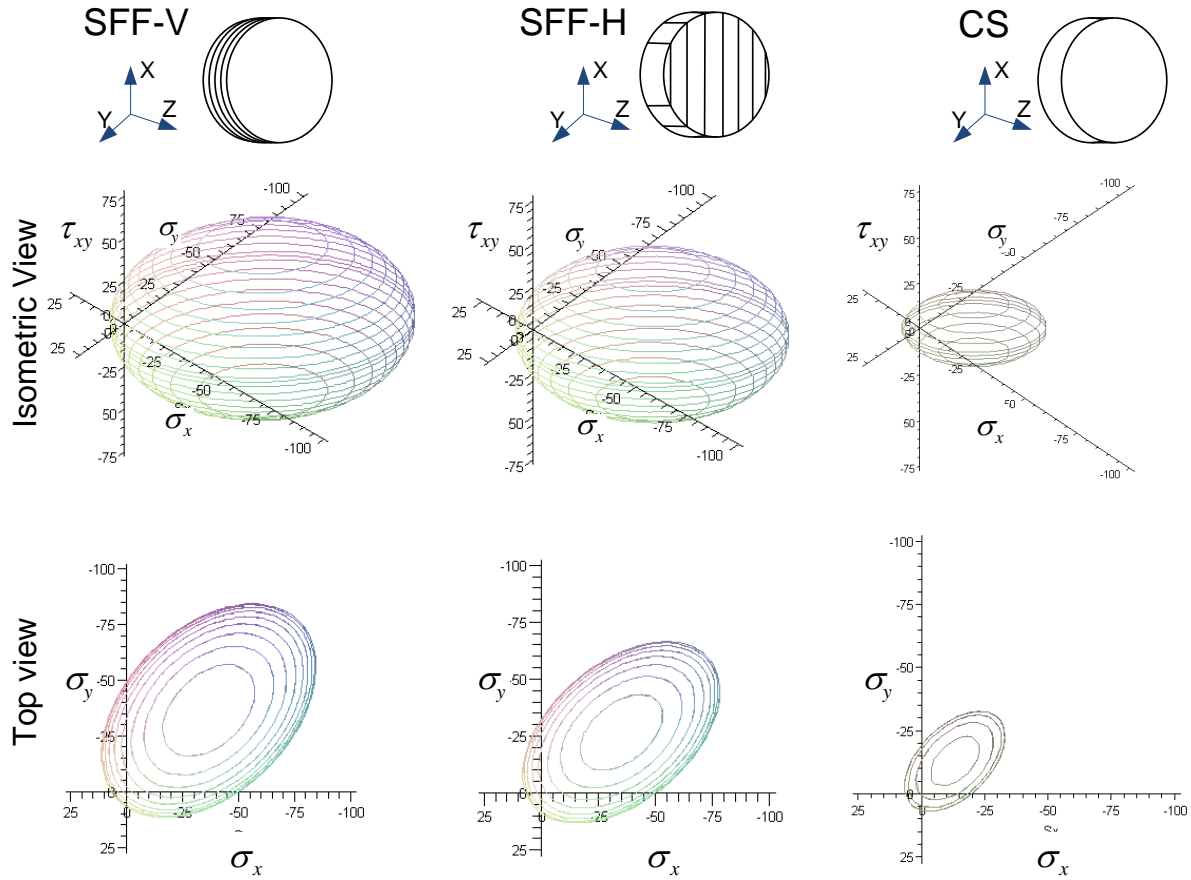


Figure 3-22: Failure elliptical iso-surfaces of SFF-V, SFF-H and CS CPP discs based on the Hoffman's orthogonal brittle fracture criteria. SFF-V discs show higher strength (larger volume) with a symmetry in x and y directions (symmetry plane of  $45^\circ$ ). SFF-H is stronger in x direction rather than y direction (symmetry plane smaller than  $45^\circ$ ). CS discs are comparably weaker than SFF-made ones.

### 3.6 Summary

The physical, chemical, and mechanical properties of the SFF-formed CPP samples were assessed and compared to those of controlled samples formed by a conventional sintering method. The results suggest that the SFF-made CPP structures appear adequate for forming porous components suitable for use as bone substitutes or osteochondral implants.

The anisotropic character of the SFF-formed porous CPP structures can be compared to that of natural bone structures in certain skeletal locations and as such, porous SFF-formed CPP may offer an advantage for making bone substitute structures with transversely isotropic properties mimicking those of the host bone structures. The results of this study suggest the possibility of forming porous CPP implants with optimum biomechanical properties for specific

in vivo loading/pressure conditions. This can be achieved by pre-designing of the powder stacked-layers orientation within the CPP structures (i.e., basically the orientation of CPP part vs. the build plane in the build chamber of the SFF machine) based on the loading/stress profile at the implant site.

## Chapter 4

# Biological Responses of CPP Constructs

In this chapter, the *in vivo* performance of the SFF-made CPP structures as bone substitutes are characterized and the results are compared to the CS samples. The biocompatibility, ability to allow bone ingrowth, and the *in vivo* rate of degradation of the CPP implants are investigated. In addition, the potential of SFF-made CPP constructs for forming biphasic implants for repair of osteochondral defects is investigated.

### 4.1 *In vivo* Performance of Porous CPP Bone Substitutes

The biocompatibility, the ability to allow bone ingrowth, the degradation at an appropriate rate and the initial and transitional load bearing are the preferred characteristics for the SFF-made CPP bone substitute which need to be assessed *in vivo*. CPP porous structures, in order to be functional skeletal replacement implants, need to have strength compatible with the in-situ applied load and the degradation rate in harmony with the growth of new bone. To investigate the suitability of the SFF-made porous CPP constructs for bone substitute applications, an *in vivo* model was utilized. According to Baksh et al. [130], the tissue interfaces (bone-CPP) formed *in vitro* and *in vivo* are quite different, where *in vivo* animal model is a more reliable investigation.

#### 4.1.1 CPP Plug Implantation Process

SFF-V, SFF-H and CS cylinders with the size of 4 mm in diameter and 6 mm in height and with  $70\pm 3\%$  full theoretical density (i.e.  $30\pm 3\%$  porosity) were fabricated for the *in vivo* study using methods described in Chapter 2. The CPP constructs were sterilized by gamma-irradiation (2.5 Mrad) before implantation. A total of 8 implants of each CPP design (SFF-V, SFF-H and CS) were randomly placed in the medial aspect of both the left and right distal femur of 3.5 to 4

kg male New Zealand white rabbits (i.e., 24 implants 12 animals – see Appendix C) (Figure 4-1). The left and right legs of each animal were purposely implanted with dissimilar CPP types. The schematic of the implantation site is presented in Figure 4-2. All rabbits were ambulatory 24 hours post surgery and were sacrificed after 6 weeks for further analysis.

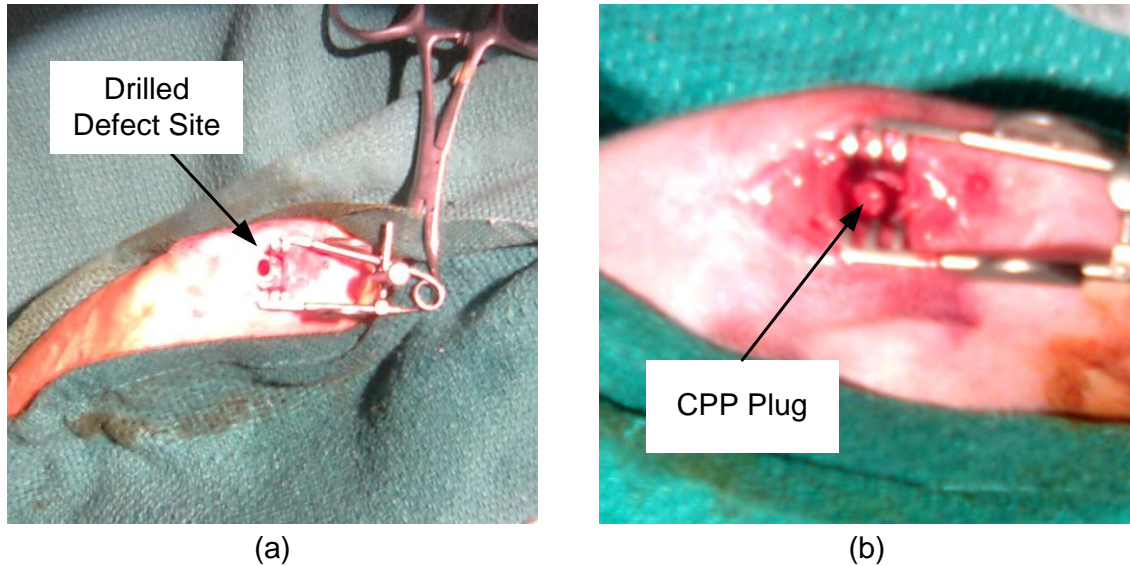


Figure 4-1: Implantation of CPP plugs in the defect site: (a) prepared defect site, (b) inserted CPP plug in the defect site.

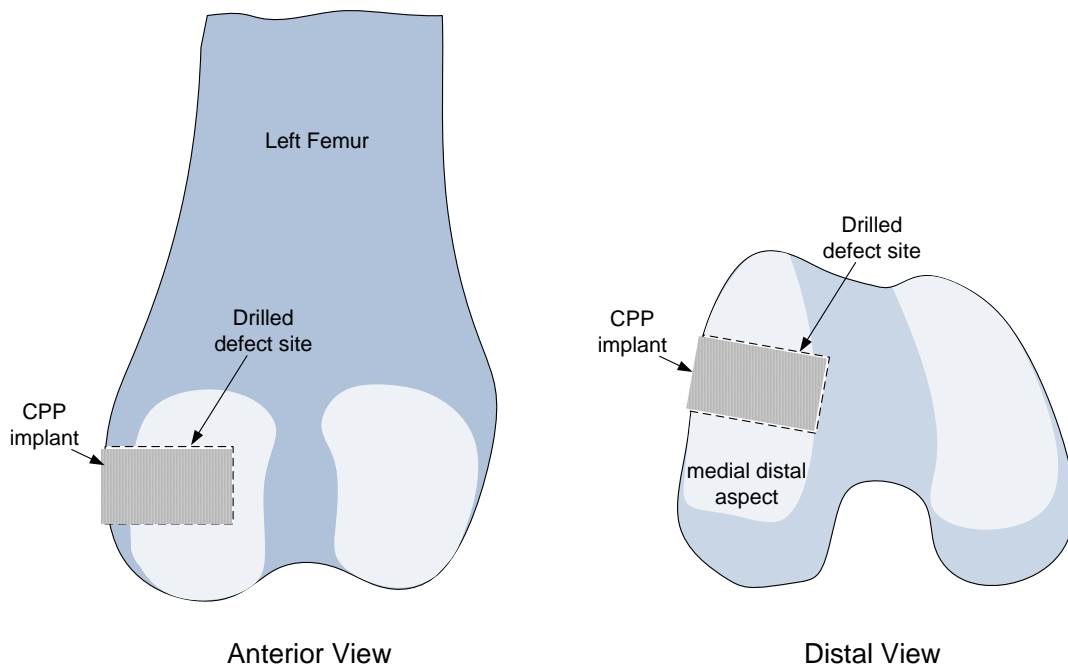


Figure 4-2: Schematic of CPP implant inserted in the drilled defect site in the medial distal femur. Femur bone is shown from the distal view.

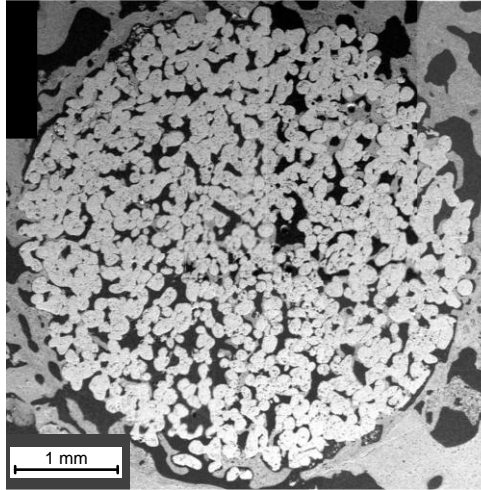
### 4.1.2 Qualitative Evaluation of Bone Ingrowth

Bone-implant specimens (cut from the sacrificed animals) were fixed in 10% buffered formalin solution for approximately one week. Dehydration was accomplished using a graded series of ethyl alcohols, 70% to 100%. For this purpose, the samples were dehydrated in 70% ethyl alcohol for 6 days with a change of medium in day 3. The process was repeated with the 100% ethyl alcohol. Then, the samples were left in xylene overnight. Infiltration was performed using a graded series Osteo-Bed (Polysciences Inc, Warrington, PA, USA resins), which contained no catalyst, followed by a catalyzed mixture of Osteo-Bed resin containing 1 gram of benzoyl peroxide per 100 ml of Osteo-Bed resin. Embedding was performed using a final catalyzed resin mixture of Osteo-Bed resin solution containing 2.5 grams of benzoyl peroxide per 100 ml of Osteo-Bed resin. Each change of Osteo-Bed lasted approximately one week. One specimen of each type of cylinders was trimmed of excess plastic and sectioned on the longitudinal and the radial axis of the implant using the Buehler Isomet Low Speed Saw (Lake Bluff IL, USA) with a 3 inches diamond blade. The surface of the blocks was polished with a series of graded silicon carbide papers, where the final grade was 4000grit<sup>4</sup>.

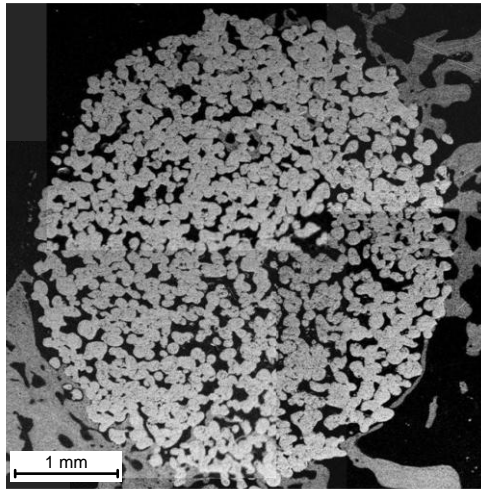
The surface of the blocks was coated with 8 nm of platinum and examined by backscattered electron (BSE) imaging using a Hitachi S-2500 scanning electron microscope (Hitachi Ltd, Tokyo, Japan) operated at an accelerating voltage of 25 kV. The BSE images of radial and longitudinal cross sections used for analysis are shown in Figure 4-3 and Figure 4-4, respectively. Also, as-made cylinders (not-implanted) were processed and sectioned in a manner similar to the tissue blocks to provide a zero time point for the image analysis.

---

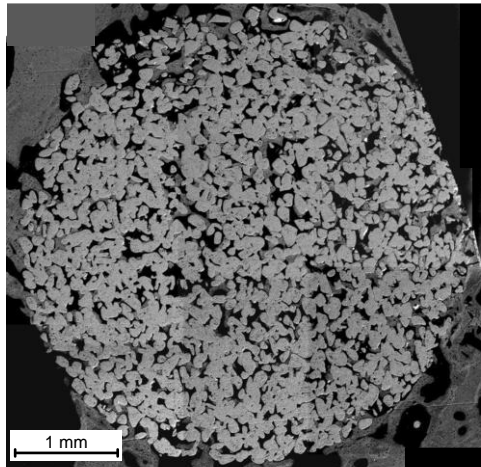
<sup>4</sup> The implantation of CPP plug, preparation of samples for BSE imaging and histology analysis, as well as BSE imaging were conducted by Nancy Valiquette at the University of Toronto.



(a)

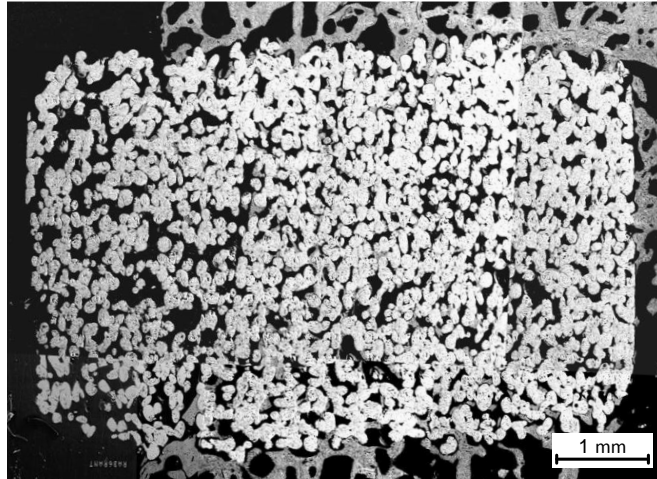


(b)

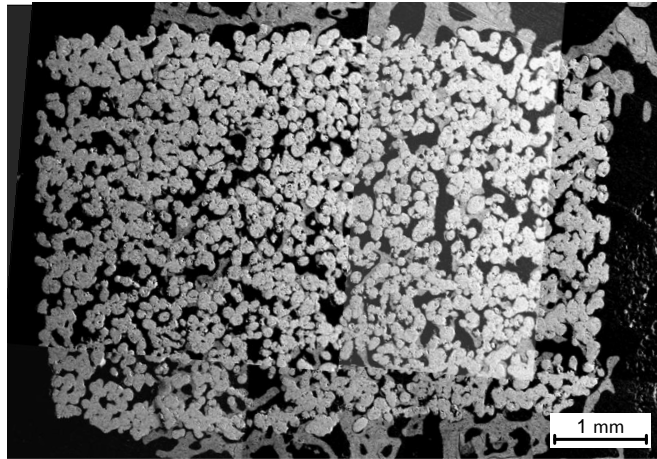


(c)

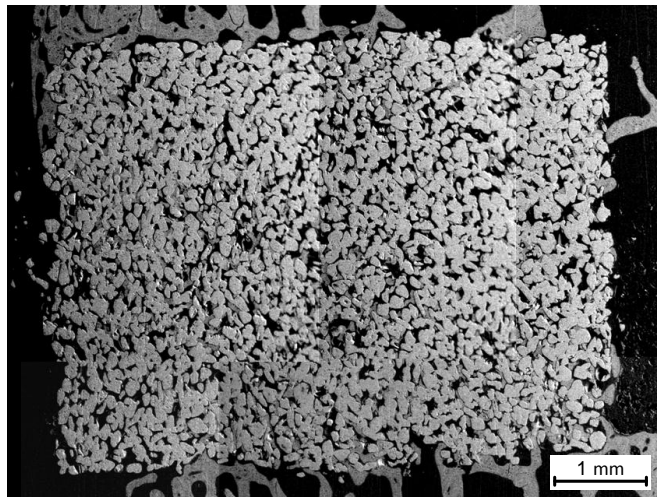
Figure 4-3: BSE images of radial cross sections: (a) SFF-V, (b) SFF-H and (c) CS samples.



(a)



(b)



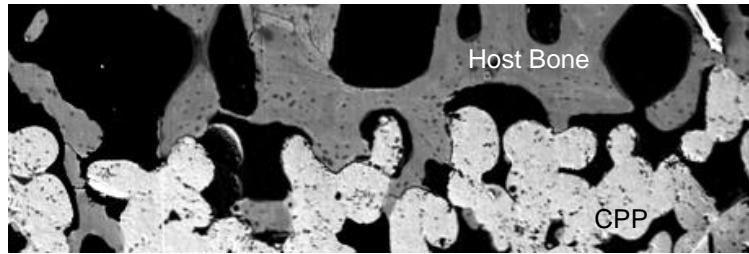
(c)

Figure 4-4: BSE images of longitudinal cross sections (a) SFF-V, (b) SFF-H and (c) CS samples.

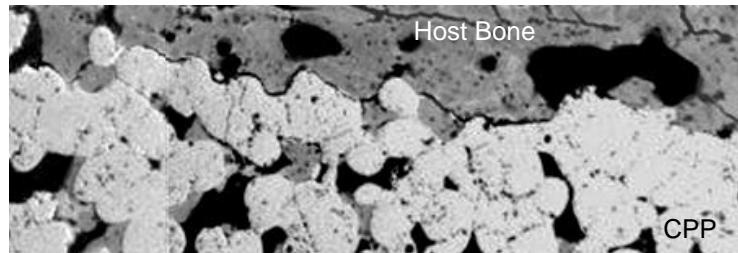
The porous CPP structures appeared to be biocompatible and did not elicit any inflammatory response. They also demonstrated bone ingrowth resulting in bone-implant osseointegration for all the CPP designs. The BSE images revealed qualitatively significant bone ingrowth. Overall, there was no evidence of adverse host response after 6 weeks of implantation. Also, no mechanical failure was observed upon implants insertion and during the 6-week implantation period. After that time, a notable integration between the CPP implants and the surrounding host bone was observed in all cases (Figure 4-5). Osseointegration is the stable anchorage of implants achieved through direct bone-implant contact. The osseointegration due to the bone-implant mechanical interlocking depends on the implant surface microtopography [117]. It can be concluded that the SFF-made and CS CPP implants have the required surface conditions and may not need any further treatment.

In addition, bone appeared to form within the core region (close to the geometric center of the cylinders) of the implants (Figure 4-6). Although no evidence has been observed in this study, bone might have formed first at the margins of the implants and then growing into the porous structure, a pattern similar to what reported in other bone-implant studies [246]. Moreover, although the amount and rate of bone ingrowth depends on the implantation site (trabecular versus cortical) [247] no difference was apparent. Also, no significant difference was seen between SFF-V, SFF-H and CS samples. The observations proved the fact that CPP material is osteoconductive.

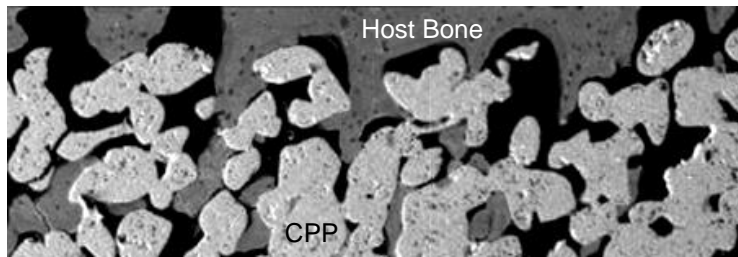




(a)

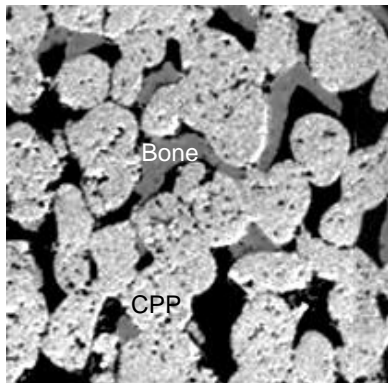


(b)

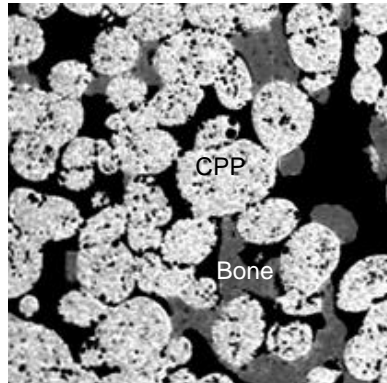


(c)

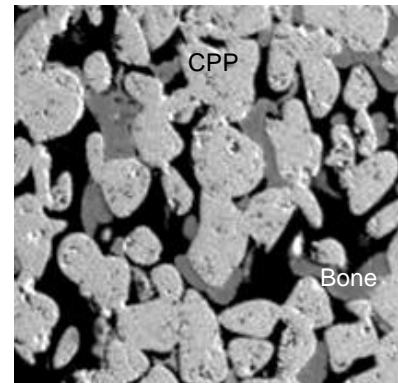
Figure 4-5: BSE images showing the integration of CPP constructs and host bone in the interface of (a) SFF-V, (b) SFF-H, and (c) CS implants and surrounding bone.



(a)



(b)



(c)

Figure 4-6: BSE images showing new bone formed in the core region of CPP implants in (a) SFF-V, (b) SFF-H, and (c) CS samples.

### 4.1.3 Quantitative Analysis of Bone Ingrowth

Quantitative analysis of the bone growth within the CPP implants was undertaken. Samples were first sectioned in a standardized fashion as shown in Figure 4-7 and up to four aspects per implant were obtained: anterior, posterior, proximal and distal. This sectioning strategy was selected in order to (1) include different regions of the implants in the analysis, and (2) investigate the bone ingrowth from different directions in the defect site. It was hypothesized that the varying principle strain profile and direction around the defect site may influence the bone ingrowth from the different directions. In addition, the effect of stacked-layers of the SFF-made constructs (i.e., the ingrowth of bone in the direction parallel to the stacked-layers versus the direction perpendicular to the stacked-layers) might be observed.

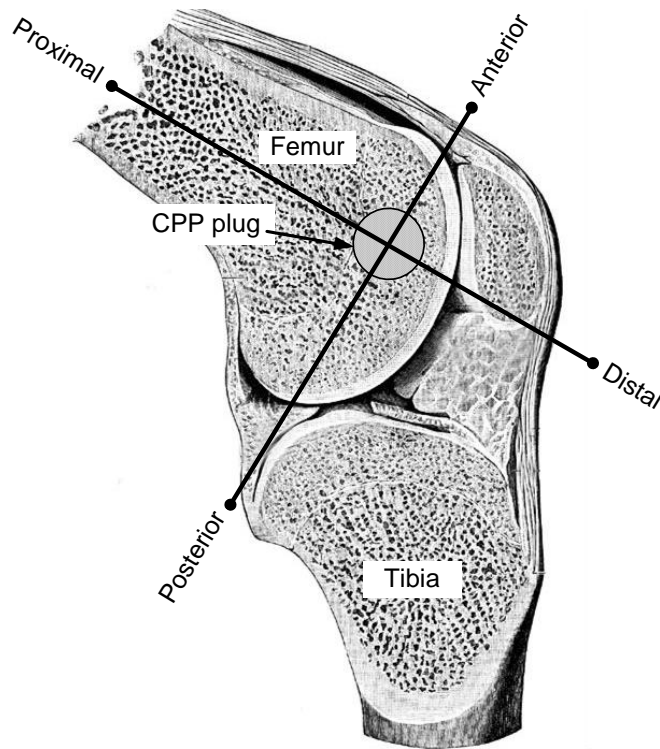


Figure 4-7: Schematic of sectioning of inserted CPP implants. Each implant was sectioned longitudinally and cross-sectionally related to femur and trough the center of the implant, generating four implant surfaces (anterior, posterior, distal and proximal) for quantitative analysis of bone ingrowth.

BSE images were obtained as described previously and underwent an image processing stage to identify the percentage of new-bone ingrowth and degradation of CPP. For that purpose, using PRTools (a MATLAB-based toolbox for pattern recognition [<http://www.prtools.org>]),

the BSE images were segmented into 3 discrete sections: (1) bone, (2) CPP, and (3) void. The constituent percentage of each section was calculated by a MATLAB code (available in Appendix C). A sample segmented image of the SFF-made structure is shown in Figure 4-8.

For image processing analysis, 6 samples of SFF-V, 7 samples of SFF-H and 7 samples of CS were examined. Some samples were destroyed during the sectioning process. A detailed list of the examined samples of each type is available in Appendix C. Comparisons between the SFF-V, SFF-H and CS CPP groups, where four different aspects (anterior, posterior, distal and proximal) were considered, were conducted through a two-way analysis of variance (ANOVA) with significance assigned at  $p < 0.05$ .

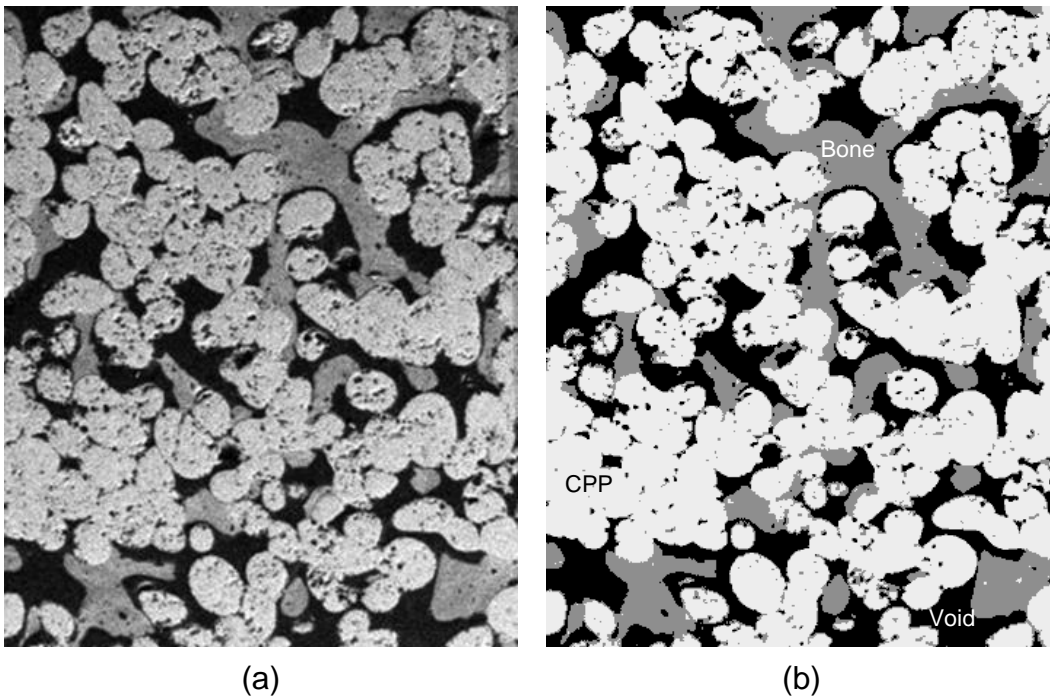


Figure 4-8: (a) a BSE image of CPP implant containing new bone, (b) the segmented image of the BSE image representing three distinct regions: CPP (white), bone (grey) and void (black).

The percentage of the voids (pores) filled by newly-formed bone (= % of bone in the regions of implant not occupied by CPP) is calculated by:

$$Bone - in - Void \% = \frac{Bone\ area}{(Bone + Void)\ area} \times 100 \quad (4-1)$$

The bone-in-void percentages for the SFF-V, SFF-H, and CS implants in the four different aspects (ANT: anterior, POST: posterior, DIST: distal, PROX: proximal) are shown in Figure 4-9. The average values show that the new mineralized bone has filled approximately ~30 to 40% of the available pore area within the CPP implants after 6 weeks. The percentage is not significantly different for the SFF-V, SFF-H, and CS implants. In addition, bone ingrowth did not vary considerably in the different aspects. It may be concluded that in this *in vivo* model, the cell infiltration and bone ingrowth within the porous CPP implants were relatively similar from the 4 sides of the implantation boundary. It might be due to the fact that the mechanical load profile (i.e., micro-strain distribution which influences the bone cell proliferation [248]) does not vary significantly within the CPP implants in the current *in vivo* model. Also, the orientation of the stacked-layers did not show any noticeable impact on the amount of bone formation. It should also be noted that the obtained results (no significant difference between the examined groups) showed that the lack of some samples (due to the damages occurred during the sectioning) did not have any apparent influence on the outcome of this study.

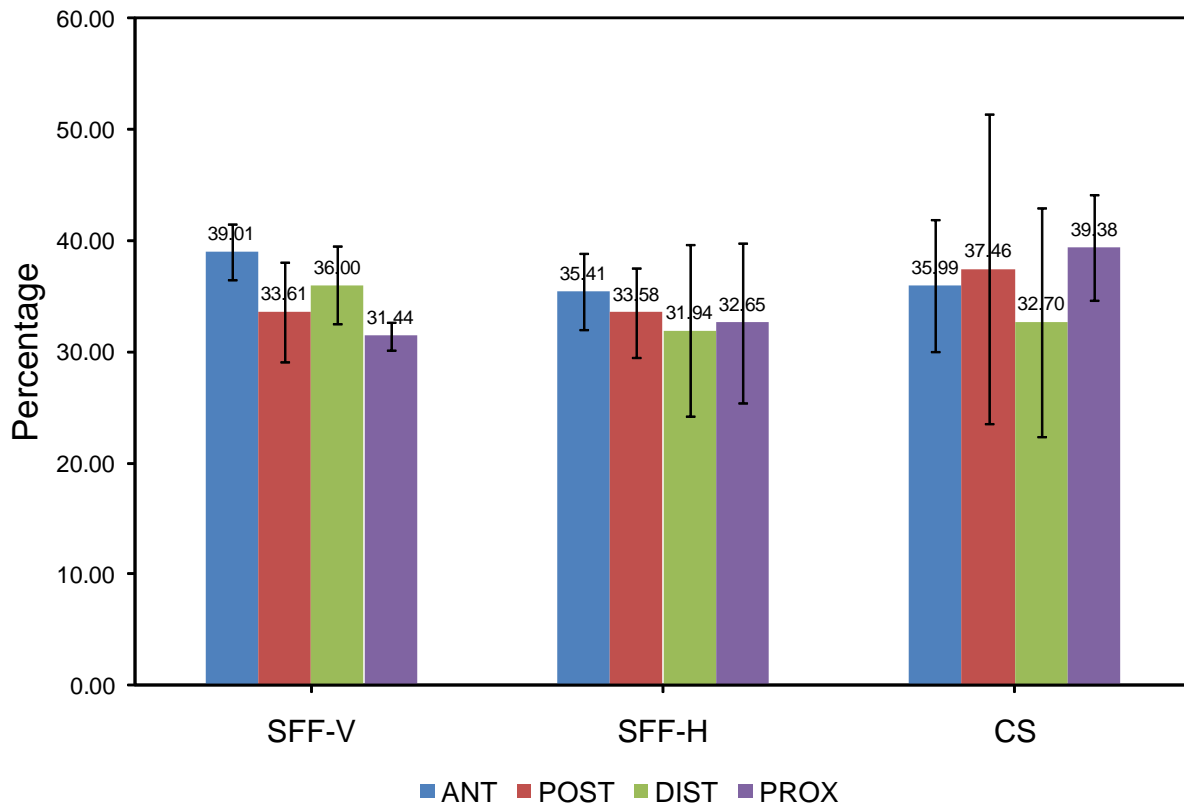


Figure 4-9: Percentage of voids that is filled with new bone in SFF-V, SFF-H, and CS CPP implants in the anterior (ANT), posterior (POST), distal (DIST), and proximal (PROX) aspects. No significant difference ( $p < 0.05$ ) was observed between the CPP implant types and the different aspect in terms of the amount of bone ingrowth.

Moreover, as reported by others [247], the rate of bone ingrowth depends on the implantation site (trabecular versus cortical). To investigate this phenomenon within the implanted CPP plugs, the BSE images were sectioned into rectangular slabs (normal to the length of the cylinder) and the image processing was conducted sequentially on the slabs. Overall, the quantitative analysis showed that no significant distinction can be claimed for the bone ingrowth between the regions which have contact with either cortical or trabecular bone and bone ingrowth did not significantly change along the length of the cylindrical CPP implants.

A previous study by Grynypas et al. [121] reported that after 6 weeks, the percentage of bone ingrowth into the 106-150  $\mu\text{m}$  particle CPP implants was about 18% of the available pore area (60% density) which is remarkably lower than what was observed in the present study. They also reported that after 1 year the bone ingrowth was measured about 19% and 25%, for the 106–150 and 45–105  $\mu\text{m}$  particle samples, respectively, as determined from the BSE images. The notable difference between Grynypas' results and the results obtained in the present study may be due to the dissimilarity of the sintering conditions (i.e., temperature and humidity).

The percentage of bone area in the whole BSE image (including CPP implant, void and bone) is also demonstrated in Figure 4-10. On average, about 10% to 15% of the whole defect site is filled with new bone after 6 weeks (approximately 11  $\text{mm}^3$  of new bone tissue).

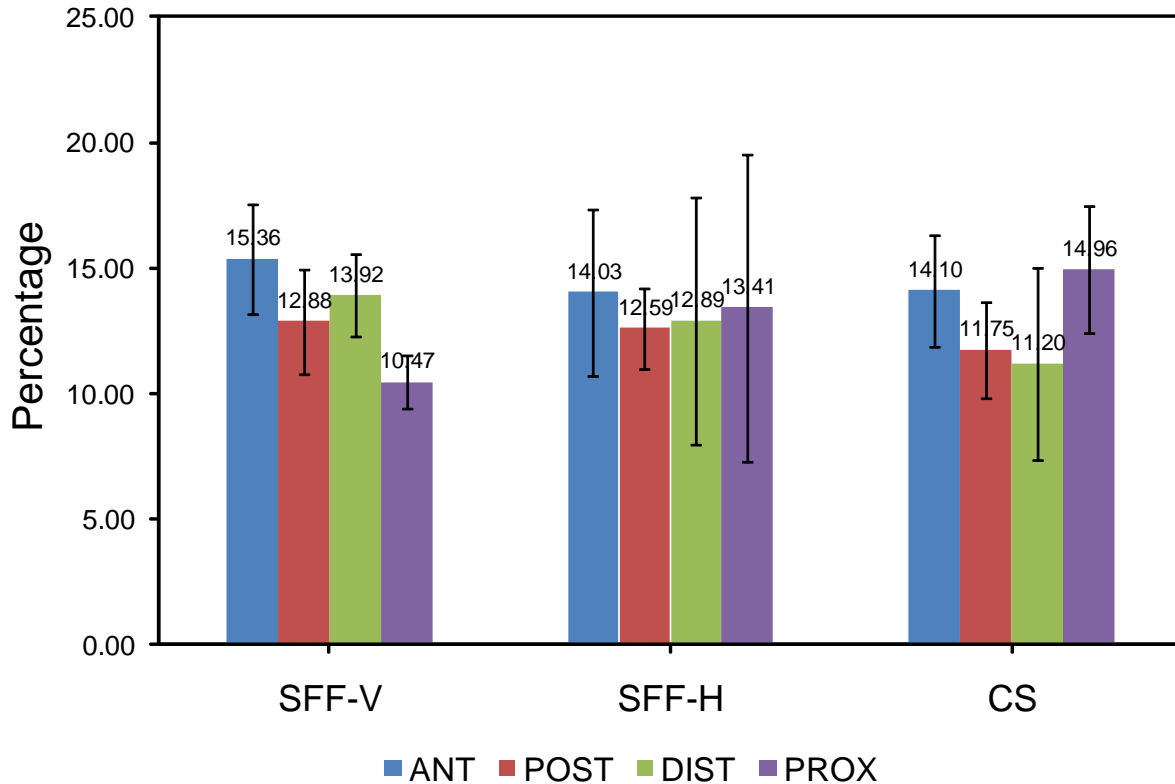


Figure 4-10: Percentage of absolute amount of bone growth within SFF-V, SFF-H, and CS CPP implants in the anterior (ANT), posterior (POST), distal (DIST), and proximal (PROX) aspects. No significant difference ( $p < 0.05$ ) was observed between the CPP implant types in terms of the amount of bone ingrowth.

Following implantation, a reduction in overall amount of CPP was observed due to degradation of CPP, which was quantifiable using image analysis of the BSE images. In Figure 4-11, the variation of area fraction of CPP (considered as degradation) is shown. The values are determined by subtracting the percentage of CPP in the BSE images of implanted plugs from the percentage of CPP in the control (not-implanted) samples (which was about 70%). The implants have degraded in the range of ~5% to 12%, on average. The change in CPP region during degradation results in a corresponding increase in the available porosity which contains either bone or soft tissue. Since only one randomly selected section from each aspect of each sample has been used in this study, the results do not represent the precise values of degradation occurs in the whole structure of the implanted CPP construct. As a result, some high standard deviations are observed (Figure 4-11).

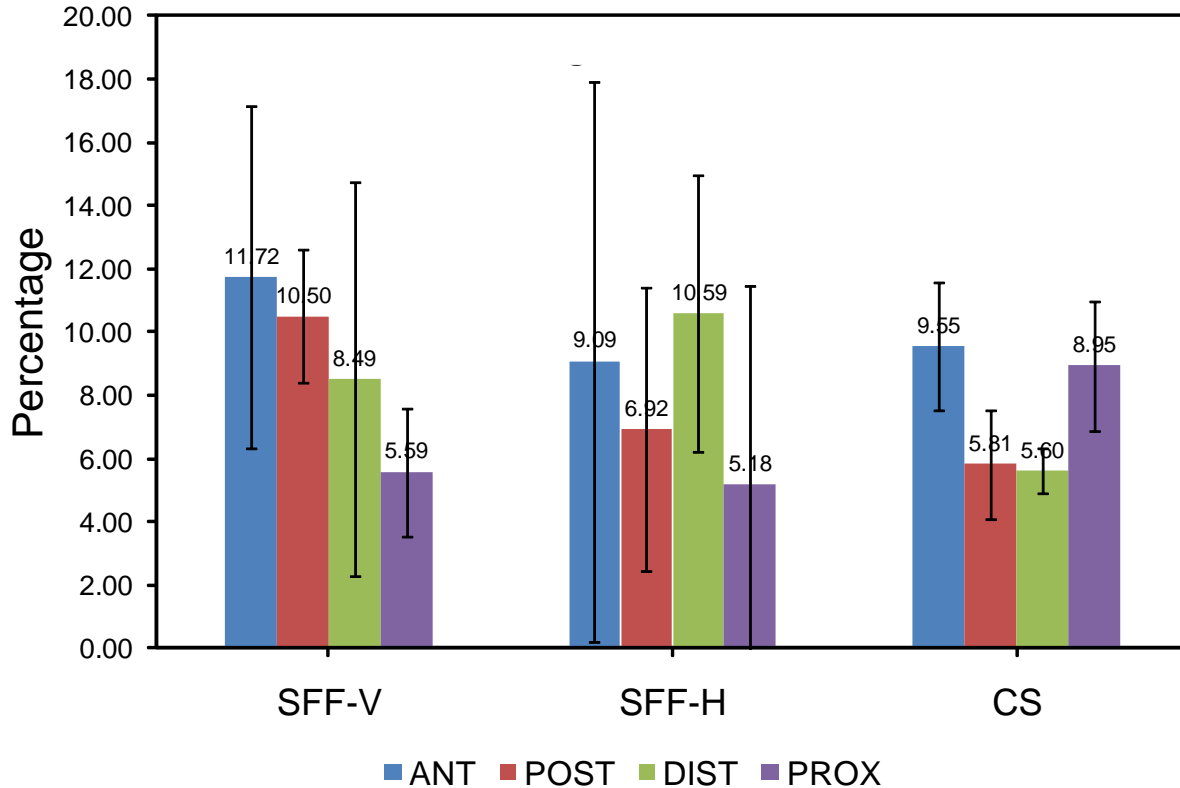


Figure 4-11: Percentage of degradation of SFF-V, SFF-H, and CS CPP implants in the anterior (ANT), posterior (POST), distal (DIST), and proximal (PROX) aspects.

The quantitative analysis revealed that about 8% of CPP implant was resorbed and the new bone formed within the implant occupied about 13% of its volume. It can be concluded that the rate of degradation and the rate of mineralization of new bone were in a balance at the 6 week implantation period. However, previous studies reported that the most rapid degradation rate occurs within the first few weeks of implantation and decreases in time [121]. Such a change in the degradation rate after the first few weeks might be attributed to the fact that the optimal amount of bone and blood supply has already formed [121]. It should be noted that the optimal amount of bone is dictated by local loading conditions. In addition, mineralization of the new bone tissue may have been accelerated by the presence of ions resulting from the degradation of the CPP i.e.,  $\text{Ca}^{2+}$  and  $(\text{PO}_4)^{3-}$  [121]. The degradation products do not appear to incite any inflammatory reaction [109].

A controlled degradation rate of CPP implants allows for gradual load transfer to bone, increasing space for bone ingrowth, and eventual filling of a defect with natural bone [2]. Longer degradation rates may be necessary for larger animals or larger defect sites due to a slower repair process [10]. Previous *in vivo* CPP studies by Grynepas et al. [121] revealed that the CPP

particle size influenced the degradation rate. CPP implants with smaller initial particles degraded faster. For instance, 47% of the implants (of 60% initial density), which were formed with 45-105  $\mu\text{m}$  CPP particles, was degraded by 6 weeks. However, it was about 9.5% for the implants formed with 150-250  $\mu\text{m}$  particles. Sinter necks of the CPP implants are more susceptible to degradation since those regions are of greater atomic disorder [121]. Smaller initial CPP particles lead to an increase in the number of sinter necks (for identical porosity); thus, resulting in higher degradation. Also, smaller particle size provides a higher specific surface area which in turn improves the degradation [121].

Initial density of the implant may also influence its degradation rate. In the previous study [121], 60% dense CPP rods made with 106-150  $\mu\text{m}$  particles showed 29% loss after 6 weeks, whereas the implants of the present study, which were initially 70% dense and were formed using 75-150  $\mu\text{m}$  powder, had lower degradation rate of about 8%. The difference may be also due to the difference in the sintering conditions i.e., temperature and humidity control.

Pores larger than 50  $\mu\text{m}$  affect the ossification whereas pores smaller than 10  $\mu\text{m}$  have an impact on bone-inducing protein adsorption, ion exchange, and bone-like apatite (cement) formation [78]. Pores should be large enough to allow cell infiltration, proliferation, and bone matrix deposition while still allowing for further cellular penetration *in vivo*. Not enough large pores can lead to the cartilage formation as opposed to osteogenesis [10]. The size of pore interconnections is also of importance as reported by Chang et al. [58]. In addition, porosity and pore size range have a noteworthy influence on the resorption of bioresorbable implants; larger pore sizes cause faster resorption [249]. Considering the mentioned parameters, a pore size of 300  $\mu\text{m}$  has been suggested in the review of the corresponding literature by Karageorgiou et al. [250]. The SFF-made CPP structures (as well as CS structures) include the required pore size range for bone formation as described in the previous chapter. Although with an identical porosity the pore size range of the SFF-made and CS CPP structures were dissimilar (which in turn led to the differences in specific surface area and permeability), the bone ingrowth and degradation outcomes did not reveal any significant distinction. This may be due to the fact that the bone ingrowth and degradation is not sensitive to about 20  $\mu\text{m}$  difference (50  $\mu\text{m}$  vs. 33  $\mu\text{m}$ ) of the mean pore size. In addition, a 6-week period of implantation might be too long to observe the early stage effects or too short to monitor the long-term effects of the micro-structural differences between the CPP constructs.

Various ceramic implants made via SFF techniques have been tested in numerous *in vivo* models and the results showed good biocompatibility [185, 198-200]. However, implant size,



animal model, porosity and pore size range are the factors that make comparison of those studies and the present research difficult.

#### **4.1.4 Histology Analysis**

A total of three representative implants, one per each CPP implant type, were used for qualitative histological assessment of the bone-implant interface. For this purpose, the polished surfaces used for BSE imaging were stained using 0.3% toluidine blue and 2% sodium borate in a 1:1 solution for 15 minutes at 50°C. After rinsing with 70% and 100% ethanol, the blocks were air dried. The blocks were then counterstained with 0.2% light green in 0.2% acetic acid for 1-3 minutes at room temperature followed by rinsing in 100% ethanol and air dried. The stained block face was then glued to a microscope slide with 5 minute epoxy and left overnight. Sections were cut with a 3-inch diameter diamond wafering blade on a Buehler Isomet Low Speed Saw (Lake Bluff IL, USA) at a thickness of 150  $\mu\text{m}$ . The section was then polished to approximately 20  $\mu\text{m}$  using a series of silicon carbide papers finishing with a 4000 grit paper. Low power photographs of the whole implant surface were taken using an Olympus BX 51-TF microscope (Center Valley PA, USA). A randomly selected image is shown in Figure 4-12. High power photographs were taken using a Nikon Eclipse Ti Inverted Microscope (Tokyo, Japan).

Histological sections demonstrated bone ingrowth within 6 weeks of implantation of the samples. After 6 weeks, bone had grown throughout the 4 mm diameter of the porous CPP plugs and the implants were well integrated through bone ingrowth. In addition, no adverse tissue reaction was seen in any of the sections examined. The SFF-made and CS samples showed similar response with significant bone ingrowth and no evidence of adverse host response.

As seen in Figure 4-12, the adjacent trabecular pattern of the host bone shows a growth around the CPP implant and new bone formation extended into the implant area. The representative histological section displayed a considerable amount of bone matrix deposition filling the pores of CPP construct. Most of the pores are filled with mineralized bone from periphery to the center.

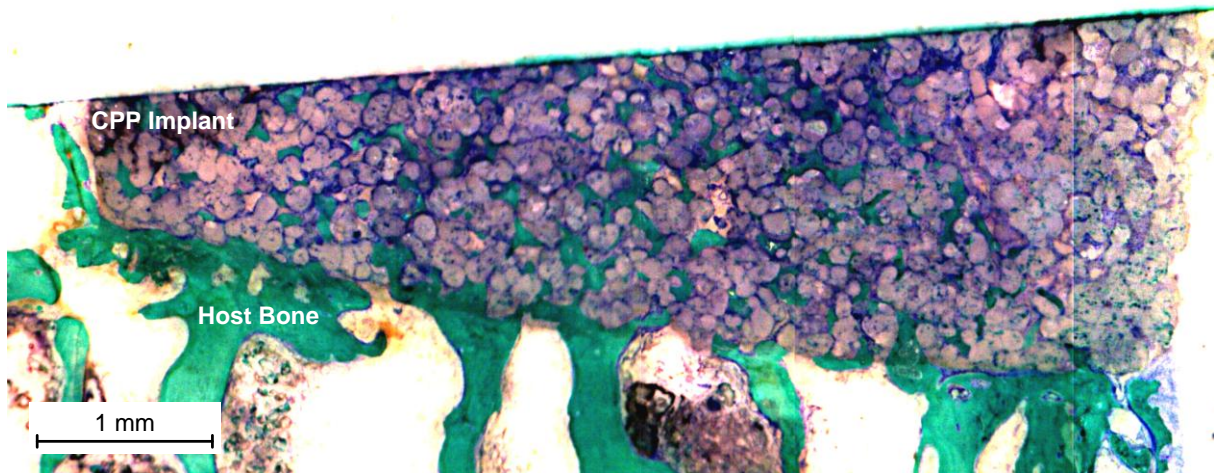


Figure 4-12 Histology image of a SFF-H implant (as a representative of SFF-made samples): green color represents for the mineralized bone tissue. Significant bone ingrowth is observed filling the pores of implant.

A higher magnification histology image is presented in Figure 4-13. The mineralized bone (stained green), osteoid (stained blue), and connective tissue (stained purple) formed within voids of the porous SFF-made CPP structures are shown. CPP and the new mineralized bone have integrated with no intervening fibrous tissue at the bone-CPP interface. This proves the high osseointegration of the CPP construct indicating that CPP is a bioactive (osteoconductive) material where the surface topography of the crystalline CPP is osteophilic i.e. attractive for bone deposition and bone bonding [117]. Also, histology analysis revealed some areas filled with osteoid at the CPP surface as shown in Figure 4-13.

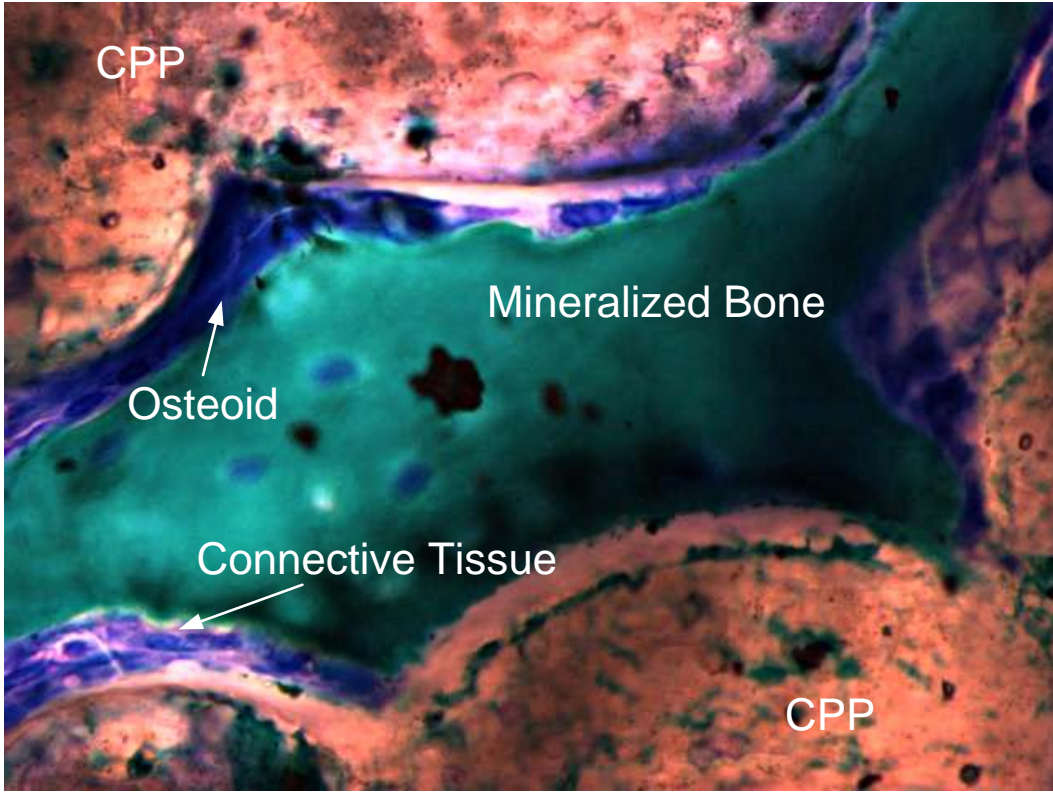


Figure 4-13: Histology image (SFF-H): mineralized bone (green), osteoid (blue), and connective tissue (purple). Osteoids are actively forming new bone.

## **4.2 *In vitro* Performance of CPP Substrates for Biphasic Osteochondral Implants**

The use of substrates for cartilage tissue engineering supports both cartilage formation and facilitates fixation after implantation by ingrowth of bone into the pores. “Biphasic constructs” consisting of a superficial cartilaginous component (corresponding to articular cartilage) and an underlying mineralized CPP bone substitute component (corresponding to subchondral bone) made via conventional sintering method have shown promising results for subchondral tissue engineering [109]. To form biphasic structures, cartilaginous tissue cells can be seeded onto or into a porous CPP structure, which provides the support for cells to proliferate, differentiate and form cartilage tissue *in vitro*. In the following, the capability of the SFF-made CPP structures for formation of biphasic implants is investigated *in vitro*.

### **4.2.1 *In vitro* Articular Cartilage Formation on CPP Substrate**

To assess the suitability of the SFF-made porous CPP substrates for the formation of biphasic cartilage-CPP constructs for osteochondral tissue engineering purpose, porous CPP discs (4 mm in diameter and 2mm in height) with 65% apparent density (i.e., 35% volume porosity) were formed by the SFF and CS techniques. As reported elsewhere [107], bovine articular cartilage was excised from metacarpal-phalangeal joints (6 to 9 month old animals), and chondrocytes isolated by sequential enzyme digestion consisting of 0.5% proteinase in Ham’s F-12 for 2 hours and then overnight with 0.1% collagenase, under standard cell culture conditions (37°C in a humidified atmosphere of 5%-CO<sub>2</sub>). The isolated chondrocytes were seeded at 160,000 cells/mm<sup>2</sup> in Ham’s F-12 supplemented with 5% fetal bovine serum (FBS; Sigma Chemical Co., St. Louis, MO) onto the top surface of the cylindrical discs made either by SFF (SFF-V) or CS method. CPP discs were surrounded by Tygon tubing (4.3 mm diameter, Thermoplastics Processor Inc., San Jose, CA, USA) and had been sterilized by gamma-irradiation (2.5 Mrad). Tygon tubing was used to prevent cell spillage over the edge of the CPP following seeding. The serum concentration was increased to 20% at day 5 and on day 7, 100 µg/mL ascorbic acid was added to the medium. Medium was changed every 2-3 days and fresh ascorbic acid was added with each change. The biphasic implant including bottom CPP substrate and top *in vitro*-cultured cartilage (after three weeks) is shown in Figure 4-14.

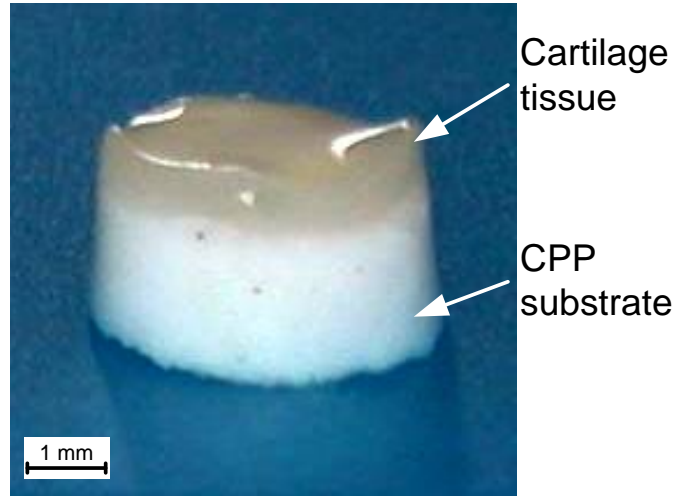


Figure 4-14: Cartilage tissue cultured on top of CPP substrate.

## 4.2.2 Assessment of Cultured Cartilage

### 4.2.2.1 Biochemical Evaluation

After three weeks of culture, the tissue was removed from the top surface of the SFF-made and CS CPP substrates using a scalpel blade and processed for further analysis. For biochemical evaluation, the tissue was digested by papain (40  $\mu\text{g}/\text{ml}$  in 20 mM ammonium acetate, 1 mM EDTA, and 2 mM DTT) for 48 hours at 65°C. Aliquots of the digest were assayed separately for proteoglycan, collagen and DNA contents. The proteoglycan content was estimated by quantifying the amount of sulphated glycosaminoglycans (GAG) using the dimethylmethylen blue dye binding assay [251]. Collagen content was estimated from the determination of the hydroxyproline (OH-proline) content. Aliquots of the papain digest were hydrolyzed in 6 N HCl at 110°C for 18 hours and the hydroxyproline content of the hydrolyzate was then determined using chloramine-T/Ehrlich's reagent assay and spectrophotometry [252]. DNA content was determined using the Hoechst 33258 dye binding assay and fluorometry as described previously [253].

For the assessment of the *in vitro*-formed cartilage, four samples were analyzed for each condition where the experiments repeated four times ( $n=16$ ). The data was pooled and expressed as mean $\pm$ SEM. Comparisons between the SFF-made and CS CPP groups were assessed using a Student's t-test with significance assigned at  $p<0.05$ .

As shown in Figure 4-15, the DNA content of the tissues formed on the SFF-made or CS CPP did not differ. Proteoglycan and collagen content of the two tissues were also not

significantly different. Thus, the SFF process and related binder used for forming CPP constructs did not have a toxic effect on cartilage cells as the DNA, GAG/DNA and OH-proline/DNA content of the three weeks old tissue did not differ significantly for the SFF-made and CS CPP substrates. The cultured cartilage tissue has been characterized previously and has been shown to resemble hyaline cartilage similar to native cartilage [107, 109].

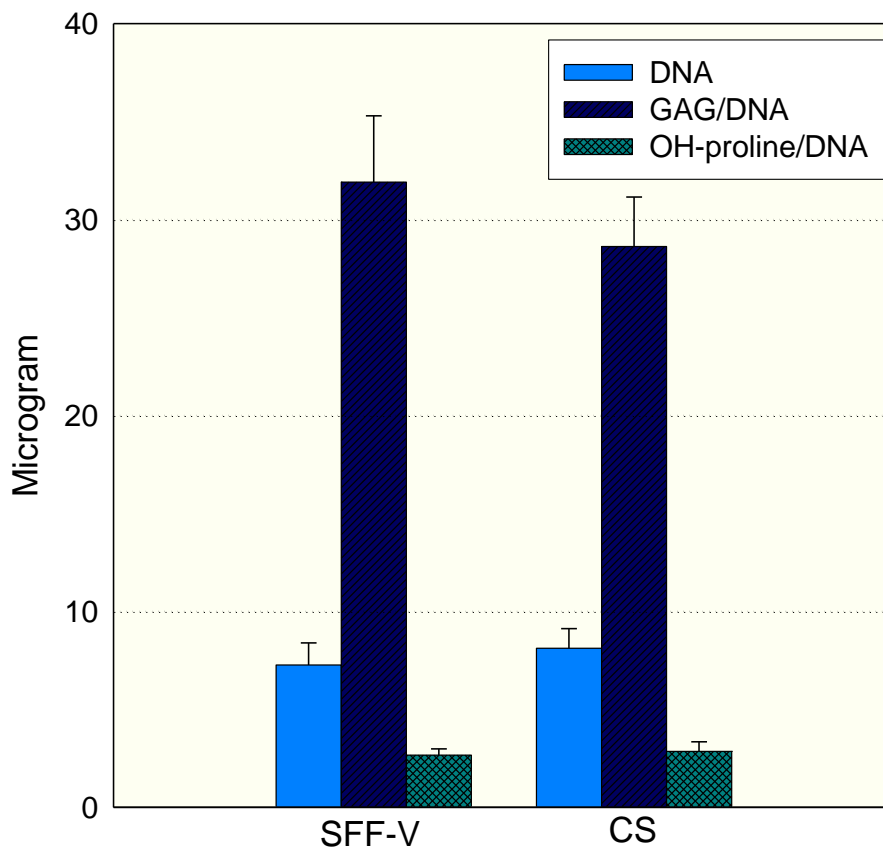


Figure 4-15: Biochemical comparison of SFF-made to CS. Cartilage cells were seeded as described in the Methods section on to the top surfaces of SFF-made and CS and cultured for 3 weeks. SFF-made was suitable as a substrate for cartilage tissue formation as there was no significant difference in DNA, proteoglycan (GAG), or collagen (OH-proline) content in SFF-made compared to CS. Results are pooled and expressed as mean  $\pm$  standard error of the mean ( $n = 16$ ).

#### 4.2.2.2 Histomorphology

In addition, the effect of the substrate on tissue morphology was assessed histologically. The tissue that had formed on the top surface of the SFF-made or CS CPP substrates was removed, fixed in 10% neutral-buffered formalin and embedded in paraffin. Sections of 5  $\mu\text{m}$  thick were cut, stained with either hematoxylin and eosin (H&E) or toluidine blue, and examined by light microscopy<sup>5</sup>.

Figure 4-16 shows the histological appearance of the cartilage tissue on the CPP substrates. There is a continuous layer of tissue composed of chondrocytes surrounded by extracellular matrix rich in proteoglycans as determined by toluidine blue staining. The histomorphology of the tissue cultured on the SFF-made CPP resembled tissue cultured on the CS one (Figure 4-16). These results are consistent with those previously reported for CS CPP biphasic implants [109].

---

<sup>5</sup> The *in vitro* cell culturing and assessment of *in vitro*-formed cartilage tissue was conducted by Dr. J.N. Amritha De Croos in Mount Sinai Hospital of the University of Toronto.

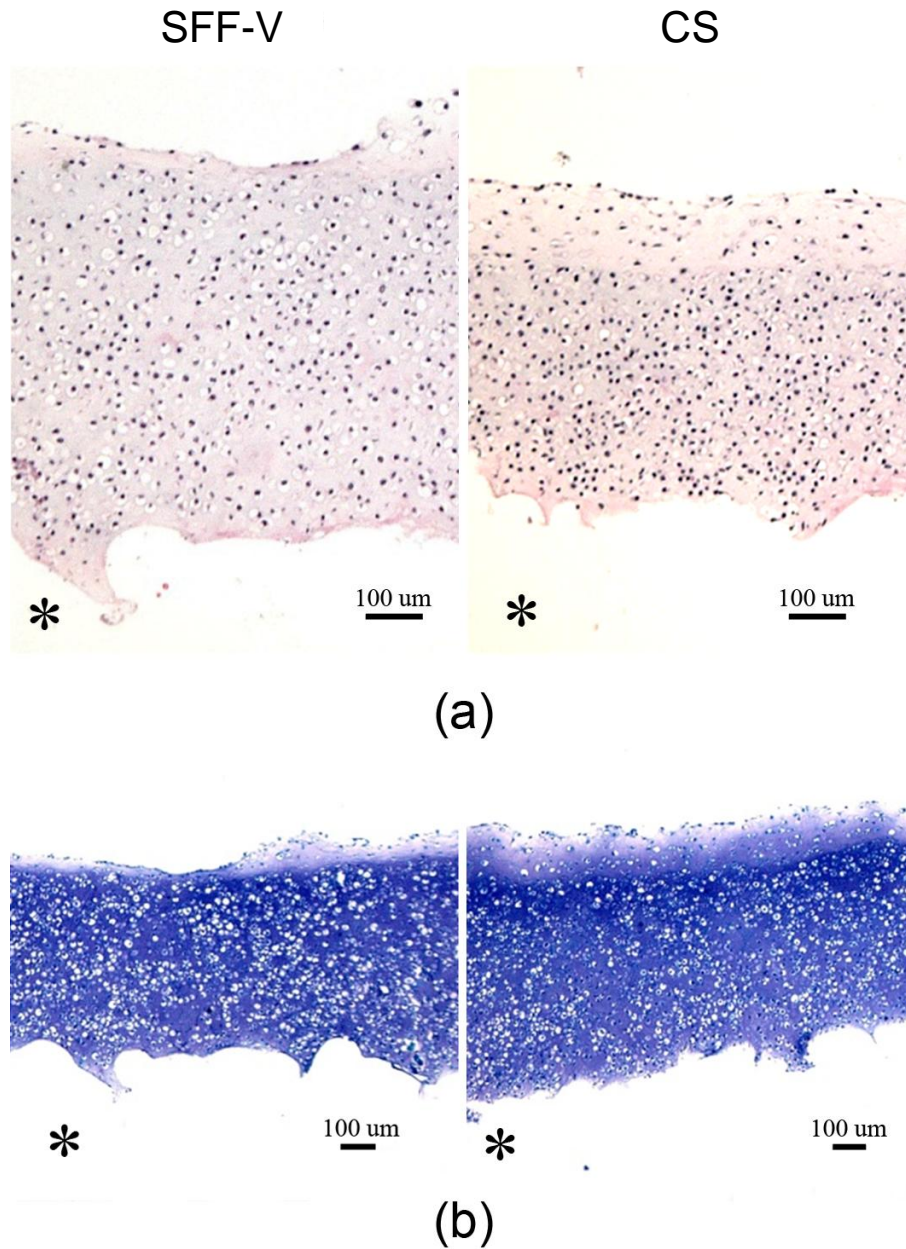


Figure 4-16: Histological appearance of tissues after 3 weeks of culture. Substrates were seeded with cartilage cells as described in the methods section, grown for 3 weeks and removed from the top surface of SFF-made and CS substrates, fixed in formalin, and stained with (a) hematoxylin and Eosin or (b) toluidine blue. Left side of figure: SFF-made, Right side of figure: CS. \* indicates where substrate was located.

While the success in growing cartilage *in vitro* has been achieved, it may require reliable merging with the native cartilage in the joint defect and integration with subchondral bone for *in vivo* studies. The biphasic implants made with CS CPP have shown superior biocompatibility and desired integration with host tissues (cartilage and bone) in animal models [109]. Previous



work demonstrated that conventionally-made CPP structures with  $65\pm 3\%$  full theoretical density (i.e.  $35\pm 3\%$  porosity) provide suitable mechanical properties and porosity for preparation of biphasic (cartilage-CPP) implants for osteochondral defect repair as shown in the sheep knee defect model previously reported. Thus, it may be concluded that the SFF-made biphasic implants are suitable for osteochondral tissue engineering purposes.

### 4.3 Summary

This chapter addressed the biological responses of the CPP implants fabricated by the SFF technique. The results of the *in vivo* model demonstrated the desired performance of the SFF-made CPP structures as an osteoconductive bone graft substitute by providing the requirements for new tissue regeneration and enhanced the bone ingrowth. The degradation rate of the SFF-made CPP construct after a 6-week period of implantation was measured to be  $\sim 8\%$ . In addition, it was shown that the SFF-made CPP constructs were suitable for forming biphasic implants for osteochondral tissue engineering applications. Cartilage tissue was successfully cultured on the top of the SFF-made and CS porous CPP substrates *in vitro*. Consequently, the CPP structures made by the SFF technique developed in this thesis appear to be a promising implant for both bone regeneration and osteochondral (bone and cartilage) tissue engineering. The *in vivo* and *in vivo* performances of the SFF-made CPP samples were not significantly different from the CS ones.

## Chapter 5

# Effects of SFF Process Parameters on the Relative Density of SFF-made Structures: Mathematical Modeling

This chapter describes a novel mathematical model developed for predicting optimum SFF parameters at a given physical property of green porous structures (i.e., relative density). The relative density (packed density) of compacted powder bed in SFF process and the distribution of mechanical stress applied by the roller mechanism are predicted by the mathematical model. An experimental set-up is proposed to be used for validation of the model.

### 5.1 Introduction

Porosity of the implant structures is a crucial factor in bone substitution and osteochondral tissue engineering. Porosity affects the biomechanical properties of the porous implant such as structural stiffness and new tissue generation capacity [254]. The porosity is introduced to the synthetic structures during the fabrication process. Porosity of the SFF-made constructs is partially determined by the density of green parts. The packed density of the green parts (before sintering) influences the annealing process and the final density of constructs after sintering. In powder-based SFF methods developed in the present study, the density of the green parts substantially depends on the compact density/porosity of individual stacked-layers of powder. In general, the powder layers are spread and compacted using a counter-rotating rolling mechanism as shown in Figure 5-1. The counter-rotating roller collects the powder from the feeding chamber and spreads it on top of the previous layers in the building chamber in a thin layer while applies a compaction pressure. To arrive at a desired compact density in the powder layers, the parameters associated with the spreading mechanism (e.g., linear and rotational speed of roller, roller surface properties, and powder layer thickness) must be carefully adjusted

in such a way that an appropriate compaction force is applied on the powder bed by the roller. Since the properties of powder materials (e.g., spreadability and flowability) are inherently nonlinear, the optimization of powder spreading and compaction process parameters is intricate.

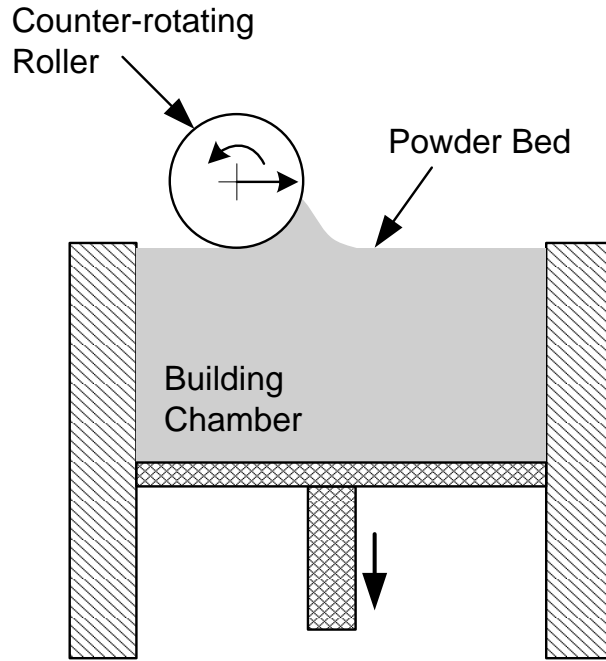


Figure 5-1: Schematic of powder spreading and compacting process via counter-rotating roller in the build chamber.

The current efforts for obtaining the optimum properties of the spread powder layer are based on trial-and-error techniques, which must be carried out for any powder material. As an alternative approach, mathematical modeling provides insight into the compaction phenomenon. By using mathematical modeling and simulation, engineers can tune the process parameters for better control of the physical properties of the SFF-made structures such as their porosity. In spite of the apparent simplicity of the counter-rotating rolling compaction, there are too many unknown aspects of this process, from an analytical perspective.

Several investigations have been conducted on powder rolling and densification, and many theories have been developed to determine the material behaviour in compaction conditions. Johanson [255] developed the first complex model for predicting the material flow undergoing continuous shear deformation between two rollers. 1D-slab method, in which the equilibrium force balance on a thin strip of material with a differential thickness is considered, has been used

to study the rolling, extrusion and drawing of materials [256]. Katashinskii et al. [257, 258] developed a mathematical model of the densification of powder by two rotating rollers, representing the stress-strain state of the powder being rolled in a densification zone. A complete review about this area of research is available in the literature [256]. However, as it is evident from the literature, no modeling has been conducted to characterize the powder spreading and compaction process in SFF methods.

This study is focused on mathematical modeling of the powder behavior in the compaction where a counter-rotating roller passes over the powder bed during the feeding step of the SFF process. The effects of the process parameters (such as friction between roller and powder, layer thickness, and roller diameter) on the kinematical characteristics of the process in the densification zone are studied. The compact density, rolling contact pressure, and stress distribution within the compacted powder bed are analyzed.

## **5.2 Mathematical Modeling**

### **5.2.1 Model Description**

The counter-rotating roller compaction of powder is analyzed with a 1D-slab approach, for which some assumptions are taken into account.

1. It is assumed that stress and strain vary only in the rolling direction and not in the thickness due to relatively smaller dimensions.
2. Since the plastic strains are substantially higher than the elastic strain, the elastic deformations are negligible.
3. Body forces (gravitational forces) can be ignored in comparison with the frictional and compaction forces.
4. It is assumed that the underneath powder layers are compacted enough so that the new layer of rolling powder is prepared onto a stationary solid plane.
5. The effects of roller rotational and linear motion speeds are taken into account by the coefficient of the friction between the roller and powder.

6. Since the material is prevented from spreading laterally during rolling, and the roller length is relatively larger than its diameter and powder layer thickness, the process is treated as a plane strain problem.
7. By considering a continuum mechanics for this process, similar to the phenomenon of the laminar flow of a viscous liquid, a steady flow of the powder takes place into the densification zone. The analysis is performed according to the plasticity theories for compressible porous media.
8. For simplification, it is assumed that the powder is first spread and then is being compacted to a certain thickness.

As shown in Figure 5-2,  $\alpha_{in}$  determines the beginning position of the densification zone beyond where the densification of the powder takes place. The lowest rolling gap  $h_s$ , which is equal to the compacted powder layer thickness, occurs at  $\alpha_{in} = 0$ . The coefficient of friction between the roller surface and the powder  $\mu_r$  is assumed to be constant in the entire roller-powder contact area. This parameter hinges on several factors, including the powder particle size and shape, roller surface smoothness, and roller rotational  $\omega$  and transverse motion speed  $V$ .

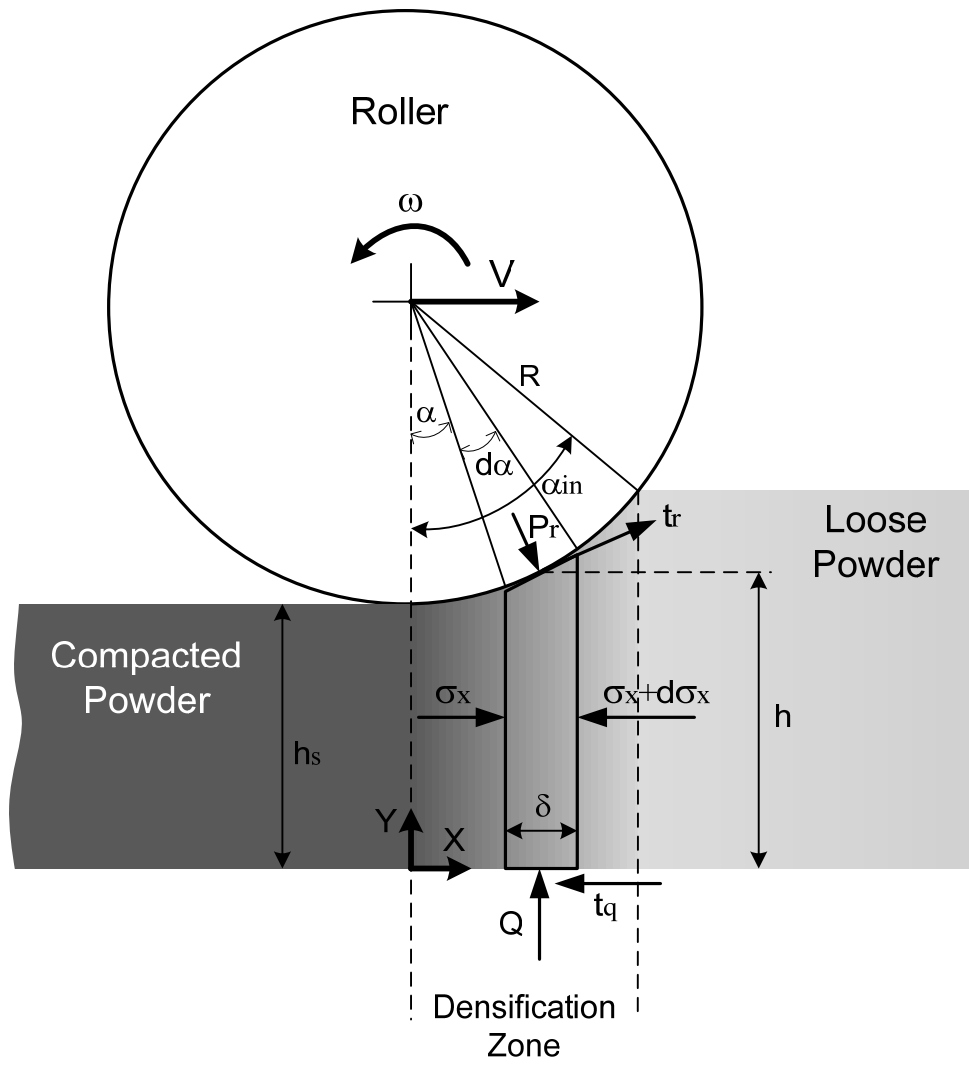


Figure 5-2: Schematic diagram of forces and stresses acting on the powder densification zone. The loose powder is gradually compacted (as shown by darker gray-scale) by the roller pressure. A slab of powder with an infinitely small thickness is depicted on which the applied stresses are determined.

The parameters which are used in the following section are listed in Table 5-1, as the nomenclature.

Table 5-1: Nomenclature representing the parameters utilized for mathematical modeling of counter-rotating roller powder compaction

Parameter	Description	Parameter	Description
$b$	Slab depth (m) in z direction	$t_r$	Shear stress between roller and loose powder (N/m <sup>2</sup> )
$e$	Rate of densification (1/s)	$\alpha$	Rolling angle (radian)
$e_x$	Rate of slab deformation in x direction (1/s)	$\alpha_{in}$	Rolling upper bound (radian)
$e_y$	Rate of slab deformation in y direction (1/s)	$\delta$	Slab width (m) in x direction
$h$	Slab height (m) in y direction	$\gamma$	Rate of shape change (1/s)
$h_s$	Powder layer thickness (m)	$\mu_p$	Coefficient of friction between loose and compacted powder
$m$	Slab mass (kg)	$\mu_r$	Coefficient of friction between roller and loose powder
$n$	Normal vector	$\Theta$	Porosity
$P$	Mean hydrostatic stress (N/m <sup>2</sup> )	$\Theta_i$	Initial porosity
$P_r$	Roller contact pressure (N/m <sup>2</sup> )	$\rho$	Density (kg/m <sup>3</sup> )
$\bar{P}_r$	Roller contact pressure / $\sigma_s$	$\sigma_x, \sigma_y, \sigma_z$	Stress in x, y, and z directions (N/m <sup>2</sup> )
$Q$	Reaction force (N)	$\bar{\sigma}_x$	Stress in x directions / $\sigma_s$
$R$	Roller radius (m)	$\sigma_s$	Yield stress of bulk material (N/m <sup>2</sup> )
$t_q$	Shear stress between loose and compacted powder (N/m <sup>2</sup> )	$\tau$	Intensity of stress deviator (N/m <sup>2</sup> )

### 5.2.2 Force Equilibrium and Constructive Model

To derive the governing equations for the behaviour of powder under the roller pressure, a slab of powder with an infinitely small width is considered as shown in Figure 5-2. It is oriented perpendicular to the rolling direction and the applied forces. The stresses acting on the slab, the roll pressure  $P_r$ , and the shear stresses  $t_r$  and  $t_q$ , are also depicted in Figure 5-2. The

equilibrium of the forces in the rolling direction, that is, the x-direction, for a unit length in the roll width, leads to the following expression:

$$\frac{d\sigma_x}{d\alpha} = \frac{R}{h} \cdot (P_r \cdot \sin \alpha + t_r \cdot \cos \alpha - t_q) \quad (5-1)$$

With the consideration of the equation of continuity, for a compressible material in 1-D, the density is not constant and the continuity equation (mass conservation) is written as follows [257]:

$$m = h \cdot \rho \cdot \delta \cdot b \Rightarrow \frac{\dot{\delta}}{\delta} + \frac{\dot{h}}{h} + \frac{\dot{\rho}}{\rho} = 0 \quad (5-2)$$

The terms  $\frac{\dot{\delta}}{\delta}$  and  $\frac{\dot{h}}{h}$  are the rates of the slab deformation in the directions  $x$  and  $y$ , respectively. Thus,

$$e_x = \frac{\dot{\delta}}{\delta} \quad \text{and} \quad e_y = \frac{\dot{h}}{h} \quad (5-3)$$

$$e = e_x + e_y = \frac{\dot{\delta}}{\delta} + \frac{\dot{h}}{h} \quad [259] \quad (5-4)$$

$$\gamma = e_x - e_y = \frac{\dot{\delta}}{\delta} - \frac{\dot{h}}{h}$$

Using (5-2) and [259] (5-4), the following can be computed:

$$\frac{\dot{\delta}}{\delta} + \frac{\dot{h}}{h} = -\frac{\dot{\rho}}{\rho} \Rightarrow e = -\left(\frac{\dot{\rho}}{\rho}\right) \quad (5-5)$$

For the plane deformation of compressible materials, the constitutive equation representing the plasticity of porous media proposed by Shtern [259] are presented in (5-6)-(5-8).



$$\frac{P^2}{\psi + \frac{1}{6} \cdot \phi} + \frac{\tau^2}{\frac{1}{2} \cdot \phi} = \frac{2}{3} \cdot (1 - \Theta) \cdot \sigma_s^2 \quad (5-6)$$

$$\frac{P}{\psi + \frac{1}{6} \cdot \phi} \cdot \gamma = \frac{\tau}{\frac{1}{2} \cdot \phi} \cdot e \quad (5-7)$$

where

$$\psi = \frac{2}{3} \cdot \frac{(1 - \Theta)^2 \cdot (\Theta_i - \Theta)}{\Theta \cdot \Theta_i}; \quad \phi = \frac{(1 - \Theta) \cdot (\Theta_i - \Theta)}{\Theta_i} \quad (5-8)$$

According to Shtern [259], in powder rolling, when the angle of upper boundary of the densification zone does not exceed 0.15-0.20 radians, the following approximation is valid and for the 1D-slab problem of this study the hydrostatic stress  $P$  and the stress deviator  $\tau$  are simplified as [257]:

$$P = \frac{1}{2} \cdot (\sigma_x + \sigma_y) \quad (5-9)$$

$$\tau = \frac{1}{2} (\sigma_x - \sigma_y)$$

$$\sigma_y = P_r \quad (5-10)$$

Therefore,

$$P = \frac{1}{2} \cdot (\sigma_x + P_r) \quad (5-11)$$

$$\tau = \frac{1}{2} \cdot (\sigma_x - P_r)$$

Using [259] (5-4), (5-7) and (5-11),  $e$  is found as:

$$e = \frac{\frac{1}{2} \cdot \phi}{\psi + \frac{1}{6} \cdot \phi} \cdot \frac{\sigma_x + P_r}{\sigma_x - P_r} \cdot \left( \frac{\dot{\delta}}{\delta} - \frac{\dot{h}}{h} \right) \quad (5-12)$$

Using (5-5)

$$\frac{\dot{\delta}}{\delta} = -\frac{\dot{\rho}}{\rho} - \frac{\dot{h}}{h} \quad (5-13)$$

Using (5-13), equation (5-12) can be solved with respect to  $\frac{\dot{\rho}}{\rho}$  and expressed in the form of

$$\frac{\dot{\rho}}{\rho} = \frac{-2}{1 + \frac{\psi + \frac{1}{6} \cdot \phi}{\frac{1}{2} \cdot \phi} \cdot \frac{P_r - \sigma_x}{P_r + \sigma_x}} \cdot \frac{\dot{h}}{h} \quad (5-14)$$

From the geometry perspective, it is observed that  $h = h(\alpha) = h_s + R \cdot (1 - \cos \alpha)$ .

Consequently,

$$\frac{\dot{h}}{h} = \frac{\sin \alpha}{\frac{h_s}{R} + (1 - \cos \alpha)} \quad (5-15)$$

Since  $\rho$  is only a function of  $\alpha$ , by substituting (5-15) into (5-14) the following relation (5-16) is obtained.

$$\frac{d\rho}{d\alpha} = \frac{-2 \cdot \rho \cdot \sin \alpha}{\left(\frac{h_s}{R} + 1 - \cos \alpha\right) \cdot \left(1 + \frac{A^2}{B^2} \cdot \frac{P_r - \sigma_x}{P_r + \sigma_x}\right)} \quad (5-16)$$

where

$$A^2 = \frac{2}{3} \cdot \left(\psi + \frac{1}{6} \cdot \phi\right) \cdot (1 - \Theta); \quad B^2 = \frac{1}{3} \cdot \phi \cdot (1 - \Theta) \quad (5-17)$$

Equation (5-6) can be rewritten as:

$$\frac{P^2}{A^2} + \frac{\tau^2}{B^2} = \sigma_s^2 \quad (5-18)$$

By substituting (5-11) in (5-18) and solving it for  $P_r$ ,

$$\bar{P}_r = \frac{A^2 - B^2}{A^2 + B^2} \cdot \bar{\sigma}_x + \frac{2 \cdot A \cdot B}{A^2 + B^2} \cdot \sqrt{A^2 + B^2 - \bar{\sigma}_x^2} \quad (5-19)$$

where  $\bar{P}_r = \frac{P_r}{\sigma_s}$  and  $\bar{\sigma}_x = \frac{\sigma_x}{\sigma_s}$  are the dimension-less stress components.

In addition, considering  $t_r = \mu_r \cdot P_r$  and  $t_q = \mu_p \cdot Q = \mu_p \cdot P_r \cdot (\cos \alpha - \mu_r \cdot \sin \alpha)$ , the ordinary differential equation (5-1) (obtained from the force equilibrium) is

$$\frac{d\bar{\sigma}_x}{d\alpha} = \frac{\bar{P}_r}{\left(\frac{h_s}{R} + 1 - \cos \alpha\right)} \cdot \left(\sin \alpha + \mu_r \cdot \cos \alpha - \mu_p \cdot (\cos \alpha - \mu_r \cdot \sin \alpha)\right) \quad (5-20)$$

Equations (5-16), (5-19), and (5-20) form a system of equations that by adjusting the initial values for  $\alpha_{in}$ , coefficients of friction  $\mu_p$  as well as  $\mu_r$ , initial density of powder  $\Theta_i$ , layer thickness (rolling gap)  $h_s$ , and roller radius  $R$ , and by using the numerical algorithm of Euler, the roller contact pressure, stress distributions, and density gradient of the powder along the rolling direction are obtained.

### 5.3 Results and Discussion

The derived governing equations were solved using some feasible range of boundary conditions and initial values for the SFF process listed in the captions of the following figures.

The distribution of the roller normal contact pressure and the stress along the densification zone in the powder layer are graphed in Figure 5-3 and Figure 5-4, respectively. The plots are represented as a function of the rolling angle for various possible values of the friction coefficient between the roller and powder. The plots revealed an increase in longitudinal stress in the powder that is compacted by the roller. It is obvious that the maximum stress occurs in the narrowest gap between the roller and the underneath powder layer, that is, at the rolling angle of zero. Both the longitudinal stress and contact pressure decrease by applying higher values of the coefficient of friction between the powder and roller. This coefficient of friction is defined by the surface condition of roller as well as its rotational and linear speed.

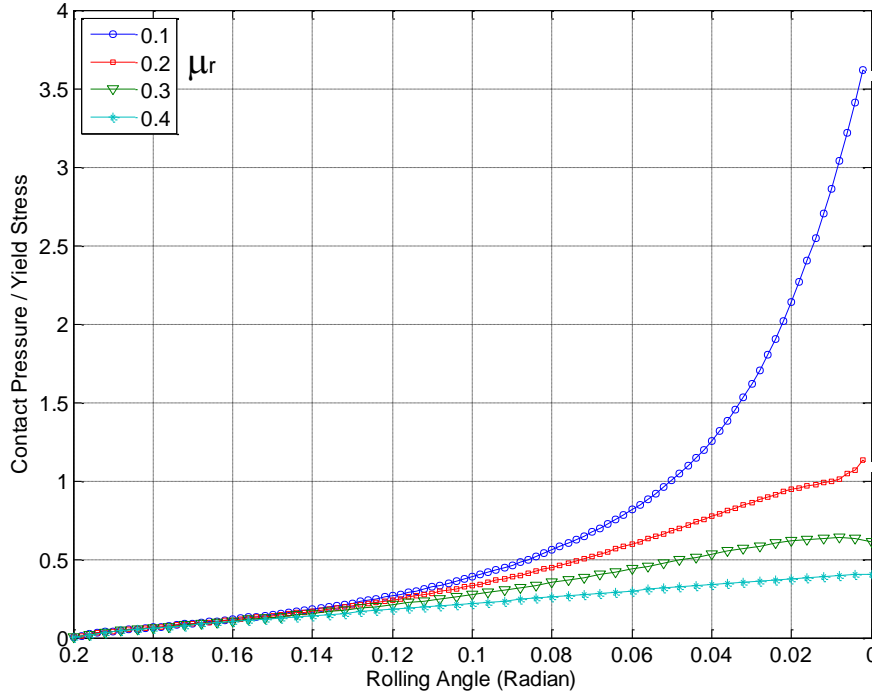


Figure 5-3: Variation of normal contact pressure distribution along the densification zone (calculated for  $\mu_p=0.5$ ,  $h_s=130 \mu\text{m}$  (0.005 in),  $R=10 \text{ mm}$ ,  $\rho_{\text{initial}}=30\%$ , and  $\alpha_{\text{in}}=0.2 \text{ Rad}$ ). The effect of the roller-powder coefficient of friction on the normal contact pressure is also shown.

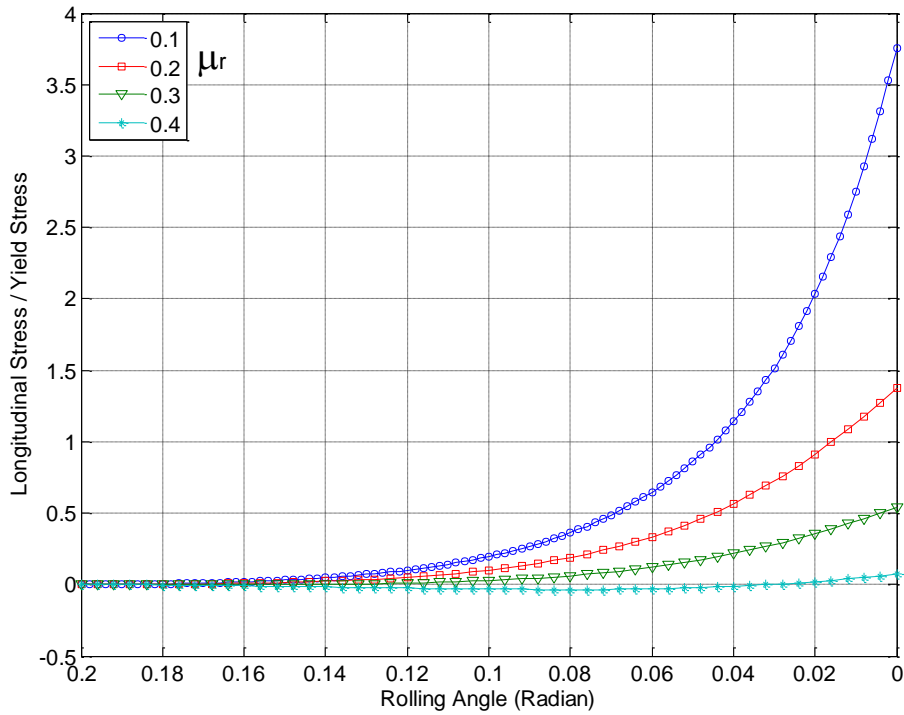


Figure 5-4: Variation of the longitudinal stress distribution along the densification zone (calculated for  $\mu_p=0.5$ ,  $h_s=130 \mu\text{m}$  (0.005 in),  $R=10 \text{ mm}$ ,  $\rho_{\text{initial}}=30\%$ , and  $\alpha_{\text{in}}=0.2 \text{ Rad}$ ). The effect of the roller-powder coefficient of friction on the longitudinal stress is also shown.

The data from the experimental investigations by others [258] show that the distribution of the powder density in the densification zone depends on two factors: (1) absolute and relative magnitudes of the longitudinal and normal stresses, and (2) the geometry of the deformation zone. Thus, from what was observed in Figure 5-3 and Figure 5-4, a change in the roller-powder contact friction would affect the compacted powder density. As shown in Figure 5-5, an increase in the coefficient of friction between the roller and the powder results in a decrease in the compacted powder density. In other words, the relative porosity (i.e., 1-relative density) of the compacted powder reduces with decreasing the coefficients of friction. Figure 5-6 represents the same effect as increasing the coefficient of friction between the loose and the underlying powder layer. The relative density (RD)/compact density was obtained according to the following expression:

$$RD = \frac{\text{bulk density of compacted powder}}{\text{powder material density}} \quad (5-21)$$

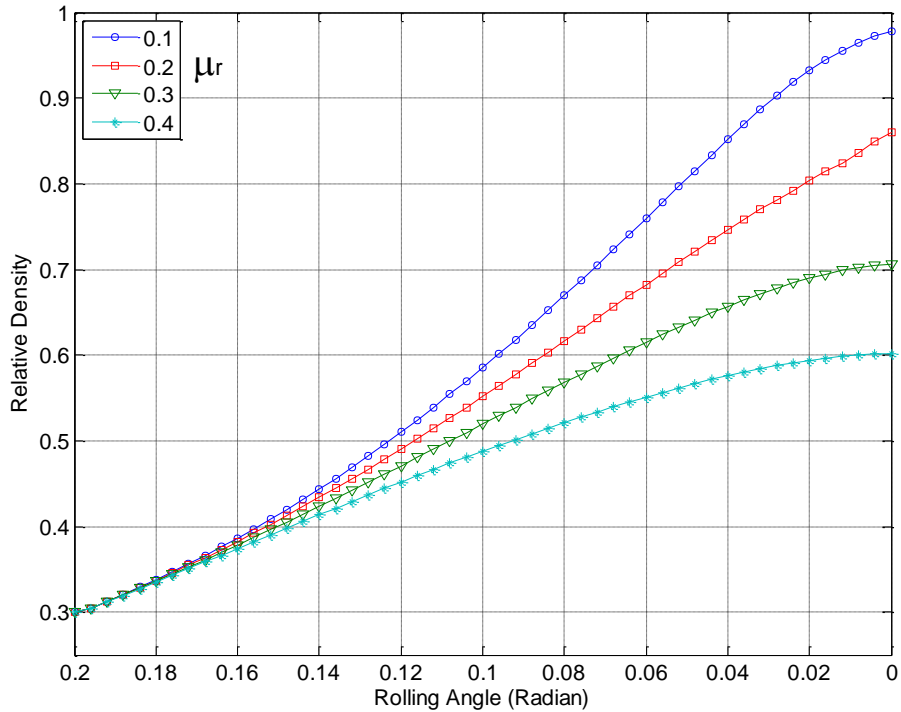


Figure 5-5: Variation of relative density distribution along the densification zone for some possible coefficient of friction between the roller and powder (calculated for  $\mu_p=0.5$ ,  $h_s=130 \mu\text{m}$  (0.005 in),  $R=10 \text{ mm}$ ,  $\rho_{\text{initial}}=30\%$ , and  $\alpha_{\text{in}}=0.2 \text{ Rad}$ ).

Powder characteristics such as particle size and shape may affect the inter-particle forces that in turn govern the flowability of powder being spread against the underneath powder layer. This effect can be considered in the developed model by the coefficient of friction between the powder and the underneath layer  $\mu_p$  and has been analyzed as shown in Figure 5-6. It is obvious that the relative density increases by an increase of  $\mu_p$ .

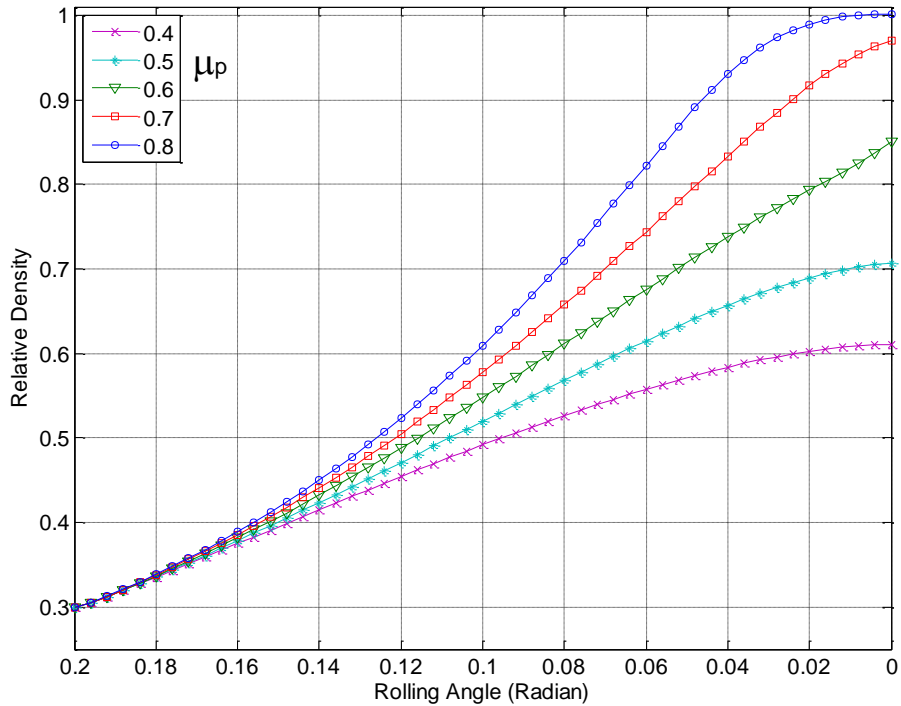


Figure 5-6: Effect of the coefficient of friction between the loose and compacted powder on the relative density distribution along the densification zone (calculated for  $\mu_r=0.3$ ,  $h_s=130 \mu\text{m}$  (0.005 in),  $R=10 \text{ mm}$ ,  $\rho_{\text{initial}}=30\%$ , and  $\alpha_{\text{in}}=0.2 \text{ Rad}$ ).

The variation of the relative density in relation to the changes in the powder layer thickness is found in Figure 5-7. The powder layer thickness is defined by the gap between the roller and the underlying powder layer at the rolling angle of zero. In the SFF machine, this parameter can be adjusted through the operating software. The powder relative density for the layer thicknesses accessible in a SFF machine is plotted in Figure 5-8. As seen, the larger the thickness, the lower the relative density in the final compacted powder.

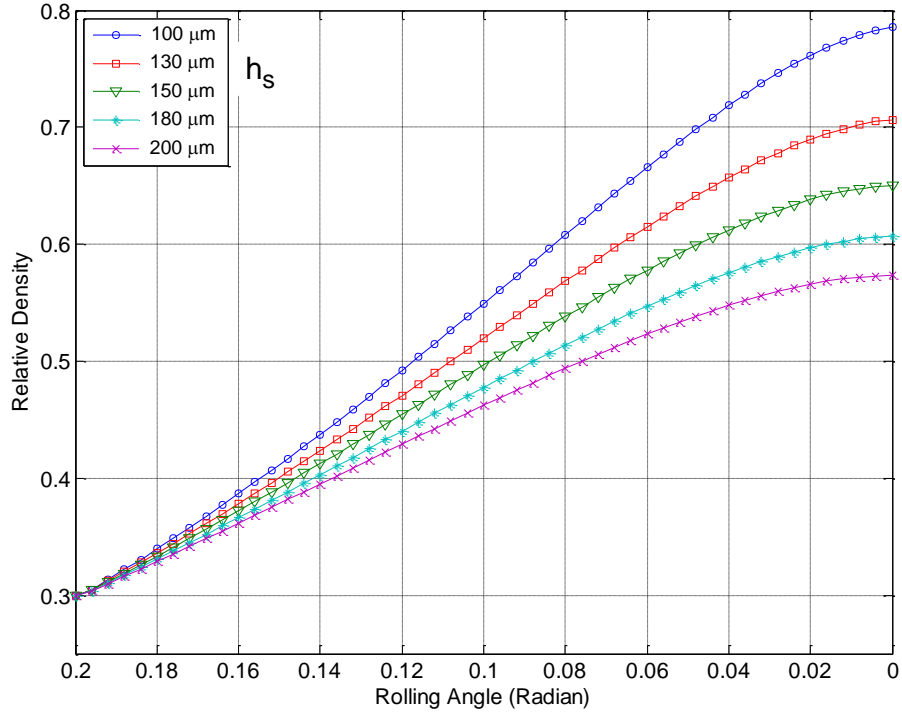


Figure 5-7: Effect of the powder layer thickness on the relative density distribution along the densification zone (calculated for  $\mu_p=0.5$ ,  $\mu_r=0.3$ ,  $R=10$  mm,  $\rho_{\text{initial}}=30\%$ , and  $\alpha_{\text{in}}=0.2$  Rad).

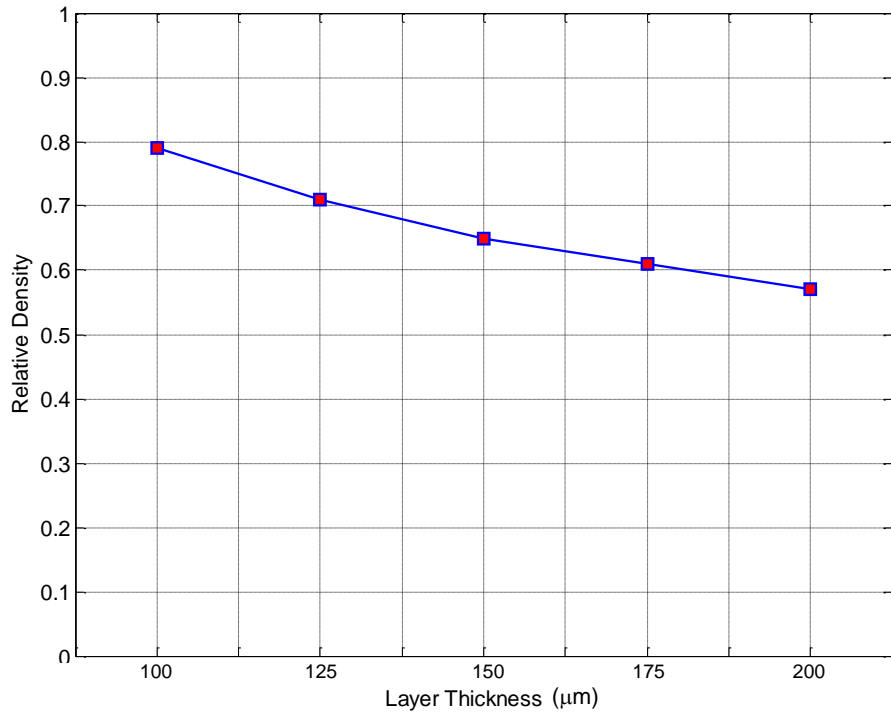


Figure 5-8: Relative density of compacted powder layer vs. the adjusted layer thickness (calculated for  $\mu_p=0.5$ ,  $\mu_r=0.3$ ,  $R=10$  mm,  $\rho_{\text{initial}}=30\%$ , and  $\alpha_{\text{in}}=0.2$  Rad).

By keeping all the parameters unchanged, an increase in the apparent density of the starting powder (initial density) results in an increase in the relative density of the compacted powder that is signified in Figure 5-9. The percentage of this increase is presented in Figure 5-10. It is observed that the powder with a lower initial density shows a higher change.

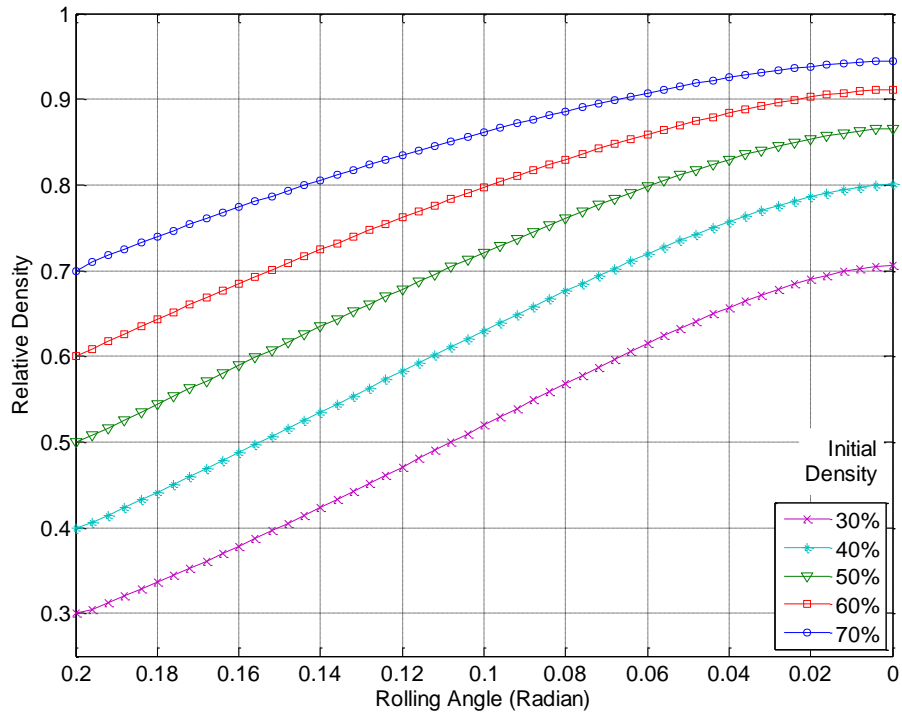


Figure 5-9: Effect of the initial apparent density of powder on the relative density along the densification zone (calculated for  $\mu_p=0.5$ ,  $\mu_r=0.3$ ,  $h_s=130 \mu\text{m}$  (0.005 in),  $R=10 \text{ mm}$ , and  $\alpha_{in}=0.2 \text{ Rad}$ ).



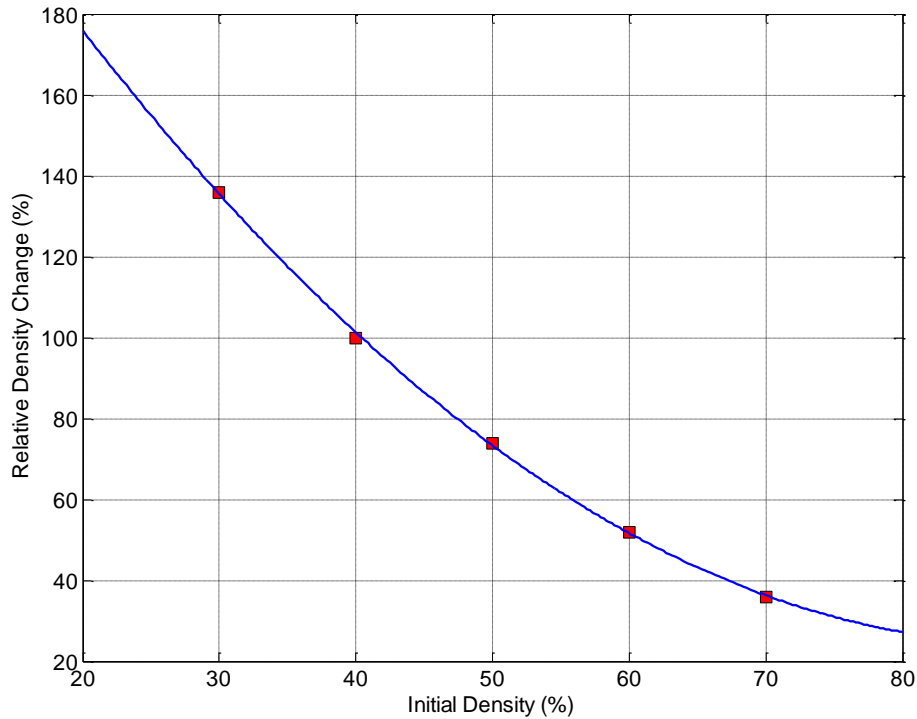


Figure 5-10: Relative density variation vs. initial apparent density of powder (calculated for  $\mu_p=0.5$ ,  $\mu_s=0.3$ ,  $h_s=130 \mu\text{m}$  (0.005 in),  $R=10 \text{ mm}$ , and  $\alpha_m=0.2 \text{ Rad}$ ).

The results of this study are useful in estimating the porosity of the SFF-made CPP structures based on the material properties and SFF process parameters. In addition, the results aid the SFF machine operator to adjust the parameters in a way that gives the desired outputs. For the cases in which the relative density attains close to the value of one, as seen in Figure 5-5 and Figure 5-6, the powder is compacted completely and converted to a solid bulk without any porosity. For bone substitutes, the existence of voids and a specific range of porosity are required for cell proliferation and new tissue formation. Consequently, those cases with the RD close to one are not appropriate for such an application.

In addition, (5-16), (5-19) and (5-20) can be solved for the inverse problem. Therefore, to fabricate a construct from a biomaterial such as CPP with a porosity of  $n\%$ , the requisite layer thickness, roller rotational and linear velocities, and powder condition (initial apparent density and particle size) can be chosen based on either of the graphs or solving the reverse problem. It is noteworthy that the minimum and maximum values for the layer thickness and rolling velocity are restricted for the SFF process. In case of CPP, this model can identify the density of green parts if the constitutive model is modified for CPP+PVA powder and the appropriate

process parameters are used. It is evident that the final density of the sintered CPP scaffold has a correlation with the green part's density. Therefore, by establishing a look up table, one can estimate the final density of the CPP implants.

During the experimental studies of this thesis, difference between relative density of green parts fabricated at different SFF layer thicknesses (i.e., 200 to 100  $\mu\text{m}$ ) was observed such that the parts fabricated with higher layer thickness exhibited lower compact density. This observation can be supported by the data shown in Figure 5-8. However, further analysis and parameters identification are required to validate and quantitate such observations. To this end, the physical parameters such as coefficients of frictions (corresponding to the linear and rotational speeds) and powder initial density must be experimentally determined.

In order to evaluate the results from the mathematical modeling, an experimental set-up is proposed as presented in Appendix D. The experimental setup is designed to measure (1) the normal pressure on the roller surface, during its contact with the powder, and (2) the density of the compacted powder.

## **5.4 Summary**

In this chapter, a 1D mathematical model for the powder compaction, which involves a counter-rotating roller for the powder layer preparation (including powder spreading and compaction) in the powder-based SFF method, was conducted. A constitutive model, suitable for powder compaction, was used to describe the behaviour of the material. The kinematical characteristics of the process, together with the porosity distribution in the powder bed along the densification zone were investigated. It was demonstrated how the roller-powder contact conditions, layer thickness, and the initial apparent density of the powder affect the density of the compacted powder layer, which directly yield to the properties of the SFF prototyped structures. The results of this simulation can be used for properly adjusting the parameters of the SFF process to attain a pre-determined porosity in the bone substitutes and osteochondral implants made from CPP or other biomaterials. Furthermore, a test-rig was proposed (Appendix D) for data collection and model verification.

# Chapter 6

## Conclusion and Future Work

### 6.1 Conclusive Summary

The following conclusion can be drawn from this thesis:

1. An adhesive-bonding powder-based SFF technique was successfully developed for fabrication of porous CPP constructs. It was shown that it is feasible to produce porous CPP structures by a powder-based SFF technique. The accuracy and resolution of the SFF-made parts was measured about  $\pm 150 \mu\text{m}$ .
2. PVA was used as polymeric binder in the SFF technique to create strong bonding between CPP particles in green parts. A successful binder removal procedure was developed. It was demonstrated that PVA had no effect on crystallinity of the sintered CPP samples. Also no sign of PVA residuals was detected. .
3. A two-step sintering was conducted to obtain a target density of 65% in CPP structures. The sintering heat treatment conditions can be modified to achieve various densities.
4. 65% porous CPP structures made by the SFF technique included pores in the range of 0-140  $\mu\text{m}$  and trabecular thickness in the range of 20-160  $\mu\text{m}$ . The pore size is in the desired range of required pore size for new bone formation. It was shown that pores of SFF-made structures are larger than those of the conventionally-made CPP parts (on average 56  $\mu\text{m}$  vs. 38  $\mu\text{m}$ ).
5. Using the porosimetry data, specific surface area and permeability of the SFF-made structures were determined to be  $24 \text{ mm}^2/\text{mm}^3$  and  $2.2 \times 10^{-12} \text{ m}^2$ , respectively. These values

suggest that the requirements for cell infiltration into and accommodation within the SFF-made CPP implants are met. The smaller pore size of the CS structures resulted in the higher specific surface area ( $31 \text{ mm}^2/\text{mm}^3$ ) but the lower permeability ( $1.0 \times 10^{-12} \text{ m}^2$ ).

6. The compressive mechanical strength of the porous SFF-made CPP structures was measured equal to  $\sim 50$  MPa. It was shown that the developed technique can produce CPP structures with about 150% higher compressive mechanical strength compared to the conventional sintering. It may be attributed to the larger trabecular thickness formed in the SFF-made structures ( $84 \mu\text{m}$  vs.  $64 \mu\text{m}$ ).
7. Orientation of stacked-layers was shown to have a great influence on mechanical strengths of the SFF-made layers. The compressive mechanical strength is about 50% higher in the direction parallel to the stacked-layers. It can be ascribed to the stronger sinter necks in that direction as formed with higher rate of shrinkage compared to the direction normal to the stacked-layers. This special phenomenon may occur due to a preferred orientation and configuration of the CPP particles in the green parts. Using plate-like shaped CPP particles with the length larger than the adjusted SFF layer thickness caused such a configuration.
8. Implantation of 30% porous CPP structures in the medial distal femur of New Zealand white rabbits resulted in about 35% new bone ingrowth in the pores with a an incredible osseointegration after 6 weeks. 8% of CPP construct degraded during that time. The results demonstrate that the SFF-made CPP constructs are suitable candidates as bone graft substitutes for bone tissue regeneration. No significant difference in the bone growth was observed within the SFF-made and CS implants. Also, bone ingrowth was similar from the anterior, posterior, distal and proximal aspects of the implantation site.
9. Successful culture of cartilage tissue on the top surface of the SFF-made CPP substrates (35% porosity) demonstrated their suitability for construction of biphasic (cartilage+CPP) implants for osteochondral tissue engineering. Biocompatibility and immune response studies have suggested that the SFF-made samples did not have a toxic effect on cartilage cells as the DNA, GAG/DNA, and OH-proline/DNA content of the 3-week old tissue did not differ significantly for SFF-made samples compared to conventionally-made constructs.

10. The potential of the developed SFF technique to produce anatomically-shaped CPP implants using the CT scans of the patient's defect site was demonstrated. In addition, CPP constructs with heterogeneous micro-structure (dual-porous) or with internal channels were successfully fabricated. Moreover, macro-pores with the one order of magnitude larger size (compared to the initial pores of CPP sintered parts) were selectively introduced into the SFF-made CPP constructs by coupling the SFF technique with porogen leaching method.
  
11. An analytical mathematical modeling was proposed to estimate the compact density of the powder bed spread in the building chamber of the SFF technique (which can be considered as the density of the SFF-made green parts). The model predicts how the compact density varies upon the change of the parameters involved in the counter-rotating roller powder spreading process. It was shown that the SFF layer thickness has a significant effect on the density of the green parts which, in turn, may influence the final density/porosity of the sintered parts. The functional physical parameters corresponding to the counter-rotating roller spreading the CPP powder need to be measured to be able to effectively estimate the density of the SFF-made CPP green parts.

In summary, results obtained during the course of this Ph.D. thesis substantiate that the developed SFF technique is able to produce CPP porous structures with the characteristics required for a desired bioresorbable bone graft substitute which promote bone regeneration in the defect site while it resorbs into the patient's body. In addition, it is proposed that the SFF-made CPP constructs have the potential to be used in orthopaedics and osteochondral tissue engineering as the bone component of a biphasic implant.

## **6.2 Recommendations and Future Work**

The outcomes of this study have opened new opportunities that may be explored through the following recommendations:

1. **Developed SFF technique:**
  - a. The flowability of powder has an important impact on the powder spreading during the SFF process which, in turn, influences the final outcome of the developed SFF technique.

For instance, for fine dry powders the Van der Waals force leads to a decrease of the flowability. Although the CPP powder with the mesh size and particle shape used in this study did not face any troublesome issue related to spreading, the flowability could be improved through modification of particle-particle force regulation by different available techniques such as plasma treatment. In addition coating CPP particles with a thin layer of PVA may enhance the flowability as well as the green strength of the parts.

- b. The level of accuracy and resolution of the developed technique may be improved if a finer powder is utilized. Also, since the printhead resolution is not fine enough, it is recommended that an advanced piezo-based printhead be used to achieve a high resolution required for the process with fine powders.
- c. Although it has not been documented, the temperature of the part drying process after printing (solvent injection) stage of the SFF procedure has an effect on the size of green parts. Thus, it is recommended to use consistent temperature in order to obtain a reasonable reproducibility.
- d. The fabrication of large CPP constructs by the developed SFF technique may be challenging although it did not appear to be the case for the feature-sizes of the current study. For instance, the sintering shrinkages may differ for small sizes compared to large ones. This issue may introduce geometrical problems for anatomically-shaped constructs i.e., anisotropic deviations from the CAD model. This problem will be critical for defects in articular locations with substantial curvature (for which the tissue engineered constructs should also have appropriate topography). Commercialized methods of 3D scanning with colorimetric feedback on the local geometrical deviations from the desired CAD model could be a reliable solution for determination of anisotropic compensation factors.
- e. The developed SFF technique has the potential to form biomedical devices, implants and tissue engineering scaffolds using a wide range of biomaterial such as hydroxyapatite, tricalcium phosphate, magnesium, titanium and etc. Some modification may be required for any individual material.

## **2. Structural and mechanical characterization of SFF-made CPP structures/implants:**

- a. In order to expand the characterization of the mechanical properties of the SFF-made CPP structures, a four-point bend test is suggested. Also, high frequency ultrasound impedance measurements can be utilized to predict the anisotropic mechanical properties of the CPP samples including tensile and shear modulus.
- b. It is also recommended to measure the fracture toughness of the CPP structures which may reveal more evidence about the difference of mechanical strength from SFF-made to CS samples as well as the effect of stacked-layer orientations.
- c. As shown in this study, the orientation of the stacked-layers has a notable influence on the mechanical compressive strength of the CPP structures. It is proposed that the mechanical resistance of complex-shaped large CPP bone substitutes can be improved by fabricating them in a way that the stacked-layers are aligned, as much as possible, with the direction of maximum principal stresses in the defect site.
- d. The mechanical properties of CPP implants may also be enhanced by formation of structures with the trabecular orientation along the principal stress trajectories. This may be achieved by using porogens with proper size and shape in the SFF-porogen leaching technique. This is suggested by the feasibility study reported in the current thesis.

## **3. In vivo animal model studies:**

- a. High resolution micro-CT scans (as a non-destructive method) will allow local quantitative analysis of bone-implant structures. The technique can be utilized to monitor the new tissue ingrowth process during the implantation period prior to animal sacrifice. Monitoring of the mineralization process will also be feasible using this method.
- b. In order to increase the precision of the bone ingrowth investigation through the BSE images of sectioned bone-implant sites, more sections per implant are required due to non-homogenous distribution of the pores and the mineralized bone.

- c. In order to investigate any possible difference between the dynamics of cell infiltration into the SFF-made structures with different orientation of the stacked-layers, fluorescent cell tracking dyes can be utilized in in vivo studies.

**4. Control over the internal architecture of SFF-made CPP implants:**

- a. The fabrication of straight internal channels was investigated in the current study. However, curved channels might be required for large implants in order to enhance bone regeneration and in-growth of blood vessels. Formation of long curved channels within the CPP structures is not feasible by the developed SFF technique since loose powder becomes trapped in the channels and is not easy to remove. Thus, the SFF technique should be enhanced with other methods such as embedding sacrificial materials such as polymers and hydrogels.
- b. Fabrication of dual-porous CPP structures through sequential use of two different powder sizes (i.e., changing the composition in z direction) was explored in the current study. However, ability to form designed heterogeneous constructs with a control over the layout of each layer (changing the composition in xy plan) have not been achieved in the three dimensional printing field. A possible solution can be the injection of the slurry of other materials or a different powder size on the targeted areas of each powder layer. This technique needs an extensive future study. Also, a step into the direction of solving that issue lies in realizing functionally-graded materials with local variations of material composition.

**5. Design of CPP implants with desired characteristics:**

- a. Coupling the image-based design techniques and the developed SFF technique enables the formation of CPP bone repair implants with hierarchical features (such as different level of pore size) and appropriate structural and mechanical properties and biological response [152]. This approach can also be used for controlling the degradation rate of porous CPP bone substitutes.
- b. An optimal resorption rate is difficult to determine as it is dependent on the animal model into which it is implanted. Longer resorption periods may be necessary for larger animals due to a slower repair process. Thus, it is recommended to investigate the relation between the micro-structure of the CPP structures and the resorption rate.



Consequently, this property of the implants can be controlled by a proper design before the fabrication stage.

**6. In vivo performance of SFF-made CPP implants:**

- a. Based on the reported outcomes of the other studies in the field, it seems that higher porosity (>50%) is preferred for tissue regeneration. It is suggested to make structures with higher porosity and investigate their mechanical and biological responses.
- b. Characterization of surface micro-topography of the SFF-made CPP structures can be conducted in order to enhance the mechanical interdigitation of the implant and new bone.
- c. The bone growth within the CPP implants with internal channels should be assessed in vivo. The comparison of the outcomes with the results of the current study reveals the effect of forming channels into the CPP implants.
- d. The CPP matrix can be drug loaded and the release kinetics can be tailored with the degradation rate of CPP. This can be feasible by making some geometrical features such as small depots in the CPP constructs and impregnating that in a liquid containing drug before implantation. Also, the presence of protein growth factors in the implant might stimulate differentiation and metabolism of the cells [263].
- e. On the biological level, novel approaches, termed intrinsic vascularisation, use vascular induction from the core of the scaffold to the periphery due to bioactive matrix and vessel driven angiogenesis. This goal can be achieved using inorganic (copper II) and organic angiogenic factors (e.g. vascular endothelial growth factor VEGF) specifically deposited at the end of a closed pore [196, 264].

**7. Mathematical modeling of powder spreading and compaction in SFF process:**

- a. Experimental evaluation of the proposed mathematical model for estimation of the compact density of spread powder layers is required. For that purpose, an experimental set-up is proposed (as presented in Appendix D) which is aimed to measure the roller-powder contact pressure and the relative density of compacted powder.

- b. The constitutive model of powder rolling used in this study should be modified for any specific powder (such as CPP) using the results of primary experimental analysis. Also, the physical parameters such as the coefficients of friction should be determined experimentally.

# Appendices

## Appendix A

### Material Properties of Polyvinyl Alcohol and Zb<sup>TM</sup>58 Solvent

- Polyvinyl Alcohol

Polyvinyl alcohol (PVA) is a water-soluble synthetic polymer which is prepared by partial or complete hydrolysis of polyvinyl acetate to remove acetate groups.

Table A- 1: Material properties of PVA

Thermal Properties	
Conductivity	0.08 (W/m ° K) [260]
Heat capacity	4.39614×T (J/kg ° K) [261]
Density	1350 (kg/m <sup>3</sup> ) [261]
Bulk density	300 (kg/m <sup>3</sup> )
Glass transition	85 ° C [261]
Decomposition	250 ° C [261]

- Aqueous Solvent Zb<sup>TM</sup>58

Table A- 2: Constituent materials of Zb<sup>TM</sup>58 solvent [262]

Ingredient	Percent	Material /Trade Name
Water	80-86%	Distilled
Humectant	6%	Glycerol
Flow rate enhancer + Solubility accelerator	8%	PVP + potassium sulfate + isopropyl alcohol + ethyl butyrate

## Appendix B

### Physical Characterization

#### B-1. Permeability Calculation Procedure

To calculate the permeability (hydraulic conductivity) of the porous CPP structures, a model proposed by Katz et al. [212, 213] was used in which the absolute permeability  $k$  is expressed in term of electrical conductivity and a characteristic length  $l_c$  as:

$$k = \frac{1}{226} \cdot l_c^2 \cdot \frac{\sigma}{\sigma_0}$$

where  $\sigma_0$  is the conductivity in the saturated condition.

$$\frac{\sigma}{\sigma_0} = \frac{l_{\max}^e}{l_c} \cdot \Theta \cdot S(l_{\max}^e)$$

where  $\Theta$  is porosity,  $l_{\max}^e$  is a length defined in terms of mercury intrusion curve as is described below, and  $S(l_{\max}^e)$  is the fractional volume of connected pore space involving pore size of  $l_{\max}^e$  and larger.

The characteristic length  $l_c$  is determined using the following relation:

$$l_c = 4 \cdot \gamma \cdot \cos\left(\frac{\theta}{P_t}\right)$$

where  $\gamma$  is surface tension,  $\theta$  is contact angle of mercury, and  $P_t$  is threshold pressure.

To determine  $l_{\max}^e$ , the amount of mercury that intrudes the sample prior to reaching the threshold pressure is subtracted from the total mercury volume and the ordinate of the intrusion curve is set equal to zero at the threshold pressure (Figure B-1-b for SFF-made sample and Figure B-2-b for CS sample). Then the ordinate of the figures is multiplied by a factor of  $l$  (pore diameter) as presented in Figure B-1-c for SFF-made sample and Figure B-2-c for CS sample. The maximum of the curves determines  $l_{\max}^e$  as well as the corresponding values of  $S(l_{\max}^e)$ . The detail of rational behind this method is available in other study [212, 213].

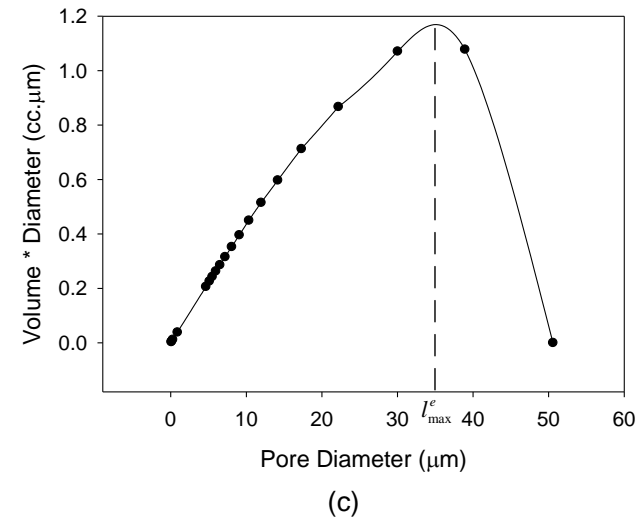
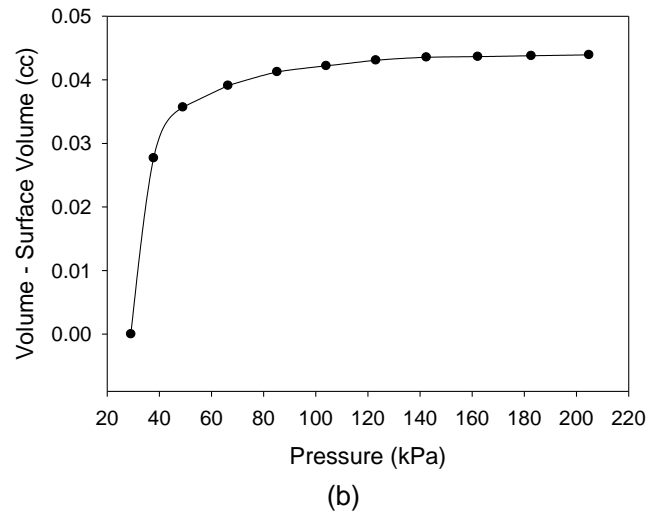
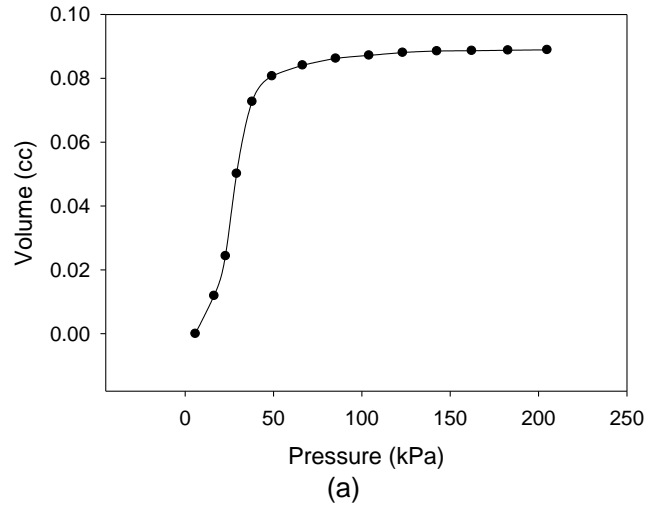
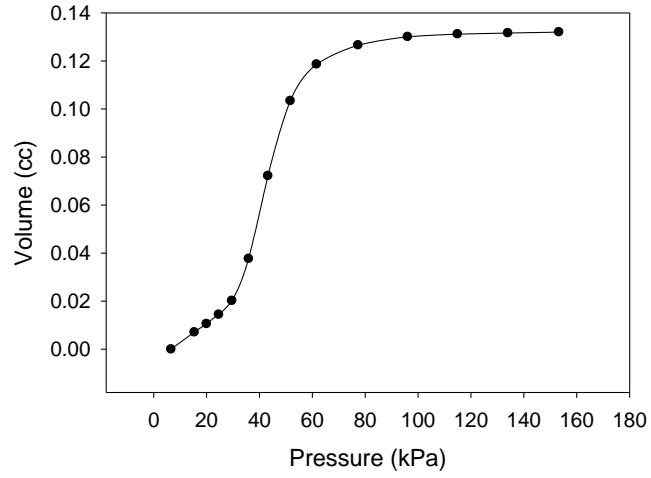
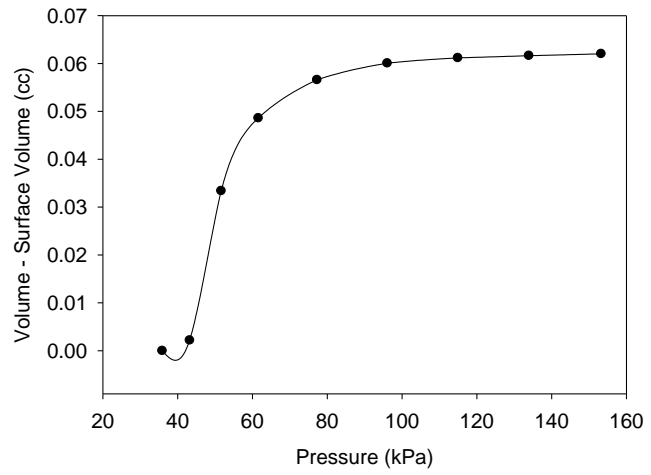


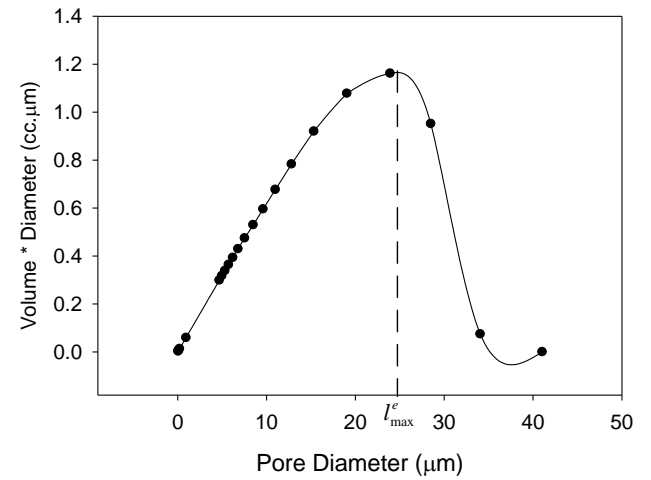
Figure B-1: The process of determining  $l_{\max}^e$  for SFF-made CPP structure.



(a)



(b)



(c)

Figure B-2: The process of determining  $l_{max}^e$  for CS CPP structure.

## B-2. Fracture Criteria for SFF-H and CS CPP Discs

The fracture failure iso-surface of SFF-V discs were presented in Chapter 3. Here the failure criteria for SFF-H and CS CPP discs are presented.

*SFF – H :*

$$\sigma_z = \tau_{yz} = \tau_{zx} = 0$$

$$\frac{\sigma_x^2 - \sigma_x \sigma_y}{F_{cx} F_{tx}} + \frac{\sigma_y^2}{F_{cx} F_{tx}} + \frac{F_{cx} - F_{tx}}{F_{cx} F_{tx}} \sigma_x + \frac{F_{cy} - F_{ty}}{F_{cy} F_{ty}} \sigma_y + \frac{\tau_{xy}^2}{F_{sxy}^2} = 1$$

( $F_{sxy}$  was estimated equal to  $\frac{F_c}{2}$ )

*CS :*

$$\sigma_z = \tau_{yz} = \tau_{zx} = 0$$

$$F_{cx} = F_{cy} = F_c$$

$$F_{tx} = F_{ty} = F_t$$

$$\frac{\sigma_x^2}{F_c F_t} + \frac{\sigma_y^2}{F_c F_t} - \frac{\sigma_x \sigma_y}{F_c F_t} + \frac{F_c - F_t}{F_c F_t} (\sigma_x + \sigma_y) + \frac{\tau_{xy}^2}{F_{sxy}^2} = 1$$

( $F_{sxy}$  was estimated equal to  $\frac{F_c}{2}$ )



## Appendix C

### In Vivo Analysis Data

#### C-1. Implantation Planning

Table C-1: Insertion table of CPP implants

Rabbit Number	Left Leg	Density	Right Leg	Density
1	CS12	69.4	SFF-V4	71.6
2	CS9	69.4	SFF-H10	69.6
3	SFF-H8	69.6	CS1	69.4
4	CS3	69.4	SFF-V3	71.6
5	SFF-V14	71.6	SFF-H4	69.6
6	SFF-H9	69.6	SFF-V11	71.6
7	SFF-H7	69.6	CS2	69.4
8	CS6	69.4	SFF-H12	69.6
9	CS10	69.4	SFF-V2	71.6
10	SFF-V6	71.6	SFF-H3	69.6
11	CS5	69.4	SFF-V5	71.6
12	SFF-H2	69.6	SFF-V10	71.6

Table C-2: Number of samples which were analyzed through image processing

	ANT	POST	DIST	PROX
SFF-V	6	6	6	2
SFF-H	7	5	7	7
CS	7	7	6	5

## C-2. In Vivo Samples Image Processing Data

Table C-3: Results of image processing of BSE images of implanted CPP plugs

SFF-V							
ANT	Rab Num	Leg	Bone%	BoneInVoid%	CPP%	Void%	Degradation
	RAB1	R	13.07	35.55	63.24	23.69	9.08
	RAB4	R	13.42	39.40	65.93	20.65	6.39
	RAB5	L	13.97	37.92	63.14	22.88	9.18
	RAB6	R	18.50	37.37	50.49	31.01	21.83
	RAB9	R	16.02	41.67	61.56	22.42	10.76
	RAB10	L	17.18	42.13	59.22	23.60	13.10
	Ave:		15.36	39.01	60.60	24.04	11.72
	STDev:		2.22	2.56	5.42	3.59	5.42
POST	Rab. Num.	Leg	Bone%	BoneInVoid%	CPP%	Void%	Degradation
	RAB1	R	9.21	26.19	64.84	25.95	7.48
	RAB4	R	13.69	33.72	59.39	26.92	12.93
	RAB5	L	14.03	37.54	62.63	23.34	9.69
	RAB6	R	11.83	32.23	63.30	24.87	9.02
	RAB9	R	13.33	33.28	59.95	26.72	12.37
	RAB10	L	15.18	38.72	60.81	24.02	11.51
	Ave:		12.88	33.61	61.82	25.30	10.50
	STDev:		2.10	4.44	2.12	1.46	2.12
DIST	Rab. Num.	Leg	Bone%	BoneInVoid%	CPP%	Void%	Degradation
	RAB1	R	13.64	32.18	57.62	28.74	14.70
	RAB4	R	10.86	37.35	70.94	18.21	1.38
	RAB5	L	15.60	34.29	71.31	29.88	1.01
	RAB6	R	14.69	42.16	65.15	20.16	7.17
	RAB9	R	13.96	34.24	59.22	26.82	13.10
	RAB10	L	14.76	35.77	58.73	26.51	13.59
	Ave:		13.92	36.00	63.83	25.05	8.49
	STDev:		1.65	3.48	6.23	4.75	6.23
PROX	Rab. Num.	Leg	Bone%	BoneInVoid%	CPP%	Void%	Degradation
	RAB1	R	-	-	-	-	-
	RAB4	R	11.22	32.34	65.30	23.48	7.02
	RAB5	L	9.72	30.54	68.16	22.12	4.16
	RAB6	R	-	-	-	-	-
	RAB9	R	-	-	-	-	-
	RAB10	L	-	-	-	-	-
	Ave:		10.47	31.44	66.73	22.80	5.59
	STDev:		1.06	1.27	2.02	0.96	2.02

SFF-H							
ANT	Rab. Num.	Leg	Bone%	BoneInVoid%	CPP%	Void%	Degradation%
	RAB2	R	18.25	41.62	56.16	25.59	12.95
	RAB3	L	11.25	32.63	65.51	23.24	3.60
	RAB5	R	9.37	31.63	70.38	20.25	-1.27
	RAB6	L	17.27	32.86	47.45	35.28	21.66
	RAB7	L	12.32	36.99	66.69	20.98	2.42
	RAB8	R	16.44	35.68	53.94	29.63	15.17
	RAB10	R	13.29	36.46	63.54	23.17	5.57
	Ave:		14.03	35.41	60.52	25.45	9.09
	STDev:		3.34	3.43	8.19	5.34	8.85
POST	Rab. Num.	Leg	Bone%	BoneInVoid%	CPP%	Void%	Degradation%
	RAB2	R	12.56	37.43	66.44	21.00	2.67
	RAB3	L	14.57	37.44	61.07	24.36	8.04
	RAB5	R	-	-	-	-	-
	RAB6	L	13.14	30.14	56.40	30.46	12.71
	RAB7	L	-	-	-	-	-
	RAB8	R	10.09	28.73	64.87	25.04	4.24
	RAB10	R	12.59	34.17	63.15	24.26	5.96
	Ave:		12.59	33.58	62.39	25.02	6.92
	STDev:		1.62	4.04	3.90	3.42	4.47
DIST	Rab. Num.	Leg	Bone%	BoneInVoid%	CPP%	Void%	Degradation%
	RAB2	R	15.16	34.01	55.44	29.40	13.67
	RAB3	L	10.13	27.04	62.54	27.33	6.57
	RAB5	R	9.95	27.50	63.81	26.24	5.30
	RAB6	L	15.92	34.86	54.33	29.75	14.78
	RAB7	L	21.65	47.29	54.22	24.13	14.89
	RAB8	R	10.24	26.11	60.79	28.97	8.32
	RAB10	R	7.23	26.75	72.99	19.78	-3.88
	Ave:		12.89	31.94	60.59	26.51	10.59
	STDev:		4.94	7.67	6.76	3.57	4.35
PROX	Rab. Num.	Leg	Bone%	BoneInVoid%	CPP%	Void%	Degradation%
	RAB2	R	10.39	29.49	64.76	24.85	4.35
	RAB3	L	13.02	31.36	58.49	28.49	10.62
	RAB5	R	6.48	19.98	67.59	25.94	1.52
	RAB6	L	13.06	40.66	67.88	19.06	1.23
	RAB7	L	25.91	41.33	70.64	36.78	-1.53
	RAB8	R	14.74	32.20	54.23	31.03	14.88
	RAB10	R	10.28	33.48	69.29	20.43	-0.18
	Ave:		13.41	32.65	64.70	26.65	5.18
	STDev:		6.13	7.22	6.10	6.13	6.30

CS							
ANT	Rab. Num.	Leg	Bone%	BoneInVoid%	CPP%	Void%	Degradation%
	RAB1	L	15.44	40.47	61.86	22.70	8.17
	RAB2	L	12.39	34.24	63.83	23.79	6.20
	RAB3	R	15.62	38.02	58.93	25.45	11.10
	RAB4	L	15.61	38.80	59.75	24.63	10.28
	RAB7	R	9.81	23.53	58.32	31.88	11.71
	RAB8	L	14.57	36.59	60.18	25.25	9.85
	RAB9	L	15.29	40.29	62.06	22.65	7.97
	Ave:		14.10	35.99	60.70	25.19	9.55
	STDev:		2.21	5.91	1.96	3.15	2.04
POST	Rab. Num.	Leg	Bone%	BoneInVoid%	CPP%	Void%	Degradation%
	RAB1	L	11.66	35.62	67.26	21.08	2.77
	RAB2	L	9.57	26.31	63.62	26.81	6.41
	RAB3	R	11.05	31.71	65.15	23.80	4.88
	RAB4	L	15.21	68.03	62.59	22.20	7.44
	RAB7	R	13.36	36.21	63.10	23.54	6.93
	RAB8	L	10.93	30.01	63.59	25.48	6.44
	RAB9	L	10.48	34.34	69.48	20.04	0.55
	Ave:		11.75	37.46	64.97	23.28	5.81
	STDev:		1.92	13.92	2.53	2.38	1.72
DIST	Rab. Num.	Leg	Bone%	BoneInVoid%	CPP%	Void%	Degradation%
	RAB1	L	14.45	39.98	63.86	21.69	6.17
	RAB2	L	4.85	13.66	64.47	30.67	5.56
	RAB3	R	11.39	31.31	63.61	25.00	6.42
	RAB4	L	12.50	36.03	65.31	22.19	4.72
	RAB7	R	-	-	-	-	-
	RAB8	L	15.06	42.92	64.91	20.03	5.12
	RAB9	L	8.91	32.31	72.41	18.68	-2.38
	Ave:		11.20	32.70	65.76	23.04	5.60
	STDev:		3.81	10.32	3.32	4.31	0.71
PROX	Rab. Num.	Leg	Bone%	BoneInVoid%	CPP%	Void%	Degradation%
	RAB1	L	-	-	-	-	-
	RAB2	L	17.83	45.66	60.96	21.22	9.07
	RAB3	R	12.06	33.22	63.69	24.25	6.34
	RAB4	L	15.91	38.51	58.68	25.41	11.35
	RAB7	R	-	-	-	-	-
	RAB8	L	16.50	42.30	61.00	22.51	9.03
	RAB9	L	12.49	37.20	66.43	21.08	3.60
	Ave:		14.96	39.38	62.15	22.89	8.95
	STDev:		2.55	4.78	2.98	1.90	2.05

### C-3. MATLAB Code for Processing of BSE Images

```
clear all, clc, close all
I = imread ( RAB6-R-POST-m-1.tif );
I(end-1:end, 1:end)=0;
% take the subset of the image
Isub1=I;
figure, imshow (Isub1);
[X,Y]=size(Isub1)

% convert to dataset format for PRTools
Isub1Set = dataset(double(Isub1(:)));
% clustering using EM approach; nmc/qdc
[lab,w] = emclust(Isub1Set,nmc,3);
% convert labels to an image corresponding to clustered image
lab1 = reshape(lab,X,Y);

% check whether the label assigned to the last row and first column is 1; if
% so it is ok, otherwise, assign label 1 to all pixels with the labels corresponding to it.
if (lab1(end,1) == 1)
    lab(find(lab == 1)) = 4;
    lab(find(lab == lab1(end,1))) = 1;
    lab(find(lab == 4)) = lab1(end,1);
end
if size(find(lab == 3),1) < size(find(lab == 2),1)
    lab(find(lab == 3)) = 4;
    lab(find(lab == 2)) = 3;
    lab(find(lab == 4)) = 2;
end

% reshape result of clustering into an image and display
figure,imshow(reshape(lab,X,Y)*50,[])
segmentedImage=reshape(lab,X,Y)*50;
segmentedImageU = uint8(segmentedImage);
imwrite(segmentedImageU, RAB6-R-POST-SEG-1.tif );

% find the number of pixels in a specific cluster
```

```
BG=size(find(lab==1))
Bone=size(find(lab==2))
CPP=size(find(lab==3))
BonePercent = Bone/(BG+Bone+CPP)*100
```

```
Totalimage (1, 1:4)=0;
Totalimage (end+1,1)=BG(1,1);
Totalimage (end, 2)=Bone(1,1);
Totalimage (end, 3)=CPP(1,1);
Totalimage (end, 4)=X;
Totalimage (end, 5)=Y
```

## Appendix D

### Mathematical Modeling of Powder Compaction

#### D-1. MATLAB Code

```
clear
alphaStart=0.2; % Radian
InitPor=0.70; % initial porosity of bulk powder
YieldStress=200;
hs=25.4*0.005; %mm - rolling gap
D=10; % radius of roller
Mur=0.3; % coefficient of friction between roller and powder
Mup=0.5; % coefficient of friction between loose and compacted powder layers
gammaN=0.0;

counter=50;
y=zeros(counter,1); % longitudinal stress
y(1)=0;
SSx=0;
PPx=zeros(counter,1); % contact pressure
alpha=zeros(counter,1);
alpha(1)=alphaStart;
Roh=zeros(counter,1);
Roh(1)=(1-InitPor); % Roh is relative density = bulk density/material density

delta=alphaStart/counter
for i = 1:counter
    Por=1-Roh(i)
    K1=(2/3*(1-Por)^2*(InitPor-Por)/(Por*InitPor))+0.00001
    K2=((1-Por)*(InitPor-Por)/InitPor)+0.00001
    AA=2/3*(K1+1/6*K2)*(1-Por)
    BB=1/3*K2*(1-Por)
    A=sqrt(AA);
    B=sqrt(BB);
    MuAlpha=Mur
```

```

PPx(i)=((AA-BB)/(AA+BB)*SSx)+(2*A*B/(AA+BB)*sqrt(AA+BB-SSx^2));
y(i+1)=y(i)+(-1*delta)*(PPx(i)/(hs/D+1-cos(alpha(i))))*(sin(alpha(i))+MuAlpha*cos(alpha(i))-
Mup*(cos(alpha(i))-MuAlpha*sin(alpha(i))))
SSx=y(i+1);

alpha(i+1)=alpha(i)-delta;
Alpha=alpha(i)

Px=PPx(i)*YieldStress
Sx=SSx*YieldStress

Roh(i+1)=Roh(i)+(-1*delta)*((-2*Roh(i)*sin(alpha(i)))/((hs/D+1-
cos(alpha(i)))*(1+(AA/BB)*((Px-Sx)/(Px+Sx)))));
RD=Roh(i+1)
end

PPx(i+1)=((AA-BB)/(AA+BB)*SSx)+(2*A*B/(AA+BB)*sqrt(AA+BB-SSx^2));
plot(alpha,y)
hold on
mesh1 = mesh([0.1:0.02:0.2], [0:0.2/50:0.2])

```



## D-2. Proposed Experimental Setup

In order to evaluate the results from the mathematical modeling, an experimental set-up is proposed. It is designed to measure (1) the normal pressure on the roller surface, during its contact with the powder, and (2) the density of the compacted powder.

To measure the contact pressure on the roller surface a very small and precise sensing mechanism should be utilized, since the scales of the roller and the roller-powder contact area are within a small range. Micro piezo-sensors may be a suitable candidate for this goal. However, according to the force equilibrium equation, in each powder slab in Figure 5-2, the contact pressure on the roller surface can be calculated, as long as the roller-powder coefficient of friction ( $\mu_r$ ) and the pressure under the powder bed ( $Q$ ) are available. The following equation shows the mathematical relationship for  $P_r$  and  $Q$ .

$$Q = P_r \cdot (\cos \alpha - \mu_r \cdot \sin \alpha)$$

The coefficient of friction between the roller surface and the powder are obtained through a simple sliding experiment, if it is assumed to be constant in the entire contact region.  $Q$  can also be measured by using simple load cells, which are located under the powder bed. The load cells are arranged with short distances, to have a desired resolution of  $\alpha$ . Thus, the contact pressure is calculated as a function of  $\alpha$ .

Despite the described method for measuring the contact pressure, a pressure load-cell, preferably a micro-piezoelectric one, on the roller surface must be considered to check the accuracy of the above mentioned method. In addition, the total contact pressure can be sensed on the roller supports by suitable load-cells. The signals of the load-cells are sent to a signal processing system through a brush system, embedded in the roller shaft.

The motion resistance, applied by the powder friction on the roller surface, is measured through gauging the changes in the driving motor's power. It may provide an estimation of the total friction force applied on the roller. The bulk density of the spread powder is measured as well, by weighing a certain volume of the compacted powder captured in a pre-placed reservoir.

Figure D-1: is a schematic of the experimental setup and the position of the load cells. The mechanism components, sensors, and their functions are listed in following table. It should also be mentioned that the constitutive model used in the mathematical modeling may need to be modified accordingly using the experimental results.

Table D-1: Components of powder compaction experimental setup.

Component	Description
1	Counter-rotating roller
2	Roller supports
3	Powder levering platform
Sensors	
LC1	Load cell located within the roller to measure the compression applied by the powder (micro-piezosensor )
LC2	Series of compression load-cells to measure the pressure under the powder bed
LC3	Load cells located on the supports of the roller
PM1	Electric power-meter to measure the resistance of the powder bed versus the roller movement

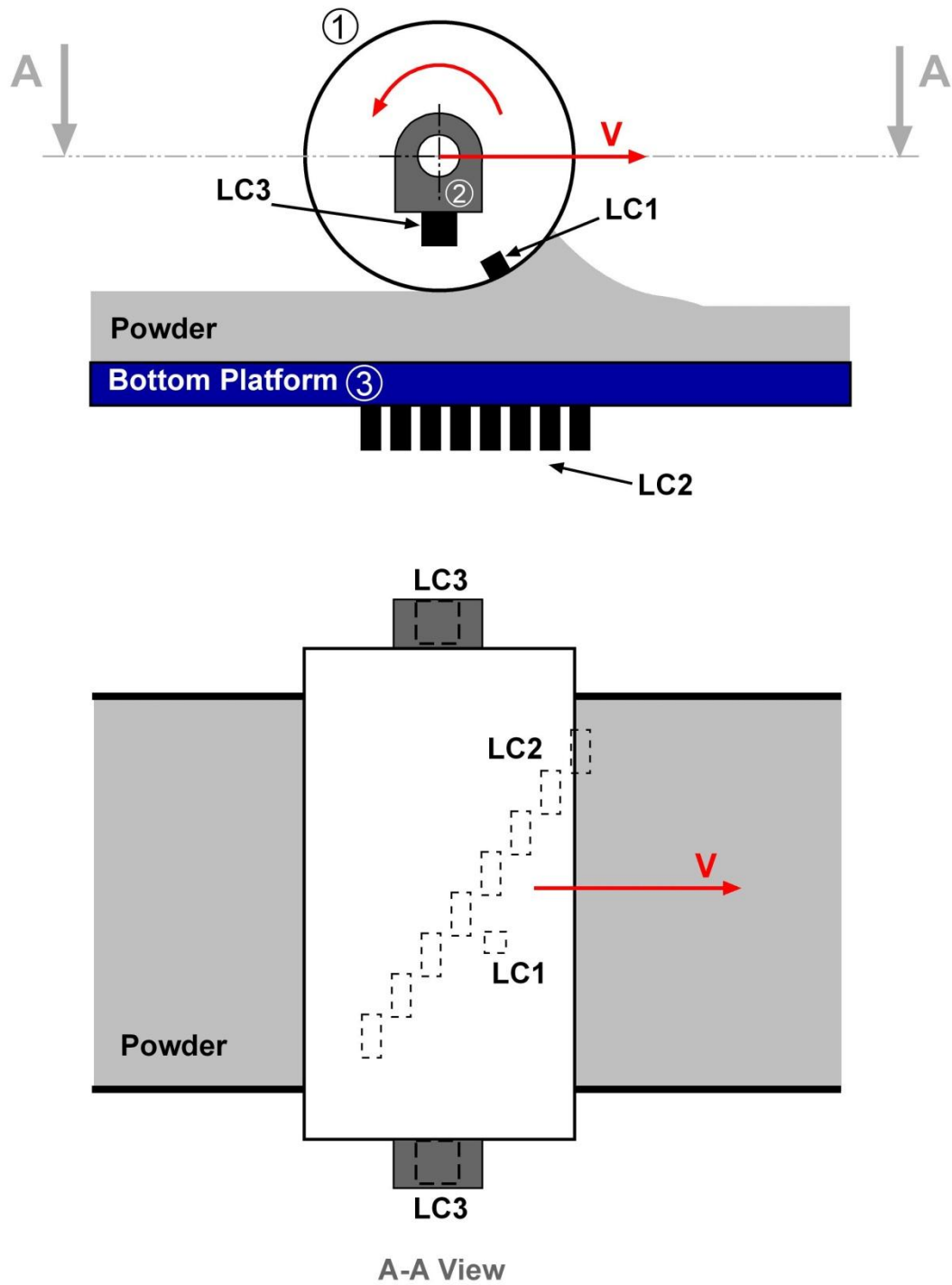


Figure D-1: Schematic of experimental setup for powder compaction analysis.

# References

- [1] NOF: National Osteoporosis Foundation. 2002 Report, "America's bone health: The state of osteoporosis and low bone mass," vol. 2011, June/15, 2002.
- [2] A. S. Mistry and A. G. Mikos, "Tissue engineering strategies for bone regeneration," *Adv Biochem Eng Biotechnol*, vol. 94, pp. 1-22, 2005.
- [3] A. S. Brydone, D. Meek and S. Maclaine, "Bone grafting, orthopedic biomaterials, and the clinical need for bone engineering," *Proceedings of the Institution of Mechanical Engineers, Part H: J Eng Med*, vol. 224, (12), pp. 1329-1343, 2010.
- [4] H. Eufinger, M. Wehmöller, E. Machtens, L. Heuser, A. Harders and D. Kruse, "Reconstruction of craniofacial bone defects with individual alloplastic implants based on CAD/CAM-manipulated CT-data," *J Craniomaxillofac Surg*, vol. 23, (3), pp. 175-181, 1995.
- [5] B. S. McAllister and K. Haghighat, "Bone augmentation techniques," *J Periodontology*, vol. 78, (3), pp. 377-396, 2007.
- [6] American Academy of Physical Medicine American, Academy of Orthopedic Surgeons, American Society for Bone Rehabilitation, American College of Rheumatology, National University of Health Sciences Orthopedic Research Society Scoliosis Research Society Mineral Research, Arthritis Foundation, the United States Bone, and Joint Decade., "Burden of Musculoskeletal Diseases in the United States: Prevalence, Societal and Economic Cost," 2008. Source: <http://www.boneandjointburden.org/>
- [7] R. C. Lawrence, D. T. Felson, C. G. Helmick, L. M. Arnold, H. Choi, R. A. Deyo, S. Gabriel, R. Hirsch, M. C. Hochberg, G. G. Hunder, J. M. Jordan, J. N. Katz, H. M. Kremers and F. Wolfe, "Estimates of the prevalence of arthritis and other rheumatic conditions in the United States. Part II." *Arthritis Rheum*, vol. 58, (1), pp. 26-35, 2008.
- [8] E. B. Hunziker, "Articular cartilage repair: are the intrinsic biological constraints undermining this process insuperable?" *Osteoarthr Cartilage*, vol. 7, pp. 15-28, 1999.
- [9] A. R. Poole, M. Kobayashi, T. Yasuda, S. Laverty, F. Mwale, T. Kojima, T. Sakai, C. Wahl, S. El-Maadawy, G. Webb, E. Tchetina and W. Wu, "Type II collagen degradation and its regulation in articular cartilage in osteoarthritis," *Ann Rheum Dis*, vol. 61, (2), pp. 78-81, 2002.
- [10] M. Keeney and A. Pandit, "The osteochondral junction and its repair via bi-phasic tissue engineering scaffolds," *Tissue Eng Part B*, vol. 15, (1), pp. 55-73, 2009.
- [11] T. W. Bauer and G. F. Muschler, "Bone graft materials. An overview of the basic science," *Clin Orthop Relat Res*, vol. 371, pp. 10-27, 2000.
- [12] J. E. Murray, "The first successful organ transplants in man," *J Am Coll Surg*, vol. 200, pp. 5-9, 2005.
- [13] J. Leon-Villapalos, M. Eldardiri and P. Dziewulski, "The use of human deceased donor skin allograft in burn care," *Cell Tissue Bank*, vol. 11, (1), pp. 99-104, 2010.

- [14] D. J. Biau, F. Thévenin, V. Dumaine, A. Babinet, B. Tomeno and P. Anract, "Ipsilateral femoral autograft reconstruction after resection of a pelvic tumor," *J Bone Joint Surg Am*, vol. 91, (1), pp. 142-151, 2009.
- [15] D. H. Kim, R. Rhim, L. Li, J. Martha, B. H. Swaim, R. J. Banco, L. G. Jenis and S. G. Tromanhauser, "Prospective study of iliac crest bone graft harvest site pain and morbidity," *Spine J.*, vol. 9, (11), pp. 886-892, 2009.
- [16] B. D. Browner, "What s new in orthopedic surgery," *J Am Coll Surg*, vol. 184, (2), pp. 169-176, 1997.
- [17] E. M. Younger and M. W. Chapman, "Morbidity at bone graft donor sites," *J Orthop Trauma*, vol. 3, pp. 192-195, 1989.
- [18] P. A. Gorer, J. F. Loutit and H. S. Micklem, "Proposed revisions of transplantese ," *Nature*, vol. 189, pp. 1024-1025, 1961.
- [19] A. Atavropoulos, "Deproteinized bovine bone xenograft," in *Musculoskeletal Tissue Regeneration: Biological Materials and Methods* ,1st ed.W. S. Pietrzak, Ed. Humana Press, 2008, pp. 119-152.
- [20] E. M. Erbe, J. G. Marx, T. D. Clineff and L. D. Bellincampi, "Potential of an ultraporous beta-tricalcium phosphate synthetic cancellous bone void filler and bone marrow aspirate composite graft," *Eur Spine J.*, vol. 10, (2), pp. S141-146, 2001.
- [21] D. K. Resnick, J. T. Alexander and W. C. Welch, "Resorbable technology for spinal stabilization," in *Advances in Spinal Stabilization* , vol. 16, R. W. Haid, B. R. Subach and G. E. Rodts, Eds. Karger, 2003, pp. 39-54.
- [22] I. Martin, S. Miot, A. Barbero, M. Jakob and D. Wendt, "Osteochondral tissue engineering," *J Biomech*, vol. 40, (4), pp. 750-765, 2007.
- [23] J. O. Hollinger, J. Brekke, E. Gruskin and D. Lee, "Role of bone substitutes," *Clin Orthop*, vol. 324, pp. 55-65, 1996.
- [24] C. J. Damien and J. R. Parsons, "Bone graft and bone graft substitutes: a review of current technology and applications," *J Appl Biomater*, vol. 25, (3), pp. 187-208, 1991.
- [25] H. S. Dobbs and J. L. M. Robertson, "Heat treatment of cast Co-Cr-Mo for orthopedic implant use," *J Mater Sci*, vol. 18, (2), pp. 391-401, 1983.
- [26] J. Beddoes and K. Bucci, "The influence of surface condition on the localized corrosion of 316L stainless steel orthopedic implants," *J Mater Sci Mater Med*, vol. 10, (7), pp. 389-394, 1999.
- [27] M. Long and H. J. Rack, "Titanium alloys in total joint replacement--a materials science perspective," *Biomaterials*, vol. 19, (18), pp. 1621-1639, 1998.
- [28] J. D. Bobyn, G. J. Stackpool, S. A. Hacking, M. Tanzer and J. J. Krygier, "Characteristics of bone ingrowth and interface mechanics of a new porous tantalum biomaterial," *J Bone Joint Surg Br*, vol. 81, (5), pp. 907-914, 1999.
- [29] J. J. Jacobs, J. L. Gilbert and R. M. Urba, "Current concepts review: Corrosion of metal orthopedic implants," *J Bone Joint Surg Am. Oct;():.*, vol. 80, (10), pp. 268-282, 1998.

- [30] E. F. DiCarlo and P. G. Bullough, "The biologic responses to orthopedic implants and their wear debris," *Clin Mater*, vol. 9, (3-4), pp. 235-260, 1992.
- [31] F. A. España, V. K. Balla, S. Bose and A. Bandyopadhyay, "Design and fabrication of CoCrMo alloy based novel structures for load bearing implants using laser engineered net shaping," *Mater Sci Eng: Part C*, vol. 30, pp. 50-57, 2010.
- [32] T. R. Rautray, R. Narayanana and K. H. Kim, "Ion implantation of titanium based biomaterials," *Prog. Mater Sci*, vol. 56, (8), pp. 1137-1177, 2011.
- [33] B. R. Levine, S. Sporer, R. A. Poggie, C. J. Della Valle and J. J. Jacobs, "Experimental and clinical performance of porous tantalum in orthopedic surgery," *Biomaterials*, vol. 27, pp. 4671-4681, 2006.
- [34] M. Navarro, A. Michiardi, O. Castaño and J. A. Planell, "Biomaterials in orthopedics," *J R Soc Interface*, vol. 5, (27), pp. 1137-1158, 2008.
- [35] A. Schuh, J. Luyten, R. Vidael, W. Hönle and T. Schmickal, "Porous titanium implant materials and their potential in orthopedic surgery," *Materialwissenschaft Und Werkstofftechnik*, vol. 38, (12), pp. 1015-1018, 2007.
- [36] T. Miyazaki, H. M. Kim, T. Kokubo, F. Miyaji, H. Kato and T. Nakamura, "Effect of thermal treatment on apatite-forming ability of NaOH-treated tantalum metal," *J Mater Sci Mater Med*, vol. 12, pp. 683-687, 2001.
- [37] J. D. Bobyn, R. A. Poggie, J. J. Krygier, D. G. Lewallen, A. D. Hanssen, R. J. Lewis, A. S. Unger, T. J. O Keefe, M. J. Christie, S. Nasser, J. E. Wood, S. D. Stulberg and M. Tanzer, "Clinical validation of a structural porous tantalum biomaterial for adult reconstruction," *J Bone Joint Surg Am*, vol. 86-A, (2), pp. 123-129, 2004.
- [38] B. D. Ratner, *Biomaterials Science: An Introduction to Materials in Medicine*. ,2nd ed. Academic Press, 2004, pp. 864-851.
- [39] K. Müller and E. Valentine-Thon, "Hypersensitivity to titanium: clinical and laboratory evidence," *Neuro Endocrinol Lett.*, vol. 27, (1), pp. 31-35, 2006.
- [40] M. Huber, G. Reinisch, G. Trettenhahn, K. Zweymüller and F. Lintner, "Presence of corrosion products and hypersensitivity-associated reactions in periprosthetic tissue after aseptic loosening of total hip replacements with metal bearing surfaces," *Acta Biomater*, vol. 5, (1), pp. 172-180, 2009.
- [41] C. Dandekar, Y. C. Shin and J. Barnes, "Machinability improvement of titanium alloy (Ti-6Al-4V) via LAM and hybrid machining," *Int J Mach Tools Manuf*, vol. 50, (2), pp. 174-182, 2010.
- [42] K. A. Athanasiou, C. M. Agrawal, F. A. Barber and S. S. Burkhart, "Orthopedic applications for PLA-PGA biodegradable polymers," *Arthroscopy*, vol. 14, (7), pp. 726-737, 1998.
- [43] R. C. Thomson, M. J. Yaszemski, J. M. Powers and A. G. Mikos, "Fabrication of biodegradable polymer scaffolds to engineer trabecular bone," *J Biomater Sci Polym Ed*, vol. 7, (1), pp. 23-38, 1995.

- [44] D. A. Shimko and E. A. Nauman, "Development and characterization of a porous poly(methyl methacrylate) scaffold with controllable modulus and permeability," *J Biomed Mater Res B Appl Biomater*, vol. 80, (2), pp. 360-369, 2007.
- [45] M. Spector, M. J. Michno, W. H. Smarook and G. T. Kwiatkowski, "A high-modulus polymer for porous orthopedic implants: biomechanical compatibility of porous implants," *J Biomed Mater Res*, vol. 12, (5), pp. 665-677, 1978.
- [46] J. Choueka, J. L. Charvet, K. J. Koval, H. Alexander, K. S. James, K. A. Hooper and J. Kohn, "Canine bone response to tyrosine-derived polycarbonates and poly(L-lactic acid)," *J Biomed Mater Res*, vol. 31, (1), pp. 35-41, 1996.
- [47] J. M. Williams, A. Adewunmi, R. M. Schek, C. L. Flanagan, P. H. Krebsbach, S. E. Feinberg, S. J. Hollister and S. Das, "Bone tissue engineering using polycaprolactone scaffolds fabricated via selective laser sintering," *Biomaterials*, vol. 26, (23), pp. 4817-4827, 2005.
- [48] L. S. Nichter, M. Yazdi, K. Kosari, R. Sridjaja, E. Ebramzadeh and M. E. Nimni, "Demineralized bone matrix polydioxanone composite as a substitute for bone graft: a comparative study in rats," *J Craniofac Surg*, vol. 3, (2), pp. 63-69, 1992.
- [49] D. Williams, "Polyetheretherketone for long-term implantable devices," *Med Device Technol*, vol. 19(1), (8), pp. 10-11, 2008.
- [50] C. M. Agrawal and R. B. Ray, "Biodegradable polymeric scaffolds for musculoskeletal tissue engineering," *J Biomed Mater Res*, vol. 55, (2), pp. 141-150, 2001.
- [51] V. Palissery, M. Taylor and M. Browne, "Fatigue characterization of a polymer foam to use as a cancellous bone analog material in the assessment of orthopedic devices," *J Mater Sci Mater Med Jan*, vol. 15, (1), pp. 61-67, 2004.
- [52] R. M. Pilliar, M. J. Filiaggi, J. D. Wells, M. D. Grynypas and R. A. Kandel, "Porous calcium polyphosphate scaffolds for bone substitution applications - in vitro characterization," *Biomaterials*, vol. 22, pp. 963-972, 2001.
- [53] T. G. van Tienen, R. G. Heijkants, P. Buma, J. H. de Groot, A. J. Pennings and R. P. Veth, "Tissue ingrowth and degradation of two biodegradable porous polymers with different porosities and pore sizes," *Biomaterials*, vol. 23, (8), pp. 1731-1738, 2002.
- [54] L. L. Hench and O. Andersson, "Bioactive glass coating," in *Advanced Series in Ceramics - Vol. 1: An Introduction to Bioceramics* L. L. Hench and J. Wilson, Eds. Singapore: World Scientific Publishing Company, 1993, pp. 239.
- [55] P. S. Eggli, W. Müller and R. K. Schenk, "Porous hydroxyapatite and tricalcium phosphate cylinders with two different pore size ranges implanted in the cancellous bone of rabbits. A comparative histomorphometric and histologic study of bony ingrowth and implant substitution," *Clin Orthop Relat Res*, vol. 232, pp. 127-138, 1988.
- [56] Q. Fu, M. N. Rahaman, F. Dogan and B. S. Bal, "Freeze-cast hydroxyapatite scaffolds for bone tissue engineering applications," *Biomed Mater*, vol. 3, (2), pp. 1-7, 2008.
- [57] T. M. G. Chu, D. G. Orton, S. J. Hollister, S. E. Feinberg and J. W. Halloran, "Mechanical and in vivo performance of hydroxyapatite implants with controlled architectures," *Biomaterials*, vol. 23, (5), pp. 1283-1293, 2002.

- [58] B. S. Chang, C. K. Lee, K. S. Hong, H. J. Youn, H. S. Ryu, S. S. Chung and K. W. Park, "Osteoconduction at porous hydroxyapatite with various pore configurations," *Biomaterials*, vol. 21, (12), pp. 1291-1298, 2000.
- [59] R. E. Holmes, R. W. Bucholz and V. Mooney, "Porous hydroxyapatite as a bone graft substitute in diaphyseal defects: A histometric study," *J Orthopaedic Res*, vol. 5, (1), pp. 114-121, 1987.
- [60] F. Peters, D. Groisman, R. Davids, T. Hanel, H. Durr and M. Klein, "Comparative Study of patient individual implants from  $\beta$ -tricalcium phosphate made by different techniques based on CT data," *Materialwissenschaft Und Werkstofftechnik*, vol. 37, (6), pp. 457-461, 2006.
- [61] M. Sous, R. Bareille, F. Rouais, D. Clément, J. Amédée, B. Dupuy and C. Baquey, "Cellular biocompatibility and resistance to compression of macroporous beta-tricalcium phosphate ceramics," *Biomaterials*, vol. 19, (23), pp. 2147-2153, 1998.
- [62] E. B. Nery, R. Z. LeGeros, K. L. Lynch and K. Lee, "Tissue response to biphasic calcium phosphate ceramic with different ratios of HA/beta TCP in periodontal osseous defects," *J Periodontol*, vol. 63, (9), pp. 729-735, 1992.
- [63] H. Petite, V. Viateau, W. Bensaïd, A. Meunier, C. de Pollak, M. Bourguignon, K. Oudina, L. Sedel and G. Guillemin, "Tissue-engineered bone regeneration," *Nat Biotechnol*, vol. 18, (9), pp. 959-963, 2000.
- [64] J. S. Sottosanti, "Calcium sulfate-aided bone regeneration: a case report," *Periodontal Clin Investig*, vol. 17, (2), pp. 10-15, 1995.
- [65] S. J. Froum, M. A. Weinberg and D. Tarnow, "Comparison of bioactive glass synthetic bone graft particles and open debridement in the treatment of human periodontal defects. A clinical study," *J Periodontol*, vol. 69, (6), pp. 698-709, 1998.
- [66] E. J. Schepers, P. Ducheyne, L. Barbier and S. Schepers, "Bioactive glass particles of narrow size range: a new material for the repair of bone defects," *Implant Dent*, vol. 2, (3), pp. 151-156, 1993.
- [67] E. J. Schepers and P. Ducheyne, "Bioactive glass particles of narrow size range for the treatment of oral bone defects: a 1-24 month experiment with several materials and particle sizes and size ranges," *J Oral Rehabil*, vol. 24, (3), pp. 171-181, 1997.
- [68] E. E. Hall, R. M. Meffert, J. S. Hermann, J. T. Mellonig and D. L. Cochran, "Comparison of bioactive glass to demineralized freeze-dried bone allograft in the treatment of intrabony defects around implants in the canine mandible," *J Periodontol*, vol. 70, (5), pp. 526-535, 1999.
- [69] K. D. Johnson, K. E. Frierson, T. S. Keller, C. Cook, R. Scheinberg, J. Zerwekh, L. Meyers and M. F. Sciadini, "Porous ceramics as bone graft substitutes in long bone defects: a biomechanical, histological, and radiographic analysis," *J Orthop Res*, vol. 14, (3), pp. 351-369, 1996.
- [70] R. Z. LeGeros, "Biodegradation and bioresorption of calcium phosphate ceramics," *Clinical Materials*, vol. 14, (1), pp. 65-88, 1993.



- [71] R. Z. LeGeros, "Properties of osteoconductive biomaterials: calcium phosphates," *Clin Orthop Relat Res*, (395), pp. 81-98, 2002.
- [72] M. Bohner, "Calcium orthophosphates in medicine: from ceramics to calcium phosphate cements," *Injury*, vol. 31, (4), pp. 37-47, 2000.
- [73] J. N. Kent, M. F. Zide, J. F. Kay and M. Jarcho, "Hydroxylapatite blocks and particles as bone graft substitutes in orthognathic and reconstructive surgery," *J Oral and Maxillofacial Surg*, vol. 44, (8), pp. 597-605, 1986.
- [74] M. P. Levin, L. Getter, D. E. Cutright and S. N. Bhaskar, "Biodegradable ceramic in periodontal defects," *Oral Surg Oral Med Oral Pathol*, vol. 38, (3), pp. 344-351, 1974.
- [75] J. R. Wagner, "A 3 1/2-year clinical evaluation of resorbable hydroxylapatite OsteoGen (HA Resorb) used for sinus lift augmentations in conjunction with the insertion of endosseous implants," *J Oral Implantol*, vol. 17, (2), pp. 152-164, 1991.
- [76] C. A. P. K. de Groot, J. G. C. Klein, J. M. A. Wolke and J. M. A. de Blicck-Hogervorst, "Chemistry of calcium phosphate bioceramics," in *Handbook on Bioactive Ceramics, Vol. II* Yamamuro T, Hench LL, Wilson J, Ed. Boca Raton, FL: CRC Press, 1990, pp. 3-16.
- [77] G. A. Gogotsi, "Fracture toughness of ceramics and ceramic composites," *Ceram Int*, vol. 29, (7), pp. 777-784, 2003.
- [78] A. Butscher, M. Bohner, S. Hofmann, L. Gauckler and R. Müller, "Structural and material approaches to bone tissue engineering in powder-based three-dimensional printing," *Acta Biomater*, vol. 7, (3), pp. 907-920, 2011.
- [79] A. J. Wagoner Johnson and B. A. Herschler, "A review of the mechanical behavior of CaP and CaP/polymer composites for applications in bone replacement and repair," *Acta Biomater*, vol. 7, (1), pp. 16-30, 2011.
- [80] T. Kasuga, H. Maeda, K. Kato, M. Nogami, K. Hata and M. Ueda, "Preparation of poly(lactic acid) composites containing calcium carbonate (vaterite)," *Biomaterials*, vol. 24, (19), pp. 3247-3253, 2003.
- [81] T. Jaakkola, J. Rich, T. Tirri, T. Närhi, M. Jokinen, J. Seppälä and A. Yli-Urpo, "In vitro Ca-P precipitation on biodegradable thermoplastic composite of poly(epsilon-caprolactone-co-DL-lactide) and bioactive glass (S53P4)," *Biomaterials*, vol. 25, (4), pp. 575-581, 2004.
- [82] M. Navarro, M. P. Ginebra, J. A. Planell, S. Zepetelli and L. Ambrosio, "Development and cell response of a new biodegradable composite scaffold for guided bone regeneration," *J Mater Sci Mater Med*, vol. 15, (4), pp. 419-422, 2004.
- [83] A. R. Boccaccini, J. A. Roelher, L. L. Hench, V. Maquet and R. Jérôme, "A composites approach to tissue engineering," in *26th Annual Conference on Composites, Advanced Ceramics, Materials, and Structures: B: Ceramic Engineering and Science Proceedings*, vol. 23, H. T. Lin and M. Singh, Eds. Hoboken, NJ, USA: John Wiley & Sons, Inc., 2008, pp. 4.
- [84] M. Bohner, "Resorbable biomaterials as bone graft substitutes," *Mater Today*, vol. 13, (1-2), pp. 24-30, 2010.
- [85] P. V. Giannoudis, H. Dinopoulos and E. Tsiridis, "Bone substitutes: An update," *Injury*, vol. 36, (3), pp. S20-27, 2005.

- [86] Frost & Sullivan, "U.S. Bone Grafts and Bone Graft Substitutes Markets," 2007.
- [87] R. W. Bucholz, "Nonallograft osteoconductive bone graft substitutes," *Clin Orthop Relat Res*, vol. 395, pp. 44-52, 2002.
- [88] E. B. Hunziker, "Articular cartilage repair: basic science and clinical progress. A review of the current status and prospects," *Osteoarthritis Cartilage*, vol. 10, (6), pp. 432-463, 2002.
- [89] W. R. Walsh, M. Walton, W. Bruce, Y. Yu, R. M. Gillies and M. Svehla, "Cell structure and biology of bone and cartilage," in *Handbook of Histology Methods for Bone and Cartilage* Y. H. An and K. L. Martin, Eds. Humana Press, 2003, pp. 46.
- [90] J. Boyle, B. Luan, T. F. Cruz and R. A. Kandel, "Characterization of proteoglycan accumulation during formation of cartilaginous tissue *in vitro*," *Osteoarthritis Cartilage*, vol. 3, (2), pp. 117-125, 1995.
- [91] H. Chuma, H. Mizuta, S. Kudo, K. Takagi and Y. Hiraki, "One day exposure to FGF-2 was sufficient for the regenerative repair of full-thickness defects of articular cartilage in rabbits," *Osteoarthritis Cartilage*, vol. 12, (10), pp. 834-842, 2004.
- [92] A. Praemer, S. Furner and D. P. Rice, *Musculoskeletal Conditions in the United States*. Park Ridge: American Academy of Orthopedic Surgeons, 1992.
- [93] D. J. Berry, W. S. Harmsen, D. Ilstrup, D. G. Lewallen and M. E. Cabanela, "Survivorship of uncemented proximally porous-coated femoral components," *Clin Orthop Relat Res*, vol. 319, pp. 168-177, 1995.
- [94] S. A. Jacobsson, K. Djerf and O. Wahlström, "Twenty-year results of McKee-Farrar versus Charnley prosthesis," *Clin Orthop Relat Res*, vol. 329, pp. S60-68, 1996.
- [95] P. Söderman, H. Malchau, P. Herberts, R. Zügner, H. Regnér and G. Garellick, "Outcome after total hip arthroplasty: Part II. Disease-specific follow-up and the Swedish National Total Hip Arthroplasty Register," *Acta Orthop Scand*, vol. 72, (2), pp. 113-119, 2001.
- [96] R. A. Kandel, R. Pilliar and M. Grynblas, "Biphasic constructs for cartilage repair," *Eur Cell Mater*, vol. 13, (2), pp. 10, 2007.
- [97] L. Hangody, G. Kish, Z. Karapati and R. Eberhart, "Osteochondral plugs: Autogenous osteochondral mosaicplasty for the treatment of focal chondral and osteochondral articular defects," *Oper Tech Orthop*, vol. 7, pp. 312-322, 1997.
- [98] S. N. Redman, S. F. Oldfield and C. W. Archer, "Current strategies for articular cartilage repair," *Eur Cell Mater*, vol. 9, pp. 23-32, 2005.
- [99] A. P. Newman, "Articular Cartilage Repair," *Am J Sports Med March*, vol. 26, (2), pp. 309-324, 1998.
- [100] T. A. Irwin, J. X. Kou and P. T. Fortin, "Classification and treatment of severe ankle articular segment deficits: osteochondral allograft reconstruction," *Foot Ankle Clin*, vol. 12, (1), pp. 41-55, 2007.
- [101] G. D. Smith, G. Knutsen and J. B. Richardson, "A clinical review of cartilage repair techniques," *J Bone Joint Surg Br*, vol. 87, (4), pp. 445-449, 2005.

- [102] B. R. Mandelbaum, J. E. Browne, F. Fu, L. Micheli, J. B. Mosely, C. Erggelet, T. Minas and L. Peterson, "Articular Cartilage Lesions of the Knee," *Am J Sports Med*, vol. 26, (6), pp. 853-861, 1998.
- [103] N. Iwasaki, H. Kato, T. Kamishima, N. Suenaga and A. Minami, "Donor Site Evaluation After Autologous Osteochondral Mosaicplasty for Cartilaginous Lesions of the Elbow Joint," *Am J Sports Med*, vol. 35, (12), pp. 2096-2100, 2007.
- [104] N. Shasha, P. P. Aubin, H. K. Cheah, A. M. Davis, Z. Agnidis and A. E. Gross, "Long-term clinical experience with fresh osteochondral allografts for articular knee defects in high demand patients," *Cell Tissue Bank*, vol. 3, (3), pp. 175-182, 2002.
- [105] D. W. Hutmacher, "Scaffolds in tissue engineering bone and cartilage," *Biomaterials*, vol. 21, (24), pp. 2529-2543, 2000.
- [106] R. Langer and J. P. Vacanti, "Tissue Engineering," *Science*, vol. 260, (5110), pp. 920-926, 1993.
- [107] S. D. Waldman, M. D. Gryn timer, R. M. Pilliar and R. A. Kandel, "Characterization of cartilaginous tissue formed on calcium polyphosphate substrates *in vitro*," *J Biomed Mater Res*, vol. 62, (3), pp. 323-330, 2002.
- [108] S. D. Waldman, M. D. Gryn timer, R. M. Pilliar and R. A. Kandel, "The use of specific chondrocyte populations to modulate the properties of tissue-engineered cartilage," *J Orthop Res*, vol. 21, (1), pp. 132-138, 2003.
- [109] R. A. Kandel, M. Gryn timer, R. Pilliar, J. Lee, J. Wang, S. Waldman, P. Zalzal and M. Hurtig, "Repair of osteochondral defects with biphasic cartilage-calcium polyphosphate constructs in a sheep model," *Biomaterials*, vol. 27, pp. 4120-4131, 2006.
- [110] X. Wang, S. P. Grogan, F. Rieser, V. Winkelmann, V. Maquet, M. L. Berge and P. Mainil-Varlet, "Tissue engineering of biphasic cartilage constructs using various biodegradable scaffolds: an *in vitro* study," *Biomaterials*, vol. 25, (17), pp. 3681-3688, 2004.
- [111] D. Schaefer, I. Martin, P. Shastri, R. F. Padera, R. Langer, L. E. Freed and G. Vunjak-Novakovic, "In vitro generation of osteochondral composites," *Biomaterials*, vol. 21, (24), pp. 2599-2606, 2000.
- [112] D. Schaefer, I. Martin, G. Jundt, J. Seidel, M. Heberer, A. Grodzinsky, I. Bergin, G. Vunjak-Novakovic and L. E. Freed, "Tissue-engineered composites for the repair of large osteochondral defects," *Arthritis Rheum*, vol. 46, (9), pp. 2524-2534, 2002.
- [113] J. Gao, J. E. Dennis, L. A. Solchaga, A. S. Awadallah, V. M. Goldberg and A. I. Caplan, "Tissue-engineered fabrication of an osteochondral composite graft using rat bone marrow-derived mesenchymal stem cells," *Tissue Eng*, vol. 7, (4), pp. 363-371, 2001.
- [114] J. K. Sherwood, S. L. Riley, R. Palazzolo, S. C. Brown, D. C. Monkhouse, M. Coates, L. G. Griffith, L. K. Landeen and A. Ratcliff, "A three-dimensional osteochondral composite scaffold for articular cartilage repair," *Biomaterials*, vol. 23, (24), pp. 4739, 2002.
- [115] R. M. Schek, J. M. Taboas, S. J. Segvich, S. J. Hollister and P. H. Krebsbach, "Engineered osteochondral grafts using biphasic composite solid free-form fabricated scaffolds," *Tissue Eng*, vol. 10, (9-10), pp. 1376-1385, 2004.

- [116] T. Cao, K. H. Ho and S. H. Teoh, "Scaffold design and in vitro study of osteochondral coculture in a three-dimensional porous polycaprolactone scaffold fabricated by fused deposition modeling," *Tissue Eng*, vol. 9, (1), pp. S103-S112, 2003.
- [117] J. E. Davies, "Mechanisms of endosseous integration," *Int J Prosthodont*, vol. 11, (5), pp. 391-401, 1998.
- [118] M. Filiaggi, R. M. Pilliar and J. Hong, "On the sintering characteristics of calcium polyphosphates," *Key Eng Mater*, vol. 192-195, pp. 171-174, 2001.
- [119] L. Guehenec, P. Layrolle and G. Daculsi, "A review of bioceramics and fibrin sealant," *Eur Cell Mater*, vol. 8, pp. 1-11, 2004.
- [120] T. S. Hin, *Engineering Materials for Biomedical Applications*. Asia: World Scientific, 2004, pp. 352-6-4.
- [121] M. D. Grynblas, R. M. Pilliar, R. A. Kandel, R. Renlund and M. Filiaggi, "Porous calcium polyphosphate scaffolds for bone substitute applications - *in vivo* studies," *Biomaterials*, vol. 23, (9), pp. 2063-2070, 2002.
- [122] E. O. Huffman and J. D. Fleming, "Calcium polyphosphate - rate and mechanism of its hydrolytic degradation," *J Phys Chem*, vol. 64, pp. 240-244, 1960.
- [123] Q. Wang, Q. Wang, J. Wang, X. Zhang, X. Yu and C. Wan, "Degradation kinetics of calcium polyphosphate bioceramic: an experimental and theoretical study," *Mater Res*, vol. 12, (4), pp. 495-501, 2009.
- [124] K. Qiu, C. X. Wan, C. S. Zhao, X. Chen, C. W. Tang and Y. W. Chen, "Fabrication and characterization of porous calcium polyphosphate scaffolds," *J Mater Sci*, vol. 41, (8), pp. 2429-2434(6), 2006.
- [125] M. Kanatani, T. Sugimoto, M. Fukase and T. Fujita, "Effect of elevated extracellular calcium on the proliferation of osteoblastic MC3T3-E1 cells: its direct and indirect effects via monocytes," *Biochem Biophys Res Commun*, vol. 181, (3), pp. 1425-1430, 1991.
- [126] X. Wu, N. Itoh, T. Taniguchi, T. Nakanishi and K. Tanaka, "Requirement of calcium and phosphate ions in expression of sodium-dependent vitamin C transporter 2 and osteopontin in MC3T3-E1 osteoblastic cells," *Biochim Biophys Acta*, vol. 1641, (1), pp. 65-70, 2003.
- [127] J. A. Planell, S. M. Best and D. LaCroix, *Bone Repair Biomaterials*. Taylor and Francis, 2009, pp. 478.
- [128] C. T. Laurencin and American Academy of Orthopaedic Surgeons, *Bone Graft Substitutes*. ASTM International, 2003, pp. 315.
- [129] C. Y. Kim, A. E. Clark and L. L. Hench, "Early stages of calcium-phosphate layer formation in bioglasses," *J Non-Cryst Solids*, vol. 113, (2-3), pp. 195-202, 1989.
- [130] D. Baksh and J. E. Davies, "Three-dimensional matrices of calcium polyphosphates support bone growth *in vitro* and *in vivo*," *J Mater Sci - Mater Med*, vol. 9, (12), pp. 743-748, 1998.

- [131] R. M. Pilliar, J. Hong and P. J. Santerre, "Method of manufacture of porous inorganic structures," US 7494614, 2009.
- [132] S. D. Waldman, C. G. Spiteri, M. D. Gryn timer, R. M. Pilliar, J. Hong and R. A. Kandel, "Effect of biomechanical conditioning on cartilaginous tissue formation *in vitro*," *The Journal of Bone and Joint Surgery*, vol. 85-A, (2), pp. 101-105, 2003.
- [133] S. D. Waldman, C. G. Spiteri, M. D. Gryn timer, R. M. Pilliar and R. A. Kandel, "Long-term intermittent shear deformation improves the quality of cartilaginous tissue formed *in vitro*," *J Orthop Res*, vol. 21, pp. 590-596, 2003.
- [134] S. D. Waldman, C. G. Spiteri, M. D. Gryn timer, R. M. Pilliar and R. A. Kandel, "Long-term intermittent compressive stimulation improves the composition and mechanical properties of tissue-engineered cartilage," *Tissue Eng*, vol. 10, (9/10), pp. 1323-1331, 2004.
- [135] S. D. Waldman, D. C. Couto, M. D. Gryn timer, R. M. Pilliar and R. A. Kandel, "Multi-axial mechanical stimulation of tissue engineered cartilage: review," *Eur Cells Mater*, vol. 13, (613), pp. 66-74, 2007.
- [136] J. N. A. De Croos, S. S. Dhaliwal, M. D. Gryn timer, R. M. Pilliar and R. A. Kandel, "Cyclic compressive mechanical stimulation induces sequential catabolic and anabolic gene changes in chondrocytes resulting in increased extracellular matrix accumulation," *Matrix Biology*, vol. 25, (6), pp. 323-331, 2006.
- [137] K. S. Allan, R. M. Pilliar, J. Wang, M. D. Gryn timer and R. A. Kandel, "Formation of biphasic constructs containing cartilage with a calcified zone interface," *Tissue Eng*, vol. 13, (1), pp. 167-177, 2007.
- [138] S. M. Lien, C. H. Chien and T. J. Huang, "A novel osteochondral scaffold of ceramic-gelatin assembly for articular cartilage repair," *Mater Sci Eng C*, vol. 29, (1), pp. 315-321, 2009.
- [139] A. Rouzrokh, C. H. Wei, K. Erkorkmaz and R. M. Pilliar, "Machining porous calcium polyphosphate implants for tissue engineering applications," *Int J Autom Technol – Special Issue on Modeling and Simulation of Cutting Process*, vol. 4, (3), pp. 291-302, 2010.
- [140] N. L. Porter, R. M. Pilliar and M. D. Gryn timer, "Fabrication of porous calcium polyphosphate implants by solid freeform fabrication: A study of processing parameters and *in vitro* degradation characteristics," *J Biomed Mater Res*, vol. 56, (4), pp. 504-515, 2001.
- [141] N. L. Porter, "Solid freeform fabrication of calcium polyphosphate: material characterization and assessment of processing parameters," pp. 84, 1999.
- [142] J. E. Nicholl, S. R. Koka, I. W. Bintcliffe and A. K. Addison, "Acetabular augmentation for the treatment of unstable total hip arthroplasties," *Ann R Coll Surg Engl*, vol. 81, (2), pp. 127-132, 1999.
- [143] A. G. Mikos, A. J. Thorsen, L. A. Czerwonka, Y. Bao, R. Langer, D. N. Winslow and J. P. Vacanti, "Preparation and characterization of poly(l-lactic acid) foams," *Polymer*, vol. 35, (5), pp. 1068-1077, 1994.

- [144] D. J. Mooney, D. F. Baldwin, N. P. Suh, J. P. Vacanti and R. Langer, "Novel approach to fabricate porous sponges of poly(-lactic-co-glycolic acid) without the use of organic solvents," *Biomaterials*, vol. 17, pp. 1417-1422, 1996.
- [145] L. E. Freed, G. Vunjak-Novakovic, R. G. Biron, D. B. Eagles, D. C. Lesnoy, S. K. Barlow and R. Langer, "Biodegradable polymer scaffolds for tissue engineering," *Nat Biotechnol*, vol. 12, pp. 689-693, 1994.
- [146] H. Lo, M. S. Ponticiello and K. W. Leong, "Fabrication of controlled release biodegradable foams by phase separation," *Tissue Eng*, vol. 1, (1), pp. 15-28, 1995.
- [147] K. Whang, C. H. Thomas, K. E. Healy and G. Nuber, "A novel method to fabricate bioabsorbable scaffolds," *Polymer*, vol. 36, (4), pp. 837-842, 1995.
- [148] W. Y. Yeong, C. K. Chua, K. F. Leong and M. Chandrasekaran, "Rapid prototyping in tissue engineering: challenges and potential," *Trends Biotechnol*, vol. 22, (12), pp. 643-652, 2004.
- [149] I. Gibson, *Advanced Manufacturing Technology for Medical Application; Reverse Engineering, Software Conversion and Rapid Prototyping*. 1st ed. John Wiley & Sons, Ltd, 2005, pp. 254.
- [150] E. Sachlos and J. T. Czernuszka, "Making tissue engineering scaffolds work. Review on the application of solid freeform fabrication technology to the production of tissue engineering scaffolds," *Eur Cell Mater*, vol. 5, pp. 29-40, 2003.
- [151] K. F. Leong, C. M. Cheah and C. K. Chua, "Solid freeform fabrication of three-dimensional scaffolds for engineering replacement tissues and organs," *Biomaterials*, vol. 24, pp. 2363-2378, 2003.
- [152] S. J. Hollister, J. M. Tobaos, R. M. Schek, C. Y. Lin and T. M. Chu, "Design and fabrication of bone tissue engineering scaffolds," in *Bone Tissue Engineering* J. O. Hollinger, T. A. Einhorn, B. Doll and C. Sfeir, Eds. CRC Press, 2004, pp. 168-185.
- [153] C. K. Chua, K. F. Leong and C. S. Lim, *Rapid Prototyping: Principles and Applications*. 2nd ed. World Scientific, 2003, pp. 421.
- [154] J. P. Kruth, "Material increment manufacturing by rapid prototyping techniques," *CIRP Annals - Manufacturing Technology*, vol. 40, (2), pp. 603-614, 1991.
- [155] S. Eosoly, D. Brabazon, S. Lohfeld and L. Looney, "Selective laser sintering of hydroxyapatite/poly- $\epsilon$ -caprolactone scaffolds," *Acta Biomater*, vol. 6, (7), pp. 2511-2517, 2010.
- [156] F. E. Wiria, C. K. Chua, K. F. Leong, Z. Y. Quah, M. Chandrasekaran and M. W. Lee, "Improved biocomposite development of poly(vinyl alcohol) and hydroxyapatite for tissue engineering scaffold fabrication using selective laser sintering," *J Mater Sci - Mater Med*, vol. 19, (3), pp. 989-996, 2008.
- [157] C. K. Chua, K. F. Leong, K. H. Tan, F. E. Wiria and C. M. Cheah, "Development of tissue scaffolds using selective laser sintering of polyvinyl alcohol/hydroxyapatite biocomposite for craniofacial and joint defects," *J Mater Sci - Mater Med*, vol. 15, (10), pp. 1113-1121, 2004.

- [158] K. H. Tan, C. K. Chua, K. F. Leong, C. M. Cheah, P. Cheang, M. S. Abu Bakar and S. W. Cha, "Scaffold development using selective laser sintering of polyetheretherketone–hydroxyapatite biocomposite blends," *Biomaterials*, vol. 24, (18), pp. 3115-3123, 2003.
- [159] K. Subramanian, N. Vail, J. Barlow and H. Marcus, "Selective laser sintering of alumina with polymer binders," *Rapid Prototyping J*, vol. 1, (2), pp. 24-35, 1995.
- [160] G. Lee and J. W. Barlow, "Selective laser sintering of bioceramic materials for implants," in *Solid Freeform Fabrication Proceedings*, 1993, pp. 376-380.
- [161] J. T. Rimell and P. M. Marquis, "Selective laser sintering of ultra high molecular weight polyethylene for clinical applications," *J Biomed Mater Res*, vol. 53, (4), pp. 414-420, 2000.
- [162] S. Eshraghi and S. Das, "Mechanical and microstructural properties of polycaprolactone scaffolds with one-dimensional, two-dimensional, and three-dimensional orthogonally oriented porous architectures produced by selective laser sintering," *Acta Biomater*, vol. 6, (7), pp. 2467-2476, 2010.
- [163] T. Traini, C. Mangano, R. L. Sammons, F. Mangano, A. Macchi and A. Piattelli, "Direct laser metal sintering as a new approach to fabrication of an isoelastic functionally graded material for manufacture of porous titanium dental implants," *Dent Mater*, vol. 24, (11), pp. 1525-1533, 2008.
- [164] P. Heintl, A. Rottmair, C. Körner and R. . Singer, "Cellular titanium by selective electron beam melting," *Adv Eng Mater*, vol. 9, (5), pp. 360-364, 2007.
- [165] L. Hao, S. Dadbakhsh, O. Seaman and M. Felstead, "Selective laser melting of a stainless steel and hydroxyapatite composite for load-bearing implant development," *J Mater Process Technol*, vol. 209, (17), pp. 5793-5801, 2009.
- [166] S. Yang, K. F. Leong, Z. Du and C. K. Chua, "The design of scaffolds for use in tissue engineering. part II. rapid prototyping techniques," *Tissue Eng*, vol. 8, (1), pp. 1-11, 2002.
- [167] M. J. Cima, E. M. Sachs, T. L. Fan, J. F. Brecht, S. P. Michaels, S. Khanuja, S. Lauder, S. J. Lee, D. Brancazio, A. Curodeau and H. Tuerck, "Three-dimensional printing techniques," US 5387380, 1995.
- [168] S. Upcraft and R. Fletcher, "The rapid prototyping technologies," *Assembly Automation*, vol. 23, (4), pp. 318-330, 2003.
- [169] P. H. Warnke, H. Seitz, F. Warnke, S. T. Becker, S. Sivananthan, E. Sherry, Q. Liu, J. Wiltfang and T. Douglas, "Ceramic scaffolds produced by computer-assisted 3D printing and sintering: characterization and biocompatibility investigations," *J Biomed Mater Res*, vol. 93B, (1), pp. 212-217, 2010.
- [170] K. Igawa, M. Mochizuki, O. Sugimori, K. Shimizu, K. Yamazawa, H. Kawaguchi, K. Nakamura, T. Takato, R. Nishimura, S. Suzuki, M. Anzai, U. I. Chung and N. Sasaki, "Tailor-made tricalcium phosphate bone implant directly fabricated by a three-dimensional ink-jet printer," *J Artif Organs*, vol. 9, (4), pp. 234-240, 2006.

- [171] W. Sun, B. Starly, J. Nam and A. Darling, "Bio-CAD modeling and its applications in computer-aided tissue engineering," *Comput Aided Des*, vol. 37, (11), pp. 1097-1114, 2005.
- [172] W. Sun, A. Darling, B. Starly and J. Nam, "Computer-aided tissue engineering: overview, scope and challenges," *Biotechnol Appl Biochem*, vol. 39, pp. 29-47, 2004.
- [173] W. Sun, B. Starly, A. Darling and C. Gomez, "Computer-aided tissue engineering: application to biomimetic modelling and design of tissue scaffolds," *Biotechnol Appl Biochem*, vol. 39, pp. 49-58, 2004.
- [174] R. A. Giordano, B. M. Wu, S. W. Borland, L. G. Cima, E. M. Sachs and M. J. Cima, "Mechanical properties of dense polylactic acid structures fabricated by three dimensional printing," *J Biomater Sci, Polymer Edition*, vol. 8, (1), pp. 63-75, 1997.
- [175] A. Park, B. Wu and L. G. Griffith, "Integration of surface modification and 3D fabrication techniques to prepare patterned poly(L-lactide) substrates allowing regionally selective cell adhesion," *J Biomater Sci, Polymer Edition*, vol. 9, (2), pp. 89-110, 1998.
- [176] L. G. Griffith, B. Wu, M. J. Cima, M. J. Powers, B. Chaignaud and J. P. Vacanti, "In vitro organogenesis of liver tissue," *Annals of the New York Academy of Sciences*, vol. 831, (1), pp. 382-397, 1997.
- [177] S. S. Kim, H. Utsunomiya, J. A. Koski, B. M. Wu, M. J. Cima, J. Sohn, K. Mukai, L. G. Griffith and J. P. Vacanti, "Survival and function of hepatocytes on a novel three-dimensional synthetic biodegradable polymer scaffold with an intrinsic network of channels," *Ann Surg*, vol. 228, (1), pp. 8-13, 1998.
- [178] L. G. Cima and M. J. Cima, "Preparation of medical devices by solid free-form fabrication methods," US 5490962, 1996.
- [179] Theriform Technology, "<http://therics.com/technology/>," 2006.
- [180] J. Zeltinger, J. K. Sherwood, D. A. Graham, R. Mueller and L. G. and Griffith, "Effect of pore size and void fraction on cellular adhesion, proliferation, and matrix deposition," *Tissue Eng*, vol. 7, (5), pp. 557-572, 2001.
- [181] C. X. F. Lam, X. M. Moa, S. H. Teoha and D. W. Hutmacher, "Scaffold development using 3D printing with a starch-based polymer," *Mater Sci Eng: C*, vol. 20, (1-2), pp. 49-56, 2002.
- [182] T. D. Roy, J. L. Simon, J. L. Ricc, E. D. Rekow, V. P. Thompson and J. R. Parsons, "Performance of hydroxyapatite bone repair scaffolds created via three-dimensional fabrication techniques," *J Biomed Mater Res Part A*, vol. 67A, (4), pp. 1228-1237, 2003.
- [183] H. Seitz, W. Rieder, S. Irsen, B. Leukers and C. Tille, "Three-dimensional printing of porous ceramic scaffolds for bone tissue engineering," *J Biomed Mater Res B Appl Biomater*, vol. 74B, (2), pp. 782, 2005.
- [184] S. H. Irsen, B. Leukers, C. Höckling, C. Tille and H. Seitz, "Bioceramic Granulates for use in 3D Printing: Process Engineering Aspects," *Materialwissenschaft Und Werkstofftechnik*, vol. 37, (6), pp. 533-537, 2006.



- [185] J. Will, R. Melcher, C. Treul, N. Travitzky, U. Kneser, E. Polykandriotis, R. Horch and P. Greil, "Porous ceramic bone scaffolds for vascularized bone tissue regeneration," *J Mater Sci - Mater Med*, vol. 19, (8), pp. 2781-2790,
- [186] J. Suwanprateeb, R. Sanngam, W. Suvannapruk and T. Panyathanmaporn, "Mechanical and in vitro performance of apatite-wollastonite glass ceramic reinforced hydroxyapatite composite fabricated by 3D-printing," *J Mater Sci - Mater Med*, vol. 20, (6), pp. 1281-1289, 2009.
- [187] B. Leukers, H. Gülkan, S. H. Irsen, S. Milz, C. Tille, M. Schieker and H. Seitz, "Hydroxyapatite scaffolds for bone tissue engineering made by 3D printing," *J Mater Sci - Mater Med*, vol. 16, (12), pp. 1121-1124, 2005.
- [188] R. Chumnanklang, T. Panyathanmaporn, K. Sitthiseripratip and J. Suwanprateeb, "3D printing of hydroxyapatite: Effect of binder concentration in pre-coated particle on part strength," *Mater Sci Eng: C*, vol. 27, (4), pp. 914-921, 2007.
- [189] U. Gbureck, T. Holzel, U. Klammert, K. Wurzler, F. A. Muller and J. E. Barralet, "Resorbable Dicalcium Phosphate Bone Substitutes Prepared by 3D Powder Printing," *Adv Funct Mater*, vol. 17, pp. 3940-3945, 2007.
- [190] U. Gbureck, T. Holzel, I. Biermann, J. E. Barralet and L. M. Grover, "Preparation of tricalcium phosphate/calcium pyrophosphate structures via rapid prototyping," *J Mater Sci - Mater Med*, vol. 19, pp. 1559-1563, 2008.
- [191] C. Bergmann, M. Lindner, W. Zhang, K. Koczur, A. Kirsten, R. Telle and H. Fischer, "3D printing of bone substitute implants using calcium phosphate and bioactive glasses," *J Eur Ceram Soc*, vol. 30, pp. 2563-2567, 2010.
- [192] M. W. Lee, H. T. Kurniawati, M. Chandrasekaran and P. Cheang, "3D printing of tricalcium phosphate scaffolds," *SIMTech Technical Reports*, vol. 7, (2), pp. 1-5, 2006.
- [193] A. Khalyfa, S. Vogt, J. Weisser, G. Grimm, A. Rechtenbach, W. Meyer and M. Schnabelrauch, "Development of a new calcium phosphate powder-binder system for the 3D printing of patient specific implants," *J Mater Sci - Mater Med*, vol. 18, (5), pp. 909-916, 2007.
- [194] A. K. Maier, L. Dezmirean, J. Will and P. Greil, "Three-dimensional printing of flash-setting calcium aluminate cement," *J Mater Sci*, vol. 46, (9), pp. 2947-2954, 2011.
- [195] R. Detsch, S. Schaefer, U. Deisinger, G. Ziegler, H. Seitz and B. Leukers, "In vitro-Osteoclastic Activity Studies on Surfaces of 3D Printed Calcium Phosphate Scaffolds," *J Biomater Appl*, 2010.
- [196] U. Gbureck, T. Hölzel, C. . Doillon, F. . Müller and J. . Barralet, "Direct printing of bioceramic implants with spatially localized angiogenic factors," *Adv Mat*, vol. 19, (16), pp. 795-800, 2007.
- [197] H. Saijo, K. Igawa, Y. Kanno, Y. Mori, K. Kondo, K. Shimizu, S. Suzuki, D. Chikazu, M. Iino, M. Anzai, N. Sasaki, U. I. Chung and T. Takato, "Maxillofacial reconstruction using custom-made artificial bones fabricated by inkjet printing technology," *J Artif Organs*, vol. 12, (3), pp. 200-205, 2009.

- [198] S. T. Becker, T. Douglas, Y. Acil, H. Seitz, S. Sivananthan, J. Wiltfang and P. H. Warnke, "Biocompatibility of individually designed scaffolds with human periosteum for use in tissue engineering," *J Mater Sci Mater Med*, vol. 21, (4), pp. 1255-1262, 2010.
- [199] F. Tamimi, J. Torres, U. Gbureck, E. Lopez-Cabarcos, D. C. Bassett, M. H. Alkhraisat and J. E. Barralet, "Craniofacial vertical bone augmentation: a comparison between 3D printed monolithic monetite blocks and autologous onlay grafts in the rabbit," *Biomaterials*, vol. 30, (31), pp. 6318-6326, 2009.
- [200] P. Habibovic, U. Gbureck, C. J. Doillon, D. C. Bassett, C. A. Blitterswijk and J. E. Barralet, "Osteoconduction and osteoinduction of low-temperature 3D printed bioceramic implants," *Biomaterials*, vol. 29, (7), pp. 944-953, 2008.
- [201] A. Gebhardt, *Rapid Prototyping*. 1st ed. Munich: Hanser, 2003, pp. 385.
- [202] A. A. Umland, R. K. Holman, S. Morissette, M. J. Cima and E. M. Sachs, "Strength of Green Ceramics with Low Binder Content," *J Am Ceram Soc*, vol. 84, (12), pp. 2809-2818, 2001.
- [203] E. Sachs, M. Cima, J. Cornie, D. Brancazio, J. Brecht, A. Curodeau, T. Fan, S. Khanuja, A. Lauder, J. Lee and S. Michaels, "Three-Dimensional Printing: The Physics and Implications of Additive Manufacturing," *CIRP Ann - Manuf Technol*, vol. 42, (1), pp. 257-260, 1993.
- [204] J. P. Vacanti, L. G. Cima and M. J. Cima, "Vascularized tissue regeneration matrices formed by solid free form fabrication techniques," US Patent 6176874, 2001.
- [205] R. M. German, *Sintering Theory and Practice*. New York: John Wiley & Sons, Inc., 1996, pp. 550.
- [206] S. J. Hollister, "Porous scaffold design for tissue engineering," *Nat Mater*, vol. 4, pp. 518-524, 2005.
- [207] V. Patel, A. S. Issever, A. Burghardt, A. Laib, M. Riesm and S. Majumdar, "MicroCT evaluation of normal and osteoarthritic bone structure in human knee specimens," *J Orthop Res*, vol. 21, (1), pp. 6-13, 2003.
- [208] S. Yang, K. F. Leong, Z. Du and C. K. Chua, "The design of scaffolds for use in tissue engineering. Part I. Traditional factors," *Tissue Eng*, vol. 7, (6), pp. 679-689, 2001.
- [209] T. S. Karande, J. L. Ong and C. M. Agrawal, "Diffusion in musculoskeletal tissue engineering scaffolds: design issues related to porosity, permeability, architecture, and nutrient mixing," *Ann Biomed Eng*, vol. 32, (12), pp. 1728-1743, 2004.
- [210] T. Tateishi, G. Chen and T. Ushida, "Biodegradable porous scaffolds for tissue engineering," *J Artif Organs*, vol. 5, (2), pp. 77-83,
- [211] S. T. Ho and D. W. Hutmacher, "A comparison of micro CT with other techniques used in the characterization of scaffolds," *Biomaterials*, vol. 27, pp. 1362-1376, 2006.
- [212] A. J. Katz and A. H. Thompson, "Prediction of rock electrical conductivity from Mercury injection measurements," *J Geophys Res*, vol. 92, (B1), pp. 599-608, 1987.

- [213] A. J. Katz and A. H. Thompson, "Quantitative prediction of permeability in porous rock," *Phys Rev B Condens Matter*, vol. 34, (11), pp. 8179-8181, 1986.
- [214] L. Guo, H. Li and X. Gao, "Phase transformations and structure characterization of calcium polyphosphate during sintering process," *Journal of Materials Science*, vol. 39, (23), pp. 7041-7047, 2004.
- [215] W. Weibull, "A statistical distribution function of wide applicability," *J. Appl. Mech. - Trans. ASME*, vol. 18, pp. 293-297, 1951.
- [216] O. Bermúdez, M. G. Boltong, F. C. M. Driessens and J. A. Planell, "Compressive strength and diametral tensile strength of some calcium orthophosphate cements: a pilot study," *J. Mater. Sci. Mater. Med.*, vol. 4, pp. 389-393, 1993.
- [217] D. K. Shetty, A. R. Rosenfield and W. H. Duckworth, "Mixed-Mode Fracture of Ceramics in Diametral Compression," *J Am Ceram Soc*, vol. 69, (6), pp. 437-443, 1986.
- [218] S. J. Ding, C. W. Wang, D. C. H. Chen and H. C. Chang, "In vitro degradation behavior of porous calcium phosphates under diametral compression loading," *Ceram Int*, vol. 31, (5), pp. 691-696, 2005.
- [219] R. I. Martin and P. W. Brown, "Mechanical properties of hydroxyapatite formed at physiological temperature," *J Mater Sci - Mater Med*, vol. 6, (3), pp. 138-143, 1995.
- [220] G. With, "Note on the use of the diametral compression test for the strength measurement of ceramics," *J Mater Sci Lett*, vol. 3, (11), pp. 1000-1002, 1984.
- [221] M. Mellor and I. Hawkes, "Measurement of tensile strength by diametral compression of discs and annuli," *Eng Geol*, vol. 5, (3), pp. 173-225, 1971.
- [222] M. N. Rahaman, *Ceramic Processing and Sintering*, 2nd ed. USA: Routledge, 2003, pp. 875-412.
- [223] J. A. Albright and R. A. Brand, *The Scientific Basis of Orthopaedics*, 1st ed. New York: Appleton-Century-Crofts, 1979, pp. 493.
- [224] P. Miranda, A. Pajares, E. Saiz, A. P. Tomsia and F. Guiberteau, "Mechanical properties of calcium phosphate scaffolds fabricated by robocasting," *J Biomed Mater Res A*, vol. 85, (1), pp. 218-227, 2008.
- [225] S. Deville, E. Saiza and A. P. Tomsia, "Freeze casting of hydroxyapatite scaffolds for bone tissue engineering," *Biomaterials*, vol. 27, (32), pp. 5480-5489, 2006.
- [226] J. Tian and J. Tian, "Preparation of porous hydroxyapatite," *J Mater Sci*, vol. 36, (12), pp. 3061-3066, 2001.
- [227] C. B. Carter and M. G. Norton, *Ceramic Materials: Science and Engineering*. 2007, pp. 716.
- [228] O. Hoffman, "The brittle strength of orthotropic materials," *J Compos Mater*, vol. 1, (2), pp. 200-206, 1967.

- [229] J. C. Le Huec, T. Schaeferbeke, D. Clement, J. Faber and A. Le Rebeller, "Influence of porosity on the mechanical resistance of hydroxyapatite ceramics under compressive stress," *Biomaterials*, vol. 113, (2), pp. 113-118, 1995.
- [230] E. Ryshkewitch, "Compression Strength of Porous Sintered Alumina and Zirconia, 9th Communication to Ceramography," *J Am Ceram Soc*, vol. 36, (2), pp. 65-68, 1953.
- [231] L. H. He, O. C. Standard, T. T. Y. Huang, B. A. Latella and M. V. Swain, "Mechanical behaviour of porous hydroxyapatite," *Acta Biomater*, vol. 4, (3), pp. 577-586, 2008.
- [232] E. Z. Wang and N. G. Shrive, "Brittle fracture in compression: Mechanisms, models and criteria," *Eng Fract Mech*, vol. 52, (6), pp. 1107-1126, 1995.
- [233] A. P. Roberts and E. J. Garboczi, "Elastic Properties of Model Porous Ceramics," *J Am Ceram Soc*, vol. 83, (12), pp. 3041-3048, 2000.
- [234] I. Vardoulakis, J. F. Labuz, E. Papamichos and J. Tronvoll, "Continuum fracture mechanics of uniaxial compression on brittle materials," *Int J Solids Struct*, vol. 35, (31-32), pp. 4313-4335, 1998.
- [235] T. Sadowski and S. Samborski, "Development of damage state in porous ceramics under compression," *Comput Mater Sci*, vol. 43, (1), pp. 75-81, 2008.
- [236] T. Sadowski and S. Samborski, "Prediction of the mechanical behaviour of porous ceramics using mesomechanical modeling," *Comput Mater Sci*, vol. 28, (3-4), pp. 512-517, 2003.
- [237] D. J. Green, *An Introduction to the Mechanical Properties of Ceramics*. Cambridge: Cambridge University Press, 1998, pp. 336.
- [238] M. J. Bannister, "Shape Sensitivity of Initial Sintering Equations," *J Am Ceram Soc*, vol. 51, (10), pp. 548-553, 1968.
- [239] N. Ramakrishnan and V. S. Arunachalam, "Effective elastic moduli of porous ceramic materials," *J Am Ceram Soc*, vol. 76, pp. 2745-2752, 1993.
- [240] A. S. Wagh, J. P. Singh and R. B. Poepfel, "Dependence of ceramic fracture properties on porosity," *J Mater Sci*, vol. 28, pp. 3589-3593, 1993.
- [241] A. R. Boccaccini and Z. Fan, "A new approach for the Young's Modulus porosity correlation of ceramic materials," *Ceram Int*, vol. 23, (3), pp. 239-245, 1997.
- [242] Q. Chang, D. L. Chen, H. Q. Ru, X. Y. Yue, L. Yu and C. P. Zhang, "Toughening mechanisms in iron-containing hydroxyapatite/titanium composites," *Biomaterials*, vol. 31, (7), pp. 1493-1501, 2010.
- [243] M. F. Ashby and R. F. Mehl Medalist, "The mechanical properties of cellular solids," *Metall Mater Trans A*, vol. 14, (9), pp. 1755-1769, 1983.
- [244] A. A. Griffith, "The Phenomena of Rupture and Flow in Solids," *Philos Trans R Soc London, Ser A*, vol. 221, pp. 163-198, 1921.
- [245] R. Hill, "A Theory of the Yielding and Plastic Flow of Anisotropic Metals," *Proc R Soc Lond A*, vol. 193, (1033), pp. 281-297, 1948.

- [246] M. A. Merkx, J. C. Maltha, H. P. Freihofer and A. M. Kuijpers-Jagtman, "Incorporation of three types of bone block implants in the facial skeleton," *Biomaterials*, vol. 20, (7), pp. 639-645, 1999.
- [247] J. X. Lu, A. Gallur, B. Flautre, K. Anselme, M. Descamps, B. Thierry and P. Hardouin, "Comparative study of tissue reactions to calcium phosphate ceramics among cancellous, cortical, and medullar bone sites in rabbits," *J Biomed Mater Res*, vol. 42, (3), pp. 357-367, 1998.
- [248] P. J. Ehrlich and L. E. Lanyon, "Mechanical strain and bone cell function: a review," *Osteoporos Int*, vol. 13, (9), pp. 688-700, 2002.
- [249] M. C. von Doernberg, B. von Rechenberg, M. Bohner, S. Grünenfelder, G. H. van Lenthe, R. Müller, B. Gasser, R. Mathys, G. Baroud and J. Auer, "In vivo behavior of calcium phosphate scaffolds with four different pore sizes," *Biomaterials*, vol. 27, (30), pp. 5186-5198, 2006.
- [250] V. Karageorgiou and D. Kaplan, "Porosity of 3D biomaterial scaffolds and osteogenesis," *Biomaterials*, vol. 26, (27), pp. 5474-5491, 2005.
- [251] R. L. Goldberg and L. M. Kolibas, "An improved method for determining proteoglycans synthesized by chondrocytes in culture," *Connect Tissue Res*, vol. 24, (3-4), pp. 265-275, 1990.
- [252] J. F. Woessner, "Determination of hydroxyproline content in connective tissues. chapter 23." in *the Methodology of Connective Tissue Research*, Hall DA ed. Anonymous Oxford: Joynson-Bruvvers Ltd, 1967, pp. 227-234.
- [253] Y. J. Kim, R. L. Sah, J. Y. Doong and A. J. Grodzinsky, "Fluorometric assay of DNA in cartilage explants using Hoechst 33258," *Anal Biochem*, vol. 174, (1), pp. 168-176, 1988.
- [254] V. T. Cleynenbreugel, V. H. Oosterwyck and V. J. Stolen, "Trabecular bone scaffolding using a biomimetic approach," *J Mater Sci - Mater Med*, vol. 13, pp. 1245-1249, 2002.
- [255] J. R. Johanson, "A rolling theory for granular solids," *ASME, J Appl Mech*, vol. 32, ser. E, (4), pp. 842-848, 1965.
- [256] J. C. Cunningham, "Experimental studies and modeling of the roller compaction of pharmaceutical powders," *Derexel University*, pp. 13, 2006.
- [257] V. P. Katashinskii and M. B. Shtern, "Stress-strain state of powder being rolled in the densification zone, I. Mathematical model of rolling in the densification zone," *Powder Metall Met Ceram*, vol. 11(251), pp. 17-21, 1983.
- [258] V. P. Katashinskii and M. B. Shtern, "Stress-strain state of powder being rolled in the densification zone, II. Distribution of density, longitudinal strain, and contact stress in the densification zone," *Powder Metall Met Ceram*, vol. 12(252), pp. 9-13, 1983.
- [259] M. B. Shtern, "Plane deformation characteristics of compressible materials," *Powder Metall Met Ceram*, vol. 3(231), pp. 14-21, 1982.
- [260] M. L. Abdel-Ati, O. M. Hemeda, M. M. Mosaad and D. M. Hemeda, "Thermal properties of pure and doped (polyvinyl-alcohol) PVA," *J Therm Anal*, vol. 42, pp. 1113-1122, 1994.

- [261] J. G. Pritchard, *Poly (Vinyl Alcohol): Basic Properties and Uses*. London: Gordon and Breach, 1970, pp. 139.
- [262] J. F. Bredt, T. C. Anderson and D. B. Russell, "Three dimensional printing materials system," US 6416850, 2002.
- [263] W. Swieszkowski, B. H. Tuan, K. J. Kurzydowski and D. W. Huttmacher, "Repair and regeneration of osteochondral defects in the articular joints," *Biomol Eng Nov*, vol. 5, (489), pp. 495, 24. 2007.
- [264] J. Barralet, U. Gbureck, P. Habibovic, E. Vorndran, C. Gerard and C. J. Doillon, "Angiogenesis in calcium phosphate scaffolds by inorganic copper ion release," *Tissue Eng Part A*, vol. 15, (7), pp. 1601-1609, 2009.